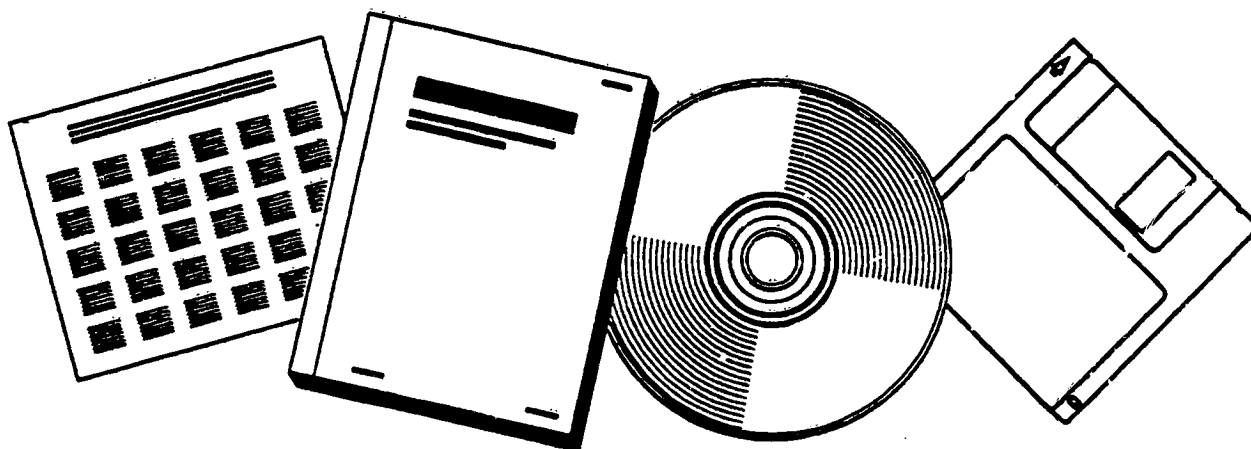NTIS.
Information is our business.

TWO-LAYER VARIABLE INFILTRATION CAPACITY LAND SURFACE REPRESENTATION FOR GENERAL CIRCULATION MODELS

WASHINGTON UNIV., SEATTLE

MAY 94

Abstract: A simple two-layer variable infiltration capacity (VIC-2L) land surface model suitable for incorporation in general circulation models (GCMs) is described. The model consists of a two-layer characterization of the soil within a GCM grid cell, and uses an aerodynamic representation of latent and sensible heat fluxes at the land surface. The effects of GCM spatial subgrid variability of soil moisture and a hydrologically realistic runoff mechanism are represented in the soil layers. The model was tested using long-term hydrologic and climatalogical data for Kings Creek, Kansas to estimate and validate the hydrological parameters. Surface flux data from three First International Satellite Land Surface Climatology Project Field Experiments (FIFE) intensive field compaigns in the summer and fall of 1987 in central Kansas, and from the Anglo-Brazilian Amazonian Climate Observation Study (ABRACOS) in Brazil were used to validate the mode-simulated surface energy fluxes and surface temperature.

Department of Civil Engineering
University of Washington
Seattle, Washington, 98195

A TWO-LAYER VARIABLE INFILTRATION CAPACITY LAND SURFACE REPRESENTATION FOR GENERAL CIRCULATION MODELS

By

XU LIANG

Water Resources Series
Technical Report No. 140

May 1994

REPORT DOCUMENTATION PAGE

PB96-197165

2 REPORT DATE	3. REPORT TYPE AND DATES COVERED
May 1994	Final

4. TITLE AND SUBTITLE

A Two-Layer Variable Infiltration Capacity Land Surface
Representation for General Circulation Models

5. FUNDING NUMBERS

816335-01-0
C DE-AC06-76RLO 1830
G NAGW-2556

6. AUTHOR(S)

Xu Liang

7. PERFORMING ORGANIZATION NAME(S) AND ADDRESS(ES)

University of Washington
Dept. of Civil Engineering
Seattle, WA 98195

8. PERFORMING ORGANIZATION REPORT NUMBER

Water Resources Series
Technical Report No. 140

9. SPONSORING/MONITORING AGENCY NAME(S) AND ADDRESS(ES)

U.S. Environmental Protection Agency

U.S. Dept of Energy

National Aeronautics and Space Administration

10. SPONSORING/MONITORING AGENCY REPORT NUMBER

11. SUPPLEMENTARY NOTES

12. DISTRIBUTION/AVAILABILITY STATEMENT

12b. DISTRIBUTION CODE

13. ABSTRACT (Maximum 200 words)

14. SUBJECT TERMS

15. NUMBER OF PAGES

236

16. PRICE CODE

17. SECURITY CLASSIFICATION OF REPORT	18. SECURITY CLASSIFICATION OF THIS PAGE	19. SECURITY CLASSIFICATION OF ABSTRACT	20. LIMITATION OF ABSTRACT
Unclassified	Unclassified	Unclassified	UL

ABSTRACT

A simple two-layer variable infiltration capacity (VIC-2L) land surface model suitable for incorporation in general circulation models (GCMs) is described. The model consists of a two-layer characterization of the soil within a GCM grid cell, and uses an aerodynamic representation of latent and sensible heat fluxes at the land surface. The effects of GCM spatial subgrid variability of soil moisture and a hydrologically realistic runoff mechanism are represented in the soil layers. In the upper layer, the spatial distribution of infiltration and soil moisture capacities is included. The lower layer is lumped spatially and uses a nonlinear drainage representation. The model partitions the area of interest into multiple land surface cover types; for each land cover type the fraction of plant roots in the upper and lower zone is specified. Evaporation occurs via canopy evaporation, evaporation from bare soil, and transpiration, which is represented using a canopy and architectural resistance formulation. The model was tested using long-term hydrologic and climatalogical data for Kings Creek, Kansas to estimate and validate the hydrological parameters. Surface flux data from three First International Satellite Land Surface Climatology Project Field Experiment (FIFE) intensive field campaigns in the summer and fall of 1987 in central Kansas, and from the Anglo-Brazilian Amazonian Climate Observation Study (ABRACOS) in Brazil were used to validate the model-simulated surface energy fluxes and surface temperature.

In addition, a derived distribution approach which accounts for the effects of subgrid scale spatial variabilities of precipitation on surface energy fluxes, soil moisture, and runoff production was developed for an extended version of VIC-2L model. The derived distribution approach differs from pixel-based approaches which discretize precipitation over a spatial domain, and from previous statistical approaches that combine the point precipitation distribution with the point statistical distribution of selected land surface characteristics. The results of the derived distribution method are compared with those obtained using an exhaustive pixel-based approach, and the results obtained by applying uniform spatially averaged precipitation to the VIC-2L model. Under most conditions, the derived distribution approach gives good approximations to the pixel-based approach, and is superior to the constant precipitation approach for surface fluxes, surface temperature, runoff, and soil moisture. Finally, VIC-2L sensitivity of predictions to model parameters were explored for two different climate regimes using both fractional factorial and one-at-a-time sensitivity analyses.

ACKNOWLEDGMENTS

TABLE OF CONTENTS

LIST OF FIGURES

vi

LIST OF TABLES

ix

LIST OF SYMBOLS

A	fraction of an area for which the infiltration capacity is less than i
$A_{cr}[n]$	fraction of soil with soil moisture greater than or equal to the critical value
$A_w[n]$	fraction of soil with soil moisture greater than or equal to the value associated with permanent wilting point
A_s	fraction of bare soil that is saturated
B	soil wetness exponent
B_p	pore size distribution index
C_m	difference between the canopy storage capacity and the water stored on the canopy divided by model time step ($mm\ hr^{-1}$) in Eq. (5.3)
$C_s[n]$	soil heat capacity ($J\ m^{-3}\ K^{-1}$)
$C_v[n]$	fraction of surface cover ($n=1,\ 2,\ \cdots,\ N,\ N+1$)
$C_w[n]$	transfer coefficient for water which is estimated taking into account atmospheric stability
D_1	depth of first thermal soil layer (m)
D_2	depth of second thermal soil layer (m)
D_m	maximum subsurface flow rate ($mm\ hr^{-1}$)
D_s	fraction of maximum subsurface flow
DET	sum of the absolute difference of monthly evaporation depth in Chapter 4 ($mm\ mo^{-1}$)
DR	sum of the absolute difference of monthly runoff depth in Chapter 4 ($mm\ mo^{-1}$)
DSH	sum of the absolute difference of monthly sensible heat flux in Chapter 4 ($W\ m^{-2}$)
E	total effective evaporation rate ($mm\ hr^{-1}$)
$E(P_\mu)$	areal mean precipitation rate over the rain-covered fraction μ of a grid cell (or an area) ($mm\ hr^{-1}$)
$E[Q_{inf}]$	expected value of the depth of infiltration excess runoff rate ($mm\ hr^{-1}$)
$E[Q_{sat}]$	expected value of the depth of saturation excess runoff rate ($mm\ hr^{-1}$)

E_1 — evaporation rate from bare soil from layer 1 (mm hr^{-1})

E_2 — evaporation rate from layer 2 underlying bare soil (mm hr^{-1})

$E_c[n]$ — canopy evaporation rate (mm hr^{-1})

$E_c^*[n]$ — maximum canopy evaporation rate (mm hr^{-1})

E_j — the effect of jth factor (Chapter 4)

$E_p[n]$ — potential evaporation rate from a free water surface (mm hr^{-1})

$E_t[n]$ — total transpiration rate from vegetation (mm hr^{-1})

$E_{\mu 1}[n]$ — evaporation rate from bare soil from layer 1 within μ (mm hr^{-1})

$E_1^t[n]$ — transpiration rate from layer 1 (mm hr^{-1})

$E_2^t[n]$ — transpiration rate from layer 2 (mm hr^{-1})

ET — annual total evaporation depth (mm yr^{-1})

$F_w[n]$ — defined by Eq. (2.7)

F^* — maximum surface infiltration rate in Eq. 5.2 (mm hr^{-1})

G — effective ground heat flux (W m^{-2})

$G[n]$ — ground heat flux (W m^{-2})

$G'[n]$ — heat flux across a horizontal soil plane at depth D_1 (W m^{-2})

$G''[n]$ — heat flux across the bottom soil boundary at depth D_2 (W m^{-2})

H — effective sensible heat flux (W m^{-2})

$H[n]$ — sensible heat flux (W m^{-2})

$H_f[n]$ — heat flux (W m^{-2})

I — a column with all plus signs in factorial experiments (Chapter 4)

K — von Karman's turbulent velocity profile constant

K_L — a constant in Eq. (2.3), taken to be 0.2 mm

K_s — saturated hydraulic conductivity (mm hr^{-1})

$LAI[n,m]$ — leaf area index for the nth surface cover class in month m

L_e — latent heat of vaporization (J kg^{-1})

N — the largest number of vegetation cover types

N+1 — corresponding to bare soil

N_j — the number of "+" signs in column j (Chapter 4)

P — precipitation rate (mm hr^{-1})

$P(x)$ — $P(x)=P_x$

P_i — point precipitation intensity (mm hr^{-1})

P_m grid cell average precipitation rate (mm hr^{-1})

$P_t[n]$ precipitation throughfall rate (mm hr^{-1})

P_x precipitation rate varying along x axis (mm hr^{-1})

$P_{x,j}$ upper and lower limits of integrals in Eq. 5.7 (j=1, 2, 3, and 4)

Q total runoff rate of an area (or a grid cell) (mm hr^{-1})

$Q_{12}[n]$ drainage rate from layer 1 to layer 2 (mm hr^{-1})

$Q_b[n]$ subsurface runoff rate (mm hr^{-1})

$Q_m(A)$ monthly maximum hourly runoff rate from average approach (mm hr^{-1})

$Q_m(D)$ monthly maximum hourly runoff rate from derived distribution approach (mm hr^{-1})

$Q_m(P)$ monthly maximum hourly runoff rate from pixel-based approach (mm hr^{-1})

$Q_b'[n]$ subsurface runoff rate from Eq. (2.28) when the water balance results in $W_2^+[n] > W_2^c$ (mm hr^{-1})

$Q_b''[n]$ soil moisture excess rate when the water balance results in $W_2^+[n] > W_2^c$; in this case, $Q_b[n]=Q_b'[n]+Q_b''[n]$ (mm hr^{-1})

$Q_d[n]$ direct runoff rate (mm hr^{-1})

$Q_{\mu 12}[n]$ drainage rate from layer 1 to layer 2 within μ (mm hr^{-1})

$Q_{\mu b}[n]$ subsurface runoff rate within μ (mm hr^{-1})

$Q_{\mu d}$ total direct runoff rate of the fraction coverage of μ (mm hr^{-1})

$Q_{\mu d}[n]$ direct runoff rate of cover class n over the fraction coverage of μ (mm hr^{-1})

R annual total runoff rate (mm yr^{-1})

$Ri_B[n]$ bulk Richardson number

R_E ratio of the monthly sum of the absolute difference between the average and pixel-based approaches to the monthly sum of the absolute difference between the derived distribution and pixel-based approaches for evaporation

R_H ratio of the monthly sum of the absolute difference between the average and pixel-based approaches to the monthly sum of the absolute difference between the derived distribution and pixel-based

approaches for sensible heat flux

R_L downward long-wave radiation (W m^{-2})

R_Q ratio of the monthly sum of the absolute difference between the average and pixel-based approaches to the monthly sum of the absolute difference between the derived distribution and pixel-based approaches for runoff

R_{T_s} ratio of the monthly sum of the absolute difference between the average and pixel-based approaches to the monthly sum of the absolute difference between the derived distribution and pixel-based approaches for surface temperature

$R_n[n]$ net radiation (W m^{-2})

R_s shortwave radiation received at soil or vegetation surface (W m^{-2})

S_i storage deficit of soil water

S_{ij} sign of row i and column j

SH   annually averaged sensible heat flux (W m^{-2})

T   annually averaged surface temperature in Chapter 4 ($^{\circ}$K)

$T[n]$ soil temperature defined by Eq. (2.43) ($^{\circ}$K)

$T_1[n]$ soil temperature at depth D_1 ($^{\circ}$K)

$T_1^-[n]$ soil temperature at depth D_1 at the beginning of a time step ($^{\circ}$K)

$T_1^+[n]$ soil temperature at depth D_1 at the end of a time step ($^{\circ}$K)

T_2 constant soil temperature at depth D_2 ($^{\circ}$K)

$T_a[n]$ air temperature ($^{\circ}$K)

T_{min} hourly minimum effective surface temperature over a year ($^{\circ}$K)

T_s effective surface temperature ($^{\circ}$K)

$T_s[n]$ surface temperature ($^{\circ}$K)

$T_s^-[n]$ surface temperature of the bottom surface of the air layer at the beginning of a time step ($^{\circ}$K)

$T_s^+[n]$ surface temperature of the bottom surface of the air layer at the end of a time step ($^{\circ}$K)

V   volume of rainfall simulated by climate model within a grid area (m^3)

V_a modified wind speed defined by Eq. (2.10) (m s^{-1})

$W_i[n]$ amount of intercepted water in storage in the canopy layer (mm)

$W_{im}[n]$ — maximum amount of water that canopy layer can intercept (mm)

$W_{initial}$ — initial soil moisture of combined layers (mm)

$W_j[n]$ — soil moisture content in soil layer j, where $j=1, 2$ (mm)

W_s — fraction of maximum soil moisture content of layer 2

$W_{\mu 1}$ — average soil moisture content of all the cover classes in layer 1 within μ (mm)

$W_{\mu 1}[n]$ — soil moisture content in layer 1 within μ (mm)

$W_1^-[n]$ — soil moisture content in layer 1 at the beginning of a time step (mm)

$W_1^+[n]$ — soil moisture content in layer 1 at the end of a time step (mm)

$W_2^-[n]$ — soil moisture content at the beginning of a time step in layer 2 (mm)

$W_2^+[n]$ — soil moisture content at the end of a time step in layer 2 (mm)

W^c — maximum soil moisture of combined layers (mm)

W_1^c — maximum soil moisture content of layer 1 (mm)

W_2^c — maximum soil moisture content of layer 2 (mm)

W_j^{cr} — critical value above which transpiration is not affected by the soil moisture stress (mm)

W_{1a}^{err} — monthly maximum relative error of upper zone moisture for the average approach

W_{1d}^{err} — monthly maximum relative error of upper zone moisture for the derived distribution approach

W_a^{err} — monthly maximum relative error of upper and lower zone moisture for the average approach

W_d^{err} — monthly maximum relative error of upper and lower zone moisture for the derived distribution approach

W_j^w — soil moisture content at permanent wilting point (mm)

$W_{\mu 1}^-[n]$ — soil moisture content in layer 1 at the beginning of a time step within μ (mm)

$W_{\mu 1}^+[n]$ — soil moisture content in layer 1 at the end of a time step within μ (mm)

$W_{\mu 2}^-[n]$ — soil moisture content at the beginning of a time step in layer 2 within μ (mm)

$W_{\mu 2}^{+}[n]$ soil moisture content at the end of a time step in layer 2 within μ (mm)

a integral limit

$a^2[n]$ surface drag coefficient for the case of near-neutral stability

b_i infiltration shape parameter

c defined by Eq. (2.11)

c_p specific heat of air at constant pressure (J kg^{-1} K^{-1})

$d_0[n]$ zero plane displacement height (m)

e vapor pressure (P_a)

e_s saturated vapor pressure (P_a)

$f[n]$ fraction of the time step required for canopy evaporation to exhaust the canopy interception storage

$f(P_x)$ pdf of P_x in Eq. 5.7

$f(z_x)$ pdf of z_x in Eq. 5.7

$f_1[n]$ fraction of roots in layer 1

$f_2[n]$ fraction of roots in layer 2

f^* infiltration rate for the upper soil layer in Eq. 5.5 (mm hr^{-1})

f_i^* infiltration rate in Eq. 5.6 (mm hr^{-1})

$f(P_i)$ probability density function (pdf) of P_i (defined in Eq. 5.1)

$f_s(s)$ two-parameter gamma pdf of s

$f_z(z)$ pdf of the local value of the topography-soils index of Topmodel

g acceleration due to gravity (m s^{-2})

$g_{sm}[n]$ soil moisture stress factor

i infiltration capacity (mm)

i_0 point infiltration capacity corresponding to A_s (mm)

i_{cr} defined by Eq. (6.3)

i_m maximum infiltration capacity (mm)

i_w defined by Eq. (6.2)

l_j the number of possible options (levels) of parameter p_j ($j=1, 2, \cdots, k$)

n	vegetation surface cover class index, $n=1, 2, \cdots, N, N+1$ (in Chapter 4, n represents the total number of experimental runs)
p_j	the jth model parameter ($j=1, 2, \cdots, k$)
q	runoff rate from a grid cell (in Eqs. 5.2, 5.4, and 5.5) (mm hr^{-1})
$r_0[n]$	architectural resistance to vapor transfer due to the variation of the gradient of specific humidity between the leaves and the overlying air in the canopy layer (s m^{-1})
$r_a[n]$	aerodynamic resistance to the transfer of momentum (s m^{-1})
$r_c[n]$	canopy resistance to water vapor movement (s m^{-1})
$r_h[n]$	aerodynamic resistance for heat transfer by convection (s m^{-1})
$r_{min}[n]$	minimum canopy resistance to vapor transport (s m^{-1})
$r_w[n]$	aerodynamic resistance to the transfer of water vapor (s m^{-1})
s	surface layer point effective relative soil saturation in Eq. 5.5
$\tan\chi$	land surface slope
t	time (s, hr)
$u_n(z_2)$	wind speed over the nth surface cover class at elevation z_2 (m s^{-1})
y_i	the value obtained from the ith experimental run
z	soil depth (m) (or local value of the topography-soils index of Topmodel in Chapter 5)
$z_0[n]$	roughness length in logarithmic wind speed representation (m)
$z_2[n]$	height (m)
$z_a[n]$	height of the top surface of the air layer (m)
$z_r[n]$	reference height defined by Eq. (2.9) (m)
z_x	a variable along the x axis in Eq. 5.7
$z_{x,j}$	upper and lower limits of integrals in Eq. 5.7
z^*	critical value of the Topmodel index at which saturation occurs
$\alpha[n]$	albedo (integral reflectivity of all wave lengths for shortwave) of nth surface cover class
γ	psychrometric constant, taken to be 66 P$_a$ K^{-1}
Δ	gradient of saturation vapor pressure-temperature relationship (P$_a$ K^{-1})

$\Delta H_s[n]$	change in energy storage in the layer per unit time, per unit area $(W\ m^{-2})$
ΔT	temporal resolution of climate model (hr)
$\Delta T[n]$	temperature gradient defined in Eq. (2.40) $(^{\circ}K)$
Δt	model time step, taken to be one hour (hr)
ΔX	spatial resolution of climate model (m)
$\epsilon[n]$	integrated emissivity primarily to long wave radiation
θ	soil porosity (fraction)
θ_{cr}	critical point (fraction)
θ_f	soil water field capacity (fraction)
θ_r	residual moisture content (mm)
θ_w	soil water vegetation wilting point (fraction)
$\kappa[n]$	soil thermal conductivity $(W\ m^{-1}\ K^{-1})$
μ	a fraction of a grid cell (or an area) covered by rainfall
ρ_a	mass density of air $(kg\ m^{-3})$
ρ_w	mass density of liquid water $(kg\ m^{-3})$
$\rho_w L_e E[n]$	latent heat flux $(W\ m^{-2})$
σ	Stefan-Boltzmann constant $(5.67 \times 10^{-8},\ W\ m^{-2}\ K^{-4})$

Note: 1. The argument n in [n] refers to the surface cover class index.

2. When "μ" is replaced with "$1 - \mu$", all the symbols represent the corresponding quantities over the area of $1 - \mu$.

CHAPTER 1   INTRODUCTION

1.1. Motivation for and dissertation structure

The parameterization of the hydrologic and thermal characteristics of the land surface is important for general circulation models (GCMs) used for climate prediction and weather forecasting (e.g., Dickinson 1991, Dickinson and Kennedy 1991, Wood 1991, Shuttleworth 1991a, Henderson-Sellers and Pitman 1992, among others). Garratt (1993) reviewed the land surface and boundary-layer treatments in some 20 GCMs through sensitivity studies of climate simulations, and found that the regional and global climate are most sensitive to albedo, surface roughness length, vegetation coverage, and soil moisture distribution. The inclusion of a canopy scheme which allows more reasonable consideration of effects of albedo, roughness, and soil moisture significantly improved the simulated climate. It also facilitated studies of the effect of deforestation on climate (see, for example, studies of the regional impact of Amazonian deforestation by Sud et al. (1990), Pitman et al. (1993), Henderson-Sellers et al. (1993), and Eltahir and Bras (1993), among others).

Although complicated canopy schemes such as BATS (Biosphere-Atmosphere Transfer Scheme, Dickinson et al. 1986), SiB (Simple Biosphere model, Sellers et al. 1986), and BEST (Bare Essentials of Surface Transfer, Pitman et al. 1991), and simpler canopy models (e.g., Noilhan and Planton 1989) have been implementated into GCMs to give more reasonable climate simulations, precipitation, evaporation, soil moisture, and surface temperature are still not, in general, well simulated. Examination of systematic errors in GCM climate simulations, particularly over land areas, is an active research area. Verseghy et al. (1993) found that the assumption made in many land surface schemes that excess surface water is removed immediately from the land surface system can result in substantial overestimates of surface temperatures in continental interiors. Garratt (1993), in his review of sensitivity studies,

suggested that there is a need for a more realistic land surface representation in GCMs, particularly with respect to (1) surface fluxes at the appropriate horizontal resolution, (2) surface runoff and canopy interception processes, and (3) the spatial distribution of rainfall within a GCM grid.

In this dissertation, a two-layer variable infiltration capacity (VIC-2L) model that attempts to incorporate the above three features suggested by Garratt (1993) is developed. The model includes a canopy layer, the effects of spatial subgrid variability of soil moisture with a hydrologically reasonable runoff mechanism, and the influence of the subgrid spatial distribution of rainfall. The development of the VIC-2L model is described in Chapter 2, and is evaluated using observed data from the FIFE (central Kansas, USA) and ABRACOS (Amazonia) sites in Chapter 3. These two sites are sufficiently small that the assumption of constant precipitation within the measurement area is reasonable. Chapter 4 explores the sensitivities of the VIC-2L model parameters. In Chapter 5, an extension of the VIC-2L model with a one-dimensional derived distribution representation of spatial subgrid variability in precipitation is described. The results for versions of the VIC-2L model with constant and spatially varying precipitation are compared and evaluated. Conclusions and recommendations of future work are given in Chapter 6. In the remainder of this chapter, several land surface parameterizations developed previously are reviewed. Land surface schemes that include the spatial variability of rainfall within a grid area are reviewed in Chapter 5.

1.2. Background

The problem of how to represent land surface processes in general circulation models that are used for climate simulation and numerical weather prediction has drawn the interest of climate modelers, and increasingly, hydrologists and systems ecologists. Early generation GCMs did not include representations of land surface hydrology, instead they used prescribed surface wetness and temperature, and thus could not account for the feedbacks between the land surface and atmosphere. In retrospect, such representations have

proved useful only for examining the limiting cases: perpetually wet and dry surfaces (Shukla and Mintz, 1982). These early studies confirmed the importance of including the interactions between the land surface hydrology and atmosphere.

Notwithstanding the desirability of better representing the land surface in GCMs, the spatial scale of the GCM "grid box" is so large (typically at least 100 km) that only relatively simple models can be justified, especially considering the other sources of uncertainty in climate and weather prediction (e.g., cloud physics, ocean circulation). Manabe et al. (1969) followed this logic in using Budyko's 'bucket' model to represent the land surface hydrology at the global scale. The bucket model assumes that all rainfall is infiltrated until soil moisture capacity is exceeded, whereafter the excess precipitation becomes runoff. Manabe's bucket model uses a simple relationship between actual and potential evaporation which is often referred to as a beta function. Milly (1992) pointed out the conceptual inconsistency in calculating the potential evaporation and the coefficient "beta" for this kind of model formulation by using the modeled surface temperature to evaluate potential evaporation. He argued that the appropriate temperature to use for evaluating potential evaporation is that of a freely evaporating surface, and described two approaches to remove the inconsistency. The bucket model is clearly simplistic with respect to infiltration and runoff production, in addition to evaporation, and ignores vegetation effects on evapotranspiration, except to the extent that the beta function acts as a surrogate. Another problem with the bucket model is that in its most common implementation, the parameters are assumed to be constant over the globe, although this assumption can be relaxed using suitable data, such as globally varying soil water holding capacities.

While the shortcomings of the bucket model and related simple representations of the land surface, such as the two-layer surface model used in the GISS GCM (Hansen et al. 1983) are clear, the pathway toward more realistic parameterizations is less obvious. The difficulty of estimating parameters globally, as well as the desire to keep the complexity of the land

surface representation compatible with that used to represent other elements of the atmosphere-land-ocean system, are important considerations in determining what form the next generation of land surface hydrology models for GCMs should take. Mintz (1984) and Rowntree (1988) reviewed the impact of land surface boundary conditions on simulated climate and pointed out that the atmosphere is sensitive to land surface evapotranspiration, which is largely affected by changes in available soil moisture or in albedo. Their review stimulated the incorporation of improved of canopy and soil formulations in land-surface schemes in GCMs (Garratt 1993).

One direction that has been pursued is to improve the representation of soil moisture dynamics, and especially to represent vegetation interactions with the soil column and the atmosphere explicitly so that effects of biosphere-climate interactions can be studied. The resulting class of models is known as soil vegetation atmosphere transfer schemes (SVATS). Among the SVATS that have been developed for GCM use are BATS (Dickinson et al. 1986, Dickinson et al. 1993) and SiB (Sellers et al. 1986). A distinguishing feature of SVATS, which is evident in both BATS and SiB, is that they have a high level of vertical resolution and structure, but a low level of horizontal resolution (Wood 1991). For instance, the parameters for the soil and vegetation properties are assumed constant within a GCM grid, thus ignoring spatial heterogeneity. In addition, most SVATS use a "flat earth" representation of the land surface which neglects the effects of topography on runoff production and soil moisture dynamics. Because of their emphasis on vertical structure, SVATS arguably do a better job of partitioning incoming solar radiation into latent and sensible heat than they do in accounting for soil moisture dynamics and runoff production.

An alternative line of investigation is to develop simpler land surface models that still incorporate important features of the governing hydrological processes. For example, Xue et al. (1991) simplified SiB in three aspects. These are the parameterization of the diurnal variation of surface albedo, the effect of root zone soil moisture on stomatal resistance, and the surface stress and fluxes of heat and moisture between the top of the vegetation canopy and

the atmospheric reference level. After these simplifications, the two vegetation stories in SiB become one layer. With negligible loss of accuracy, the number of parameters of SiB model was reduced by Xue et al. (1991) from 44 to 21.

Mahrt and Pan (1984) developed a two-layer soil hydrological scheme for use in GCMs and numerical weather prediction models. There are three major features in their scheme. First, it has a thin upper layer used to represent the large vertical moisture gradient near the surface during evaporation. Second, it includes a strong dependence of hydraulic diffusivity on the vertical distribution of soil moisture. Finally, it estimates surface evaporation by using near-surface soil water flux information. They also suggests that transpiration can be estimated by relating it to layer-averaged moisture and potential evaporation if vegetation is present.

Abramopoulos et al. (1988) developed a simple land surface scheme that includes multiple soil layers with specified hydraulic conductivity and matric potential functions rather than a constant diffusivity to describe the soil water dynamics by using Darcy's law. Vegetative resistance, evaporation from intercepted precipitation and dew, evaporation from bare soil, and transpiration are all explicitly represented. Abramopoulos et al. (1988) compared the evaporation predicted using an areally weighted average of a heterogeneous land surface with the evaporation obtained using area-weighted vegetation and soil characteristic parameters, and found that it is better to average the subgrid fluxes than to average the soil and vegetation parameters.

Noilhan and Planton (1989) developed a simple land surface parameterization for meteorological models. Unlike BATS and SiB where the canopy and soil temperatures can vary, they treated the system as isothermal with equal canopy and the upper soil layer temperatures. Also, their model does not calculate soil fluxes beneath the vegetation. BATS and SiB both calculate detailed fluxes from the soil beneath the canopy, the open areas between the canopy, and the canopy itself.

Pan (1990) used the bucket concept to estimate the actual evaporation with vegetation lumped with soil in the National Meteorological Center medium-

range forecast (NMC MRF) model. He overcame the inconsistency problem noted by Milly (1992) by calculating the potential evaporation with a hypothetical temperature from a wet surface using the Mahrt and Ek (1984) method, rather than with the unsaturated surface temperature when the soil is dry. When vegetation is present, potential evaporation is calculated using Monteith's minimum resistance concept.

Pitman et al. (1991) and Yang and Pitman (199ɔ, developed a land surface scheme which uses simplified (as compared with BATS) albedo and stomatal resistance formulations, and explicit representation of frozen soils. In addition, it calculates infiltration, runoff, and soil evaporation following Eagleson's (1970) approach. The canopy layer is formulated as a nonisothermal system like BATS, although the algorithm for canopy temperature is different.

Sievert et al. (1992) developed a soil-vegetation model for use in a mesoscale atmospheric model. The canopy model is based on the work of Deardorff (1978) and Dickinson (1984). The soil model is based on Sievers et al. (1983) which includes a complicated treatment of heat and moisture transport within the soil. The soil temperature and moisture content are represented by two coupled differential equations.

Pollard and Thompson (Bonan et al. 1992, Bonan et al. 1993) developed a six-layer soil model for GCMs that explicitly represents the effects of soil freezing and thawing on latent heat flux. The snow cover is represented by three-layers. The canopy layer is formulated in a similar way to BATS and SiB, but is less complex. The scheme has been used to study the effects of boreal forests on climate in the National Center for Atmospheric Research community climate model CCM1 (Bonan et al. 1992).

Kondo and Watanabe (1992) developed a multilayer energy budget model for a vegetation canopy. The model represents the energy budget of leaf surfaces, the ground surface, and turbulent and radiative transfer processes within the canopy. The vegetation is partitioned into 50 layers and the energy budget equation for each layer is solved for steady and horizontally homogeneous flow.

Numerical weather modelers have begun to include simplified parameterizations of land surface processes into operational numerical weather prediction models. Examples are the models of the European Center for Medium-range Weather Forecasting (ECMWF), the U.S. National Meteorological Service (NMC), the UK Meteorological Office, the French Meteorological Service (Direction de la Meteorologie), and the Japan Meteorological Agency (Blondin 1991). These models have many features in common. They all simulate the diurnal cycle, have their first atmospheric level inside the constant flux layer (CFL), use Monin-Obukhov similarity theory, and use only one roughness length for momentum, heat, and moisture. The surface moisture flux, however, is treated differently in each model.

Although the models discussed above have various degrees of complexity in their canopy and soil representations, none of them considers subgrid scale spatial variability in either meteorological inputs to the land surface or land surface characteristics. Representation of heterogeneities in terrain, soil, vegetation, and precipitation at scales smaller than those resolved by GCMs has been a relatively recent concern. Warrilow et al. (1986) took account of spatial variations in rainfall by assuming that only a fraction of a grid cell receives rainfall, and that within the fraction covered, rainfall depth is distributed exponentially. However, in their parameterization, the interception of rainfall was assumed to be uniformly distributed over the entire grid cell, and thus evaporation was overestimated (Lean and Warrilow 1989). Following the formulation of Dolman and Gregory (1992), Lean and Rowntree (1993) incorporated a new interception representation which assumed that interception occurred only over a fraction of the grid cell within which the rainfall was governed by an exponential distribution.

Wetzel and Chang (1988) incorporated the effect of subgrid variability in soil moisture into the evaporation process by using a statistical distribution to represent the soil moisture within a grid cell. The soil column in their model consists of three layers with a thin surface layer and two thicker sublayers. The first sublayer is assumed to contain 50% of all plant roots and is used to

represent the diurnal variation of soil moisture; and the second sublayer contains the other half of the roots and is used to represent time scales of one day or longer. Evaporation is evaluated based on the Ohm's law analog form. The grid-cell-average evapotranspiration was then summed based on weighting factors obtained from the statistical distribution of the soil moisture.

Avissar and Pielke (1989) investigated the subgrid scale variability associated with land surface heterogeneities in a mesoscale model by classifying the surface into similar homogeneous patches. After regrouping into subgrid classes, a parameterization for homogeneous surfaces was applied. The total fluxes of energy of each grid cell were then evaluated according to the distribution of the different subgrid types within the grid cell. Their work showed that spatial heterogeneity in vegetation can have significant effects on temperature and precipitation.

Entekhabi and Eagleson (1989) prescribed the subgrid spatial variability of soil moisture and storm precipitation statistically and derived expressions for hydrologic fluxes based on assumed subgrid soil and precipitation variability. However, their analysis is limited to specific assumed statistical distributions. The scheme was implementated into the NASA Goddard Institute for Space Studies (GISS) GCM by Johnson et al. (1993).

Pielke et al. (1991) illustrated the range of observed spatial variabilities of landscape characteristics using observational evidence from field and satellite data. They investigated the effects of spatial variability in land surface characteristics on lower tropospheric fluxes of energy in the absence of clouds. On this basis, they argued that the influence of mesoscale landscape spatial variability on the atmosphere should be explicitly parameterized.

Avissar (1991) numerically aggregated grid scale surface fluxes for nine classes of stomatal resistance. In the aggregation, two stages of scaling were used. The first was from the leaf scale to the patch scale; the second was from the patch scale to the GCM scale.

Avissar (1992) used a statistical-dynamical approach to investigate

subgrid scale heterogeneity in stomatal resistance, where a probability density function rather than a single representative value was used. Each term in the land surface energy budget was expressed as an integral of a probability density function of stomatal resistance. Five different probability density functions for stomatal resistance were explored. Comparisons between the results obtained by the statistical-dynamical approach and by use of a single representative stomatal resistance showed that there were large absolute and relative differences due to the nonlinearity of land-atmosphere interactions. The observations of stomatal conductances in a potato field in New Jersey during the summer of 1989 supported use of a two parameter lognormal distribution to describe the distribution of stomatal conductances. Bonan et al. (1993) also used the statistical-dynamic approach to study the effects of subgrid scale heterogeneity in leaf area index, minimum and maximum stomatal resistances, and soil moisture on grid scale fluxes.

Koster and Suarez (1992a) proposed a mosaic strategy, similar to that used by Avissar and Pielke (1989), to account for the effects of different vegetation on surface energy fluxes. In the mosaic strategy, each vegetation type is represented by a tile, which is coupled independently to the atmosphere. The rest of the canopy and soil parameterization is similar to SiB (Sellers et al. 1986). Koster and Suarez (1992b) extended their earlier mosaic strategy by separating the total turbulent flux into latent and sensible heat components. In addition, they compared the mosaic approach with a mixture approach in which different vegetation types were assumed to be homogeneously mixed over a GCM grid cell.

The land surface scheme for the Canadian Climate Center GCMs was developed by Verseghy (1991) and Verseghy et al. (1993). In this model, three soil layers are used to represent both thermal and moisture regimes. When snow is present, it is assumed that the entire area is covered if the snow depth is greater than an assumed surface roughness height of 0.10 m; otherwise, only a fraction of ground area is covered by snow with a fixed depth of 0.10 m. At the end of each time step, the temperature and moisture content are averaged by

the relative fraction of snow covered area. In addition, the model calculates the canopy and ground surface temperatures separately. As in the strategy adopted by Avissar and Pielke (1989), each grid cell is divided into four different subareas. They are bare soil, snow-covered, vegetation-covered, and vegetation-and-snow covered areas. Within the vegetation-covered area, average canopy parameters based on the presence of four different vegetation types are calculated.

Ducoudre et al. (1993) developed a set of parameterizations of the hydrologic exchanges at the land/atmosphere interface within a GCM. The model allows seven different vegetation classes to be present simultaneously within the same grid cell. The total latent heat flux transferred to the atmosph₁ ˑe is obtained by taking the average of evaporation from bare soil, transpir₁₁ion and interception loss from each of the 7 vegetation types. In the soil parameterization of the model, rain fills the soil column from top to bottom, and water is removed from the closest level where it is available.

Famiglietti and Wood (1994a) developed a local water and energy balance model which is appropriate for a stream catchment, but could be generalized to a region such as a GCM grid cell. The model partitions the land surface into bare soil, wet canopy, and dry canopy using a pixel-based representation of the land surface derived from digital elevation data. Spatial variability is explicitly incorporated by discrete variation of the model parameters and inputs over the spatial domain. The local fluxes of each grid element are aggregated either explicitly or by statistically aggregating the local fluxes through integration over their respective spatial probability density functions (Famiglietti and Wood 1994b).

One of the major complications in developing and testing land surface parameterizations for GCMs is that validation opportunities are few. A recent exception is the work of Betts et al. (1993) who compared surface energy fluxes and soil temperatures predicted by the ECMWF land surface model with data collected at the FIFE site in central Kansas during the summer of 1987. Their work identified problems with four components of the model: the incoming

shortwave radiation for clear sky conditions, the ground heat flux, surface evaporation, and the entrainment at the top of the boundary layer. They concluded that the relatively thin (70 mm) top ground layer in the model was the main reason for the errors in ground heat flux, and that deficiencies in the surface evaporation algorithm were responsible for large errors in the latent heat flux.

1.3. Research objectives

The objectives of this research are: (1) to develop a simple land surface scheme appropriate for GCMs that represents spatial variability in soil characteristics, vegetation, and precipitation, and simulates explicitly direct surface runoff and subsurface runoff; (2) to evaluate the model using observed data; and (3) to explore the model parameters using sensitivity analysis.

The scheme to be developed is a generalization of the VIC model described by Wood et al. (1992) and implemented in the GFDL-GCM by Stamm et al. (1994). The new model consists of a simple two-layer characterization of the soil column, and uses an aerodynamic representation of the latent and sensible heat fluxes at the land surface. The soil moisture algorithm is a generalization of the Arno model (Francini and Pacciani 1991) in which the infiltration, evaporation, soil moisture, and runoff generation vary within an area (or within a grid cell in GCMs). The infiltration algorithm in the VIC model can be interpreted within the context of a spatial distribution of soils of varying infiltration capacities. It allows different types of vegetation to be present simultaneously. In addition, it accounts for the spatial variability in precipitation. Simplifications of the Arno model using the traditional beta function representation of evapotranspiration, have previously been incorporated in the Geophysical Fluid Dynamics Laboratory (GFDL) GCMs by Stamm et al. (1994), and in the Max Planck Institut GCM by Dumenil and Todini (1992).

There are major differences between the two-layer VIC model to be described here and the earlier versions incorporated in the GFDL and MPI GCMs. The most important differences are the following: (1) both of the earlier

schemes have a single soil layer, and neither explicitly represents vegetation in the surface energy flux; (2) both of the earlier models distribute precipitation uniformly over the grid cell. Stamm et al. (1994) concluded that "... the results over North American and Eurasia [suggest] the need to represent the surface hydrology with a two layer soil system ...".

CHAPTER 2 DESCRIPTION OF TWO-LAYER VIC MODEL

In this chapter, the structure and the characteristics of the two-layer variable infiltration capacity model (Liang et al. 1994) are described. The definition of and dimension of each variable used in this and the following chapters are given in the list of symbols at the start of this dissertation.

2.1. Introduction

The model developed here characterizes the subsurface as consisting of two soil layers. The surface is described by N+1 land cover types, where $n = 1$, $2, \cdots$, N represents N different types of vegetation, and $n = N+1$ represents bare soil. There is no restriction on the number of vegetation types in the model, but in the interest of model parsimony, N will almost always be less than 10. The vertical and horizontal characterizations are shown schematically in Fig. 2.1. The land cover types are specified by their leaf area index (LAI), canopy resistance, and relative fraction of roots in each of the two soil layers. The evapotranspiration from each vegetation type is characterized by potential evapotranspiration, together with canopy resistance, aerodynamic resistance to the transfer of water, and architectural resistance. Associated with each land cover class is a single canopy layer, soil layer 1 (upper zone) and soil layer 2 (lower zone).

The upper layer (soil layer 1) is designed to represent the dynamic behavior of the soil that responds to rainfall events, and the lower layer (soil layer 2) is used to characterize the seasonal soil moisture behavior. The lower layer only responds to rainfall when the upper layer is wet, and thus can separate the subsurface flow from storm quick response. Roots can extend to layer 1 or layers 1 and 2, depending on the vegetation and soil type. For the bare soil class, there is no canopy layer. In the present form of the model, the soil characteristics (that is, the distribution of water holding capacities, as

described below) are the same for all land cover classes. However, each cover class may have different soil moisture distributions at each time step. Infiltration, drainage of moisture from layer 1 to layer 2, surface runoff, and subsurface runoff are computed for each cover type. The total latent heat flux transferred to the atmosphere, total sensible heat and ground heat fluxes, the effective surface temperature, and the total surface runoff and subsurface runoff are then obtained by summing over all of the surface cover classes.

2.2. Evapotranspiration

Three types of land-atmosphere vapor transport are considered in the model. They are evaporation from the canopy layer of each vegetation class, transpiration from each of the vegetation classes, and evaporation from bare soil. Total evapotranspiration over a grid cell (or an area) is computed as the sum of the canopy, vegetation, and bare soil components, weighted by the respective surface cover area fractions (see Section 2.6).

The maximum canopy evaporation rate for the nth surface cover class, $E_c^*[n]$, is specified as

$$E_c^*[n] = \left(\frac{W_i[n]}{W_{im}[n]}\right)^{2/3} E_p[n] \frac{r_w[n]}{r_w[n]+r_0[n]}. \tag{2.1}$$

In Eq. (2.1), the argument n refers to the vegetation surface cover class index; throughout the remainder of this thesis the dependence of many of the surface and subsurface characteristics on surface cover class is implied by this argument even if not noted specifically. In Eq. (2.1), $W_i[n]$ is the amount of intercepted water in storage in the canopy layer, $W_{im}[n]$ is the maximum amount of water that the canopy layer can intercept, $E_p[n]$ is the potential evaporation rate from a thin free water surface (Shuttleworth 1993), $r_0[n]$ is the architectural resistance that is due to the variation of the gradient of specific humidity between the leaves and the overlying air in the canopy layer (Saugier and Katerji

1991), and $r_w[n]$ is the aerodynamic resistance to the transfer of water. The power of 2/3 in Eq. (2.1) is used according to Deardorff (1978). The form of Eq. (2.1) is a "beta" representation, where $E_p[n]$ can be obtained by either Penman's formulation (1948) or Penman-Monteith's formulation for a free water surface (Shuttleworth 1993). Penman's formulation can be expressed as,

$$E_p[n] = \frac{\Delta R_n[n] + \rho_a c_p(e_s - e)/r_a[n]}{\rho_w \cdot L_e \cdot (\Delta + \gamma)} \qquad (2.2)$$

where Δ is the rate of change of saturation vapor pressure with temperature, $R_n[n]$ is the net radiation, ρ_a is the mass density of air, c_p is the specific heat of air at constant pressure, e_s and e are the saturated vapor pressure and vapor pressure respectively, $r_a[n]$ is the aerodynamic resistance to the momentum transfer in the atmosphere (subscripts "a" could be "w", "h", etc.), ρ_w is the density of liquid water, L_e is the latent heat of vaporization, and γ is the psychr metric constant. The Penman-Monteith's formulation for a free water surface is expressed similarly to Eq. (2.2), except that the available energy is substituted for net radiation (Monteith and Unsworth 1990).

The maximum amount of water intercepted by the canopy can be calculated using the formulation of Dickinson (1984),

$$W_{im}[n] = K_L \times LAI[n,m] \qquad (2.3)$$

where K_L is a constant, taken to be 0.2 mm following Dickinson (1984), and $LAI[n,m]$ is leaf area index for the nth surface cover class in month m. The leaf area index of a canopy is the projected leaf area per unit ground surface area (Campbell 1977).

The aerodynamic resistance to the transfer of water $r_w[n]$ (i.e., subscript "a" becomes "w") is calculated as (Monteith and Unsworth 1990):

$$r_w[n] = \frac{1}{C_w[n] \, u_n(z_2)} \qquad (2.4)$$

where $u_n(z_2)$ is the wind speed over the nth surface cover class at level $z_2[n]$, and $C_w[n]$ is the transfer coefficient for water which is estimated taking into account atmospheric stability (Louis 1979) as follows:

$$C_w[n] = 1.351 \times a^2[n] \times F_w[n] \qquad (2.5)$$

where

$$a^2[n] = \frac{K^2}{[\ln (\frac{z_2[n] - d_0[n]}{z_0[n]})]^2} \qquad (2.6)$$

is the drag coefficient for the case of near-neutral stability, K is von Karman's constant, which we take as 0.4; $d_0[n]$ is the zero plane displacement height, and $z_0[n]$ is the roughness length. $F_w[n]$ is defined as

$$F_w[n] = 1 - \frac{9.4 Ri_B[n]}{1 + c \cdot |Ri_B[n]|^{1/2}}, \qquad Ri_B[n] < 0 \qquad (2.7a)$$

$$F_w[n] = \frac{1}{(1 + 4.7 Ri_B[n])^2}, \qquad 0 \leq Ri_B[n] \leq 0.2 \qquad (2.7b)$$

where $Ri_B[n]$ is the bulk Richardson number and is estimated as,

$$Ri_B[n] = \frac{g \cdot z_r[n] \cdot (T_a[n] - T_s[n])}{T_a[n] \cdot V_a^2} \qquad (2.8)$$

where g is the acceleration due to gravity, $T_a[n]$ is the air temperature, $T_s[n]$ is the surface temperature, and $z_r[n]$ and V_a^2 are the reference height and the modified wind speed, and they are expressed following Dickinson et al. (1992) and Smith et al. (1993),

$$z_r[n] = z_2[n] - d_0[n] \qquad (2.9)$$

and

$$V_a^2 = (u_n(z_2))^2 + U_c^2 \qquad (2.10)$$

with $U_c=1.0$ m/s for unstable conditions and $U_c=0.1$ m/s for stable conditions. The parameter c in Eq. (2.7a) is expressed as

$$c = 49.82 \times a^2[n] \times (\frac{z_2[n] - d_0[n]}{z_0[n]})^{1/2} . \qquad (2.11)$$

In the Louis (1979) representation, the transfer coefficients for water and heat are taken to be equal, but they can be different from the coefficient for momentum which has been shown by experimental and theoretical work (e.g. Garratt and Hicks 1973, Garratt 1978, Brutsaert 1982, and Duynkerke 1992).

Based on the formulation of Blondin (1991) and Ducoudre et al. (1993), the transpiration rate was obtained using the form

$$E_t[n] = [1 - (\frac{W_i[n]}{W_{im}[n]})^{2/3}] E_p[n] \frac{r_w[n]}{r_w[n] + r_0[n] + r_c[n]} \qquad (2.12)$$

where $r_c[n]$ is the canopy resistance. It is expressed as

$$r_c[n] = \frac{r_{min}[n] g_{sm}[n]}{LAI[n,m]} . \qquad (2.13)$$

In Eq. (2.13), $r_{min}[n]$ is the minimum canopy resistance, $g_{sm}[n]$ is a soil moisture stress factor depending on the water availability in the root zone for the nth surface cover class. It is expressed as

$$g_{sm}^{-1}[n] = 1 , \qquad\qquad W_j[n] \geq W_j^{cr} \qquad\qquad (2.14a)$$

$$g_{sm}^{-1}[n] = \frac{W_j[n] - W_j^{w}}{W_j^{cr} - W_j^{w}} , \qquad W_j^{w} \leq W_j[n] < W_j^{cr} \qquad (2.14b)$$

$$g_{sm}^{-1}[n] = 0 , \qquad\qquad W_j[n] < W_j^{w} \qquad\qquad (2.14c)$$

where $W_j[n]$ is the soil moisture content in layer j, $j=1, 2$. W_j^{cr} is the critical value above which transpiration is not affected by the moisture stress in the soil, and W_j^{w} is the soil moisture content at permanent wilting point. Water can be extracted from layers 1 and/or 2 depending on the fractions of roots $f_1[n]$ and $f_2[n]$ in each layer.

There is no soil moisture stress, i.e., $g_{sm}[n]=1$ in Eq. (2.14), if either (i) $W_2[n]$ is greater or equal to W_2^{cr}, and $f_2[n] \geq 0.5$ or (ii) $W_1[n]$ is greater or equal to W_1^{cr}, and $f_1[n] \geq 0.5$. In case (i), the transpiration is supplied by layer 2 with no soil moisture stress, i.e., $E_t[n]=E_2^t[n]$ (regardless of water availability in layer 1); in case (ii), the transpiration takes water from layer 1, i.e., $E_t[n]=E_1^t[n]$, also without any soil moisture stress. Otherwise, the transpiration rate is

$$E_t[n] = f_1[n] \cdot E_1^t[n] + f_2[n] \cdot E_2^t[n] \qquad\qquad (2.15)$$

where $E_1^t[n]$, $E_2^t[n]$ are the transpiration rate from layer 1 and layer 2 respectively, computed by using Eq. (2.12). If the roots only extend to layer 1, then $E_t[n] = E_1^t[n]$ with $f_2[n] = 0$.

For the case of a continuous rainfall with a rate lower than the canopy evaporation rate, it is important to consider evaporation from the vegetation when there is insufficient intercepted water to supply the atmospheric demand within one time step. Thus in general, the evaporation rate from the canopy layer, $\dot{E}_c[n]$, can be expressed as

$$E_c[n] = f[n] \cdot E_c^*[n] \qquad (2.16)$$

where $f[n]$ is the fraction of the time step required for canopy evaporation to exhaust the canopy interception storage. It is given by

$$f[n] = \min(1, \frac{W_i[n] + P \cdot \Delta t}{E_c^*[n] \cdot \Delta t}) \qquad (2.17)$$

where P is the precipitation rate, and Δt is the time step which is taken as one hour in the model calculation. The transpiration during the time step is then

$$\dot{E}_t[n] = (1.0 - f[n]) \cdot E_p[n] \frac{r_w[n]}{r_w[n] + r_0[n] + r_c[n]} +$$

$$f[n] \cdot [1 - (\frac{W_i[n]}{W_{im}[n]})^{2/3}] \cdot E_p[n] \frac{r_w[n]}{r_w[n] + r_0[n] + r_c[n]} \qquad (2.18)$$

where the first term represents the fraction of the time step for which no evaporation occurs from the canopy interception storage, and the second term represents the fraction of the time step for which both evaporation from the canopy and transpiration occur.

Evaporation from bare soil is extracted only from layer 1; bare soil evaporation $\dot{E}_2$ from layer 2 is assumed to be zero. When layer 1 is saturated, it evaporates at the potential rate $E_p[N+1]$, i.e.,

$$\ddot{E}_1 = E_p[N+1] . \tag{2.19}$$

When it is unsaturated, it evaporates at rate E_1 which varies within the bare soil area due to the inhomogeneities in infiltration, topography and soil characteristics. E_1 is computed using the Arno evaporation formulation (Francini and Pacciani 1991). The Arno model uses the structure of the Xinanjiang model (Zhao et al. 1980, see also Wood et al. 1992), and assumes that the infiltration capacity varies within an area, and can be expressed as

$$i = i_m [1 - (1 - A)^{1/b_i}] \tag{2.20}$$

where i and i_m are the infiltration capacity and maximum infiltration capacity respectively, A is the fraction of an area for which the infiltration capacity is less than i, and b_i is the infiltration shape parameter. Let A_s represent the fraction of the bare soil that is saturated, and i_0 represent the corresponding point infiltration capacity. Then, as suggested by Fig. 2.2, E_1 can be expressed as

$$E_1 = E_p[N+1]\{\int_0^{A_s} dA + \int_{A_s}^1 \frac{i_0}{i_m [1 - (1 - A)^{1/b_i}]} dA\}. \tag{2.21}$$

In Eq. (2.21), the first integral represents the contribution of the saturated area, which evaporates at the potential rate. Since there is no analytical expression for the second integral in Eq. (2.21), E_1 is obtained through a power series expansion:

$$E_1 = E_p[N+1]\{A_s + \frac{i_0}{i_m}(1 - A_s)[1 + \frac{b_i}{1+b_i}(1 - A_s)^{1/b_i} + \frac{b_i}{2+b_i}(1 - A_s)^{2/b_i} + \frac{b_i}{3+b_i}(1 - A_s)^{3/b_i} + \cdots]\}. \tag{2.22}$$

This approach accounts for the subgrid variability in soil moisture within the area covered by bare soil.

2.3. Canopy layer

The water balance in the canopy layer (interception) can be described by

$$\frac{dW_i[n]}{dt} = P - E_c[n] - P_t[n], \qquad 0 \leq W_i[n] \leq W_{im}[n] \qquad (2.23)$$

where $P_t[n]$ is the throughfall rate of precipitation which occurs when $W_{im}[n]$ is exceeded for the nth surface cover class.

2.4. Surface runoff from bare soil

Surface runoff is computed using the formulation for infiltration given by Eq. (2.20). The Xinanjiang formulation, which is described in detail by Wood et al. (1992), is assumed to hold for the upper soil layer only. The maximum soil moisture content of layer 1, W_1^c, is related to i_m and b_i as follows,

$$W_1^c = \frac{i_m}{1 + b_i}. \qquad (2.24)$$

The Xinanjiang model effectively assumes that runoff is generated by those areas for which precipitation, when added to soil moisture storage at the end of the previous time step, exceeds the storage capacity of the soil. The direct runoff from these areas is $Q_d[N+1]$, where $N+1$ indicates the bare soil class. In integrated form, the result is

$$Q_d[N+1] \cdot \Delta t = P \cdot \Delta t - W_1^c + W_1^-[N+1], \qquad i_0 + P \cdot \Delta t \geq i_m \qquad (2.25a)$$

$$Q_d[N+1] \cdot \Delta t = P \cdot \Delta t - W_1^c + W_1^-[N+1] + W_1^c [1 - \frac{i_0 + P\Delta t}{i_m}]^{1+b_i},$$

$$i_0 + P \cdot \Delta t \leq i_m \qquad (2.25b)$$

where $W_1^-[N+1]$ is the soil moisture content in layer 1 at the beginning of the time step. Note that, for the bare soil class, there is no canopy storage, hence "throughfall" is equal to precipitation P. For bare soil, the water balance in layer 1 is

$$W_1^+[N+1] = W_1^-[N+1] + (P - Q_d[N+1] - Q_{12}[N+1] - E_1) \cdot \Delta t \quad (2.26)$$

where $W_1^+[N+1]$ is the soil moisture content in layer 1 at the end of each time step, and $Q_{12}[N+1]$ is the drainage from layer 1 to layer 2. Assuming that the drainage is driven by gravity, we use the Brooks and Corey (1964) relation to estimate the hydraulic conductivity, and thus we can express the drainage rate from layer 1 to layer 2 as

$$Q_{12}[N+1] = K_s \cdot \left(\frac{W_1[N+1] - \theta_r}{W_1^c - \theta_r}\right)^{\frac{2}{B_p}+3} \quad (2.27)$$

where K_s is the saturated hydraulic conductivity, θ_r is the residual moisture content and can be taken as zero in general due to its very small magnitude, and B_p is the pore size distribution index.

2.5. Subsurface runoff from bare soil

The formulation of subsurface runoff (baseflow) follows the Arno model conceptualization (Francini and Pacciani 1991), which is applied only to the lower soil layer (drainage from layer 1 goes only to layer 2, and does not contribute to runoff). The baseflow rate is given by:

$$Q_b[N+1] = \frac{D_s D_m}{W_s W_2^c} W_2^-[N+1] ,$$

$$\text{for } 0 \leq W_2^-[N+1] \leq W_s W_2^c \quad (2.28a)$$

$$Q_b[N+1] = \frac{D_sD_m}{W_sW_2^c}W_2^-[N+1] + (D_m - \frac{D_sD_m}{W_s})(\frac{W_2^-[N+1] - W_sW_2^c}{W_2^c - W_sW_2^c})^2,$$

for $W_2^-[N+1] \geq W_sW_2^c$ (2.28b)

where $Q_b[N+1]$ is the subsurface runoff rate, D_m is the maximum subsurface flow rate, D_s is a fraction of D_m, W_2^c is the maximum soil moisture content of layer 2, W_s is a fraction of W_2^c, with $D_s \leq W_s$, and $W_2^-[N+1]$ is the soil moisture content at the beginning of the time step in layer 2. Eqs. (2.28a) and (2.28b) describe a recession that is linear below a threshold (Eq. (2.28a)), and nonlinear at higher soil moisture values (Eq. (2.28b)) as shown in Fig. 2.3. The nonlinear drainage is required to represent situations where substantial subsurface storm flow occurs. Eqs. (2.28a) and (2.28b) have a continuous first derivative at the transition from the linear to nonlinear drainage as shown in Fig. 2.3.

Using Eqs. (2.28a) and (2.28b), and the notation that $W_2^+[N+1]$ is the layer 2 soil moisture content at the end of the current time, the water balance for layer 2 is

$$W_2^+[N+1] = W_2^-[N+1] + (Q_{12}[N+1] - Q_b[N+1] - E_2) \cdot \Delta t \qquad (2.29a)$$

when $W_2^-[N+1] + (Q_{12}[N+1] - Q_b[N+1] - E_2) \cdot \Delta t < W_2^c$, in which case Q_b is given by Eq. (2.28a) or (2.28b).

In the case $W_2^-[N+1] + (Q_{12}[N+1] - Q_b'[N+1] - E_2) \cdot \Delta t > W_2^c$ (where $Q_b'[N+1]$ is given by Eq. (2.28a) or (2.28b)),

$$W_2^+[N+1] = W_2^c \qquad (2.29b)$$

and

$$Q_b''[N+1] = W_2^-[N+1] + (Q_{12}[N+1] - Q_b'[N+1] - E_2) \cdot \Delta t - W_2^c.$$

When Eq. (2.29b) applies, the total subsurface runoff from layer 2 is given by $Q_b[N+1] = Q_b'[N+1] + Q_b''[N+1]$. In practice, this condition occurs rarely.

2.6. Surface and subsurface runoff from soil with vegetation cover

The equations for surface and subsurface flow rate, and the water balance in each layer are the same for cover classes with vegetation as for the bare soil case, except that P, E_1, and E_2 are changed to $P_t[n]$, $E_1^t[n]$, and $E_2^t[n]$, respectively in Eqs. (2.25), (2.26), and (2.29), to reflect the vegetation class.

The total evapotranspiration rate E_* and the total runoff rate Q can be then expressed as

$$E = \sum_{n=1}^{N} C_v[n] \cdot (E_c[n]+E_t[n]) + C_v[N+1] \cdot E_1 \qquad (2.30)$$

$$Q = \sum_{n=1}^{N+1} C_v[n] \cdot (Q_d[n] + Q_b[n]) \qquad (2.31)$$

where $C_v[n]$ is the fraction of vegetation cover for the nth ($n=1, 2, \cdots, N$) surface cover class of interest, $C_v[N+1]$ is the fraction of the bare soil covered area, and $\sum_{n=1}^{N+1} C_v[n] = 1$.

2.7. Aerodynamic flux representation

The two-layer hydrological model described above is used in conjunction with the energy balance at the land surface and the thermal properties of soils to calculate the surface temperature, and simultaneously, the fluxes of sensible heat and ground heat which depend on surface temperature. The energy balance equation for an ideal surface of the nth surface cover class can be expressed as

$$R_n[n] = H[n] + \rho_w L_e E[n] + G[n] \qquad (2.32)$$

where $\dot{E}[n]$ is given by

$$E[n] = E_c[n] + E_t[n] , \qquad n=1, 2, \cdots, N \qquad (2.33a)$$

$$\dot{E}[N+1] = E_1 \qquad (2.33b)$$

where $H[n]$ is the sensible heat flux, $\rho_w L_e \dot{E}[n]$ is the latent heat flux (e.g., with units of Wm^{-2}), and $G[n]$ is the ground heat flux. For a surface that is relatively flat and homogeneous, the energy balance equation for a layer of the air column bounded by the ground surface at the bottom and a surface of given height in the atmosphere above, can be expressed as

$$R_n[n] = H[n] + \rho_w L_e E[n] + G[n] + \Delta H_s[n] \qquad (2.34)$$

where $\Delta H_s[n]$ is the change in the energy storage in the layer per unit time, per unit area. The sensible and latent heat fluxes, as well as the net radiation, are associated with the top surface of the air layer, and the ground heat flux with the bottom of the layer. The rate of heat energy storage in the layer is

$$\Delta H_s[n] = \frac{\rho_a c_p (T_s^+[n] - T_s^-[n]) \, z_a[n]}{2 \cdot \Delta t} \qquad (2.35)$$

where $T_s^+[n]$ and $T_s^-[n]$ are the surface temperature of the bottom surface of the air layer at the end and at the beginning of a time step respectively, and $z_a[n]$ is the height of the top surface of the air layer which is used only when $\Delta H_s[n]$ is considered to be significant.

The net radiation $\dot{R}_n[n]$ is given by

$$\dot{R}_n[n] = (1 - \alpha[n]) \, R_s + \epsilon[n] \cdot (R_L - \sigma T_s^4[n]) \qquad (2.36)$$

where $\alpha[n]$ is the albedo of the nth surface cover class, R_s is the downward

shortwave radiation at the surface, $\epsilon[n]$ is the emissivity of the nth surface cover class, R_L is the downward long-wave radiation at the surface, and σ is the Stefan-Boltzmann constant. The latent heat flux, which is the link between the water and energy balances, is obtained from Eq. (2.33). The sensible heat flux is given by

$$H[n] = \frac{\rho_a c_p}{r_h[n]} (T_s[n] - T_a[n]) \qquad (2.37)$$

where $r_h[n]$ is the aerodynamic resistance for heat transfer. We take $r_h[n]$ to be equal to $r_w[n]$ in Eq. (2.4). The ground heat flux $G[n]$ is estimated through the two thermal soil layers (Fig. 2.4). The two thermal soil layers are different from the two soil moisture layers (i.e., the upper zone and lower zone) discussed above. For the first soil layer, with soil depth D_1 (subsequently assumed to be 50 mm), we have,

$$G[n] = \frac{\kappa[n]}{D_1} (T_s[n] - T_1[n]) \qquad (2.38)$$

where $\kappa[n]$ is the soil thermal conductivity, and $T_1[n]$ is the soil temperature at depth D_1. For the second soil layer with depth D_2, at which the bottom boundary condition is a constant soil temperature T_2, the law of energy conservation (assuming that the heat storage in the first soil thermal layer is negligible) gives,

$$\frac{\partial(C_s[n]T[n])}{\partial t} = -\frac{\partial H_f[n]}{\partial z} \qquad (2.39)$$

where $C_s[n]$ is the soil heat capacity, $T[n]$ is the soil temperature, $H_f[n]$ is the heat flux, and t and z are the time and the soil depth respectively. Assuming that $C_s[n]$ does not change with time, from Fig. 2.4, Eq. (2.39) can be written

as

$$C_s[n] \cdot \frac{\Delta T[n]}{\Delta t} = -\frac{G''[n] - G'[n]}{D_2} \tag{2.40}$$

where $\Delta T[n]$ is the temperature gradient, $G''[n]$ is the heat flux across the bottom boundary at depth D_2, and the $G'[n]$ is the heat flux across the soil face at depth D_1 (see Fig. 2.4). Since it is assumed that there is no heat storage within soil depth D_1, we have

$$G[n] = G'[n] . \tag{2.41}$$

In addition, $G''[n]$ can be expressed as

$$G''[n] = \frac{\kappa[n]}{D_2} \cdot (T_1[n] - T_2) . \tag{2.42}$$

If we assume that

$$T[n] = \frac{T_1[n] + T_2}{2} \tag{2.43}$$

then

$$\frac{\Delta T[n]}{\Delta t} = \frac{T_1^+[n] - T_1^-[n]}{2\Delta t} \tag{2.44}$$

where $T_1^+[n]$ and $T_1^-[n]$ are the soil temperature at depth D_1 at the end and the beginning of a time step respectively.

By substituting Eqs. (2.41-2.44) into Eq. (2.40), we can obtain

$$\frac{C_s[n] \cdot (T_1^+[n] - T_1^-[n])}{2 \cdot \Delta t} = \frac{G[n]}{D_2} - \frac{\kappa[n] \cdot (T_1[n] - T_2)}{D_2^2} \tag{2.45}$$

At present, $C_s[n]$ and $\kappa[n]$ are not considered to be functions of the soil water

content (although such an adjustment would be straightforward), and are taken to be the same for both soil thermal layers. From Eqs. (2.38) and (2.45), the ground heat flux G[n] can be expressed as,

$$G[n] = \frac{\frac{\kappa[n]}{D_2}(T_s[n] - T_2) + \frac{C_s[n] \cdot D_2}{2 \cdot \Delta t}(T_s[n] - T_1^-[n])}{1 + \frac{D_1}{D_2} + \frac{C_s[n] \cdot D_1 \cdot D_2}{2 \cdot \Delta t \cdot \kappa[n]}} \qquad (2.46)$$

For the case where $\Delta H_s[n]$ is not significant or there are not enough data available to evaluate the energy balance within a layer, the energy balance equation for an ideal surface (Eq. (2.32)) can be used instead of Eq. (2.34). From Eqs. (2.36), (2.37), (2.46), and Eq. (2.33) (scaled by the latent heat of vaporization and the density of liquid water), we can obtain the sensible heat and ground heat fluxes and the surface temperature for the nth cover class. In the case where $\Delta H_s[n]$ is negligible, the surface temperature $T_s[n]$ is solved iteratively from Eq. (2.47) below,

$$\epsilon[n]\sigma T_s^4[n] + \left(\frac{\rho_a c_p}{r_h[n]} + \frac{\frac{\kappa[n]}{D_2} + \frac{C_s[n] \cdot D_2}{2 \cdot \Delta t}}{1 + \frac{D_1}{D_2} + \frac{C_s[n] \cdot D_1 \cdot D_2}{2 \cdot \Delta t \cdot \kappa[n]}}\right) \cdot T_s[n] = (1 - \alpha[n])R_s +$$

$$\epsilon[n]R_L + \frac{\rho_a c_p}{r_h[n]} T_a[n] - \rho_w L_e E[n] + \frac{\frac{\kappa[n] \cdot T_2}{D_2} + \frac{C_s[n] \cdot D_2 \cdot T_1^-[n]}{2 \cdot \Delta t}}{1 + \frac{D_1}{D_2} + \frac{C_s[n] \cdot D_1 \cdot D_2}{2 \cdot \Delta t \cdot \kappa[n]}} . \qquad (2.47)$$

For the case where $\Delta H_s[n]$ cannot be ignored, Eqs. (2.34) to (2.37), and (2.46) are combined to give

$$\epsilon[n]\sigma(T_{s-}^{+}[n])^4 + (\frac{\rho_a c_p}{r_h[n]} + \frac{\rho_a c_p z_a[n]}{2\cdot\Delta t} + \frac{\frac{\kappa[n]}{D_2} + \frac{C_s[n]\cdot D_2}{2\cdot\Delta t}}{1 + \frac{D_1}{D_2} + \frac{C_s[n]\cdot D_1\cdot D_2}{2\cdot\Delta t\cdot\kappa[n]}})T_s^{+}[n] =$$

$$(1-\alpha[n])\cdot R_s + \epsilon[n]\cdot R_L + \frac{\rho_a c_p}{r_h[n]} T_a[n] - \rho_w L_e \dot{E}[n] + \frac{\rho_a c_p z_a[n]\cdot T_s^{-}[n]}{2\cdot\Delta t}$$

$$+ \frac{\frac{\kappa[n]\cdot T_2}{D_2} + \frac{C_s[n]\cdot D_2\cdot T_1^{-}[n]}{2\cdot\Delta t}}{1 + \frac{D_1}{D_2} + \frac{C_s[n]\cdot D_1\cdot D_2}{2\cdot\Delta t\cdot\kappa[n]}} . \tag{2.48}$$

$T_s[n]$ is determined in the same manner as for Eq. (2.47). Therefore, the effective surface temperature T_s, sensible heat flux H, and ground heat flux G can be obtained as,

$$T_s = \sum_{n=1}^{N+1} C_v[n]\cdot T_s[n] , \tag{2.49}$$

$$H = \sum_{n=1}^{N+1} C_v[n]\cdot H[n] , \tag{2.50}$$

$$G = \sum_{n=1}^{N+1} C_v[n]\cdot G[n] . \tag{2.51}$$

2.8. Snow

When snow is present, the model is coupled with a single-layer, energy- and mass-balance snow accumulation and ablation model (Wigmosta et al. 1994). At the snow-air interface, the energy exchange is described by the net radiation, sensible heat, evaporation from the water in the snowpack and sublimation or condensation, and the heat advected to the snowpack by rainfall. The snow-ground interface is assumed to be a zero energy flux boundary. Snow albedo is

determined based on snow age. The present version of the snowmelt model does not consider fractional snow coverage; it is assumed that the entire area is covered by a uniform depth of snow if a snowpack is present.

2.9. Model calculation procedure

In the formulation of the two-layer VIC model, many variables are a function of the surface temperature. For example, the surface temperature is needed to calculate the bulk Richardson number, vapor pressure deficit, and net radiation. Once the bulk Richardson number is determined, the aerodynamic resistance can be calculated, accounting for stability correction. Given the stability-corrected aerodynamic resistance, the vapor pressure deficit, and net radiation, the potential evaporation can then be estimated. However, computation of the surface temperature requires an iterative solution of Eq. (2.47) or (2.48), which is implemented as follows:

(1). Set the surface temperature to the air temperature at the first time step. This allows computation of the initial values of the bulk Richardson number, vapor pressure deficit and net radiation that are needed to estimate $E_p[n]$ through the Penman-Monteith formulation.

(2). Iterate Eq. (2.47) or (2.48) to solve for the surface temperature.

(3). Use the surface temperature obtained from step (2) to calculate the bulk Richardson number, vapor pressure deficit, and net radiation again.

(4). Recalculate the surface temperature iteratively using Eq. (2.47) or (2.48). The surface temperature obtained from this step is then considered to be the surface temperature of the first time step of the model simulation.

(5). For subsequent time steps, use the surface temperature from the previous time step to calculate the bulk Richardson number, vapor pressure deficit, and net radiation, then repeat steps 2-4.

The procedure described above is not iterative in the same sense as the procedure used to solve for the surface temperature from Eq. (2.47) or (2.48), since the steps are only repeated once. The use of a single iteration is justified by the relatively smooth variation usually observed in surface temperatures due to the thermal inertia of the soil column. Of course, multiple iterations could be performed if required. Such an approach in fact implies two nested iterations; one to solve Eq. (2.47) or (2.48), and the other to determine the bulk Richardson number and related quantities needed to compute the surface energy fluxes.

2.10. Summary

A generalization of the VIC (Variable Infiltration Capacity) model which incorporates a two-layer description of the soil column has been described. In the soil column, the upper layer is characterized by the usual VIC spatial distribution of soil moisture capacities, and the lower layer is spatially lumped and uses the Arno (Francini and Pacciani 1991) drainage representation. The model is designed for application within coupled land-atmosphere-ocean GCMs, such as are used for numerical weather prediction and global climate simulation. The model partitions the area of interest (e.g., grid cell) into N+1 land surface cover types; for each land cover type the fraction of roots in the upper and lower zone is specified. Evaporation occurs via canopy evaporation, evaporation from bare soils (land cover class N+1) and transpiration, which is represented with a canopy and architectural resistance formulation.

The two-layer VIC model described here has been tested against observed data. The behavior of the model is described in Chapter 3 using surface flux data from two sites: the FIFE experiment in central Kansas, and the ABRACOS experiment in Brazil.
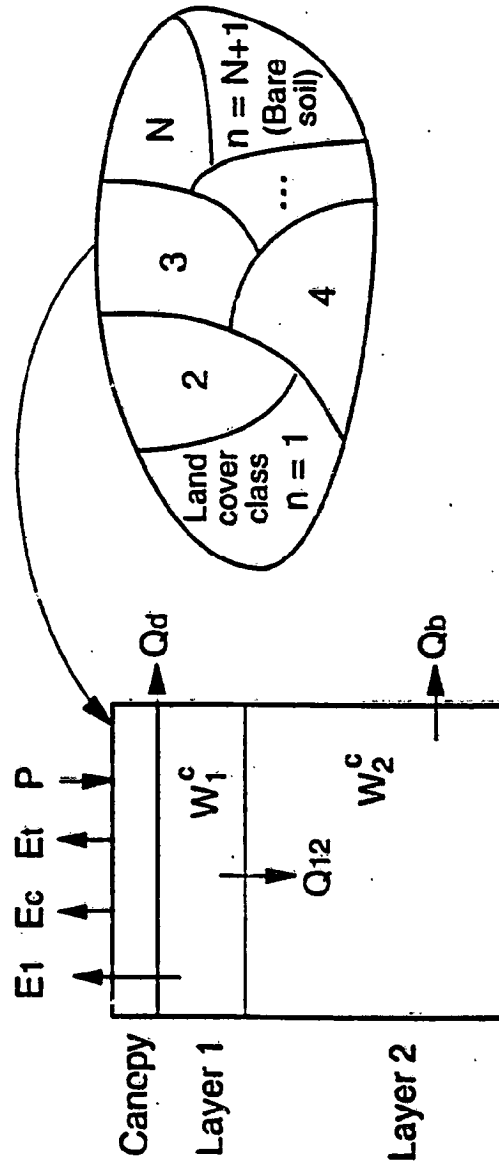
Fig. 2.1   Schematic representation of the two-layer VIC model.
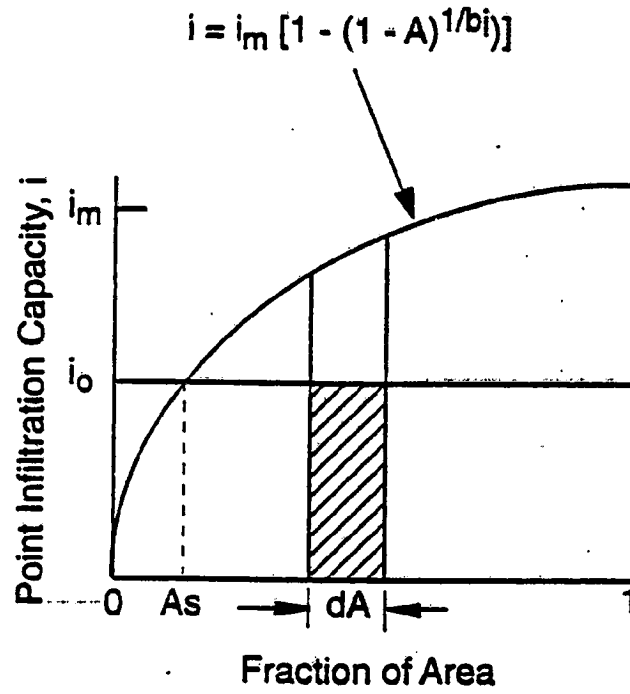
Fig. 2.2   Schematic representation of the computation of evaporation from bare soil.
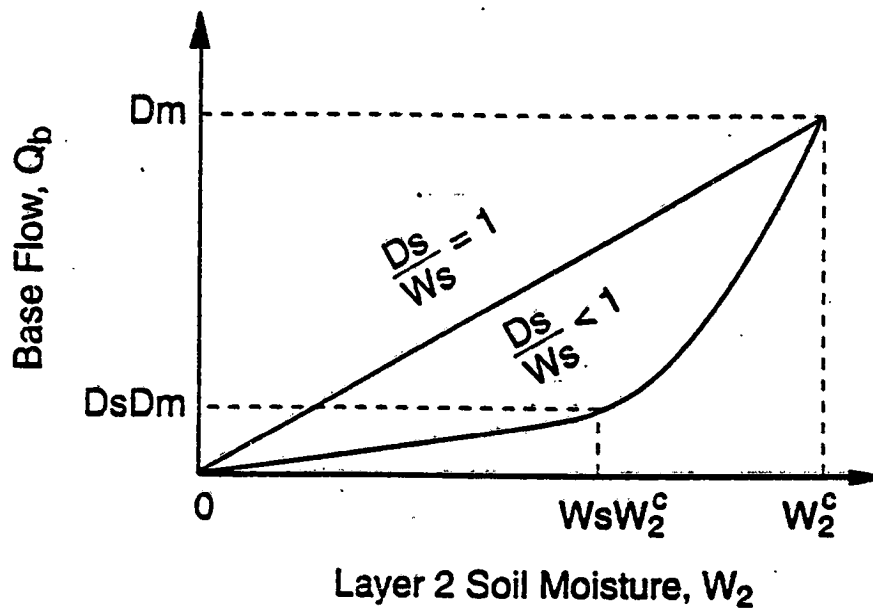
Fig. 2.3   Schematic representation of Arno nonlinear base flow algorithm.
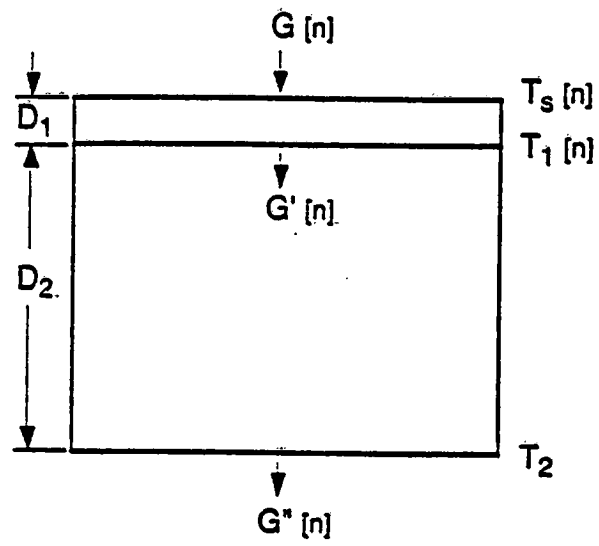
Fig. 2.4   Schematic representation of two thermal soil layers.

CHAPTER 3   MODEL APPLICATION

In Chapter 2, the two-layer VIC model was described. In this chapter, the performance of the model is evaluated for two applications.

3.1. FIFE site

The first test location for the model was the FIFE (First ISLSCP Field Experiment) site in central Kansas in the United States. The FIFE site is a 15×15 km^2 region on the Konza Prairie, a native grassland preserve near Manhattan, Kansas. It has a fairly homogeneous tall grass cover. The Kings Creek catchment, of area 11.7 km^2, lies within the FIFE site. The FIFE site is of interest because of the detailed measurements of surface fluxes that were collected in the summer of 1987. A detailed description of the site is provided by Sellers et al. (1992).

3.1.1. Data description

During the period May-October, 1987, four intensive field campaigns (IFCs) were conducted at the FIFE site, during which tower-based measurements of latent, sensible, and ground heat fluxes were made (Sellers et al. 1992). In addition, throughout the summer of 1987, a network of portable automated mesonet (PAM) stations was operated, from which measured values of incoming solar and long-wave radiation, and other meteorological data are available. Furthermore, long-term streamflow data exist for Kings Creek, along with long-term climatalogical data at nearby Manhattan, KS, which allows for validation of the hydrological portion of the VIC model. The strategy for validation of the model was to estimate the hydrological parameters using precipitation and streamflow data for part of the long-term Kings Creek record, and to evaluate its hydrological performance using the remaining part of the record. The model's surface flux algorithms were then parameterized and

37

validated using measured fluxes observed during the summer, 1987, IFCs. A schematic of the FIFE site with approximate locations of King's Creek catchment (shaded area), flux stations, and meteorological stations is shown in Fig. 3.1.

Daily precipitation and temperature maxima/minima have been collected at Manhattan, KS, which is about 11 km from the centroid of the Kings Creek catchment, since the late 1800s. Daily average stream discharge data for Kings Creek (U.S. Geological Survey Station No. 06879650, 11.7 km^2) have been collected since about 1980. Surface meteorological and surface flux data at the FIFE site are limited to selected periods during the summer of 1987. Data from the PAM stations include surface pressure (p), mixing ratio (ω) and air temperature (T_a) at the 2 m level and horizontal wind speed (u) measured 5.4 m above ground level, surface temperature (T_s), ground soil temperature, T_{10} and T_{50}, at 10 cm and 50 cm below the surface, respectively, and downward short and long-wave radiation. Radiation data were also collected from flux stations (eddy correlation and Bowen ratio). Data from both PAM stations and flux stations were averaged for each date and time among all the stations by Betts et al. (1993). They found from consistency analysis of the calculated and measured net radiation that the flux data were more self-consistent than the PAM data. Therefore, we used the radiation data from the flux stations and the atmospheric data from PAM stations to test our model surface flux and surface temperature predictions. Data for 35 days common to the two data sets in the summer of 1987 were used. They are June 30 – July 11, August 9 – 20, and October 6 – 16.

3.1.2. Parameter estimation

The model parameters can be classified into hydrological parameters and atmospherically related parameters. The hydrological parameters include the infiltration shape parameter b_i (Eq. (2.20)), the soil pore size distribution index B_p, the residual moisture content θ_r, the saturated hydraulic conductivity K_s (Eq. (2.27)), the three base flow-related parameters D_s, D_m, and W_s (Eq.

(2.28)), the maximum soil moisture contents W_1^c and W_2^c in layers 1 and 2, respectively (Eqs. (2.24) and (2.28)), the wilting point W_j^w and the critical point W_j^{cr} (j=1, 2) in Eq. (2.14). Atmospherically related parameters include architectural resistance $r_0[n]$ (Eq. (2.1)), minimum canopy resistance $r_{min}[n]$ (Eq. (2.13)), leaf area index LAI[n,m] (n=1, 2, $\cdots$, N; m=1, 2, $\cdots$, 12) for each surface cover class (Eq. (2.13)), the zero plane displacement height $d_0[n]$, roughness length $z_0[n]$, and the relative fraction of roots in each of the two soil zones $f_1[n]$ and $f_2[n]$ (Eq. (2.15)). We classify $f_1[n]$ and $f_2[n]$ as atmospherically related parameters because they determine the canopy resistance (Eqs. (2.13-2.15)).

Among the hydrological parameters, only three (b_i, D_s, and W_s) are best estimated using streamflow data if they are available (both A_s and i_0 in Eqs. 2.22 and 2.25 are not model parameters, they are evaluated at each time step). The other hydrological parameters can be estimated using soil characteristics. Clearly, for application in GCMs, global parameter estimation using streamflow data is infeasible; for GCM applications Dumenil and Todini (1992) have suggested values for b_i, D_s, and W_s. An ongoing research topic, which will be investigated in the GEWEX Continental Scale International Project (GCIP) is to develop regional relationships for GCM hydrological parameters. However, because streamflow data were available for Kings Creek, we made use of the observed data to estimate b_i, D_s, and W_s.

Since the FIFE site has a fairly homogeneous tall grass cover, the number of vegetation types n in this model application can be taken to be 1, i.e., $C_v[n]=1.0$. To estimate b_i, D_s, and W_s through calibration, we need to know $E_p[1]$ and $r_w[1]$, in addition to parameters W_j^c, W_j^w, W_j^{cr} (j=1, 2), K_s, B_p, θ_r, $f_1[1]$, $f_2[1]$, $u_n(z_2)$, $d_0[1]$, $z_0[1]$, $r_0[1]$, $r_{min}[1]$, and LAI[1,m] (m=1, 2, $\cdots$, 12). At the FIFE site, the data required to estimate $E_p[1]$ by the Penman-Monteith method and $r_w[1]$ by Eq. (2.4) are available only during the IFCs. Therefore, for the purposes of estimating the hydrological parameters, we used Hamon's method (Hamon et al. 1954, Hamon 1961) which requires only daily air temperature and latitude to estimate $E_p[1]$. During summer, 1987 we

also used Hamon $E_p[1]$ during the between-IFC periods to allow continuous computation of soil moisture (needed as initial values during the IFCs). The daily $E_p[1]$ computed using the Hamon formula was compared with the daily $E_p[1]$ obtained using Penman-Monteith's equation for the 35 days of the 1987 FIFE IFCs. The comparison indicated that the Hamon equation gives smaller $E_p[1]$ estimates, but the pattern over the 35 day period was similar for both $E_p[1]$ estimates. Therefore, we scaled the Hamon estimates to have the same mean as the Penman-Monteith estimates, using an adjustment factor k_e, which was determined to have a mean of 1.64 with a standard deviation of 0.70. The scaled Hamon estimates were used for the long-term hydrologic water balance computations, except during the IFC periods, when the data needed for computation of the Penman-Monteith $E_p[1]$ were available. During the IFC periods, $E_p[1]$ and $r_w[1]$ were estimated by the Penman-Monteith method and by Eq. (2.4), respectively.

For the 35 days of the IFCs, we calculated an average aerodynamic resistance (equal to the inverse of the product of the drag coefficient from Eq. (2.6) and the wind speed under the assumption that the resistance to the transfer of momentum and water are equal). This average aerodynamic resistance was then used for the purpose of estimating the hydrological model parameters, and for computing the soil moisture at the beginning of the first IFC and between IFCs (but not for validation of the energy fluxes during the IFCs reported in Section 3.2). The average aerodynamic resistance over the 35 days was 40.8 s/m with a standard deviation of 29.7 s/m. This value is within the range given for short grass and crops by Monteith and Unsworth (1990). Since the roughness length of many crops decreases as wind speed increases, the inverse of aerodynamic resistance is approximately a constant over a range of low wind speeds. The daily average wind speed during the 35 days was 2.38 m/s, and the aerodynamic resistance (40.8 s/m) was taken as constant for the estimation of the three hydrological parameters. In addition, we did not correct for atmospheric stability, primarily to assure compatibility of $E_p[1]$ between the IFCs and during the longer period of hydrological water balance simulation, when the data needed to make the corrections were not available. However, the

stability correction given by Eqs. (2.4) and (2.5) was applied to the energy flux computations performed for the model validations reported in Section 3.2.

At the FIFE site, the depths of layer 1 (upper zone) and layer 2 (lower zone) are about 0.5 m and 2.5 m respectively (Famiglietti and Wood 1993). Since the soil texture at FIFE is silt loam (EPA 1991), the porosity was taken to be 0.5, and thus $W_1^c=0.25$ m and $W_2^c=1.25$ m, and W_j^w and W_j^{cr} are about 26% and 46%, respectively, of the total water that the soil can hold. However, Smith et al. (1993) reported that evapotranspiration was not observed to be limited by soil moisture in the 20%−30% range, and they took 18% as the wilting point instead, which we also used as our estimate. In this study, we used 70% of field capacity as our critical point (we found via sensitivity analysis that almost the same results were obtained when the critical point was 75% of field capacity). The K_s, B_p, θ_r were taken as 6.44 mm/h, 0.16, and 0.01 m respectively, following Famiglietti and Wood (1993). Since the vegetation is dominated by grass, we assumed that all the roots are in the upper zone (i.e., $f_1[1]=1.0$ and $f_2[1]=0.0$).

Because the wind speed from the PAM stations was measured at 5.4 m above the ground surface, and the other meteorological data were measured at $z_2[1]=2$ m above ground surface, the wind speed was converted to the 2 m level through a logarithmic velocity profile. Sugita and Brutsaert (1990) estimated the zero plane displacement height $d_0[1]=26.9$ m, and the surface roughness length $z_0[1]=1.05$ m at FIFE by analyzing neutral wind velocity profiles measured by radiosondes. They found that a logarithmic velocity profile only holds over the height ranges between 50 m±19 m and 202 m±101 m above the ground surface. However, their values should be interpreted in the context of the Flint Hills region, which is characterized by relief of about 25m between steep ridges and valleys. By contrast, Smith et al. (1992a) used much smaller local values of $d_0[1]=0.25$ m, and $z_0[1]=0.07$ m. Their values fall between uncut grass and long grass/crops for a relatively flat area (Arya 1988). Since the FIFE site is only a small part of the Flint Hills region which covers a 50-80 km wide north-south strip in Kansas from Nebraska to Oklahoma, we decided to use the

smaller values for $d_0[1]$ and $z_0[1]$, and assumed a logarithmic velocity profile locally. The 2 m wind speed can then be estimated as

$$u_n(z_2) = u_n(z_1) \cdot \frac{\ln(\frac{z_2[1] - d_0[1]}{z_0[1]})}{\ln(\frac{z_1[1] - d_0[1]}{z_0[1]})} \tag{3.1}$$

where $z_1[1]$=5.4 m, and $u_n(z_1)$ is the corresponding measured wind speed (m/s). The value of $r_0[1]$ for grassland is taken as 2.0 s/m (Ducoudre et al. 1993). Monteith and Unsworth (1990) suggest that for crops $r_{min}[1]$=100 s/m. Smith et al. (1993) found, based on optimization, that the best values of $r_{min}[1]$ are in the range $100-125$ s/m. We take $r_{min}[1]$=100 s/m to be consistent with Monteith and Unsworth (1990).

· The monthly average LAI[1,m] (m=1, 2, $\cdots$, 12) were derived from the average normalized difference vegetation index (NDVIs) given by EPA (1991) with LAI_{max}=6.0 and LAI_{min}=0.1 which are consistent with the values used by Smith et al. (1993),

$$LAI[1,m] = 0.1 + 0.0628(NDVI[1,m] - 53.0). \tag{3.2}$$

The average monthly NDVIs for 1986, 1987, and 1988 at FIFE are listed in Table 3.1.

The hydrological parameter D_m can be either estimated by identifying extended dry periods during the calibration interval 1982-85 using the precipitation data, and recession rates inferred from the observed Kings Creek streamflows during these periods; or by multiplying saturated hydraulic conductivity by an average soil slope. We used the first approach, which gave $D_m = 8.2$ mm/d. The hydrological parameters b_i, D_s, and W_s, were estimated using streamflow at Kings Creek, and precipitation, and maximum/minimum temperature data at Manhattan, KS from 1982-1985. The

calibration gave $b_i=0.008$, $D_s=7.7 \times 10^{-5}$, and $W_s=0.96$. The one-layer snowmelt model was not used to obtain the above model parameters, since not much snow occurs in the Kings Creek catchment. Hydrographs for two of the calibration years (1983 and 1984) are shown in Figs. 3.2a and 3.2b. The model reproduces the streamflow reasonably well; discrepancies are attributed to a) the distance of the precipitation gage from the Kings Creek catchment; b) the inability of a single gage to represent spatial variations in precipitation; c) the use of a daily time step for a relatively small catchment whose time of concentration is on the order of an hour or less; and d) small scale heterogeneities which can strongly affect runoff production in small catchments, and are not captured by a macroscale model such as VIC.

With the parameters described above, together with the parameters $\alpha[1]$, $\kappa[1]$, $C_s[1]$, D_2, and T_2, we then used the PAM and flux data to test our model-predicted surface fluxes and surface temperature against the measured values. The albedo $\alpha[1]$ was taken as 0.2 during the IFCs following Famiglietti and Wood (1993). The thermal conductivity $\kappa[1]$ and soil heat capacity $C_s[1]$ in Eq. (2.46) were estimated to be 0.514 $Wm^{-1}K^{-1}$ and 2.13×10^6 $Jm^{-3}K^{-1}$, respectively, following Smith et al. (1992b, 1993). The depth D_2 was taken to be 0.45 m, and the temperature T_2 (i.e., T_{50}) in Eq. (2.46) was prescribed as 293.6 $^\circ K$, which was the average of T_{50} for the selected 35 days of the IFCs. The standard deviation of T_{50} for the 35 days was 3.1 $^\circ K$. The values of the hydrologically and atmospherically related model parameters are listed in Table 3.2. We compared the surface energy budgets computed using both Eq. (2.32) and Eq. (2.34), and found that there was almost no difference in the results when we took $z_a[1]=z_2[1]=2$ m.

3.2. Model validation at FIFE site

Figs. 3.3a and 3.3b show predicted and observed streamflow for 1986 and 1987, two years not in the calibration period. Generally, the results are consistent with those of the calibration period – the dry period flows are fairly well represented, as is the timing of the major peaks, but the magnitudes of the

peaks, especially the largest ones, are subject to major errors. In this study, streamflow prediction is not of primary importance; the purpose in evaluation of the predicted hydrographs is to provide evidence that the model is producing a plausible soil water balance. To this extent, the hydrograph simulations were adequate.

After estimating the hydrological model parameters, we used the FIFE surface fluxes and meteorological measurements for the summer of 1987 to test the model predictions of latent heat, sensible heat and ground heat fluxes, and the surface temperature. We used the Kings Creek precipitation network, as well as the precipitation, air temperature, and downward solar and long-wave radiation composited from the PAM and flux stations by Betts et al. (1993) to test the model heat fluxes and surface temperature. Results are shown in Figs. 3.4, 3.5, and 3.6 for parts of the June, July, August, and October IFCs.

Fig. 3.4 shows part of IFC 2 (from June 30 – July 11). There were precipitation events on June 30 and July 7. On the rest of the days, there was little or no rainfall. During this period, the latent heat flux for dry days was typically about 400 Wm^{-2}. The model predicted the latent heat and sensible heat fluxes fairly well, except that it somewhat underpredicted the July 9, 10, and 11 latent heat fluxes and overpredicted the sensible heat fluxes on the same days. These days were characterized by relatively high winds, high potential evaporation, and high soil moisture. The modeled surface temperatures agree with the observed ones quite well, but the magnitude of the diurnal cycle of the ground heat flux was underpredicted on some of the days.

Fig. 3.5 shows predicted and observed latent, sensible, and ground heat fluxes, and surface temperature, for the August 9-20, 1987 portion of the third IFC. Rainfall occurred on August 12, 13 and 18. Before the August 12-13 storm, the soil was moderately dry. During this period, the observed latent heat fluxes were less than 300 Wm^{-2}. After the rainfall, the latent heat fluxes increased to about 400 Wm^{-2}. During this period, the model predicted the latent heat and sensible heat fluxes quite well, except during the nights of August 14 and 15, when the latent heat fluxes were overpredicted and the

sensible heat fluxes were underpredicted. This is mainly due to the high potential evaporation obtained during that time. From Eqs. (2.1) and (2.12), it can be seen that large evaporation would be obtained if the potential evaporation is large, even though $r_w[n]$ and $r_c[n]$ are reasonable. During this period, the ground heat fluxes were predicted reasonably well, although the magnitude of the diurnal cycle was underestimated. The surface temperatures were well predicted in general.

Fig. 3.6 shows the energy fluxes and surface temperature for October 6-16, 1987, a portion of IFC 4 which was characterized by low soil moisture. During this period, the observed latent heat fluxes were about 100 Wm^{-2} or less, while the sensible heat fluxes increased to about 300 Wm^{-2} (from about 200 Wm^{-2} in July and August). The model predicts the latent and sensible heat fluxes, and surface temperature reasonably well, but it overpredicts the ground heat fluxes on most of the days during this period.

In general, the model performed satisfactorily, especially given its simplicity. There are some caveats in interpretation of the results. First, the FIFE site is a native grassland, which is characterized by a single vegetation type. Therefore, the portion of the model dealing with heterogeneous vegetation was not exercised in these tests, so the effects of certain associated simplifications are not reflected in the results. A second, related limitation is that since the FIFE vegetation is all grassland, the algorithms dealing with trees, which usually extract moisture from the lower, rather than the upper, soil moisture zone have not been exercised. The model has, however, been implemented for a tropical forest application in connection with the Project for Intercomparison of Land-surface Parameterization Schemes (PILPS) (Pitman et al. 1993, Liang et al. 1993) and the model results were comparable to those of most of the participating models.

3.3. ABRACOS site

The second application was to the field site of the Anglo-Brazilian Amazonian Climate Observation Study (ABRACOS). The ABRACOS site is

located in a ranch clearing surrounded by forest in the moist, tropical rain forest climate regime typical of Amazonia. The site was selected to characterize the local and large-scale effects of the amazonian deforestation that has taken place over the past 20 years (Myers 1991). ABRACOS is an ongoing project which started in 1990 and will continue through 1994 (Shuttleworth et al. 1991). The site is extensively instrumented for micrometeorological and climatological measurements. During the three year period of routine monitoring of the near-surface climate and soil moisture, five intensive micrometeorological and plant physiological studies are planned to be carried to supplement the long-term routine measurements.

The time frame of the intensive measurement campaigns is summarized in Fig. 3.7 (taken from Shuttleworth et al. (1991)). One of the objectives of ABRACOS is to collect data from cleared Amazonian forest and thus to provide energy and water balance and near-surface climate measurements for GCM studies. The clearing site selected in the ABRACOS project is at Fazenda Dimona, which is located about 100 km north Manaus ($2^{\circ}19$'S, $60^{\circ}19$'W) in central Amazonia (Fig. 3.8). It is a typical large cattle ranch created by felling and burning the primary forest and sowing the clay soil with hardy pasture grasses about 12 years ago. The studied area consists of about 84% grass, 11% bare soil, 5% trunks, and less than 1% bushes. The height of the grass cover was about 28 cm in September 1990. This selected site was well managed, and there was no overgrazing. A more detailed description of the site is given by Wright et al. (1992). The climate is moist and hot with mean annual rainfall of about 2400 mm. The driest months are from July to October, and the wettest months are from March to May.

3.3.1. Data description

During 1990 and 1991, two intensive field measurements, Mission 1 and Mission 2, were carried out. Mission 1 started on September 15 and ended on November 5 in 1990, while Mission 2 was from June 30 to September 11 in 1991.

Four major instruments were used for micrometeorological data collection

at the site. These are a profile tower with six logarithmically spaced anemometers and psychrometers, a Hydra eddy-correlation device, a Bowen ratio device (from Campbell Scientific Ltd.), and an automatic weather station. Net all-wave radiation, specific humidity, and horizontal wind speed were recorded at the profile tower. Soil temperatures were recorded by thermistors located 15 m upwind of the profile tower. Ground heat flux was measured as the average of nine soil heat flux plates that were installed at 5 mm depth under the grass and bare soil, located at equal distances along a transect about 15 m upwind of the profile tower. The Hydra device, sampled with a frequency of 10 Hz, recorded air temperature, specific humidity, and wind speed. A net all-wave radiometer was connected to the Hydra. The Bowen ratio device measured the temperature and humidity gradients between levels of 0.9 m and 3.2 m. In addition, it had its own net all-wave radiometer. The automatic weather station recorded the wet bulb temperature, dry bulb temperature, net all-wave radiation, wind speed, total incoming shortwave radiation, reflected shortwave radiation, soil heat flux, and rainfall. Hourly rainfall was measured by a 0.2 mm tipping-bucket rain-gauge attached to the automatic weather station (Wright et al. 1992). All of the four instruments were located within a few meters of each other (Shuttleworth 1993, personal communication).

The hourly summary data for the first two ABRACOS missions were provided by INPE (Instituto Nacional de Pesquisas), Sao Paulo, Brazil. These data were aggregated from ten minute measurements and were subjected to a data quality control process by staff at INPE. For purposes of determining consistency between measurements, the following priorities were assigned: 1) profile tower, 2) Hydra eddy-correlation device, 3) Bowen ratio device, and 4) automatic weather station. Missing and unreliable data were indicated by "-99" in the data base. The two-layer VIC model validation was conducted using 17 days from Mission 1 and 42 days from Mission 2 that had continuous data.

Mission 1 started on September 15 and ended on November 5, but there were only 18 days (from October 15 to November 1) that have almost continuous

measurements of net radiation, precipitation, specific humidity, air temperature, and wind speed that are needed to drive the two-layer VIC model, and latent heat flux, sensible heat flux, and the ground heat flux that are needed to validate the model predictions. Soil temperatures were measured at depths of 0.05 m, 0.1 m, 0.2 m, and 0.4 m. Soil moisture was measured weekly in general, and twice each week during the two missions using neutron probes. A schematic outlining the profile of the soil water measurements is shown in Fig. 3.9. The soil moisture in the soil surrounding the eight neutron probe tubes was measured at the depths of 0.1 m, 0.2 m, 0.4 m, 0.6 m, 0.8 m, 1.0 m, 1.2 m, 1.4 m, 1.6 m, 1.8 m, and 2.0 m below the ground surface. Since soil moisture was not measured on October 15, but on October 16, only 17 days (from October 16 to November 1) were finally selected. Among the selected 17 days, the wind speed at 0200 LMT on October 16 (Julian day 289) was missing, and was estimated by interpolation. In addition, a few wind speed measurements on October 16 were taken from the automatic weather station at the elevation of 2.0 m above the ground. These wind speeds were corrected to the 3.6 m level so that they were consistent with the wind speed in the rest of the data of the selected 17 days. The individual flux data were checked for errors to make sure they fell within the ranges given by Betts et al. (1993) as follows:

Solar radiation	-5 to 1200 (Wm^{-2})
Solar reflected	-5 to 250 (Wm^{-2})
Net radiation	-98 to 1000 (Wm^{-2})
Latent heat	-100 to 500 (Wm^{-2})
Sensible heat	-200 to 500 (Wm^{-2})
Ground heat	-150 to 300 (Wm^{-2}).

The check against the above criteria indicated no gross discrepancies in the flux data. However, when the measured net radiation was compared with the sum of the derived latent and sensible heat fluxes, and the measured ground heat flux, three hourly values were found to have large relative errors. These are LMT 2100 on Julian day 293, 1900 on Julian day 301, and 0700 on Julian day 303

with relative errors of 176%, 198%, and 41% respectively. These data were replaced by interpolated values. The corrected data agreed well with the consistency check. The average wind speed for the 17 days was 1.67 m/s with a standard deviation of 1.10 m/s; the average of the specific humidity was 17.5 g/kg with a standard deviation of 1.0 g/kg; the average of air temperature was 26.6°C with a standard deviation of 3.7°C. The total precipitation of the 17 days was 6.6 mm, indicating that the period was generally dry.

The surface air pressure was not measured during either Mission 1 or Mission 2. However, there were 26 days (from April 18 to May 13) in 1987 that had surface pressure measurements at GMT 0000 on each day, and 5 days (from May 1 to May 5) in 1987 that had six pressure measurements on each day at 0000, 0600, 1200, 1500, 1800, and 2100 GMT. The first set of pressure measurements (26 days) had an average of 1004.1 mb with a standard deviation of 1.1 mb. The second set of measurements (from May 1 to May 5) had an average of 1003.5 mb with a standard deviation of 1.6 mb. Based on these limited available pressure measurements and discussions with INPE scientists, for the model runs, the surface pressure was taken to be constant 1003.8 mb, which is an average of all the measurements.

Mission 2 started on June 30 and ended on September 11, 1991, and there were some missing observations. Among the 74 days, 72 days (from June 30 to September 9) have almost continuous measurements of the quantities that are required to drive the two-layer VIC model and to compare the model predictions with the observations. The Betts et al. validation criteria for solar radiation, solar reflected radiation, net radiation, latent heat, sensible heat, and ground heat fluxes were applied as they were for the Mission 1 data set. The results indicated that all the data were within the specified ranges. However, the data passed the consistency check for net radiation on only 42 days (from July 5 to August 15). Large errors occurred on other days as shown in Fig. 3.10. These large inconsistencies between the observed net radiation and the calculated net radiation from the derived latent and sensible heat fluxes, and the measured ground heat flux at the end of Mission 2 (i.e., after August 15) were probably

due to drift in the hygrometer (Wright 1993, personal communication). Therefore, only the 42 days (from July 5 to August 15) in Mission 2 were used for model testing.

Among the 42 selected days, there were six measurements of specific humidities at 1.2 m height, while the rest were measured at 3.6 m. Since the specific humidities do not change much between the heights of 1.2 m and 3.6 m above the surface, the 1.2 m measurements were not corrected for height. The average wind speed for the 42 days was 1.43 m/s with a standard deviation of 0.98 m/s; the average specific humidity was 16.5 g/kg with a standard deviation of 1.1 g/kg; the average air temperature was 24.8°C with a standard deviation of 3.3°C; and the total precipitation of the 42 days was 105 mm. Although still relatively dry in a climatalogical sense, the Mission 2 data include several storm periods. From Fig. 3.14 it can be seen that there were major storms before July 5.

3.3.2. Parameter estimation.

The ABRACOS site consists of about 84% short grass with average height 0.28 m, 11% bare soil, 5% tree trunks, and less than 1% bushes (Wright et al. 1992). Since measurements were not conducted under the surface covers of the trunks and bushes, these trunks and bushes are assumed to be bare soil which then covers 16% of the area. This consideration is consistent with the measurements of the soil heat flux described by Wright et al. (1992). Thus, the number of surface covers at the clearing site is two, with $C_v[1]=0.84$ (n=1 for grass) and $C_v[2]=0.16$ (N+1=2 for bare soil).

As described in Chapter 2, the two-layer VIC model has two soil layers, an upper zone and lower zone. The upper zone in the model was designed to represent the dynamic behaviour of the soil responding to rainfall events. In other words, the soil moisture in the upper zone varies dynamically with rainfall events and atmospheric moisture transport conditions, while the soil moisture in the lower zone tends to characterize the seasonal soil moisture variations. The lower zone only responds to rainfall when the upper zone is relatively wet and

thus it can separate the subsurface flow from the rainfall quick response. At the clearing site, the soil moisture measurements at the eleven different soil depths described above showed that the soil moisture storage in the first 1 m depth varied between 0.3 m and 0.45 m from mid-September 1990 to December 1991, while th moisture storage between 1 m and 2 m depth varied only from about 0.45 m to about 0.5 m for the same period (Hodnett et al. 1993). Therefore, the upper layer was taken to be from the surface to a depth of 1 m. Following Hodnett et al. (1993), the depth of the lower layer was taken to be 9 m.

The soil at the clearing site consists of clayey oxisols from the Tertiary Barreiras sediments. According to the Brazilian classification, oxisols are generally classified as latossolos amarelos, alicos, and textura argilosa. In the USDA Soil Taxonomy, oxisols correspond to the aplic acrorthox. From soil moisture measurements, the porosity was estimated as $\theta=0.64$, the wilting point as $\theta_w=0.34$, and the field capacity as $\theta_f=0.51$ (Hodnett et al. 1993). As before, the critical point was taken as 70% of the field capacity ($\theta_{cr}=0.36$). Based on field work by the Institute of Hydrology (U.K.) and INPE (Rocha 1993, personal communication), the saturated hydraulic conductivity is $K_s=79.2$ mm/h, the pore size distribution index is $B_p=0.053$, the root depths of upper and lower layers are $f_1[1]=1.0$ and $f_2[1]=0.0$, and the soil thermal conductivity and soil heat capacity are 0.69 $Wm^{-1}K^{-1}$ and 7.74×10^5 $Jm^{-3}K^{-1}$ respectively. According to Wright et al. (1992), the displacement height for the entire area is 0.17 m and the roughness length is 0.026 m, and thus $d_0[1]=d_0[2]=0.17$ m and $z_0[1]=z_0[2]=0.026$ m.

Since hourly net radiation was measured at the site, but not long-wave radiation, albedo and solar radiation were not used in this model application. The study by McWilliam et al. (1993) indicated that the leaf area index (LAI) at the clearing site is about 1.5. In addition, due to the climatic conditions in central Amazonia, the LAI is relatively constant throughout the year. Monteith and Unsworth (1990) suggest that for crops during the growing season, the minimum stomatal resistance varies from 50 s/m to 100 s/m. The growing season minimum stomatal resistance was measured to be 50 s/m (Bougeault

1991). Sellers and Dorman (1987) reported that the minimum stomatal resistance is about 50 s/m for short vegetation. Following the approach used by Smith et al. (1993) to determine the minimum stomatal resistance at FIFE site, an optimization on the stomatal resistance within the range (50, 100) was carried out using the data of the selected 17 days in Mission 1. The optimization indicated that $r_{min}[1]=50$ s/m gave the best results, although the difference in the latent heat flux due to $r_{min}[1]=50$ s/m and $r_{min}[1]=100$ s/m, for example, is small. The absolute relative changes of the mean latent heat and sensible heat fluxes during this period in Mission 1 were 8.0% and 12.1% respectively, while the relative change in minimum stomatal resistance was 100%. Thus, the stomatal resistance was taken as 50 s/m. The optimization on minimum stomatal resistance $r_{min}[1]$ was not carried out for the 42 days in Mission 2. As for the application at FIFE site, the architectural resistance of grass was taken as $r_0[1]=2.0$ s/m (Ducoudre et al. 1993).

The soil temperatures were measured at four different depths as described in Section 3.3.1, and are shown in Figs. 3.11 (from September 25 to October 5 in 1990), 3.12 (from October 15 to November 1 in 1990), and 3.13 (from June 30 to September 10 in 1991). From Fig. 3.11, it can be seen that the soil temperature at 0.05 m depth dropped below 0°C around September 30. This was due to a measurement problem (Wright 1993, personal communication). Fig. 3.12 shows the fluctuation of the soil temperatures at 0.05 m and 0.4 m depths is suspiciously large from October 17 to 28. During Mission 1, the variation of the soil temperature from its mean at 0.4 m depth is about 14 times larger than the variation of the temperature at depth 0.2 m, and about 4 times larger than the variation at depth 0.1 m. Therefore, the temperature measurements at the 0.4 m depth in Mission 1 appear inconsistent, so are the measurements at 0.05 m depth. The soil temperature measurements at depths 0.05 m and 0.4 m in Mission 2 indicated alarming drifts. Thus, the Mission 2 soil temperature at depth 0.4 m could not be used. Since the fluctuation of the soil temperature at 0.2 m depth is small (mean 26.8°C and standard deviation of 0.6°C in Mission 1; 27.1°C mean and 0.6°C standard deviation in Mission 2), the mean of the soil temperature at the depth 0.2 m was assumed to be a

constant and $T_2 = 300^\circ K$ was used in the model. Thus, depth D_2 that corresponds to the constant temperature T_2 is 0.15 m.

Since there were no streamflow data available in the studied area, the hydrological parameters b_i, D_s, W_s could not be estimated through the standard hydrological calibration method, nor could the maximum subsurface flow D_m be estimated by analyzing the dry period streamflow as was done in the FIFE application. Instead, D_m was estimated by multiplying the saturated hydraulic conductivity by the average soil slope. At the clearing site, the slope is about 3°. As for the three hydrological parameters b_i, D_s, and W_s, they were assigned values based on the ranges suggested by Dumenil and Todini (1992). The effect of specifying the three parameters in this way is insignificant to the model predicted latent heat and sensible heat fluxes (see Chapter 4). The value of each parameter used at the clearing site is given in Table 3.3.

As noted in Section 3.3.1, soil moisture was measured at 11 depths, and thus the average soil water content could be derived for both the upper layer and the lower layer. Since the soil moisture was measured on October 16 of 1990 and on July 5 of 1991, the average water contents on each day were derived as $\theta = 0.368$ (0.368 m) and $\theta = 0.436$ (3.924 m) for the upper and lower layers on October 16, respectively, and as $\theta = 0.420$ (0.420 m) and $\theta = 0.466$ (4.191 m) for layers 1 and 2, on July 5, respectively. These values were used as the initial soil moisture contents of the two test runs for Missions 1 and 2 respectively. The initial value of the intercepted water by the canopy was estimated based on precipitation information for the days prior to October 16 and July 5. On October 14 and 15, the two days before the beginning of the Mission 1 calculations, there was no rainfall. Therefore, the initial intercepted water for Mission 1 was set to zero. For the Mission 2 application, there was some rainfall on July 3 and 4, but there was no rainfall for the four hours before the beginning calculation time at 0000 LMT on July 5. Since the maximum intercepted water by the given LAI was 0.17 mm and the average evaporation rate at that time was 0.18 mm/hr (Hodnett et al. 1993), the small intermittent rainfall with rates less than 0.2 mm/hr before 2000 LMT on July 4 should have evaporated within

the four hours before 0000 LMT on July 185, and the initial intercepted water for Mission 2 was also set to zero.

3.4. Model validation at ABRACOS site

With the model parameters determined above, the two-layer VIC model was applied to the hourly data of the 17 days in Mission 1 and the 42 days in Mission 2. The model predictions of the hourly latent heat, sensible heat, and ground heat fluxes were tested against the hourly observations. Since surface temperature was not measured, the model-predicted effective surface temperature was not tested.

Fig. 3.15 shows the model predicted (dotted) latent, sensible, and ground heat fluxes and the corresponding observed quantities (solid line) for Mission 1. During the 17 days of Mission 1, there was little rainfall, except for the one on October 24 which reached about 3.6 mm for one hour (see Fig. 3.14). During the first 6 days, the observed latent heat fluxes were about 300 Wm^{-2}, and the sensible heat fluxes were about 200 Wm^{-2}, while the latent heat and sensible heat fluxes both had smaller values on the last 6 days. The model predicts latent heat and sensible heat fluxes well for the first 12 days. For the remaining 5 days of Mission 1, the model underpredicts the latent heat fluxes and overpredicts the sensible heat fluxes on the same days.

The reason for the underpredictions of latent heat fluxes at the end of Mission 1 might be due to underestimation by the model of the soil moisture during that time (Fig. 3.19). In fact, for the 17 days of Mission 1, the model indicates that reduction of upper zone soil moisture (first 1 m depth) is accompanied by a reduction of latent heat and an increase in sensible heat, but the observed data do not support this. From Fig. 3.19, it can be seen that the observed upper zone soil moisture increased during October 25 to 27 with no rainfall events observed during that period. This increase of soil moisture makes it possible to evaporate more during the next few days as is shown in the observed latent heat fluxes. In contrast, the model shows a decrease in upper zone soil moisture that is consistent with the no rainfall period. This decrease of

soil moisture reduces the latent heat flux and increases the sensible heat flux as shown in Fig. 3.15. The increase of observed soil moisture during the no rainfall period might be due to moisture movement from the lower zone. Such capillary movement is not represented in the current two-layer VIC model. The largest difference between model-simulated and observed soil moisture in Mission 1 was about 20 mm.

For the ground heat fluxes, the model predicts the peaks fairly well for the first 7 days, and overpredicts the peaks for the remainder of Mission 1. The model-simulated ground heat fluxes tend to give larger negative values on the days where small spikes occurred on either observed latent heat flux or sensible heat flux such as on October 17, 18, 19, 20, 21, etc., while reasonable negative ground heat fluxes were predicted on October 22, 23, and 24, for example, where such small spikes were not present in the measurements. The means and their standard deviations of the model predicted fluxes and the ones of the corresponding observed quantities for Mission 1 are listed in Table 3.4a. From Table 3.4a, it can be seen that the differences between model predicted statistics (mean and standard deviation) and the observed statistics are small.

The comparison between model predicted and the observed fluxes for the 42 days of Mission 2 is shown in Figs. 3.16 (from July 5 to 18), 3.17 (from July 19 to August 1), and 3.18 (from August 2 to 15). The soil was moister during Mission 2 than it was during Mission 1. The upper zone soil moisture was above the critical point for the duration of Mission 2, while it was only slightly above the wilting point at the end of Mission 1. The observed latent heat fluxes were about 400 Wm^{-2} on the days with no rainfall. From Fig. 3.16, it can be seen that the model predicts the latent heat fluxes very well on both raining days and non-raining days. In general, the model overpredicts the sensible heat fluxes slightly and underpredicts the ground heat fluxes slightly as well, but the overall prediction is quite good during these days. The model predicts the latent heat, sensible heat, and ground heat fluxes quite well from July 19 to August 1 (Fig. 3.17), and from August 2 to 15 (Fig. 3.18). The same statistics used to summarize the model performance for Mission 1 were computed for the 42 days

in Mission 2 and are listed in Table 3.4b. The large negative simulated ground heat fluxes predicted in Mission 1 did not occur in Mission 2 (see Figs. 3.16, 3.17, and 3.18). A closer look at the observed fluxes during Mission 2 indicates that the small spikes in the observed latent heat and sensible heat fluxes were not present in Mission 2, suggesting that some of the apparent Mission 1 model error may in fact have been attributable to measurement errors.

During Mission 2, the model simulated moistures were larger than the observed ones before August 7, and smaller than the observed ones after August 7. Nevertheless, the largest difference was less than 30 mm (Fig. 3.19). The statistics of the soil moisture predictions and observations for Missions 1 and 2 are given in Table 3.5.

3.5. Summary of the model application

The two-layer VIC model performed well for a hot and moist condition which is much different from the FIFE site. The applications to the ABRACOS and FIFE sites suggest that the two-layer VIC approach, coupled with a simplified vegetation model, may be sufficient to represent land surface fluxes. Nonetheless, it must be emphasized that the model testing to date is for two small areas with the specific land covers and climates; more testing will be required at other sites where detailed surface flux data are available before the model can be considered to be globally validated. This latter concern, however, is not limited to this model alone; a major thrust of such projects as GCIP (GEWEX (global energy and water cycle experiment) continental-scale international project), and large scale field experiments such as BOREAS (boreal ecosystem-atmosphere study), is to provide better large area surface moisture and energy flux data for validation of GCM land surface algorithms. The approach described in Chapter 2 may be considered as a candidate protocol for future validations of GCM land surface parameterizations.

Table 3.1. Average monthly NDVIs at the FIFE site

Mo	J	F	M	A	M	J	J	A	S	O	N	D
NDVI	53	58	66	89	132	147	145	136	122	84	66	62

Table 3.2. Model parameters at the FIFE site

Parameter	Value	Parameter	Value
b_i	0.008	$r_o[1]$ (s/m)	2.0
D_m (mm/h)	0.34	$r_{min}[1]$ (s/m)	100.0
D_s	7.7×10^{-5}	$d_o[1]$ (m)	0.25
W_s	0.96	$z_o[1]$ (m)	0.07
B_p	0.16	$C_v[1]$	1.0
K_s (mm/h)	6.44	$f_1[1]$	1.0
W_1^c (mm)	250.0	$f_2[1]$	0.0
W_2^c (mm)	1250.0	T_2 (^{o}K)	293.6
W_j^w (mm)	$0.18 W_j^c$	$\alpha[1]$	0.2
W_j^{cr} (mm)	$0.46 W_j^c$	$\kappa[1]$ (Wm^{-1}K^{-1})	0.514
θ	0.5	$C_s[1]$ (Jm^{-3}K^{-1})	2.13×10^6

Table 3.3. Model parameters at the ABRACOS site

Parameter	Value	Parameter	Value
b_i	0.1	$r_o[1]$ (s/m)	2.0
D_m (mm/h)	4.15	$r_{min}[1]$ (s/m)	50.0
D_s	0.008	$d_o[1]$ (m)	0.17
W_s	0.9	$z_o[1]$ (m)	0.026
B_p	0.053	$C_v[1]$	0.84
θ	0.64	$LAI[1, m]$	1.50
K_s (mm/h)	79.2	$f_1[1]$	1.0
W_1^c (mm)	640.0	$f_2[1]$	0.0
W_2^c (mm)	5760.0	T_2 (^oK)	300.0
W_j^w (mm)	$0.53W_j^c$	$\kappa[1]$ ($Wm^{-1}K^{-1}$)	0.69
W_j^{cr} (mm)	$0.56W_j^c$	$C_s[1]$ ($Jm^{-3}K^{-1}$)	7.44×10^5

Table 3.4c. Comparison of statistics for ABRACOS Mission 1

Names	Mean(cal) (Wm^{-2})	Std(cal) (Wm^{-2})	Mean(obs) (Wm^{-2})	Std(obs) (Wm^{-2})
Latent	67.63	98.88	64.46	102.16
Sensible	40.38	69.91	41.19	67.99
Ground	-0.33	27.80	2.07	18.52

Table 3.4b. Comparison of statistics for ABRACOS Mission 2

Names	Mean(cal) (Wm^{-2})	Std(cal) (Wm^{-2})	Mean(obs) (Wm^{-2})	Std(obs) (Wm^{-2})
Latent	93.73	128.86	95.86	134.69
Sensible	30.98	44.87	24.35	38.31
Ground	-4.05	21.63	0.43	22.41

Table 3.5. Comparison of upper zone soil moisture for
ABRACOS Missions 1 and 2

Names	Mean(cal) (mm)	Std(cal) (mm)	Mean(obs) (mm)	Std(obs) (mm)
Mission 1	348.34	9.17	354.61	8.78
Mission 2	402.64	19.10	395.06	14.49
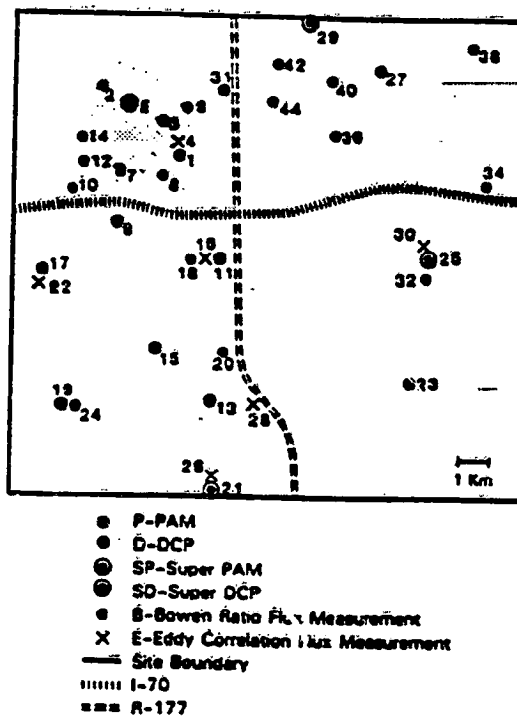
Fig. 3.1 Schematic representation of the FIFE site with approximate locations of King's Creek catchment (shaded area), fluxes stations, and meteorological stations (After Famiglietti et al. 1992).

Kings Creek, KS
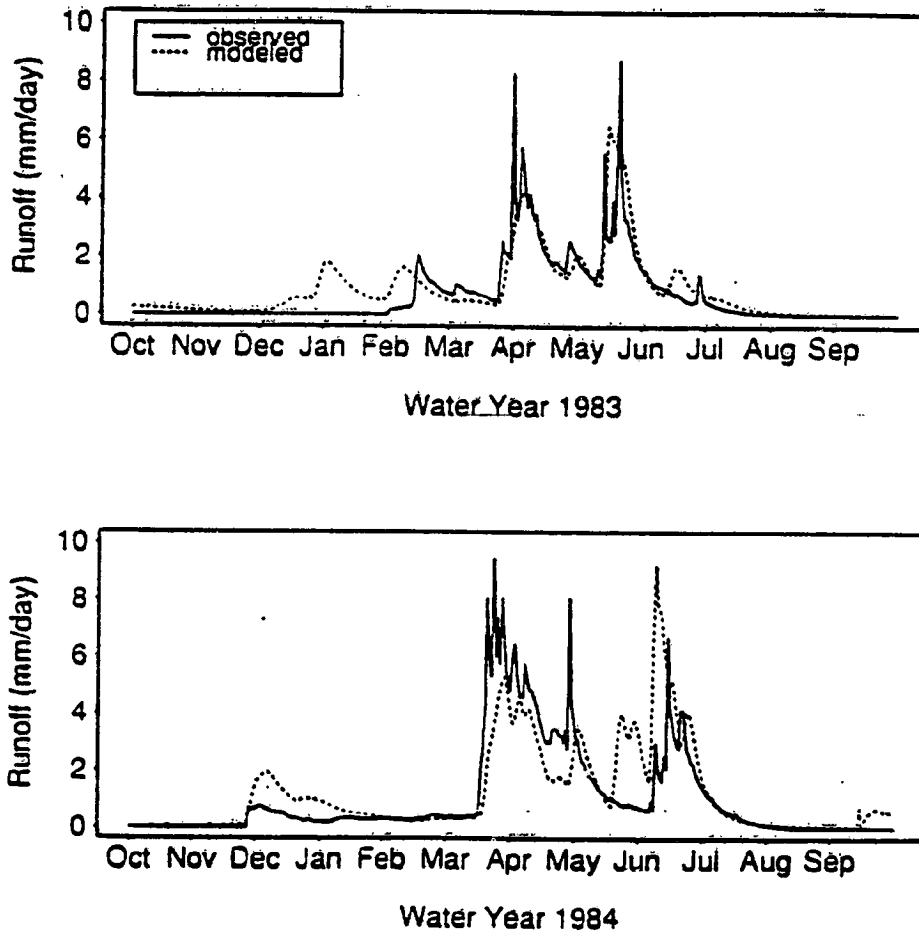
Fig. 3.2   Predicted (dotted) and observed (solid) streamflow for Kings Creek for calibration years 1983-1984.

Kings Creek, KS
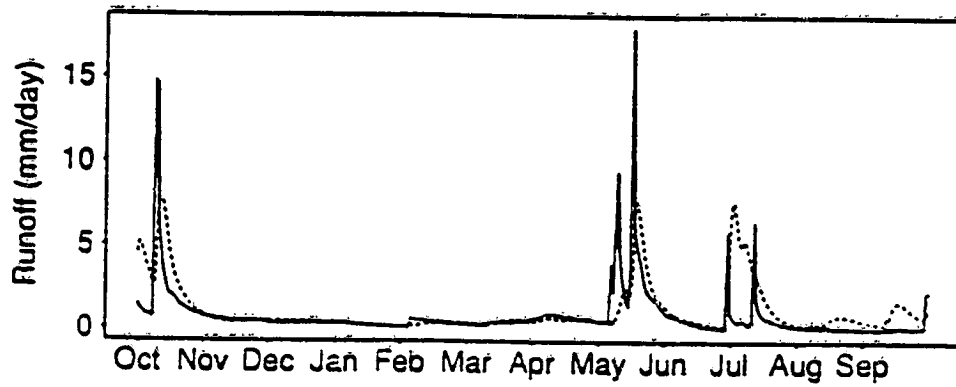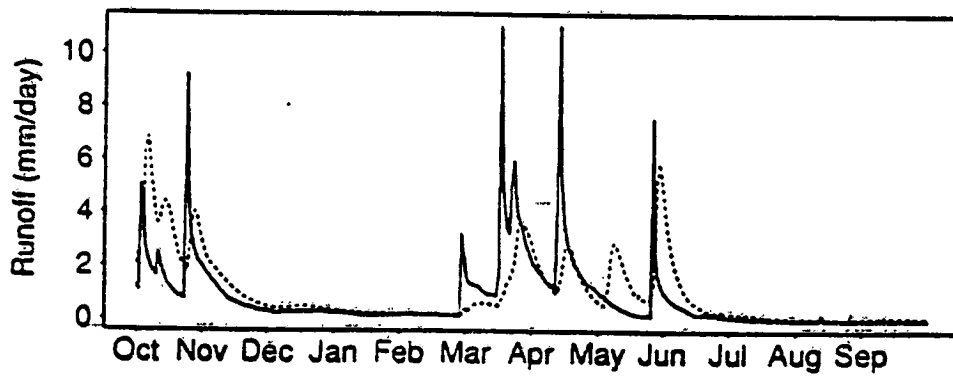
Fig. 3.3   Predicted (dotted) and observed (solid) streamflow for Kings Creek for validation years 1986-1987.
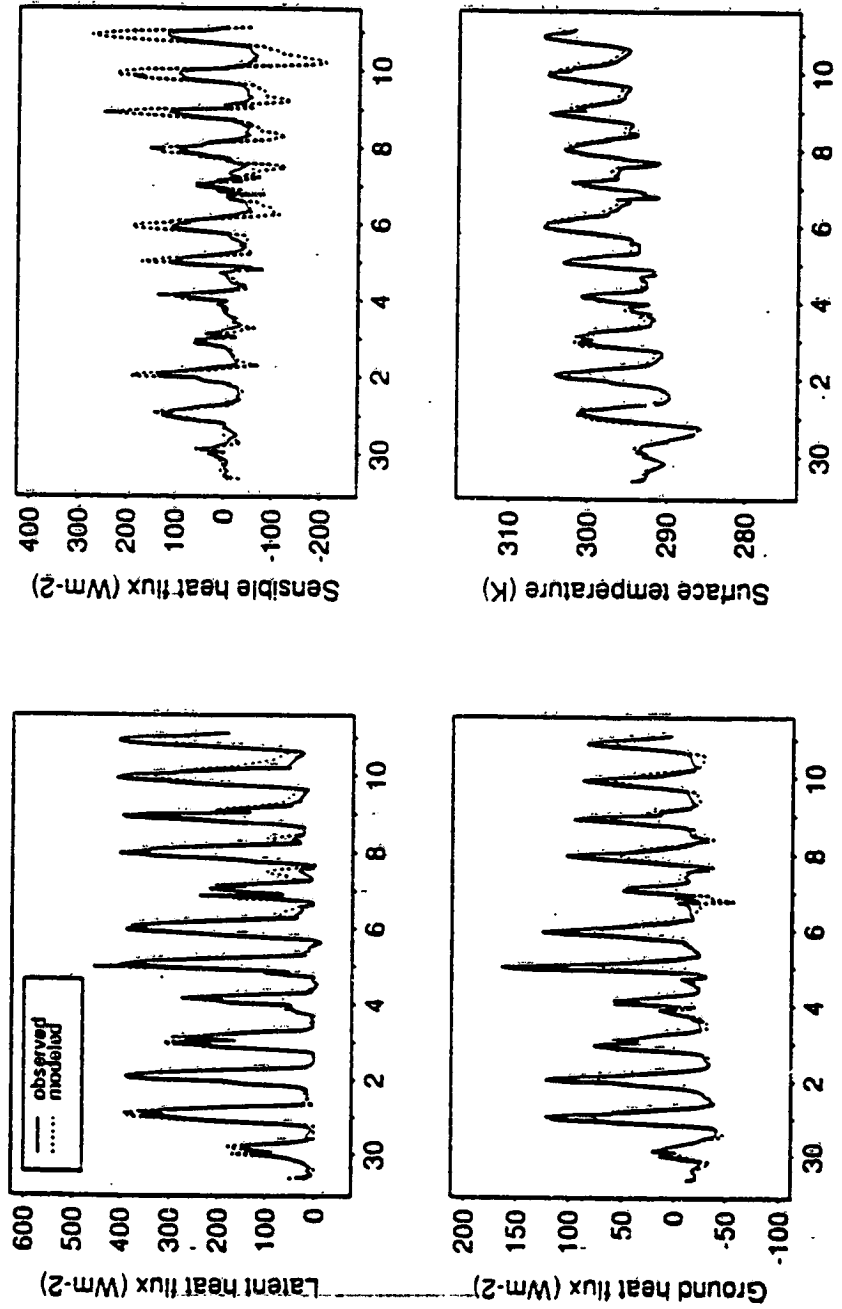
Fig. 3.4   Comparison of predicted (dotted) and observed (solid) surface fluxes and surface temperature at the FIFE site for June 30-July 11, 1987 (IFC 2).

64
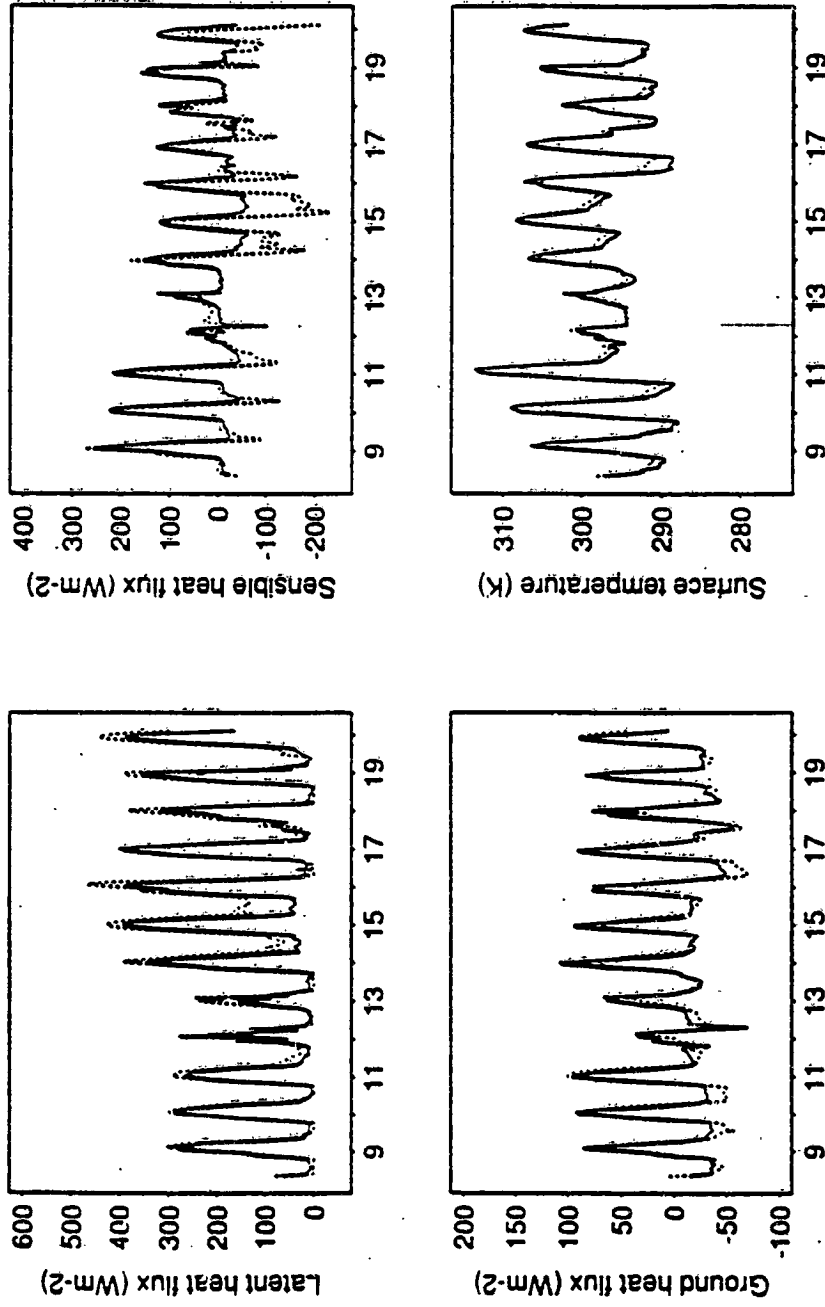
Fig. 3.5   Comparison of predicted (dotted) and observed (solid) surface fluxes and surface temperature at the FIFE site for August 9-20, 1987 (IFC 3).
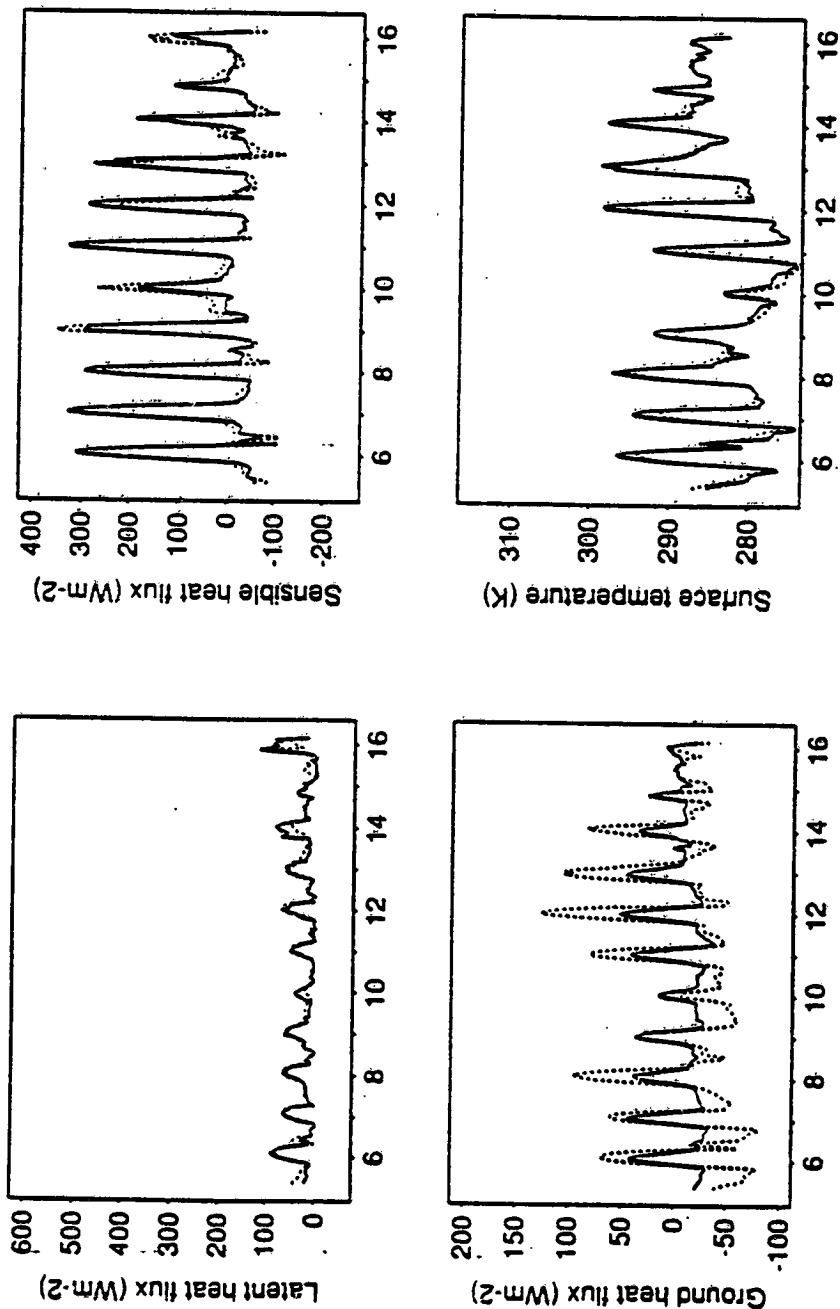
Fig. 3.6 Comparison of predicted (dotted) and observed (solid) surface fluxes and surface temperature at the FIFE site for period of extremely dry soil moisture during October 6-16, 1987 (IFC 4).
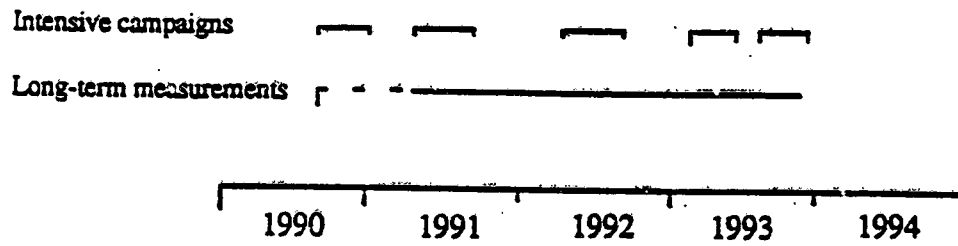
Fig. 3.7   Schematic representation of the time frame for the Anglo-Brazilian
Amazonian Climate Observation Study (ABRACOS) (After
Shuttleworth et al. 1991).
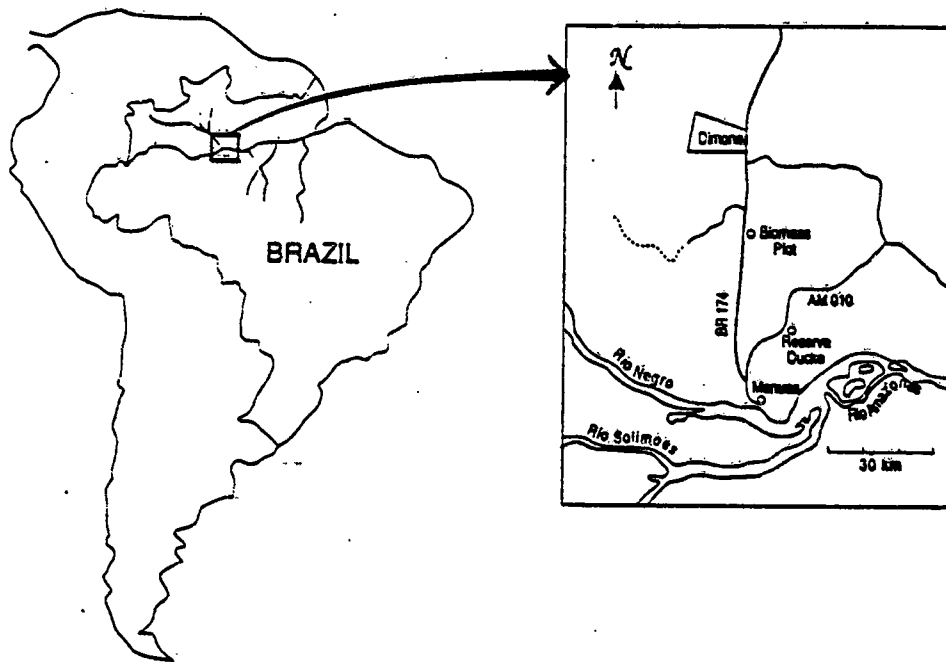
Fig. 3.8   Location of the ABRACOS site (After McWilliam et al. 1993).
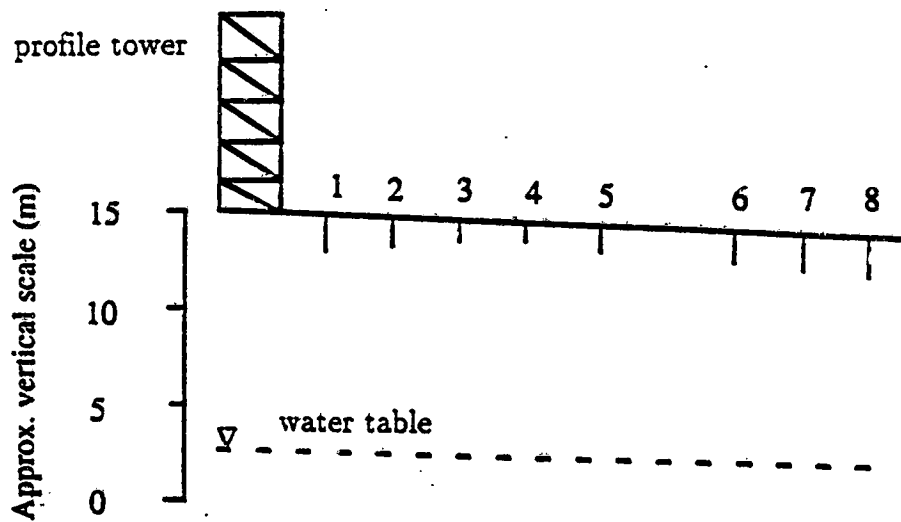
Fig. 3.9 Vertical schematic representation (not to scale) of the location of the profile tower (9 m in height) and the eight neutron probe tubes (over about 500 m horizontally) used for soil water measurements at the ABRACOS site (After Hodnett et al. 1993).
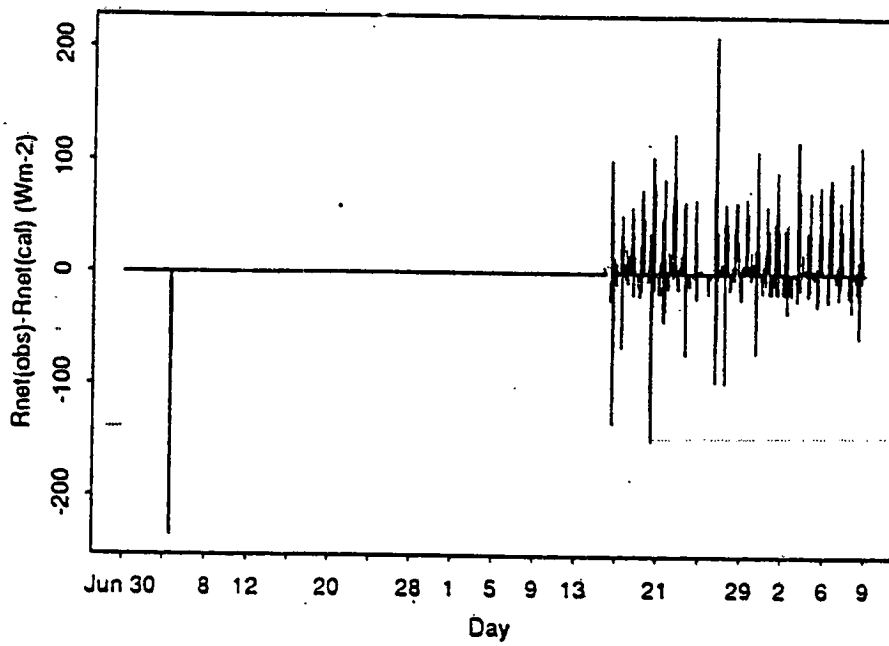
Fig. 3.10   Consistency check of hourly fluxes for ABRACOS Mission 2 (June 30-September 9, 1991).
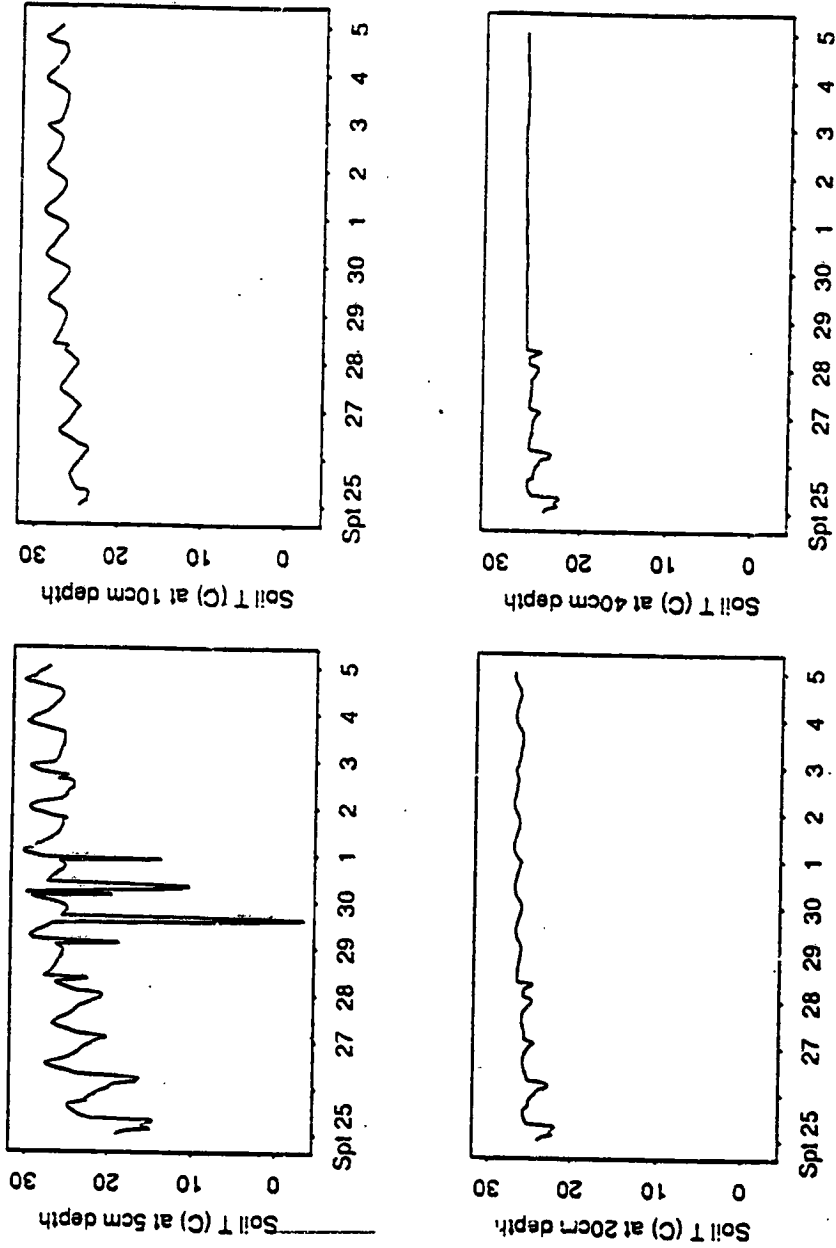
Fig. 3.11 Soil temperatures at different depths for ABRACOS Mission 1
(September 25-October 5, 1990).

"Page missing from available version"
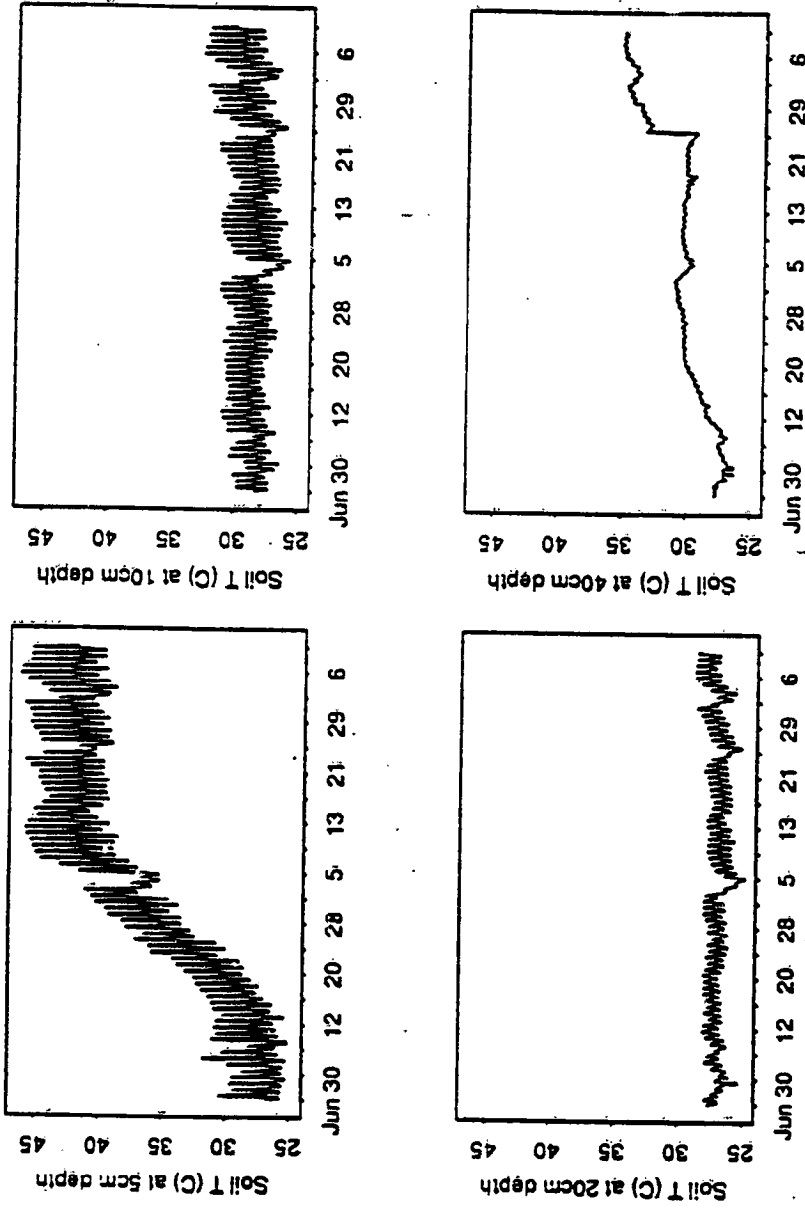
Fig. 3.13 Soil temperatures at different depths for ABRACOS Mission 2 (June 30-September 10, 1991).
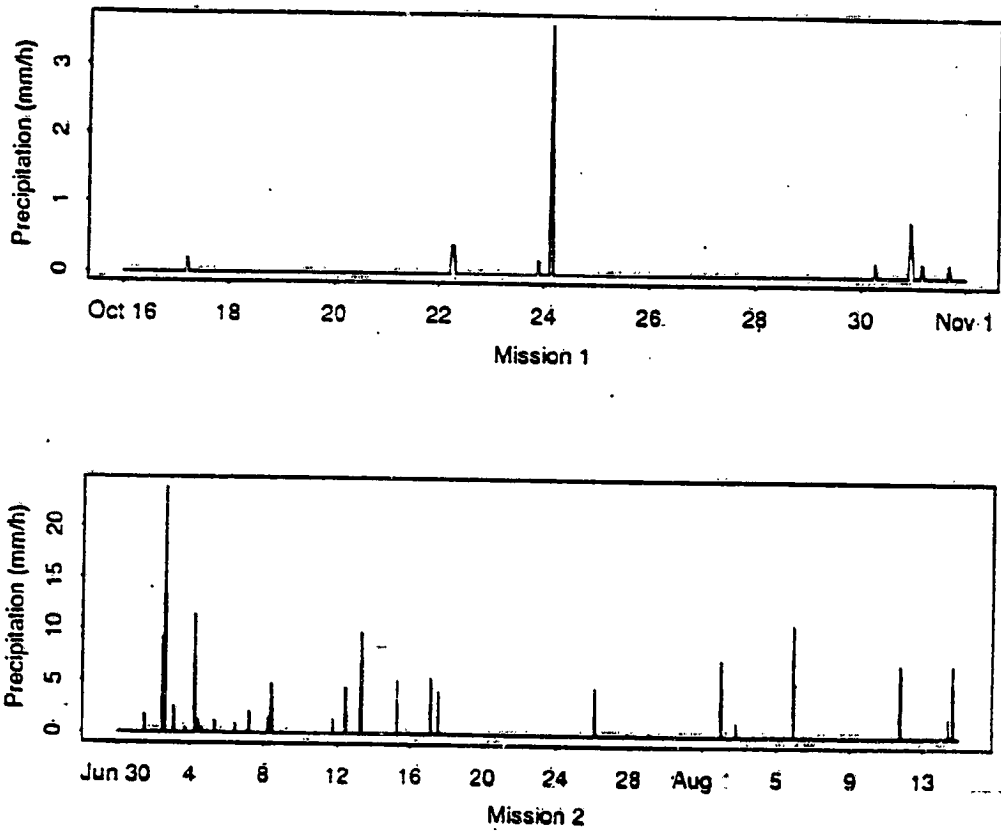
Fig. 3.14 Hourly precipitation for ABRACOS Mission 1 (October 16-November 1) and Mission 2 (June 30-August 15, 1991).

74
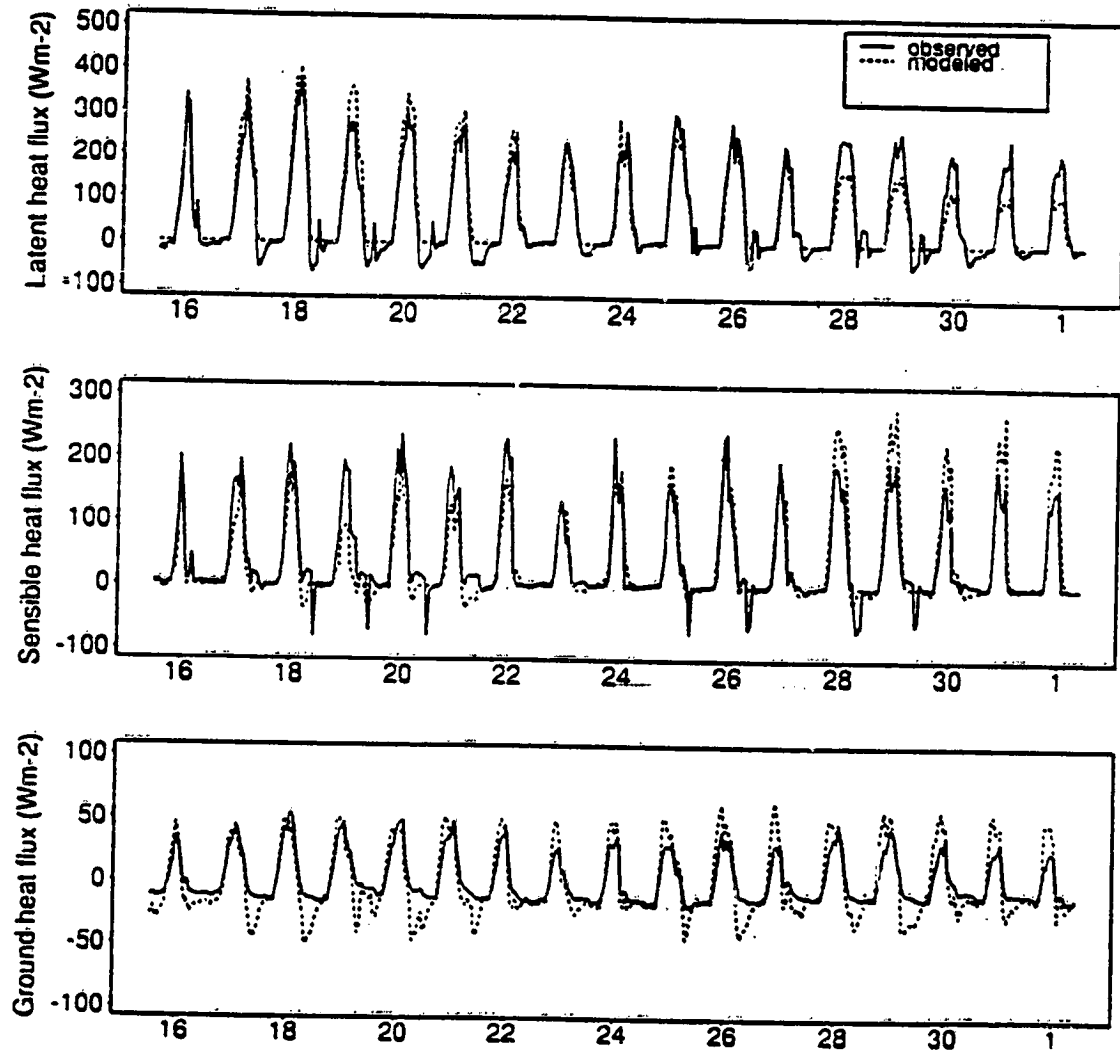
Fig. 3.15 Comparison of predicted (dotted) and observed (solid) surface fluxes at the ABRACOS site for October 16-November 1, 1990 portion of Mission 1.
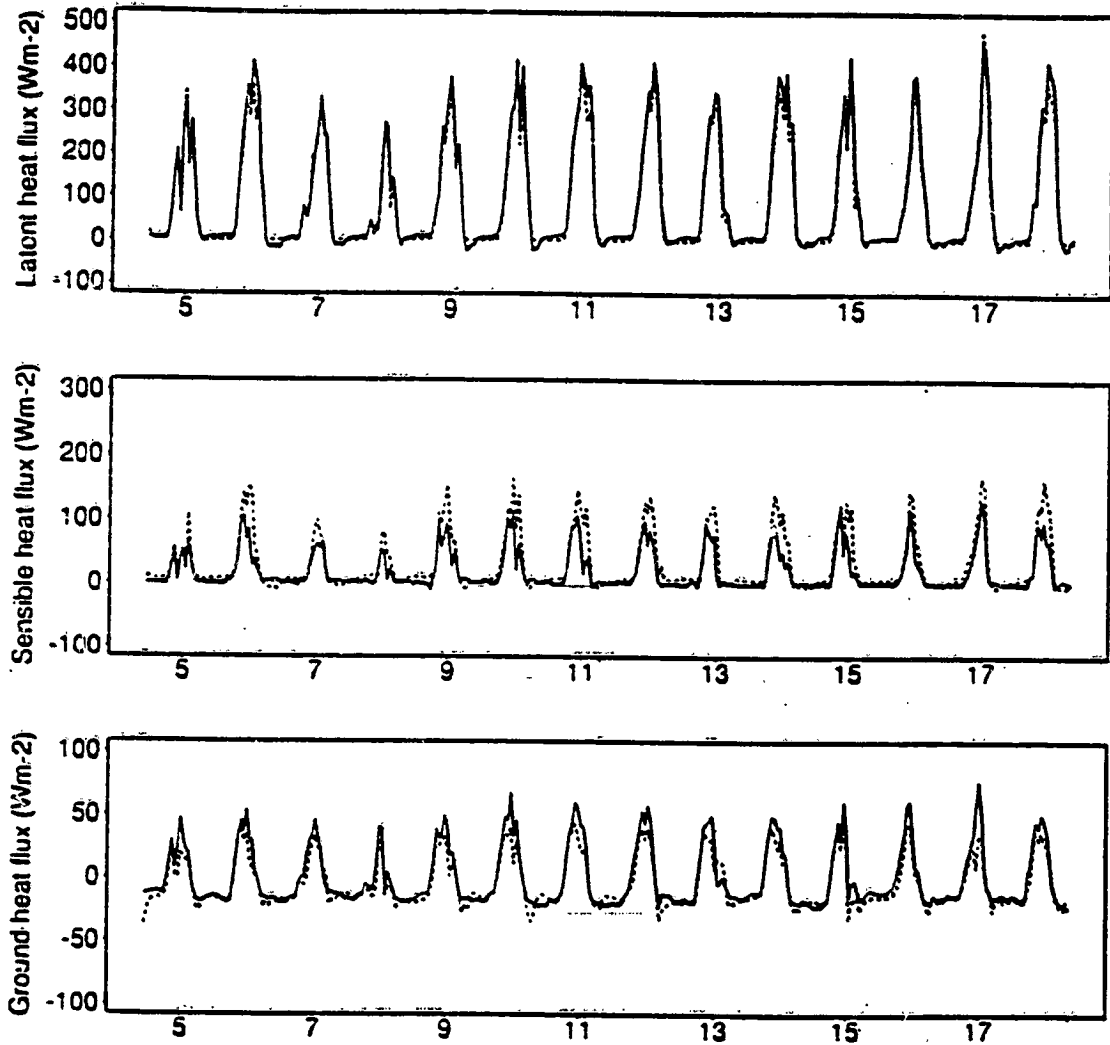
Fig. 3.16   Comparison of predicted (dotted) and observed (solid) surface fluxes at the ABRACOS site for July 5-18, 1991 portion of Mission 2.
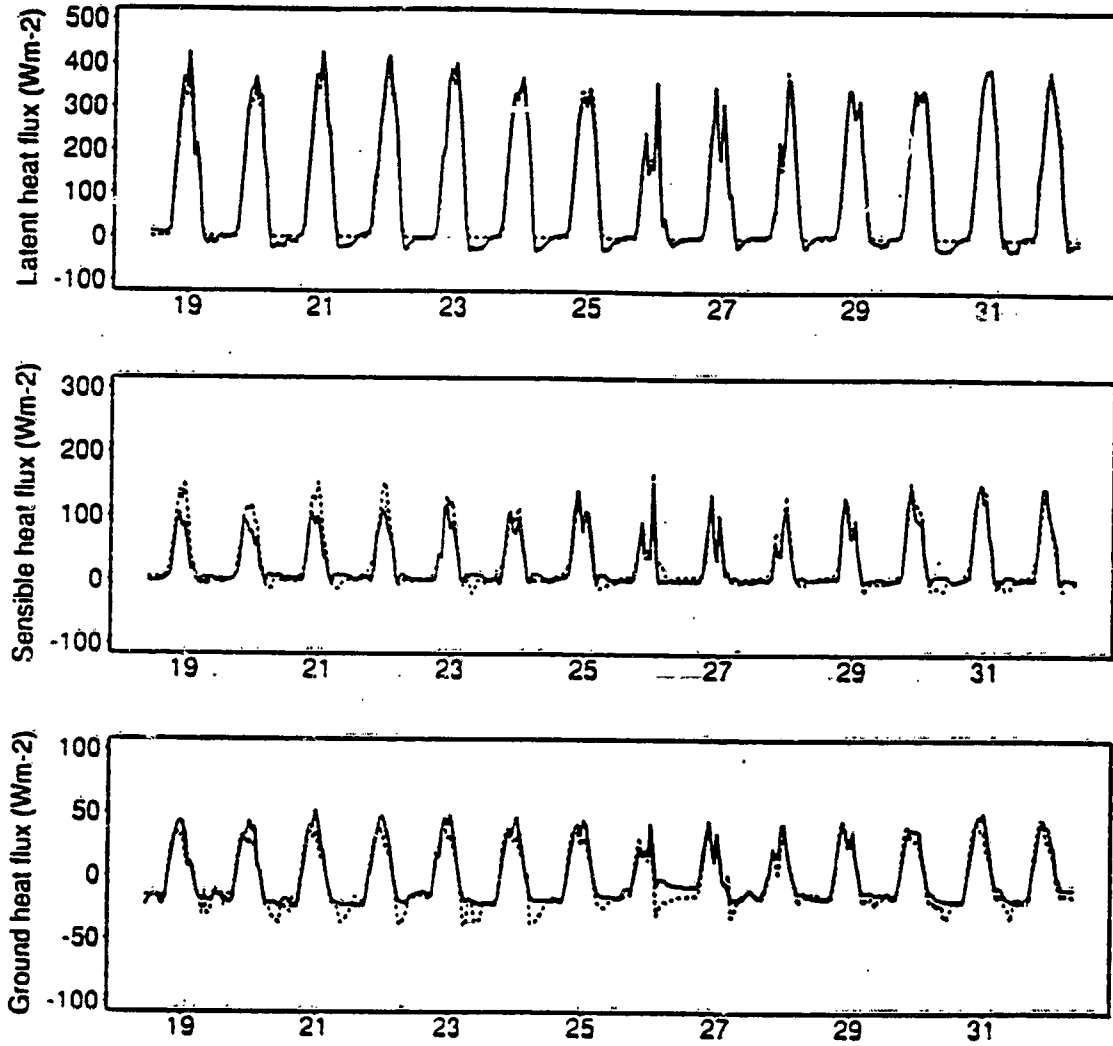
Fig. 3.17   Comparison of predicted (dotted) and observed (solid) surface fluxes at the ABRACOS site for July 19 – August 1, 1991 portion of Mission 2.
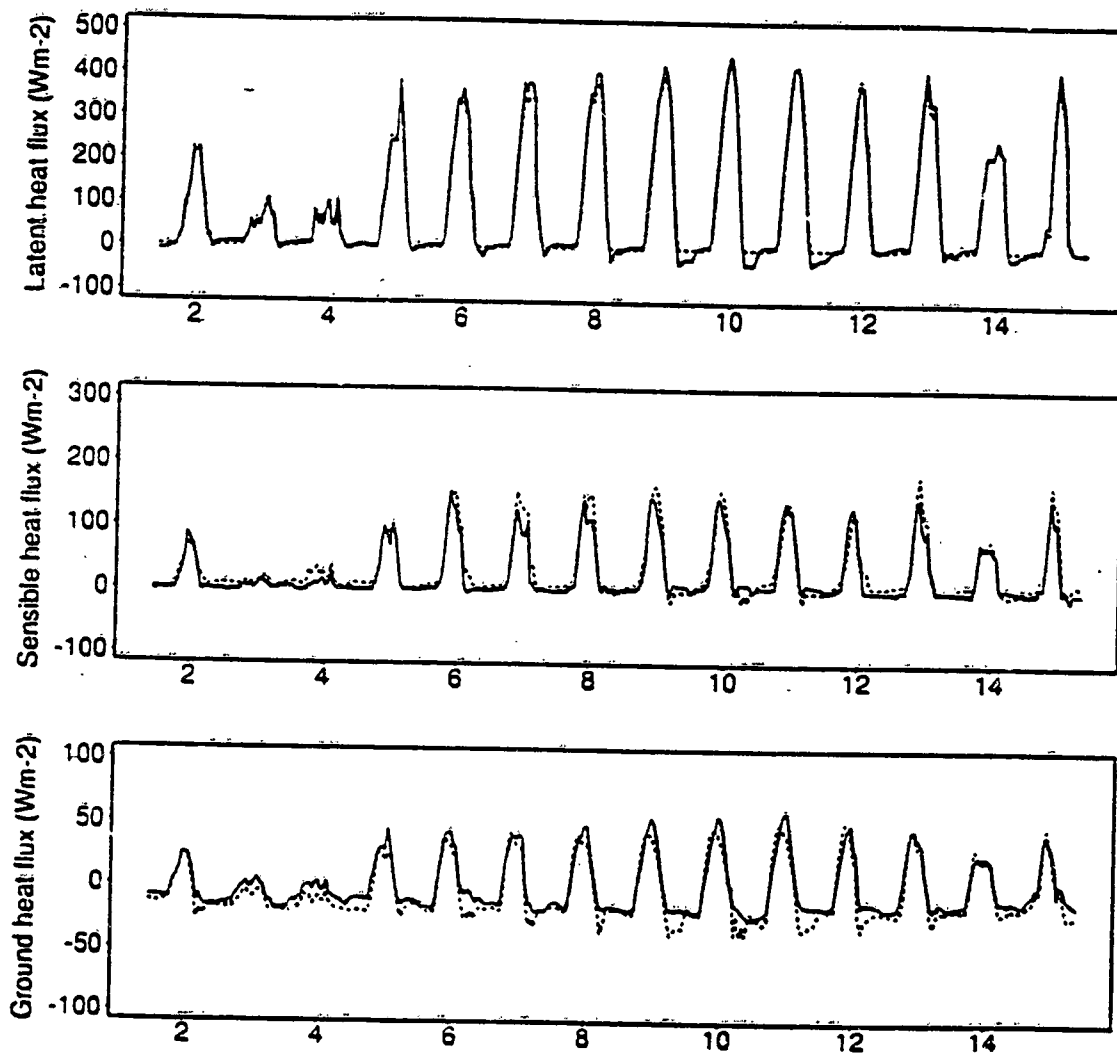
Fig. 3.18   Comparison of predicted (dotted) and observed (solid) surface fluxes ...
at the ABRACOS site for August 2-15, 1991 portion of Mission 2.
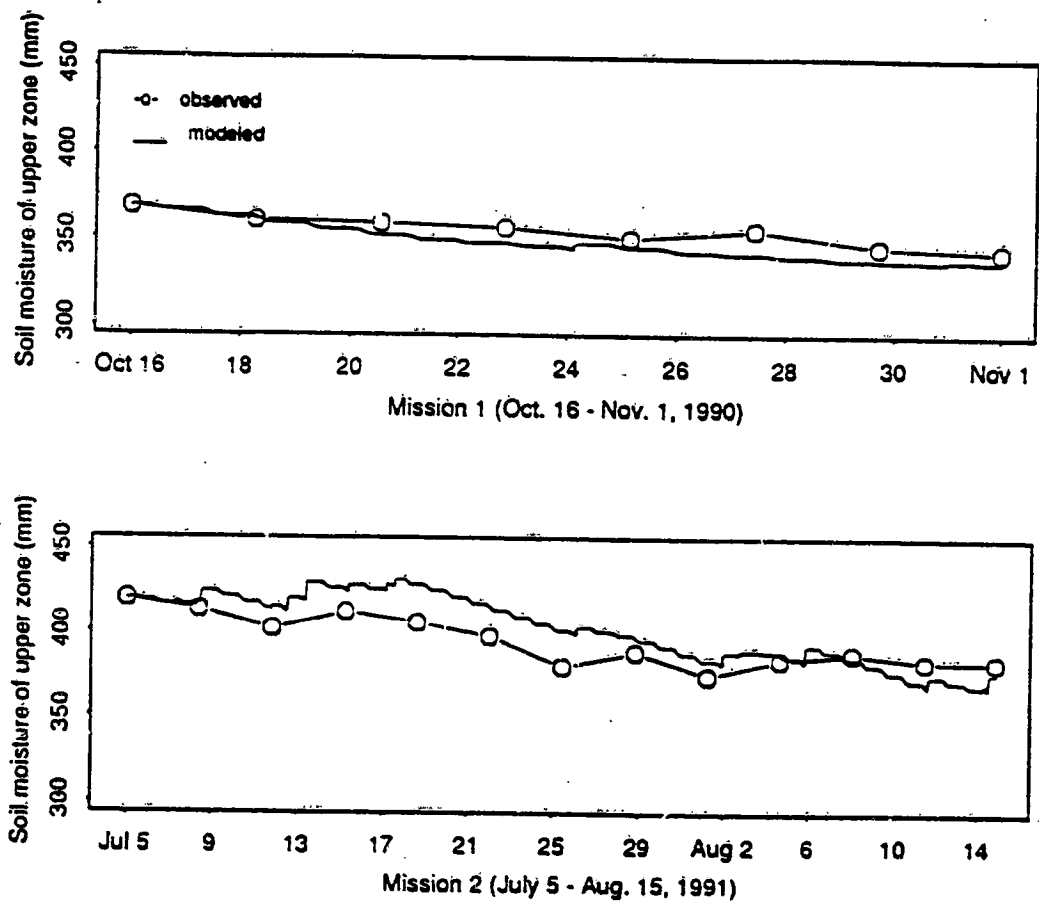
Fig. 3.19   Comparison of predicted and observed upper zone soil moisture at the ABRACOS site for October 16-November 1, 1990 portion of Mission 1 and for July 5-August 15, 1991 portion of Mission 2.

CHAPTER 4 SENSITIVITY ANALYSIS

In Chapter 3, the two-layer version of the variable infiltration capacity (VIC) model (described in Chapter 2) was evaluated by comparing model-simulated surface heat fluxes with those observed at two sites: a native tallgrass prairie of the FIFE site in the United States and a deforested tropical forest of the ABRACOS site in Brazil. However, further validation opportunities are limited due to the small number of locations globally where surface fluxes of moisture and energy have been measured.

An alternative approach to model testing is sensitivity analysis. Although lacking the benefit of comparison with observations, a systematic analysis of the model sensitivity can at least help us understand how the parameters affect the model results. The most commonly used sensitivity analysis method is the one-factor-at-a-time approach. The other, recently suggested for climate model assessments by Henderson-Sellers (1992, 1993), is the so called factorial design method (Box et al. 1978) which has the advantage of investigating and identifying multiple factor interactions among the parameters. In this chapter, the two methods are combined to investigate and identify the model parameters that most strongly affect the two-layer VIC model.

4.1. Factorial designs

Unlike the "change one-factor-at-a-time" approach, the factorial design method tests both the sensitivity to changes in individual parameters, and to interactions between groups of parameters. A general factorial design tests a fixed number of possible values for each of the model parameters, and then investigates and identifies the ranks of effects of each parameter by running the model through all the possible combinations of the parameters. For example, if there are k parameters (p_1, p_2, ..., p_k) in the model, and there are l_1 possible options (called levels) for the first variable (p_1), l_2 options for p_2, ..., and l_k options for p_k, then, a complete factorial design would include $l_1 \times l_2 \times \cdots \times l_k$ combinations. In this analysis, however, a factorial design at only two levels

was considered. Thus, there will be only 2^k combinations of the model parameters in the above example.

Consider a $k=3$ parameter (2^3 factorial) design as an example to illustrate the method. Assume that the three parameters are roughness length z_0, leaf area index LAI, and the minimum stomatal resistance r_{min}. If the prediction variable of interest is annual latent heat flux, the design matrix is:

Run	z_0	LAI	r_{min}	$\rho_w L_e E$
1	−	−	−	y_1
2	+	−	−	y_2
3	−	+	−	y_3
4	+	+	−	y_4
5	−	−	+	y_5
6	+	−	+	y_6
7	−	+	+	y_7
8	+	+	+	y_8

where "+" and "−" signs represent the two possible values of each parameter, with "+"-for high values and "−" for low values. With this design matrix, the effects due to each parameter alone can be estimated as,

$$E_j = \frac{\sum_{i=1}^{n} (S_{ij} \cdot y_i)}{N_j} \qquad (4.1)$$

where E_j represents the effect of jth factor (i.e., in jth column), n is the total number of experimental runs (i.e., $n=8$), S_{ij} represents the sign in row i and column j, y_i represents the value (e.g., annual latent heat flux) obtained from the ith experimental run, and N_j is the number of "+" signs in column j. Using Eq. (4.1) and the above design matrix, the effects of parameter interactions on the model results can also be estimated based on the signs for the parameter

interactions as shown below. The signs are obtained by using the rule that plus (" + ") times minus (" - ") gives a minus (" - "), and that minus (" - ") times minus (" - ") or plus (" + ") times plus (" + ") gives a plus (" + ").

Run	$z_0 \cdot LAI$	$z_0 \cdot r_{min}$	$LAI \cdot r_{min}$	$z_0 \cdot LAI \cdot r_{min}$
1	+	+	+	−
2	−	−	+	+
3	−	+	−	+
4	+	−	−	−
5	+	−	−	+
6	−	−+	−	−
7	−	− −	+	−
8	+	+	+	+

With all the E_j's estimated from Eq. (4.1), the degree of importance of the parameters and their interactions can be determined. One way of doing this is to plot the E_j's on a normal probability scale (Box et al. 1978). Any points that are outliers from the straight line on normal probability paper could be considered to affect the model results significantly, since it is assumed that changes in levels of the variables have no real effect on the model results, and thus the model results (i.e., E_j's) would occur simply as a result of random variation about a fixed mean. The others are noise, assuming that all the higher interactions are negligible. Neglecting higher order parameter interactions is conceptually similar to neglecting higher order terms in a Taylor expansion (Box et al. 1978). Another way of identifying the parameters which have major effects on the model results was suggested by Henderson-Sellers (1992, 1993). She used an iterative method to find thresholds that were two, three, or four standard deviations from zero. Any E_j's greater than the estimated thresholds were considered to have significant effects on the model results.

4.2. Fractional factorials

From the experimental design described above, it can be seen that the

number of experimental runs increases geometrically with the number of model parameters. A land-surface parameterization scheme with 10 parameters, for example, would need $2^{10}=1024$ experimental runs to investigate all the single and interacting parameter effects. This number of runs is computer intensive, if not totally impossible. However, from a mathematical point of view, it is not necessary to conduct all of the experimental runs, since not all of the parameter interactions would have appreciable effects on the model results. In fact, there tends to be a hierarchy in terms of the magnitude of the parameter effects. The single parameter effects (called main effects) tend to have greater absolute magnitudes than the two-parameter interactions, and the two-parameter interactions tend to have greater effects than the three-parameter effects, and so on. The terms of a Taylor series expansion of a response function can be associated with the main effects and the interactions (Box et al. 1978). Therefore, the higher orders (or higher interactions) in the Taylor expansion series have larger opportunities to be ignored. In addition, when a large number of experimental runs is introduced, some of the runs are redundant (Box et al. 1978) Therefore, only a fraction of the experimental runs of the factorial design is needed.

When a fractional factorial design is used, it implies a tradeoff between the loss of information about higher order interactions and the number of experimental runs. In addition, it will introduce confounding patterns where certain combinations of the parameters are indistinguishable from others. These confounding patterns can be between single parameter and two parameter interactions, two parameter interactions and other two parameter interactions, two- and three-parameter interactions, and so on, depending on the "resolution" at which the fractional factorial experiment is designed. A design with resolution R is defined as the one in which no k-parameter effect is confounded with any other effect containing fewer than R-k parameters (Box et al. 1978). For example, a design with resolution 4 won't have any main effects confounded with any two parameter interactions. However, the main effects can be confounded with three parameter interactions, the two parameter interactions with other two parameter interactions, and so on. When

confounding patterns occur, it is usually considered that lower order effects are more likely than higher order effects. However, to be sure that this is the case, either further experiments need to be conducted, or physical reasoning is used to eliminate certain parameter(s) within the confounding sets.

The procedure for conducting a fractional factorial design is:

(1). Determine the number of model parameters that need to be investigated and the number of experimental runs to be conducted;

(2). Determine the design resolution;

(3). Select the parameters to which signs will be assigned ("primary parameters"), and specify their plus and minus signs;

(4). Determine the signs of the remaining parameters that are selected in (1) based on defining relations (defining relations are the equations through which the plus and/or minus signs of the rest of the parameters are determined based on the signs assigned to the primary parameters);

(5). Write out the design matrix, with "+" and "−" signs representing the two possible levels of each parameter;

(6). Calculate the effects (also called contrasts) by using Eq. 4.1;

(7). Find the confounding patterns, and check if further experiments are needed;

(8). Rank the degree of importance of these investigated parameters based on their absolute magnitudes of effects.

4.3. Fractional factorial experiments with the two-layer VIC model

The two level fractional factorial experiment method is used in this section to investigate the sensitivities of the parameters in the two-layer VIC model. An off-line mode (i.e., prescribe the input forcing data such as solar and long-wave radiation, precipitation, wind, air temperature, and specific humidity) sensitivity testing was used. Off-line testing has been reported to be an efficient way of exploring the effects of model parameters for GCM land-surface parameterizations (Dickinson and Henderson-Sellers 1988). Henderson-Sellers (1992, 1993) used the second year results from a two year simulation period to analyze the parameter sensitivity of BATS. Use of a second year simulation following a "warm up" year is preferable to the shorter period used in some previous studies, e.g., 10 days (Wilson et al. 1987) or 150 days (Dickinson and Henderson-Sellers 1988) since initialization effects are removed (Henderson-Sellers 1992, 1993).

In this analysis, the one year of PILPS (Project for Intercomparison of Land-surface Parameterization Schemes) prescribed atmospheric forcing representing two climatic regimes was used: (1) moist, tropical forest; and (2) a midlatitude grassland. The PILPS atmospheric forcing data were obtained from the NCAR CCM1-Oz (Henderson-Sellers et al. 1993) for a forested grid cell centered at 3°S, 60°W, and a grassland grid cell centered at 52°N, 0°E respectively. The atmospheric forcing data include (1) downward shortwave radiation, (2) downward long-wave radiation, (3) precipitation, (4) air temperature, (5) wind speed, (6) surface pressure, and (7) specific humidity. Pitman et al. (1993) provide details of the PILPS experiments where the above two sets of forcing data (i.e., at the tropical forest and midlatitude grassland) were used by twenty different land-surface schemes run to equilibrium. The simulated latent and sensible heat fluxes, surface temperature, runoff, and other surface fluxes and state variables predicted by the twenty schemes are to be compared. The two-layer VIC model is among the twenty participants. From the monthly precipitation forcing data shown in Fig. 4.1, it can be seen that there is considerable seasonality in the precipitation at both sites. The monthly precipitation is highest in February, October and December, and lowest in May-August at the forest site. For the grassland site, monthly

precipitation is highest in July-September, and uniformly lower in the rest months.

There are 23 parameters associated with the canopy/land-cover types in the two-layer VIC model (Table 4.1.). In the PILPS study, parameters for Manabe bucket, SiB-, and BATS- type models were suggested for both grassland and forest sites. Although the two-layer VIC model is not strictly similar to any of these types, there are some common parameters. Therefore, the VIC model parameters were determined as was most appropriate based on the given information. For example, the model pore size distribution index B_p, and the model maximum subsurface flow D_{max} can be expressed in terms of the PILPS parameters as,

$$B_p = \frac{1}{B}$$

$$D_{max} = K_s \cdot \tan\chi$$

where B is the soil wetness exponent, and $\tan\chi$ is the surface slope. In addition, the soil moisture critical point was taken as 70% of field capacity, and the surface albedo (snow-free) was obtained by weighting the albedos with the corresponding fractional coverages of vegetation and bare soil. There remained four parameters that could not be determined based on the PILPS information. They are the architectural resistance r_0, the infiltration shape parameter b_i, the fraction of the maximum subsurface flow D_s, and the fraction of the maximum soil moisture content in the lower layer W_s. The values of the architectural resistance can be obtained from the literature. They are 25 s/m and 2 s/m for the rain forest and grassland respectively (Ducoudre et al. 1993). The values for the other three parameters, however, cannot be estimated well unless streamflow data are available and are via a hydrograph fitting procedure. Since no streamflow data were available, their values were specified according to Dumenil and Todini (1992). The values of the twenty-three VIC model parameters are listed in Table 4.1.

Of the 23 parameters, 12 are either relatively easily estimated from field data or have relatively narrow feasible ranges compared with the remaining parameters. Therefore, these 12 parameters were fixed at the nominal values given in Table 4.1. The two level fractional factorial sensitivity analysis was only applied to the remaining 11 parameters, where their two levels (high and low) were determined based on 50% perturbation about the values given in Table 4.1. Therefore, the high level "+" is related to the value given in Table 4.1 for the parameter plus 50%, and the low level " -" corresponds to the value given in Table 4.1 minus 50%. If the values (high and low) determined in this way exceeded either the range of that parameter reported in the literature or its physical range, then the high and/or low values were adjusted to the literature or physical bound. For the three parameters (b_i, D_s, and W_s), the two levels were obtained based on the ranges suggested by Dumenil and Todini (1992). Adding or subtracting 50% error to the parameters may be an exaggeration of the parameter estimation errors in some cases, but their ranges should be helpful in exploring the parameters sensitivity of the two-layer VIC model. The eleven parameters with their high "+" and low " -" values are given in Table 4.2.

Four metrics were selected for investigating the sensitivity of the two-layer VIC model. They are the annual total evaporation (mm/yr), annually averaged sensible heat flux (Wm^{-2}), annual total runoff (mm/yr), and hourly minimum surface temperature (K). To eliminate initialization effects, the PILPS procedure of running the simulations for n-year repetitions of the one year forcing was followed until convergence was reached. In this case, convergence is taken to occur when the monthly maximum, minimum, and mean of the land surface fluxes, surface temperature, and runoff were essentially identical for the subsequent simulation years. The total evaporation and runoff are the hourly accumulated quantities for the equilibrium year; the sensible heat flux is an hourly average of the equilibrium year; and the minimum surface temperature is the single lowest hourly temperature simulated for any hour in the equilibrium year. These four measures were selected to represent the radiative and hydrological characteristics of the two-layer VIC model.

Since there are 11 model parameters in the sensitivity analysis, there would be $2^{11}=2048$ experiment runs if a full factorial experiment were used. However, this number of runs is not necessary as discussed earlier. A fractional factorial experiment of 32 runs with resolution 4 (i.e., $2_{IV}^{11-6}=32$) was designed in this analysis. Using the notation of Box et al. (1978), in the 2_{IV}^{5} design, there are 5 primary parameters, and the remaining 6 parameters are associated with them. The five primary parameters were selected arbitrarily as roughness length z_0, soil moisture content at critical point θ_{cr}, minimum stomatal resistance r_{min}, soil thermal conductivity κ, and LAI. Let us represent the 11 parameters by parameter index numbers where the symbol $\overline{10}$, for example, represents the tenth parameter, then we can specify them as (see Table 4.2),

$$z_0 - 1 \quad \theta_{cr} - 2 \quad r_{min} - 3 \quad \kappa - 4 \quad LAI - 5$$
$$C_s - 6 \quad \theta - 7 \quad \theta_w - 8 \quad b_i - 9 \quad D_s - \overline{10} \quad W_s - \overline{11}$$

The last 6 parameters are related to the first 5 primary parameters through the defining relations given by Box et al. (1978). The defining relations are:

$$I = 1236, \quad I = 2347, \quad I = 3458, \tag{4.2a}$$
$$I = 1349, \quad I = 145\overline{10}, \quad I = 245\overline{11}. \tag{4.2b}$$

where 'I' represents a column of all plus signs, and 1236 represents the resultant sign from the signs of parameters 1, 2, 3, and 6 based on the plus times minus rule discussed earlier. In other words, the above equalities mean that the signs on both sides are the same. For example, if the signs for 1, 2, 3, and 6 are "+", "+", "−" and "−" respectively for run 1, the sign of 1236 is then "+" according to the plus times minus rule, and it has the same sign as 'I'. If the sign of 1236 is "−", then it won't be equal to 'I', i.e., $I \neq 1236$. From the above six defining relations, the sign of a parameter index number can be determined if the signs of the remaining variables are known. This can be done by multiplying the number (i.e., parameter) on both sides of an equation. For instance, the sign of number 6 can be determined by $6=I \cdot 6=1236 \cdot 6=123 \cdot I=123$.

Since the first five numbers have been chosen as the primary parameters, their signs can be specified, and the signs for the remaining numbers can be then obtained by multiplying its number on both sides of the equation. The six relations from the above defining relations are,

$$6 = 123, \quad 7 = 234, \quad 8 = 345, \qquad (4.3a)$$
$$9 = 134, \quad \overline{10} = 145, \quad \overline{11} = 245. \qquad (4.3b)$$

The above six relations are called generators. Thus, by specifying the plus and minus signs to the five primary parameters for the 32 experimental runs, the signs of the remaining six parameters in the 32 runs can be obtained through the above six generators. The relations in the above six generators are not unique. There are other ways to define the six generators for the 11 parameters. However, the design shown here is preferred because it ensures that all the main effects are not confounded with the effects of any of the two parameter interactions. Only two parameter interactions are confounded with each other if higher order effects are not considered (Box et al. 1978). In other words, the design shown here guarantees a design with resolution IV in 32 experimental runs. The design matrix with all the plus "+" and minus " −" signs for each of the 11 parameters in the 32 runs is shown in Table 4.3.

From the above six defining relations, all the confounding patterns of this resolution IV design with 32 experimental runs for 11 parameters can be found based on the procedures described by Box et al. (1978). In the following, however, only the confounding patterns for the two parameter interactions are discussed; higher order interactions are assumed to be negligible. Multiplying two of the six defining relations at a time (e.g., $I = I \cdot I = 1236 \cdot 2347 = 1 \cdot 2 \cdot 2 \cdot 3 \cdot 3 \cdot 467 = 1 \cdot I \cdot I \cdot 467 = 1467$) gives the I's with only four parameter combinations as follows,

$$I = 1467 = 2469 = 2578 = 1279 = 357\overline{11}$$
$$= 1589 = 138\overline{10} = 238\overline{11} = 359\overline{10} = 12\overline{10}\,\overline{11} \qquad (4.4)$$

Multiplying three at a time gives the I's with only four parameter combinations as follows,

$$I = 367\overline{9} = 567\overline{10} = 478\overline{11} = 489\overline{10} = 36\overline{10}\ \overline{11}$$
$$= 268\overline{10} = 168\overline{11} = 569\overline{11} \tag{4.5}$$

Multiplying four at a times gives the I's with only four parameter combinations as follows,

$$I = 79\overline{10}\ \overline{11} \tag{4.6}$$

Multiplying five and six at a time won't end up with any I's that can be expressed by only four parameter combinations. Therefore, they cannot result in any confounding patterns among two parameter interactions. By multiplying 12 through Eqs. 4.2, 4.4 − 4.6 and omitting words with three or more numbers, for example, we obtain

$$I \cdot 12 = 1236 \cdot 12 = 1279 \cdot 12 = 12\overline{10}\ \overline{11} \cdot 12$$

i.e.,

$$12 = 36 = 79 = \overline{10}\ \overline{11}$$

Thus, the two parameter interaction 12 is confounded with interactions of 36, 79, and $\overline{10}\ \overline{11}$. Following this procedure, the confounding patterns for the two parameter interactions for the entire design can be obtained based on the relationships defined in Eqs. 4.2, 4.4 − 4.6. The confounding patterns for two parameter interactions are:

$$12 = 36 = 79 = \overline{10}\ \overline{11} \qquad 13 = 26 = 49 = 8\overline{10}$$
$$14 = 39 = 5\overline{10} = 67 \qquad 15 = 4\overline{10} = 89$$
$$16 = 23 = 47 = 8\overline{11} \qquad 17 = 29 = 46$$
$$18 = 3\overline{10} = 59 = 6\overline{11} \qquad 19 = 27 = 34 = 58$$
$$1\overline{10} = 2\overline{11} = 38 = 45 \qquad 1\overline{11} = 2\overline{10} = 68$$
$$24 = 37 = 5\overline{11} = 69 \qquad 25 = 4\overline{11} = 78$$

$$28 = 3\overline{11} = 57 = 6\overline{10} \qquad 35 = 48 = 7\overline{11} = 9\overline{10}$$
$$56 = 7\overline{10} = 9\overline{11}$$

(4.7)

The matrix having all the plus and minus signs for the two parameter interactions are shown in Table 4.4.

4.4. Results of fractional factorial experiments

With the 2_{IV}^{11-6} design discussed above, the thirty-two experimental runs were conducted for the grassland site and the forest site respectively. The results for the four metrics of the 32 two-layer VIC model runs are listed in Tables 4.5a and 4.5b for grassland and forest respectively. The eleven main effects and the two parameter interaction effects (specified in Eq. 4.7) are listed in Tables 4.6a and 4.6b for grassland and forest respectively. The iterative method (Henderson-Sellers 1992, 1993) discussed in Section 4.1 was used to find the two-, and/or three-standard deviations (2σ and 3σ). All the main effects and the two parameter interaction effects that are greater than 3σ in any of the four measures at both sites are shown in Tables 4.7a and 4.8a respectively.

From Table 4.7a, it can be seen that only LAI was significant for three metrics (the total evaporation and runoff, and the hourly average sensible heat flux). For the minimum hourly surface temperature metric, two single parameter effects (κ and C_s) and a two-parameter interaction effect ($\overline{\kappa C_s}$) were detected to be important. In the forest case (Table 4.8a), on the basis of the 3σ criterion all the effects were insignificant on all metrics except for the metric of minimum hourly surface temperature where κ, C_s, and $\overline{\kappa C_s}$ were found to be significant. The effect of $\overline{\kappa C_s}$ are confounded by the effects of $\overline{z_0 \theta}$ and $\overline{\theta_{cr} b_i}$ as shown in Eq. 4.7. In general, additional small full factorial experiment runs can be conducted to resolve these aliases if the physical reasoning is not obvious. In this case, however, since z_0 and θ, and θ_{cr} and b_i are much less correlated than κ and C_s, and also z_0, θ, θ_{cr}, and b_i have insignificant main effects compared with that of κ and C_s, it is likely that the greatest effect in the confounding patterns is from $\overline{\kappa C_s}$ rather than from $\overline{z_0 \theta}$ or $\overline{\theta_{cr} b_i}$. Thus, the interaction

between κ and C_S was considered to have the greatest effect on the minimum surface temperature metric.

At the 2σ threshold, more parameters were shown to have large effects on the four selected metrics (Tables 4.7b and 4.8b). From Tables 4.7b and 4.8b, the importance of the single parameters and the two-parameter interactions can be ranked based on absolute values of their effects. These identified parameters were classified into two categories, primary importance and secondary importance as shown in Tables 4.9 and 4.10. The effects of the parameters were also identified by plotting the values in Tables 4.6a and 4.6b on a normal probability scale. The outliers shown on the plots (Figs. 4.2 and 4.3) are the parameters that have significant effects. From Fig. 4.2, it can be seen that for all the metrics except for the minimum hourly temperature metric, the outliers that are identified by the probability scale approach are the primary ones detected by the threshold method for the grassland site. For the forest site, all the primary and secondary outliers from the threshold method are identified by the probability scale approach.

Although the model parameters and their ranks that were identified are not exactly the same for the grassland and forest sites (Tables 4.9 and 4.10), there is some consistency in the results. The leaf area index LAI, porosity θ, the minimum stomatal resistance r_{min}, critical point and wilting point of soil moisture have important effects on the first three metrics of the two-layer VIC model at both sites. For the grassland site, the roughness length z_0 and the interaction between porosity θ and the minimum stomatal resistance r_{min} are of secondary importance for the same three metrics. For the minimum hourly surface temperature, the soil thermal conductivity and soil heat capacity were of primary importance at both sites, and the interaction between the two is secondarily important.

Henderson-Sellers (1992, 1993) used the fractional factorial method to analyze the parameter sensitivities of BATS. BATS has 23 model parameters that are related to the canopy/land-cover types. In the interquartile-range ecotype parameter experiment, ten parameters were kept constant, and thus,

the experiments had 13 parameters with two different levels each. The metrics used were the maximum canopy temperature, evapotranspiration, annual runoff, the minimum daily upper-layer soil temperature, and the net carbon gain. Based on the thresholds 4σ and 3σ, the vegetation roughness length, soil porosity, and stomatal resistance to vegetation light sensitivity were found to be primarily important, while vegetation albedo, soil color, wilting point, minimum leaf area index, soil moisture diffusivity, and the soil thermal conductivity were found to be of secondary importance (Henderson-Sellers 1992, 1993). In the full-range ecotype parameter experiment runs with the same threshold criterion (Henderson-Sellers 1992), the maximum leaf area index, roughness length, shortwave vegetation albedo, the interaction of roughness length and albedo, the stem-area index, and the near-infrared vegetation albedo were found to be important. Comparing the results described in this analysis with the ones obtained by Henderson-Sellers (1992, 1993), it can be seen that among the parameters common to both models, the leaf area index, porosity, roughness length, soil thermal conductivity, and the parameter related to the stomatal resistance are important, despite the significant differences in the structure of BATS and two-layer VIC.

From the study results, it can be seen that the experiments are highly fractional. That is, there are many higher order interactions that were not studied. There may exist three or higher order parameter interactions that require examination. Even though this analysis is preliminary, it reveals some common parameter effects that are important to the two-layer VIC model, and perhaps, to other land-surface schemes as well.

4.5. One-at-a-time analysis

From the fractional factorial analysis, it is seen that the infiltration shape parameter b_i, the fraction parameter of maximum subsurface flow D_s, the fraction parameter of the lower layer maximum soil moisture W_s, and their interactions do not significantly affect the four model metrics (Tables 4.6a and 4.6b). Among the parameters that show important effects, the above analysis

indicates that the ranks of some parameters at the grassland site are different from those at the forest site. For example, at the forest site, the critical soil moisture had the least influence on the annual total evaporation, and the minimum stomatal resistance parameter had the greatest influence of all the parameters tested. At the grassland site, the critical soil moisture affected evaporation more than the minimum stomatal resistance. To explore the characteristics of these parameters further, the one-at-a-time method was used to allow investigation of more than two levels.

First, the three parameters b_i, D_s, and W_s were investigated at four levels each. The four different values for each of the three parameters (Table 4.11) were specified based on the ranges suggested by Dumenil and Todini (1992). The annually averaged latent heat flux (Wm^{-2}), sensible heat flux (Wm^{-2}), annually averaged surface temperature (K), annually total evaporation (mm/yr), and the total runoff (mm/yr) from the equilibrium year are shown in Tables 4.11 and 4.12 for both grassland and forest sites respectively. Fig. 4.4 shows the monthly means of the control and the sensitivity runs for latent and sensible heat fluxes, the surface temperature, and the monthly total runoff at both sites. The control runs shown in Fig. 4.4 were obtained by running the model to the equilibrium year with the parameter values given in Table 4.1.

From Fig. 4.4, and Tables 4.11 and 4.12, it is clear that the infiltration shape parameter b_i does not significantly affect latent and sensible heat fluxes, and the surface temperature, especially at the grassland site. At the forest site, changing b_i did not change the monthly latent heat and sensible heat fluxes much, except in August, where increased b_i values reduced the amount of water infiltrated into the soil, and thus decreased the latent heat flux and increased the sensible heat flux. The apparent change in latent heat flux in August was because it was very dry in that month (see Fig. 4.1), so any change in the infiltration amount would strongly affect the water available for evaporation. In comparison, b_i has stronger effect on runoff. Figures 4.5 and 4.6 partition the runoff into surface and subsurface flow for the range of b_i values for the grassland and forest sites respectively. The total monthly runoff (Figs.

4.5 and 4.6), especially the totally annual runoff (Tables 4.11 and 4.12), were much less sensitive to b_i. This was due to the partitioning into surface and subsurface flow. D_s and W_s had minimal effect on the monthly and annual latent and sensible heat fluxes, and the surface temperature (Tables 4.11 and 4.12). Only the monthly runoff distributions vary with different parameter values (Fig. 4.7). Tables 4.11 and 4.12 show that, although the total annual runoff is insensitive to D_s and W_s, the monthly runoff distribution varies significantly (Fig. 4.7).

The results from the one-at-a-time method confirmed the findings from the fractional factorial experiment, and also showed the effect of the three hydrologic parameters b_i, D_s, and W_s on the redistribution of runoff (both surface and subsurface). The wetness indices (the ratios of annual latent heat plus sensible heat to annual precipitation), equal to 0.44 at grassland and 0.5 at forest, indicated that both sites studied here were climatologically moist. The results obtained here might be different from the ones under a dry climate condition, especially for parameter b_i.

The one-at-a-time method was also used to study the sensitivities of the critical point and the minimum stomatal resistance, both of which were found to be important in the fractional factorial studies. The results are given in Tables 4.13 and 4.14, for grassland and the forest, respectively. Table 4.13 indicates that for the grassland site, a change of 7% to 14% in the critical point results in almost the same sensitivities as a change of 15% in the minimum stomatal resistance for all the measures. Table 4.14, however, indicates that at the forest site, a smaller change in the minimum stomatal resistance than in the critical point caused larger changes in the latent and sensible heat fluxes, and total runoff. Therefore, the sensitivities of the same parameters under different climatic conditions can be different. The relative order of importance of the two parameters at different sites was the same as indicated by the fractional factorial method.

4.6. Supplementary fractional factorial experiments

From Sections 4.4 and 4.5, it can be seen that the annual total evaporation (mm/yr), annually averaged sensible heat flux (Wm^{-2}), annual total runoff (mm/yr), and the hourly minimum surface temperature (K) are not sensitive to b_i, D_s, and W_s, but the monthly runoff distributions are sensitive to these parameters. To examine the sensitivities of the three hydrologically related parameters further, three different metrics were used. They are the sum of the absolute difference of monthly evaporation (mm/mo), runoff (both surface and subsurface) (mm/mo), and the sensible heat flux (Wm^{-2}) between the control experiment and the 32 experiments described in Section 4.4.

The results of the 32 experiment runs with the three new metrics are shown in Tables 4.15a and 4.15b, for the grassland and forest sites, respectively. The parameter effects with the new metrics are shown in Tables 4.16a and 4.16b, for the grassland and the forest cases, respectively. By combining the 3σ and 2σ threshold approach and the probability scale approach (Section 4.4), the parameters that are sensitive are identified. From Figs. 4.8 and 4.9 (or Tables 4.17 and 4.18), it is clear that the effects of parameter interactions are more important than the effect from the single parameters under the new metrics for evaporation and sensible heat flux for both the grassland and forest sites. Since the two parameter interactions are confounded with each other in this resolution IV experimental design, further experiment runs would be needed to identify the confounding patterns. Rather than performing such runs, the confounding patterns that cannot be excluded based on physical grounds are retained as possibly important two parameter interactions (see Tables 4.17 and 4.18).

For the sum of the absolute difference of monthly runoff (combined surface and subsurface) between the control experiment and the 32 experiments, the fractional factorial experiment analysis identified the two parameter interactions of $b_i D_s$ (confounded by θW_s, $r_{min} LAI$), $\theta_w b_i$, and $b_i W_s$ (confounded by θD_s), and the parameter W_s as sensitive at the grassland site. For the forest site, the single parameters b_i, D_s, and W_s are sensitive. Like the grassland case, the two parameter interactions $b_i D_s$ (confounded by θW_s, $r_{min} LAI$), and $b_i W_s$ (confounded by θD_s) are important. These findings are

consistent with those obtained from the one-at-a-time analysis discussed in Section 4.5. The analysis conducted here indicates that different metrics used in the fractional factorial analysis could result in the identification of different parameters and parameter interactions.

4.7. Additional analysis of model sensitivity experiments

In Sections 4.3 – 4.6, the sensitivity of the two-layer VIC model to the model parameters were studied on the basis of several metrics. In this section, the model structure is explored for a few special cases, with the model parameters fixed at the values given in Table 4.1. The four cases are:

(1). Vegetation (grass in grassland, and tree in the forest) covers 100% of the land surface, instead of 80% in grassland and 90% in the forest as used previously;

(2). As case (1), but without atmospheric stability correction, and with architectural resistance set to zero (see Chapter 2);

(3). As case (1), but the surface was kept wet so that the actual evaporation equals the potential evaporation;

(4). As case (1) and (2), but with wet surface.

The results for the above four cases and for the standard case are given in Tables 4.19 and 4.20 for the grassland and forest sites respectively. At the grassland site in case (1), the change of the 20% vegetation cover from the bare soil to grass reduced the evaporation from 617.21 mm/yr to 565.51 mm/yr, and increased the annually averaged sensible heat flux from -5.10 Wm^{-2} to 0.02 Wm^{-2}, and the total annual runoff from 648.83 mm/yr to 700.54 mm/yr. Changes in the annually averaged surface temperature were negligible. At the forest site, the change of the 10% vegetation cover from bare soil to trees resulted in similar model effects. The annual evaporation decreased from 1357.59 mm/yr to 1176.49 mm/yr, the sensible heat increased from 25.93 Wm^{-2} to 41.84 Wm^{-2}, and the runoff changed from 1909.50 mm/yr to 2090.55 mm/yr. Again,

the surface temperature changes were negligible. Elimination of the stability correction resulted in only a small increase in evaporation at the grassland site, but the effect at the forest site was large. The relative increase of evaporation at the forest site was 49.8%, while it was only 1% at the grassland. Such a big difference was partially due to setting the architectural resistance to zero under the no stability correction case at both sites. The architectural resistance (see Table 4.1) in the forest site (25.0 s/m) was much greater than that at the grassland site (2.0 s/m), thus by setting it to zero, it had a greater effect on evaporation at the forested site than at the grassland site. In spite of the effects of different values of architectural resistance, the influence of the stability correction on the latent heat flux was apparent, as was the different effects according to climatic conditions. Although the annual total evaporation increased at both sites under case (2), the surface temperature at both sites increased slightly instead of decreasing.

By keeping the surface wet in cases (3) and (4), only five of twenty-three (see Table 4.1) parameters remained that would affect the model results. These are aerodynamic roughness length, displacement height, surface albedo (snow free), soil thermal conductivity, and soil heat capacity.

By comparing the results (Tables 4.19 and 4.20) of cases (3) and (4), it was found again that the effect of the atmospheric stability correction varies significantly with the climatic conditions. For example, the annual total evaporation obtained in case (4) at the forest site was more than three times as large as that obtained from case (3). However at the grassland site, the annual total evaporation in case (4) was only 1.2 times as large as that in case (3). This result implies that under some cases, the atmosphere is closer to the neutral condition than the others, and thus, the stability correction is not as important for these cases as for the others.

4.8. Summary of sensitivity analysis

The studies conducted here show that the combined use of the fractional factorial method and the one-at-a-time method is an efficient way of examining

the relative importance of model parameters. From the analysis discussed in this chapter, it was found that the leaf area index LAI, porosity θ, and the minimum stomatal resistance r_{min} were the most important parameters of the two-layer VIC model in terms of the three metrics associated with annual total or average surface fluxes, while the roughness length z_0, critical point and wilting point of soil moisture, and the interaction between porosity θ and the minimum stomatal resistance r_{min} were of secondary importance for the same metrics. For the minimum hourly surface temperature, the soil thermal conductivity and soil heat capacity were primarily important, and the interaction between the two was secondarily important.

The studies indicated that the surface fluxes and surface temperature were not sensitive to the fraction of the maximum subsurface flow and the fraction of lower layer maximum soil moisture for the four metrics. Both parameters resulted in redistribution of the monthly runoff within a year, but they did not change the total amount of the annual runoff. Under relatively wet climatic conditions, it was found that the surface fluxes and the surface temperature are not sensitive to the infiltration shape parameter. This parameter partitioned the streamflow into surface and subsurface flows differently based on its different values, but it did not affect significantly the total amount of annual runoff.

When the sum of the absolute difference of monthly runoff (both surface and subsurface runoff) (mm/mo) from the control experiment was used as the metric, the parameters b_i, D_s, and W_s, and their interactions among themselves and with parameters θ or θ_w are found to be important and sensitive. In addition, when the metrics were the sum of the absolute difference of monthly evaporation and sensible heat flux between the control experiment and the 32 experiments, similar parameters as those indicated by the metrics of the annual total evaporation and annually averaged sensible heat flux were identified. However, it was the two parameter interactions of those parameters rather than the single parameter effect that were found to be more important this time.

Finally, the analysis conducted in Section 4.7 showed that the model results were sensitive to the inclusion of the stability correction. This was especially the case for the forested site where evaporation was primarily atmospherically controlled, and less so for the grassland site where evaporation was mostly soil controlled.

Table 4.1. Two-layer VIC model parameters for PILPS grassland and forest sites

Parameter names	Grass	Forest
Fractional coverage of vegetation C_v	0.8	0.9
Depth of upper layer d_1 (m)	1.0	1.0
Depth of lower layer d_2 (m)	9.0	9.0
Roots in upper layer f_1	100%	90%
Roots in lower layer f_2	0%	10%
Saturated hydraulic conductivity K_s (mm/s)	0.45×10^{-2}	0.16×10^{-2}
Soil wetness exponent (B parameter)	6.8	9.2
Slope χ	0.17	0.17
Displacement height d_0 (m)	0.0	18.0
Surface albedo α (snow free)	0.21	0.131
Constant soil temperature at 1m depth T_2 (K)	274.6	299.6
Architectural resistance r_0 (s/m)	2.0	25.0
Soil porosity θ	0.51	0.6
Fract. of water cont. at which perm. wilt. occurs θ_w	0.373	0.487
Fract. of water cont. at which criti. point occurs θ_{cr}	0.7	0.6
Infiltration shape parameter b_i	0.1	0.03
Fraction of maximum subsurface flow D_s	0.008	0.008
Fraction of lower layer maximum soil moisture W_s	0.9	0.9
Aerodynamic roughness length z_0 (m)	0.1	2.0
Leaf area index LAI	Monthly LAIs	5.0
Minimum stomatal resistance r_{min} (s/m)	200.0	150.0
Soil thermal conductivity κ (Wm^{-1}K^{-1})	1.03	0.866
Soil heat capacity C_s (Jm^{-3}K^{-1})	2.085×10^6	1.756×10^6

Table 4.2a.   Range of the eleven parameters at PILPS grassland site

No.	Parameter names	High(+)	Low(−)
1	Aerodynamic roughness length z_0 (m)	0.15	0.05
2	Critical point of soil moisture θ_{cr}	0.536	0.179
3	Minimum stomatal resistance r_{min} (s/m)	200.0	100.0
4	Soil thermal conductivity κ (Wm^{-1}K^{-1})	1.545	0.515
5	Leaf area index LAI	$1.5 \cdot LAI$	$0.5 \cdot LAI$
6	Soil heat capacity C_s (Jm^{-3}K^{-1})	3.128×10^{-6}	1.043×10^{-6}
7	Soil porosity θ	0.66	0.33
8	Permanent wilting point of soil moisture θ_w	0.29	0.097
9	Infiltration shape parameter b_i	0.50	0.10
10	Fraction of maximum subsurface flow D_s	0.50	0.004
11	Fraction of lower layer max. soil moist. W_s	0.90	0.10

Table 4.2b.   Range of the eleven parameters at PILPS forest site

No.	Parameter names	High(+)	Low(−)
1	Aerodynamic roughness length z_0 (m)	3.00	1.00
2	Critical point of soil moisture θ_{cr}	0.54	0.18
3	Minimum stomatal resistance r_{min} (s/m)	200.0	75.0
4	Soil thermal conductivity κ ($Wm^{-1}K^{-1}$)	1.299	0.433
5	Leaf area index LAI	7.5	5.0
6	Soil heat capacity C_s ($Jm^{-3}K^{-1}$)	2.634×10^{-6}	0.878×10^{-6}
7	Soil porosity θ	0.66	0.33
8	Permanent wilting point of soil moisture θ_w	0.438	0.146
9	Infiltration shape parameter b_i	0.50	0.001
10	Fraction of maximum subsurface flow D_s	0.50	0.004
11	Fraction of lower layer max. soil moist. W_s	0.90	0.10

Table 4.3.   Design matrix of the eleven parameters

Runs	1	2	3	4	5	6	7	8	9	$\overline{10}$	$\overline{11}$
1	-	-	-	-	-	-	-	-	-	-	-
2	+	-	-	-	-	+	-	-	+	+	-
3	-	+	-	-	-	+	+	-	-	-	+
4	+	+	-	-	-	-	+	-	+	+	+
5	-	-	+	-	-	+	+	+	+	-	-
6	+	-	+	-	-	-	+	+	-	+	-
7	-	+	+	-	-	-	-	+	+	-	+
8	+	+	+	-	-	+	-	+	-	+	+
9	-	-	-	+	-	-	+	+	+	+	+
10	+	-	-	+	-	+	+	+	-	-	+
11	-	+	-	+	-	+	-	+	+	+	-
12	+	+	-	+	-	-	-	+	-	-	-
13	-	-	+	+	-	+	-	-	-	+	+
14	+	-	+	+	-	-	-	-	+	-	+
15	-	+	+	+	-	-	+	-	-	+	-
16	+	+	+	+	-	+	+	-	+	-	-
17	-	-	-	-	+	-	-	+	-	+	+
18	+	-	-	-	+	+	-	+	+	-	+
19	-	+	-	-	+	+	+	+	-	+	-
20	+	+	-	-	+	-	+	+	+	-	-
21	-	-	+	-	+	+	+	-	+	+	+
22	+	-	+	-	+	-	+	-	-	-	+
23	-	+	+	-	+	-	-	-	+	+	-
24	+	+	+	-	+	+	-	-	-	-	-
25	-	-	-	+	+	-	+	-	+	-	-
26	+	-	-	+	+	+	+	-	-	+	-
27	-	+	-	+	+	+	-	-	+	-	+
28	+	+	-	+	+	-	-	-	-	+	+
29	-	-	+	+	+	+	-	+	-	-	-
30	+	-	+	+	+	-	-	+	+	+	-
31	-	+	+	+	+	-	+	+	-	-	+
32	+	+	+	+	+	+	+	+	+	+	+

Table 4.4.   Computation matrix for two parameter interactions

Runs	12	13	14	15	16	17	18	19	110	111	24	25	28	35	56
1	+	+	+	+	+	+	+	+	+	+	+	+	+	+	+
2	-	-	-	-	+	-	-	+	+	-	+	+	+	+	-
3	-	+	+	+	-	-	+	+	+	-	-	-	-	+	-
4	+	-	-	-	-	+	-	+	+	+	-	-	-	+	+
5	+	-	+	+	-	-	-	-	+	+	+	+	-	-	-
6	-	+	-	-	-	+	+	-	+	-	+	+	-	-	+
7	-	+	+	+	+	+	-	-	+	-	-	-	+	-	+
8	+	+	-	-	+	-	+	-	+	+	-	-	+	-	-
9	+	+	-	+	+	-	-	-	-	-	-	+	-	+	+
10	-	-	+	-	+	+	+	-	-	+	-	+	-	+	-
11	-	+	-	+	-	+	-	-	-	+	+	-	+	+	-
12	+	-	+	-	-	-	+	-	-	-	+	-	+	+	+
13	+	-	-	+	-	+	+	+	-	-	-	+	+	-	-
14	-	+	+	-	-	-	-	+	-	+	-	+	+	-	+
15	-	-	-	+	+	+	+	+	-	+	+	-	-	-	+
16	+	+	+	-	+	+	-	+	-	-	+	-	-	-	-
17	+	+	+	-	+	+	-	+	-	-	+	-	-	-	-
18	-	-	-	+	+	-	+	+	-	+	+	-	-	-	+
19	-	+	+	-	-	-	-	+	-	+	-	+	+	-	+
20	+	-	-	+	-	+	+	+	-	-	-	+	+	-	-
21	+	-	+	-	-	-	+	-	-	-	+	-	+	+	+
22	-	+	-	+	-	+	-	-	-	+	+	-	+	+	-
23	-	-	+	-	+	+	+	-	-	+	-	+	-	+	-
24	+	+	-	+	+	-	-	-	-	-	-	+	-	+	+
25	+	+	-	-	+	-	+	-	+	+	-	-	+	-	-
26	-	-	+	+	+	+	-	-	+	-	-	-	+	-	+
27	-	+	-	-	-	+	+	-	+	-	+	+	-	-	+
28	+	-	+	+	-	-	-	-	+	+	+	+	-	-	-
29	+	-	-	-	-	+	-	+	+	+	-	-	-	+	+
30	-	+	+	+	-	-	+	+	+	-	-	-	-	+	-
31	-	-	-	-	+	-	-	+	+	-	+	+	+	+	-
32	+	+	+	+	+	+	+	+	+	+	+	+	+	+	+

Table 4.5a.   Results of 32 runs at PILPS grassland site

Runs	ET(mm/yr)	SH(Wm-2)	R(mm/yr)	Tmin(K)
1	604.56	-1.56	661.47	254.03
2	622.51	-2.59	643.52	256.32
3	598.10	-0.67	667.92	256.13
4	620.12	-2.80	645.91	253.97
5	544.37	2.85	721.66	256.15
6	566.79	0.82	699.24	254.01
7	396.12	12.10	869.91	254.37
8	423.29	10.95	842.74	256.37
9	649.82	-10.38	616.21	256.32
10	677.21	-11.11	588.82	257.22
11	408.62	6.12	857.41	257.36
12	435.49	2.89	830.54	256.47
13	531.16	-1.63	734.87	257.33
14	555.19	-4.62	710.84	256.45
15	529.11	-2.84	736.92	256.35
16	541.37	-2.31	724.85	257.24
17	664.66	-5.54	601.37	253.88
18	673.62	-6.00	592.41	256.24
19	700.76	-7.33	565.27	256.09
20	712.10	-9.16	553.93	253.90
21	723.20	-8.74	542.83	256.10
22	762.23	-12.49	503.80	253.93
23	585.47	-0.41	680.56	254.03
24	620.15	-2.49	645.88	256.32
25	852.36	-22.79	413.87	256.26
26	911.43	-26.03	354.60	257.14
27	659.25	-9.39	606.78	257.26
28	698.85	-14.21	567.18	256.34
29	601.86	-5.72	664.16	257.27
30	616.57	-8.79	649.46	256.39
31	626.29	-9.01	639.74	256.33
32	635.52	-8.55	630.50	257.22

Table 4.5b.   Results of 32 runs at PILPS forest site

Runs	ET(mm/yr)	SH(Wm-2)	R(mm/yr)	Tmin(K)
1	1358.52	27.73	1908.55	278.82
2	1333.75	28.96	1933.32	281.91
3	1506.33	17.38	1760.74	281.72
4	1473.13	18.78	1793.94	278.85
5	1149.47	42.40	2117.40	281.90
6	1227.79	36.38	2039.28	278.91
7	953.33	56.26	2313.74	279.10
8	997.80	53.30	2269.27	282.00
9	1351.37	24.90	1915.51	284.79
10	1437.59	19.64	1829.48	285.61
11	1057.90	46.42	2209.17	286.17
12	1201.96	36.08	2065.10	285.60
13	1218.36	35.06	2048.70	285.88
14	1190.92	36.95	2076.14	285.52
15	1261.56	31.13	2005.51	285.22
16	1248.03	33.46	2020.52	286.00
17	1381.12	26.10	1885.94	278.76
18	1378.51	25.86	1888.56	281.84
19	1401.40	24.74	1865.67	281.77
20	1383.33	25.12	1883.54	278.93
21	1399.09	25.03	1867.97	281.80
22	1475.02	18.64	1792.05	278.86
23	1123.91	44.18	2143.16	279.02
24	1232.39	36.40	2034.68	281.93
25	1658.31	3.27	1610.24	284.56
26	1741.38	-2.41	1525.69	285.51
27	1363.92	25.03	1903.15	285.82
28	1430.62	19.45	1836.44	284.87
29	1276.05	31.08	1991.02	285.68
30	1250.32	32.69	2016.74	284.84
31	1310.30	27.63	1956.77	285.14
32	1215.74	35.76	2051.13	286.09

Table 4.6a. Parameter effects at PILPS grassland site

Par Index No.	ET (mm/yr)	R. (mm/yr)	SH (Wm-2)	Tmin (K)
1	24.80	-24.80	-1.97	0.017
2	-35.43	85.43	5.45	0.044
3	-76.92	76.92	4.98	0.058
4	7.00	-6.98	-5.96	1.694
5	146.28	-146.28	-9.49	-0.087
6	-0.21	0.20	1.01	1.546
7	97.09	-97.06	-6.23	-0.129
8	-67.62	67.60	4.36	0.024
9	-9.73	9.76	0.66	0.023
10	1.73	-1.75	-0.15	-0.022
11	2.57	-2.59	-0.17	0.008
12	-1.90	1.92	0.19	-0.028
13	-1.85	1.88	0.21	-0.017
14	1.85	-1.85	-0.16	-0.018
15	2.28	-2.31	-0.38	0.016
16	17.43	-17.40	-0.98	0.031
17	0.55	-0.55	0.38	-0.654
18	-6.28	6.28	0.47	-0.011
19	-5.07	5.07	0.20	-0.032
110	12.99	-12.99	-0.58	0.021
111	-0.12	0.12	0.03	-0.014
24	-22.20	22.20	1.27	-0.021
25	14.49	-14.51	-1.01	-0.009
28	3.34	-3.34	-0.22	0.034
35	-10.79	10.77	0.55	0.002
56	1.11	-1.14	0.01	0.027

Table 4.6b.   Parameter effects at PILPS forest site

Par Index No.	ET (mm/yr)	R (mm/yr)	SH (Wm-2)	Tmin (K)
1	27.96	-27.96	-2.08	0.070
2	-104.12	104.12	7.43	0.190
3	-183.07	183.06	13.08	0.147
4	27.46	-27.28	-4.45	5.074
5	128.35	-128.35	-9.14	-0.161
6	-4.61	4.61	0.80	1.865
7	155.65	-155.51	-11.23	-0.131
8	-127.58	127.34	9.08	0.052
9	-57.95	58.08	4.17	0.054
10	-16.17	15.99	1.10	-0.040
11	11.07	-11.25	-0.74	-0.008
12	-2.42	2.55	0.28	-0.031
13	-9.72	9.90	0.93	-0.019
14	-0.61	0.61	0.47	0.027
15	-3.81	3.57	0.14	-0.030
16	-1.37	1.56	0.06	-0.051
17	-7.44	7.44	0.70	-1.087
18	-1.45	1.44	0.24	-0.006
19	24.09	-24.10	-1.66	0.033
110	31.52	-31.52	-2.25	-0.124
111	-13.52	13.52	0.95	0.009
24	-25.16	25.16	1.80	0.125
25	-33.15	32.92	2.33	0.025
28	-12.19	12.19	0.86	0.119
35	1.10	-1.28	-0.05	0.015
56	4.06	-4.24	-0.25	0.068

Table 4.7a.   Parameters selected at the PILPS grassland site
based on a threshold of $|3\sigma|$

	Outliers
Evaporation (mm/yr)	LAI
Runoff (mm/yr)	LAI
Sensible heat (Wm^{-2})	LAI
Min. surface temperature (K)	κ, C_s, $\overline{\kappa C_s}$

Table 4.7b.   Parameters selected at the PILPS grassland site
based on a threshold of $|2\sigma|$

	Outliers
Evaporation (mm/yr)	LAI, θ, θ_{cr}, r_{min}, θ_w, z_0, $\overline{r_{min}\theta}$
Runoff (mm/yr)	LAI, θ, θ_{cr}, r_{min}, θ_w, z_0, $\overline{r_{min}\theta}$
Sensible heat (Wm^{-2})	LAI, θ, κ, θ_{cr}, r_{min}, θ_w, z_0, $\overline{r_{min}\theta}$
Min. surface temperature (K)	κ, C_s, $\overline{\kappa C_s}$

Table 4.8a.   Parameters selected at the PILPS forest site
based on a threshold of $|3\sigma|$

	Outliers
Evaporation (mm/yr)	None
Runoff (mm/yr)	None
Sensible heat (Wm^{-2})	None
Min. surface temperature (K)	κ, C_s, $\overrightarrow{\kappa C_s}$

Table 4.8b.   Parameters selected at the PILPS forest site
based on a threshold of $|2\sigma|$

	Outliers
Evaporation (mm/yr)	r_{min}, θ, LAI, θ_w, θ_{cr}
Runoff (mm/yr)	r_{min}, θ, LAI, θ_w, θ_{cr}
Sensible heat (Wm^{-2})	r_{min}, θ, LAI, θ_w, θ_{cr}
Min. surface temperature (K)	κ, C_s, $\overline{\kappa C_s}$

Table 4.9. Identified important parameters (ranked from left to right) at the PILPS grassland site for the annual quantity metrics

	Primary	Secondary
Evaporation (mm/yr)	LAI, θ, θ_{cr}, r_{min}, θ_{w}	z_0, $\overline{r_{min}\theta}$
Runoff (mm/yr)	LAI, θ, θ_{cr}, r_{min}, θ_{w}	z_0, $\overline{r_{min}\theta}$
Sensible heat (Wm^{-2})	LAI, θ, κ, θ_{cr}, r_{min}, θ_{w}	z_0, $\overline{r_{min}\theta}$
Min. surface temperature (K)	κ, C_s	$\overline{\kappa C_s}$

Table 4.10. Identified important parameters (ranked from left to right) at the PILPS forest site for the annual quantity metrics

	Primary	Secondary
Evaporation (mm/yr)	r_{min}, θ	LAI, θ_{w}, θ_{cr}
Runoff (mm/yr)	r_{min}, θ	LAI, θ_{w}, θ_{cr}
Sensible heat (Wm^{-2})	r_{min}, θ	LAI, θ_{w}, θ_{cr}
Min. surface temperature (K)	κ, C_s	$\overline{\kappa C_s}$

Table 4.11. Results for b_i, D_s, and W_s from one-at-a-time
sensitivity analysis at the PILPS grassland site

	T(K)	$\rho_W L_e E(Wm^{-2})$	SH(Wm^{-2})	ET(mm/yr)	R(mm/yr)
Control run	282.12	47.87	−5.10	617.21	648.83
$b_i = 0.01$	282.11	48.04	−5.24	619.44	646.59
$b_i = 0.03$	282.11	48.00	−5.20	618.84	647.19
$b_i = 0.3$	282.12	47.49	−4.77	612.20	645.42
$b_i = 0.5$	282.13	47.20	−4.53	608.47	652.84
$D_s = 0.01$	282.12	47.87	−5.10	617.21	648.84
$D_s = 0.05$	282.12	47.87	−5.10	617.21	648.73
$D_s = 0.1$	282.12	47.87	−5.10	617.21	648.83
$D_s = 0.3$	282.12	47.87	−5.10	617.21	648.84
$W_s = 0.1$	282.12	47.87	−5.10	617.21	648.83
$W_s = 0.3$	282.12	47.87	−5.10	617.21	648.83
$W_s = 0.5$	282.12	47.87	−5.10	617.21	648.84
$W_s = 0.7$	282.12	47.87	−5.10	617.21	648.84

Table 4.12. Results for b_i, D_s, and W_s from one-at-a-time
sensitivity analysis at the PILPS forest site

	T(K)	$\rho_w L_w E(Wm^{-2})$	SH(Wm^{-2})	ET(mm/yr)	R(mm/yr)
Control run	300.29	104.55	25.93	1357.56	1909.50
$b_i = 0.01$	300.29	104.88	25.62	1361.88	1905.20
$b_i = 0.1$	300.29	103.81	26.64	1347.72	1912.17
$b_i = 0.3$	300.31	102.17	28.17	1326.32	1939.46
$b_i = 0.5$	300.32	101.00	29.28	1310.96	1955.85
$D_s = 0.01$	300.29	104.55	25.93	1357.57	1909.52
$D_s = 0.05$	300.29	104.55	25.93	1357.59	1908.76
$D_s = 0.1$	300.29	104.55	25.93	1357.59	1909.49
$D_s = 0.3$	300.29	104.55	25.93	1357.59	1909.52
$W_s = 0.1$	300.29	104.55	25.93	1357.59	1909.50
$W_s = 0.3$	300.29	104.55	25.93	1357.59	1909.52
$W_s = 0.5$	300.29	104.55	25.93	1357.59	1909.52
$W_s = 0.7$	300.29	104.55	25.93	1357.59	1909.51

Table 4.13.   Results for r_{min} and θ_{cr} from one-at-a-time sensitivity
analysis at the PILPS grassland site

	T(K)	$\rho_w L_e E(Wm^{-2})$	SH(Wm^{-2})	ET(mm/yr)	R(mm/yr)
$r_{min}=170$ (s/m)	282.08	49.33	−6.33	635.94	630.08
$r_{min}=230$ (s/m)	282.14	46.61	−4.01	600.93	665.11
$\theta_{cr}=0.306$	282.07	49.40	−6.33	636.94	629.09
$\theta_{cr}=0.383$	282.14	46.77	−4.15	602.94	663.06

Table 4.14.   Results for r_{min} and θ_{cr} from one-at-a-time sensitivity
analysis at the PILPS forest site

	T(K)	$\rho_w L_e E(Wm^{-2})$	SH(Wm^{-2})	ET(mm/yr)	R(mm/yr)
$r_{min}=140$ (s/m)	300.28	105.72	24.83	1372.65	1894.45
$r_{min}=160$ (s/m)	300.30	103.78	27.02	1342.42	1924.62
$\theta_{cr}=0.33$	300.29	104.69	25.79	1359.42	1907.67
$\theta_{cr}=0.39$	300.29	104.22	26.24	1353.36	1913.73

Table 4.15a. Results of 32 runs for the sum of the monthly absolute
difference metrics at PILPS grassland site

Runs	DET(mm/mo)	DSH(Wm-2)	DR(mm/mo)
1	16.63	64.24	305.98
2	20.61	43.76	150.76
3	37.08	63.64	85.12
4	25.40	56.90	241.58
5	72.84	103.72	304.67
6	51.94	89.62	255.21
7	221.08	216.26	370.96
8	193.93	198.58	203.31
9	45.94	63.29	222.62
10	60.06	97.01	86.56
11	208.59	134.95	281.13
12	181.72	108.56	181.71
13	86.06	42.06	228.90
14	62.01	27.95	193.04
15	88.08	32.85	339.31
16	75.86	44.12	316.58
17	159.53	133.31	164.16
18	196.28	151.11	244.78
19	83.58	48.43	272.18
20	94.90	57.14	231.74
21	105.99	64.09	224.48
22	145.01	90.45	202.57
23	32.23	79.87	172.13
24	25.34	46.68	299.28
25	235.15	212.29	265.03
26	294.23	256.96	337.92
27	74.25	77.93	174.52
28	93.83	109.25	248.26
29	97.34	99.12	200.27
30	117.00	118.92	180.77
31	16.75	46.84	46.39
32	20.69	64.19	219.76

Table 4.15b. Results of 32 runs for the sum of the monthly absolute
difference metrics at PILPS forest site

Runs	DET(mm/mo)	DSH(Wm-2)	DR(mm/mo)
1	123.55	98.86	799.03
2	196.60	150.74	361.78
3	148.74	102.65	427.95
4	115.90	88.49	545.81
5	208.12	197.59	544.46
6	129.81	125.41	1049.71
7	404.26	363.98	723.21
8	359.80	328.41	836.55
9	254.42	235.86	496.20
10	244.72	218.28	294.07
11	309.24	259.61	488.83
12	184.78	157.56	477.93
13	139.22	111.73	1023.77
14	171.24	139.37	432.10
15	124.53	95.31	1269.52
16	133.40	113.36	559.87
17	194.30	152.18	920.04
18	252.99	200.27	432.92
19	189.14	143.04	1006.10
20	243.64	199.74	465.76
21	86.25	78.25	568.41
22	117.43	92.22	463.68
23	235.04	220.51	479.92
24	125.21	125.69	794.89
25	300.71	271.90	620.20
26	383.78	340.14	1276.18
27	148.39	131.39	365.44
28	184.13	173.34	955.33
29	113.06	106.89	706.26
30	153.94	143.47	381.22
31	91.77	95.93	295.19
32	155.27	135.91	524.92

Table 4.16a. Parameter effects for the sum of the monthly absolute
difference metrics at PILPS grassland site

Par Index No.	DET (mm/mo)	DR (mm/mo)	DSH (Wm-2)
1	4.86	-4.00	4.90
2	-18.33	7.26	-16.98
3	-25.98	16.47	-19.59
4	17.20	-12.88	1.78
5	21.52	-17.70	16.82
6	4.10	0.55	1.79
7	-20.81	3.24	-16.31
8	25.28	-19.95	26.13
9	-1.39	21.09	-0.69
10	0.96	14.58	1.88
11	-9.51	-58.60	-2.40
12	-11.10	29.06	-6.81
13	-8.43	1.93	-5.43
14	1.80	4.80	9.81
15	17.95	59.74	11.71
16	10.30	14.96	28.66
17	5.48	20.52	10.26
18	-3.50	-28.32	0.01
19	-52.77	-25.56	-53.43
110	-3.90	-4.42	37.52
111	1.46	19.34	6.11
24	-11.42	4.30	-20.38
25	-95.29	-26.73	-57.51
28	45.87	11.25	19.34
35	-57.95	-65.59	-34.94
56	-3.68	57.22	-6.73

Table 4.16b. Parameter effects for the sum of the monthly absolute
difference metrics at PILPS forest site

Par Index No.	DET (mm/mo)	DR (mm/mo)	DSH (Wm-2)
1	4.81	-55.11	4.17
2	4.88	-9.55	4.49
3	-45.10	45.01	-28.13
4	-2.07	-15.82	3.88
5	-16.77	-4.65	-11.02
6	10.59	-10.15	5.61
7	-23.32	14.30	-20.62
8	47.51	-81.28	45.64
9	31.90	-287.82	28.92
10	12.15	236.33	10.42
11	-5.67	-123.50	-6.35
12	-23.43	68.23	-15.41
13	-12.45	-15.86	-12.46
14	10.81	9.64	9.93
15	26.79	96.78	22.17
16	58.27	48.86	56.04
17	10.23	49.11	7.46
18	-10.35	-34.54	-9.92
19	-70.24	-17.67	-77.64
110	13.58	14.95	19.51
111	11.96	13.26	8.87
24	-59.20	-27.07	-55.14
25	-34.24	-50.62	-24.46
28	42.81	8.75	33.54
35	-56.66	-273.44	-48.52
56	-18.33	146.88	-16.53

Table 4.17. Identified important parameters (ranked from left to right)
at the PILPS grassland site for the sum of the
monthly absolute difference metrics

	Importance		
Evaporation (mm/mo)	$\overline{LAI\theta_{cr}}$ ($\overline{\theta\theta_w}$),	$\overline{r_{min}LAI}$,	$\overline{LAI\theta_w}$ ($\overline{\theta\theta_{cr}}$)
Runoff (mm/mo)	$\overline{b_iD_s}$ ($\overline{\theta W_s}$, $\overline{r_{min}LAI}$),	$\overline{\theta_w b_i}$, W_s,	$\overline{b_iW_s}$ ($\overline{\theta D_s}$)
Sensible heat (Wm^{-2})	$\overline{LAI\theta_{cr}}$ ($\overline{\theta\theta_w}$),	$\overline{LAI\theta_w}$ ($\overline{\theta\theta_{cr}}$),	$\overline{r_{min}LAI}$ ($\overline{\theta_w\kappa}$)

Table 4.18. Identified important parameters (ranked from left to right)
at the PILPS forest site for the sum of the
monthly absolute difference metrics

	Importance		
Evaporation (mm/mo)	– – –		
Runoff (mm/mo)	b_i, $\overline{b_iD_s}$ ($\overline{\theta W_s}$, $\overline{r_{min}LAI}$),	D_s, $\overline{b_iW_s}$ ($\overline{\theta D_s}$),	W_s
Sensible heat (Wm^{-2})	$\overline{LAI\theta_w}$ ($\overline{\theta\theta_{cr}}$),	$\overline{r_{min}\theta}$ ($\overline{\theta_{cr}\kappa}$),	$\overline{r_{min}LAI}$ ($\overline{\theta_w\kappa}$)

Table 4.19.   Results of model effects at the PILPS grassland site

	T(K)	$\rho_W L_e E(Wm^{-2})$	SH(Wm^{-2})	ET(mm/yr)	R(mm/yr)
Std. Case	282.12	47.87	−5.10	617.21	648.83
Case (1)	282.18	43.80	0.02	565.51	700.54
Case (2)	282.64	48.30	−7.90	623.72	642.32
Case (3)	280.35	113.64	−57.11	1459.56	− − −
Case (4)	280.51	137.02	−83.00	1761.69	− − −

Table 4.20.   Results of model effects at the PILPS forest site

	T(K)	$\rho_W L_e E(Wm^{-2})$	SH(Wm^{-2})	ET(mm/yr)	R(mm/yr)
Std. Case	300.29	104.55	25.93	1357.59	1909.50
Case (1)	300.34	90.60	41.84	1176.49	2090.55
Case (2)	300.50	157.04	−25.81	2034.11	1232.97
Case (3)	299.78	146.09	−9.65	1900.05	− − −
Case (4)	297.11	484.35	−332.38	6293.91	− − −
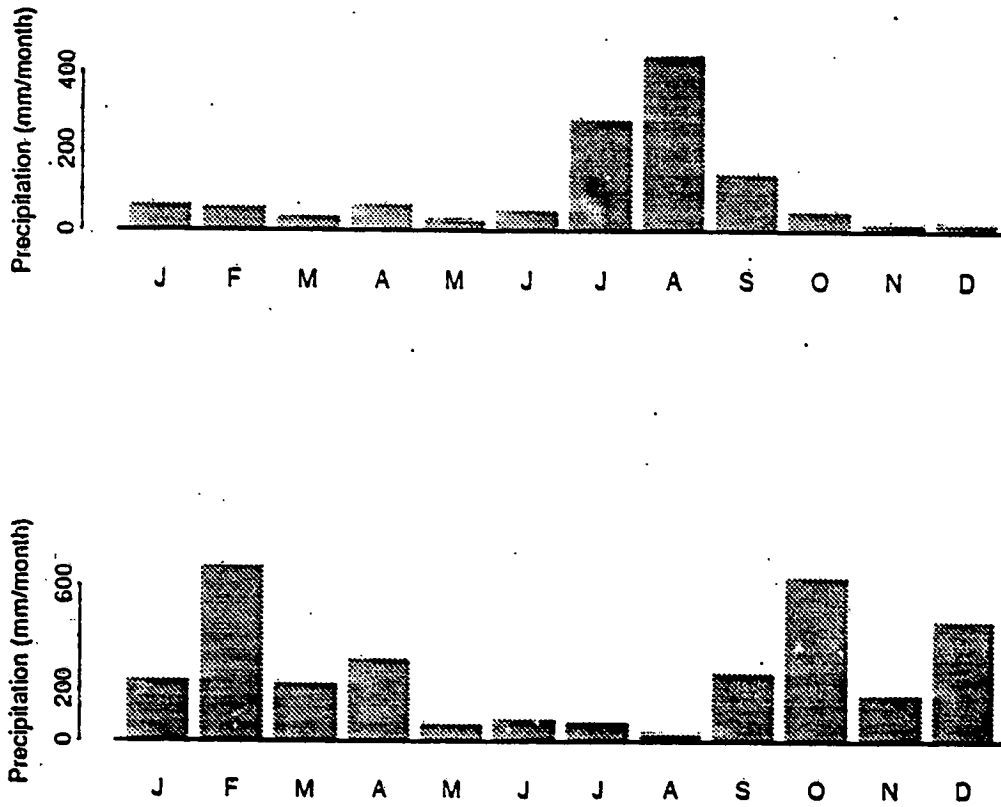
Fig. 4.1   Monthly precipitation at PILPS grassland (upper) and forest (lower) sites.
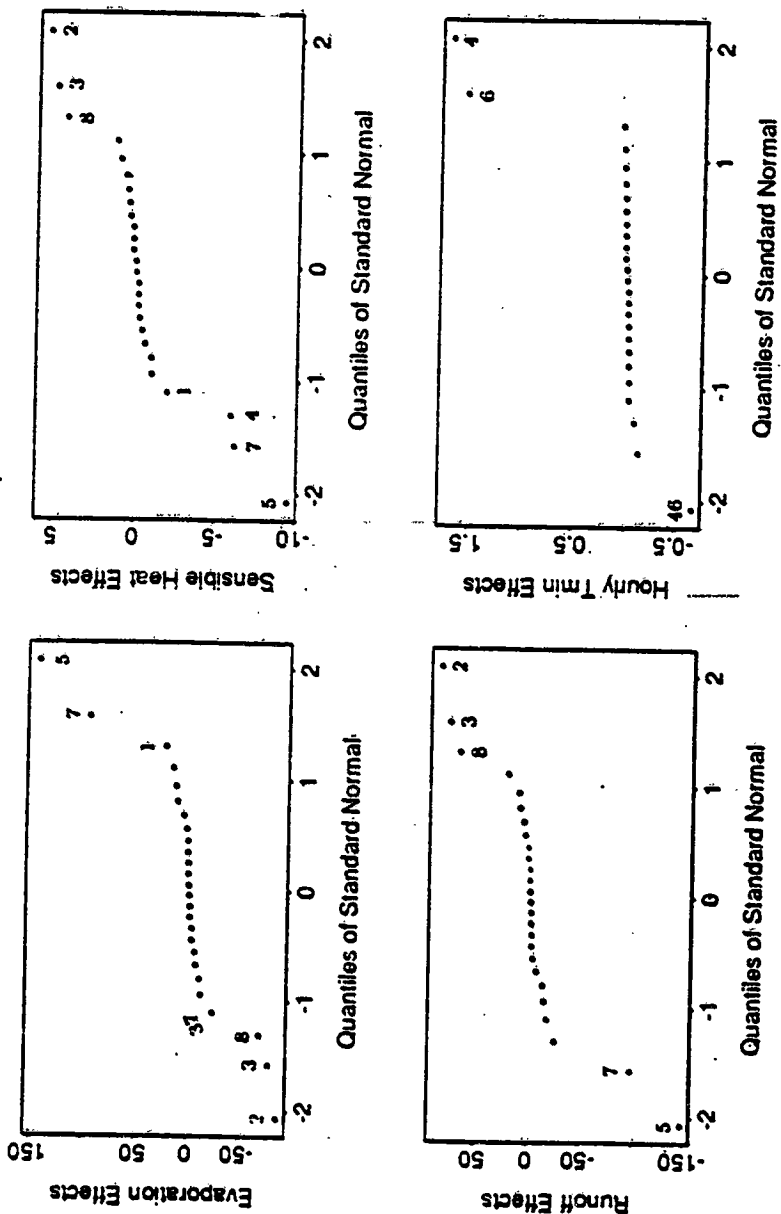
Fig. 4.2   Parameter effects at the PILPS grassland site.
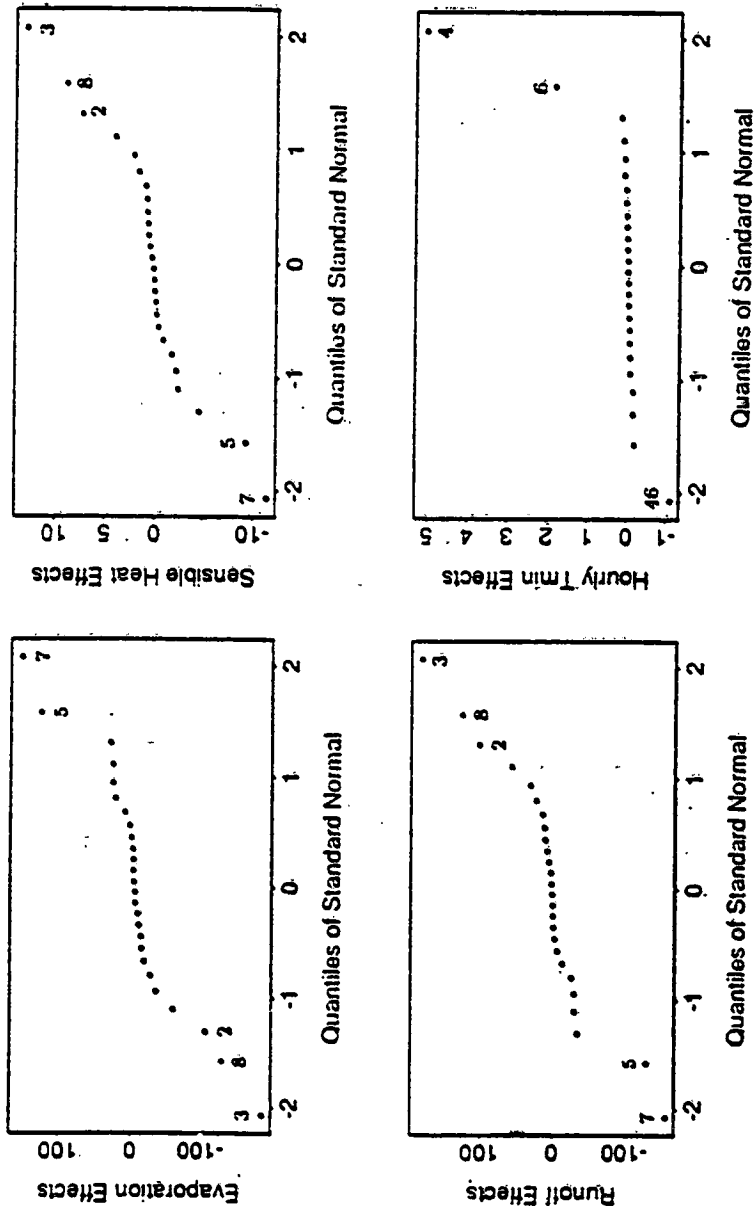
Fig. 4.3   Parameter effects at the PILPS forest site.
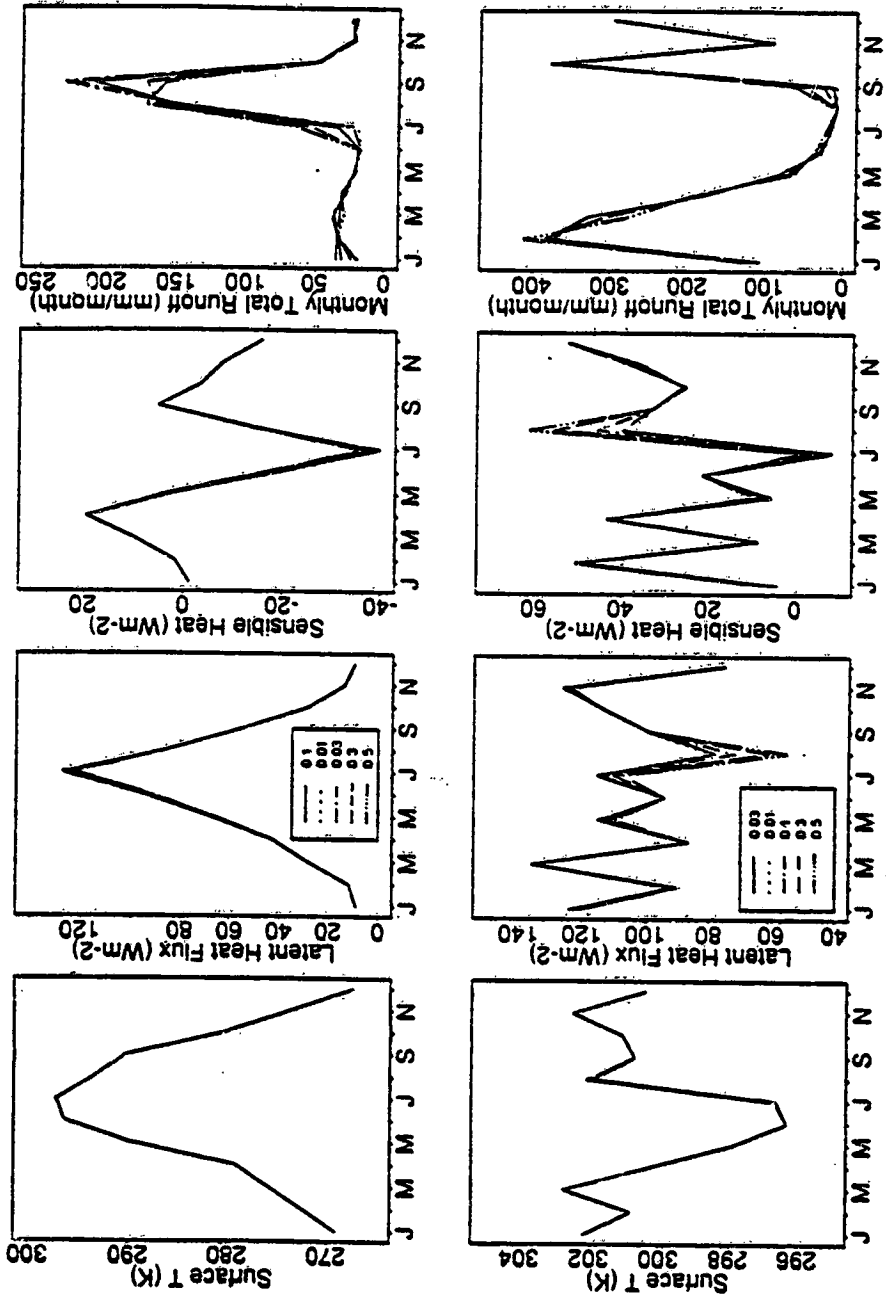
Fig. 4.4   Sensitivity analysis of parameter b_i at the PILPS grassland (upper) and forest (lower) sites.

Fig. 4.5   Effects of parameter b_i on runoff at the PILPS grassland site.

"Page missing from available version"

Fig. 4.7 Effects of parameters D_s and W_s on runoff at the PILPS grassland (upper) and forest (lower) sites.

Fig. 4.8   Parameter effects at the PILPS grassland site with the absolute difference as metrics.
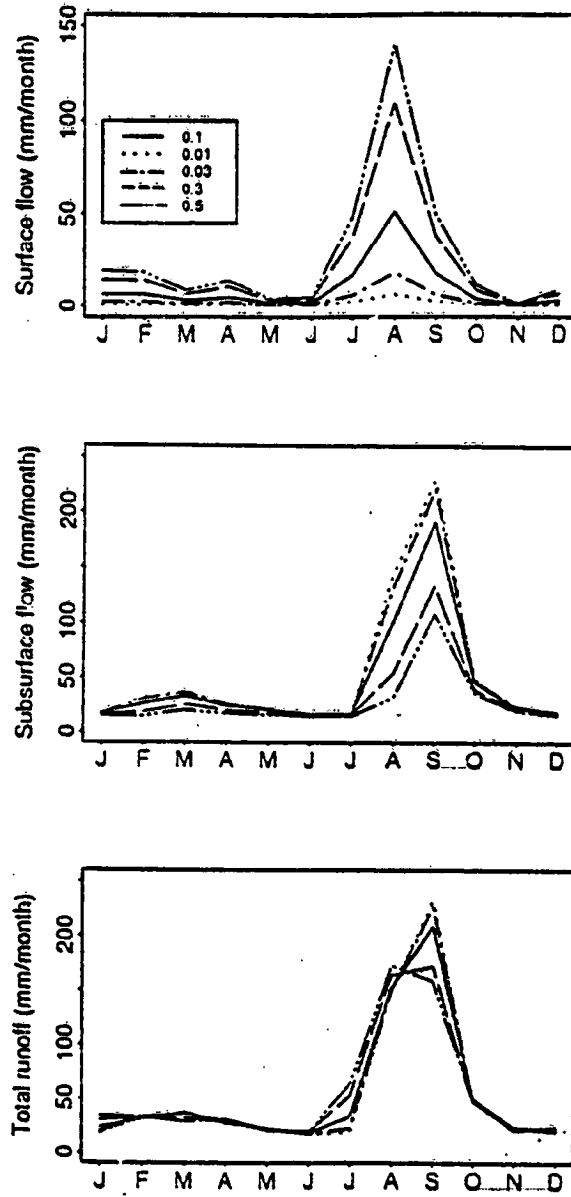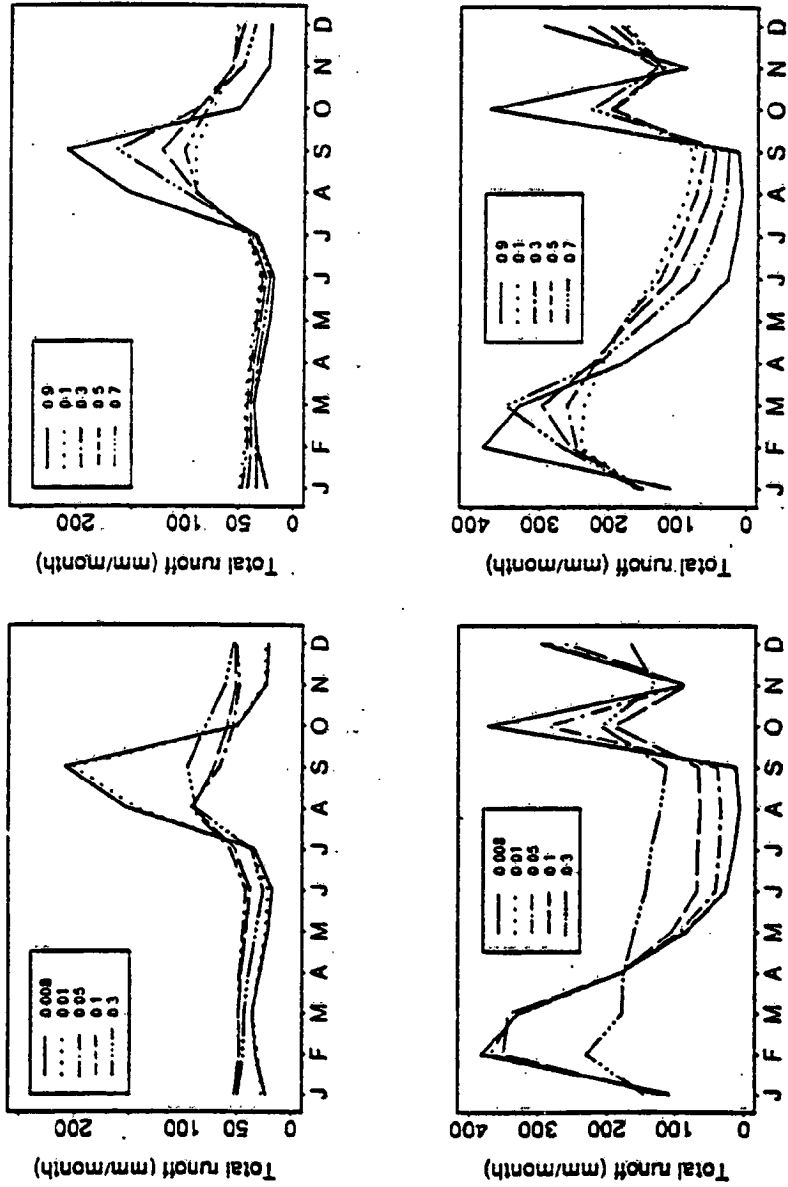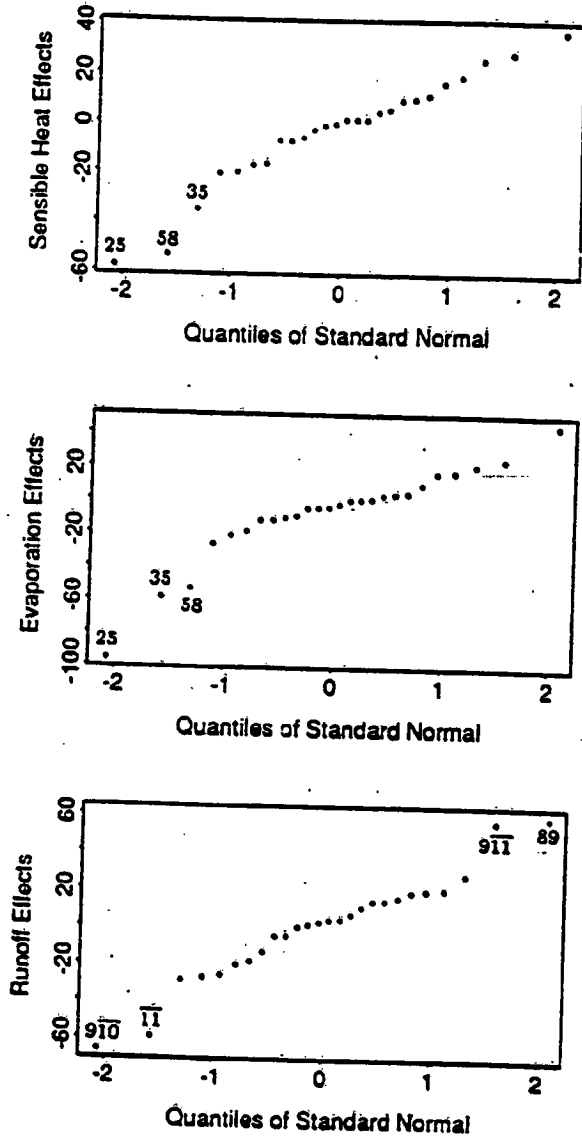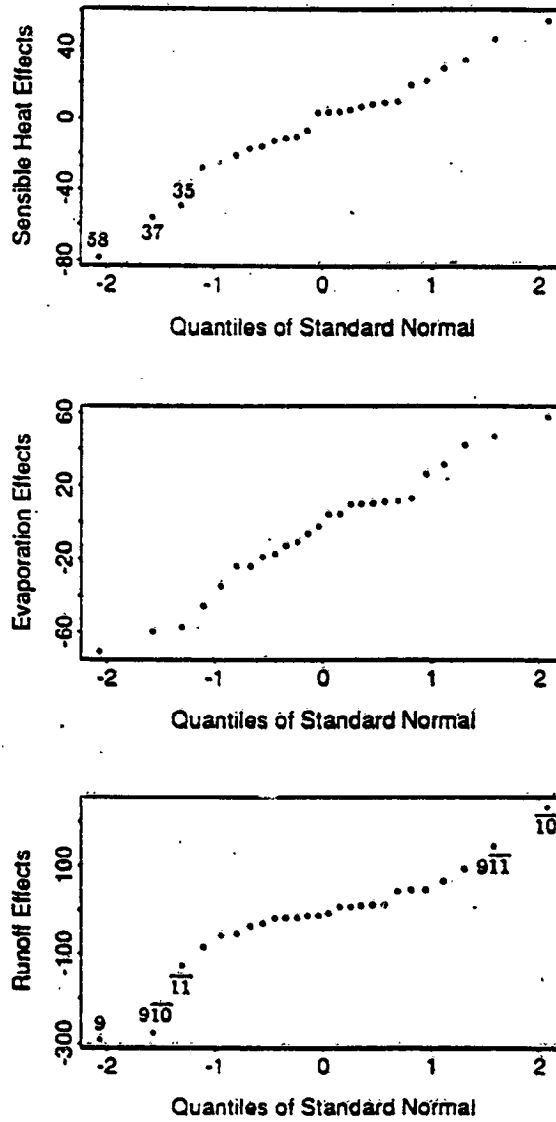
Fig. 4.9   Parameter effects at the PILPS forest site with the absolute difference as metrics.

CHAPTER 5   A PARAMETERIZATION OF SPATIAL VARIABILITY OF PRECIPITATION IN THE TWO-LAYER VIC MODEL

In Chapters 2-4, the structure of a two-layer VIC model was developed, and its performance and parameter sensitivities were evaluated. In the two applications, the model was driven with spatially-average precipitation which was justifiable, since both sites were small. The FIFE site is a 15×15 km^2 region and the ABRACOS site is essentially a point. For a large area (e.g., a GCM grid cell), however, the effects of subgrid scale spatial variations of precipitation on surface energy fluxes, soil moisture, and runoff production may be significant. In practice, the subgrid land surface variations have been largely ignored in GCM land surface schemes. Most GCMs, for instance, assume uniform soil characteristics within a grid cell, and ignore spatial variability in precipitation. The two-layer VIC model described in Chapter 2 is a simple approach for representing subgrid variability in soil properties. In this chapter, an extension of the model to incorporate a representation of subgrid variability in precipitation is described. With this new representation, the effects of subgrid scale spatial variability of precipitation on surface fluxes, soil moisture, and runoff can be examined. The results of this method are compared with those obtained using an exhaustive pixel-based application of the two-layer VIC model, and those obtained by applying uniform spatial average precipitation to the two-layer VIC model.

5.1. Introduction

The feedbacks from land surfaces to atmospheric general circulation models (GCMs) are important determinants of regional and global climate. Land surface schemes used in the GCMs have to deal with spatial variations that occur at scales smaller than a GCM grid cell, in the same way that the atmospheric part of the GCM must parameterize subgrid scale atmospheric

variability. Natural land surfaces are heterogeneous within the scales resolvable by GCMs. There are two major types of heterogeneities. One is related to the subgrid scale hydrologic and topographic heterogeneity of the land surface itself; the other is related to the subgrid scale variability of meteorological inputs, such as precipitation, downward shortwave and long-wave radiation, wind speed, temperature and humidity. Among the meteorological inputs, the subgrid scale variability in precipitation is particularly important (Raupach 1993). Blyth et al. (1993) showed that correct prediction of the total evaporation can be obtained by using simple averages of surface parameters when comparing the results from a one-dimensional model with those from a three-dimensional mesoscale model. However, their results indicated that a reasonable partitioning of the total evaporation into transpiration, evaporation from intercepted water, and evaporation of the bare soil cannot be obtained unless the spatial distribution of rainfall is considered at least.

The spatial variability in precipitation has been widely recognized to have a major effect on evaporation, soil moisture variability, and runoff production (for example, Warrilow et al. 1986, Shuttleworth 1988, Entekhabi and Eagleson 1989, Famiglietti and Wood 1990, Pitman et al. 1990, Henderson-Sellers and Pitman 1992). Two approaches could be taken to incorporate spatial variability in precipitation in a model. One is the pixel-based approach which discretizes precipitation over a spatial domain. The work of Famiglietti et al. (1992), and Wigmosta et al. (1994), among others, for example, falls into the pixel-based category. Although such a pixel-based representation is able to account for the spatial variability in precipitation throughout a grid cell (or a catchment) in a straightforward manner, the associated computation time and data demands using this method make it untouchable for implementations within GCMs.

Another option is the statistical-dynamic approach to representing the spatial variability in precipitation. The advantage of this approach is that, if an appropriate statistical distribution is assumed, it can result in a closed form solution which would be computationally much less demanding than pixel-based

approaches. Also, this approach requires less data, since only the statistical distribution of precipitation needs to be specified, and not the values associated with specific spatial locations. Previous applications of the statistical-dynamical approach are briefly reviewed below.

Warrilow et al. (1986) combined a subgrid precipitation distribution with a constant maximum surface infiltration rate to estimate runoff from a grid cell. They assumed that over a fraction, μ, of a grid cell (or an area), the point precipitation intensity, P_i, is exponentially distributed and can be expressed as,

$$f(P_i) = \frac{\mu}{P_m} \exp\left(-\frac{\mu P_i}{P_m}\right) , \qquad 0 \leq \mu \leq 1 \qquad (5.1)$$

where P_m is the grid cell average precipitation generated in the GCM. The runoff from the grid cell is then given by

$$q = \mu \cdot \int_{F^*}^{\infty} (P_i - F^*) \, f(P_i) \, dP_i = P_m \exp\left(-\frac{\mu F^*}{P_m}\right) \qquad (5.2)$$

where F^* is the maximum surface infiltration rate.

Shuttleworth (1988) derived an expression for canopy throughfall based on the assumption that the precipitation rate over a fraction μ of a grid cell was expressed by Eq. (5.1). Assuming that C_m is the difference between the canopy storage capacity and the water stored on the canopy divided by the model time step, the throughfall over the grid cell is then given by

$$P_t = \mu \cdot \int_{C_m}^{\infty} (P_i - C_m) \, f(P_i) \, dP_i = P_m \exp\left(-\frac{\mu C_m}{P_m}\right) \qquad (5.3)$$

and the runoff over the grid cell becomes

$$q = P_m \exp[-\frac{\mu (F^*+C_m)}{P_m}]$$

(5.4)

Entekhabi and Eagleson (1989) represented the subgrid hydrologic processes in a GCM land surface scheme by assuming the same precipitation distribution (Eq. (5.1)) and combined it with a two-parameter gamma probability density function (pdf) of the surface layer point effective relative soil saturation to describe the spatial heterogeneity in surface soil moisture. By assuming independence of the point precipitation intensity, P_i, and the surface layer point effective relative soil saturation, s, they derived a general relationship for runoff rate (q) for the entire GCM grid during a time step as,

$$\mu^{-1}q = \int_0^1 \int_{f^*}^\infty (P_i - f^*)f(P_i)dP_i\ f_s(s)ds + \int_1^\infty \int_0^\infty P_i f(P_i)dP_i\ f_s(s)ds$$

(5.5)

where f^* is the infiltrability (infiltration rate) of the first soil layer, $f(P_i)$ is defined in Eq. (5.1), and $f_s(s)$ is a two-parameter gamma pdf of s.

Famiglietti and Wood (1991) considered the subgrid scale variability in topography, soils, soil moisture and precipitation by combining the same point precipitation distribution (Eq. (5.1)) with the distribution of the topography-soils indices from Topmodel (Beven and Kirkby 1979). They obtained an expression of the expected value of the depth of infiltration excess runoff for a large area, $E[Q_{inf}]$, as,

$$E[Q_{inf}] = \int_0^{z^*} \int_{f_i^*}^\infty (P_i - f_i^*)f(P_i)dP_i\ f_z(z)dz$$

(5.6a)

where $z^* = \ln^*(bT_E/T_0\ \tan\beta)$, f_i^* is the infiltration rate, $z = \ln(bT_E/T_0\tan\beta)$ is the local value of the topography-soils index of Topmodel, z^* represents the critical value of the Topmodel index at which saturation occurs, and $f_z(z)$ is the

pdf of z, which is assumed to follow a three-parameter gamma distribution according to Sivapalan et al. (1987) and Wolock et al. (1989). The expected value of the depth of saturation excess runoff, $E[Q_{sat}]$, is expressed as,

$$E[Q_{sat}] = \int_{z^*}^{\infty} \int_0^{\infty} P_i f(P_i) dP_i \, f_z(z) dz + \int_0^{z^*} \int_{S_i}^{\infty} (P_i - S_i) f(P_i) dP_i \, f_z(z) dz \qquad (5.6b)$$

where S_i is the storage deficit. The first integral in Eq. (5.6b) represents runoff generated on those areas that are saturated at the start of a time step, the second integral represents the runoff generated on those areas that become saturated during a time step.

Pitman et al. (1990) incorporated the parameterization suggested by Warrilow et al. (1986) and Shuttleworth (1988) into the Biosphere-Atmosphere Transfer Scheme (BATS) of Dickinson et al. (1986) to study the sensitivity of evaporation and runoff due to Eq. (5.1) within a grid cell. When incorporating Eq. (5.1) in BATS, they assumed that the soil moisture and intercepted water were distributed uniformly within a grid cell at the end of a time step. They found out, on the basis of results from a sensitivity study, that the monthly distributions of evaporation and runoff were quite sensitive to the spatial precipitation distribution and the fractional coverage μ of precipitation.

Among the parameterizations discussed above, only the ones by Entekhabi and Eagleson (1989), and by Famiglietti and Wood (1991) considered the effects of interactions of subgrid spatial variabilities in precipitation and subgrid variabilities in land surface characteristics. However, the runoff computed by both of their models (Eq. (5.5) or Eq. (5.6)) is a point average over the fraction μ of the grid cell on which precipitation falls. In other words, the runoff given by these models is equivalent to the runoff that would be generated by assuming that each point within the fraction μ is independent from each other and has the same statistical distribution of precipitation, soil moisture, and/or topography-soil index. Thomas and Henderson-Sellers (1991) pointed out that

these treatments ignore the absolute spatial location within the grid cell of the precipitation.

In this chapter, a derived distribution approach which combines the spatial subgrid variability in precipitation with subgrid variability in other land surface features, including soil moisture capacity, is described. To distinguish the statistical-dynamic approach used by Entekhabi and Eagleson (1989), and by Famiglietti and Wood (1991) from the one described here, we will refer their methods as point statistical-dynamic approach. The model developed here is described as a one-dimensional statistical-dynamic model by using a derived distribution approach.

5.2. One-dimensional statistical-dynamic model

Assume that within a grid cell (or an area), precipitation, infiltration capacity, and/or other features (or attributes) only vary along one direction, which is arbitrarily taken as the x axis, and they are kept constants along its orthogonal (y) axis (one-dimensional concept), where x and y are scaled to give $x \cdot y =$ unit area. Ideally then, the general relationship for runoff rate $Q_{\mu d}$ of the area with a precipitation coverage μ during a time step would be,

$$Q_{\mu d} = \mu \cdot \int_0^1 \left\{ \int_{P_{x,1}}^{P_{x,2}} \int_{z_{x,1}}^{z_{x,2}} [P(x) - f^*(x)] \cdot f(P_x) dP_x \, f(z_x) dz_x + \right.$$

$$\left. \int_{P_{x,3}}^{P_{x,4}} \int_{z_{x,3}}^{z_{x,4}} P(x) \cdot f(P_x) dP_x \, f(z_x) dz_x \right\} \cdot dx = \mu \cdot \int_0^1 dQ_{\mu d}, \quad 0 < x \le 1 \quad (5.7)$$

where $P(x)$ and $f^*(x)$ are precipitation and infiltration capacity within the fraction of area μ in which rain occurs, $f(P_x)$ and $f(z_x)$, both of which vary with x, are pdfs of $P_x = P(x)$ and z_x respectively, and z_x is a variable which varies along x axis. This variable could be an effective relative soil saturation like that

in Eq. (5.5), or a topography-soils indices like that in Eq. (5.6), or some other variable, depending on the specific formulation. $P_{x,2}$, $z_{x,2}$, $P_{x,4}$, and $z_{x,4}$ are the upper limits of the integrals in Eq. (5.7), while $P_{x,1}$, $z_{x,1}$, $P_{x,3}$, and $z_{x,3}$ are the lower limits of the integrals in the same equation. It can be seen that Eq. (5.7) reduces to a point statistical-dynamic approach (i.e., Eqs. (5.5) and/or (5.6)) if the integrands in the bracket {} do not vary along the x axis. Since it is difficult to determine $f(P_x)$ and $f(z_x)$, and also to evaluate the triple integrals, we will simplify Eq. (5.7) without loss of the one-dimensional treatment of subgrid spatial variabilities. In the derivations below, four assumptions are made:

(1). The precipitation P is a one-dimensional function varying along the x axis (i.e., $P(x)$) within the fractional coverage μ. This assumption is, in a sense, equivalent to assuming that storms are distributed as circles around the storm centers.

(2). At the end of each time step t (i.e., at the beginning of the next time step t+1), the soil moisture content of each strip "ydx" (defined in Section 5.2.1) within the fractional coverage μ of the same vegetation cover becomes the same. This assumption avoids the necessity for tracking the storm center movement.

(3). Prior to the beginning of the next storm, the soil moistures over the fractional coverage μ are assumed to be the same as the moistures over the non-rainfall fractional coverage of $1 - \mu$, which is accomplished by spatial averaging. This assumption becomes reasonable in practice if the inter-arrival time between two storms is long enough so that the recently wetted soil drains to a comparable moisture level to that which was not covered by the storm. Here we define the inter-arrival time as the time between two storms whose magnitudes are above a specified threshold (taken to be 1 mm/hr in this study). If a storm with magnitude below a specified threshold occurs, the soil moistures over μ and $1 - \mu$ are not averaged. It should be noted that if storms smaller than the specified threshold occur, they are not ignored, but from the standpoint of the soil

moisture distribution, they are treated as a continuation of the previous storm. The effect of this assumption is that the track of previous storm centers relative to the present storm need not be specified.

(4). Each strip of area ydx is assumed to have an identical infiltration capacity distribution, which is defined by Eq. (2.20).

5.2.1. One-dimensional representation for bare soil

As discussed previously, Eq. (5.7) has to be simplified to obtain a one-dimensional runoff representation that could be implemented into GCMs. In the following, we use the direct runoff concept of the VIC model to obtain an expression for $dQ_{\mu d}$ of Eq. (5.7). Let us begin with the simplest case by assuming that only bare soil is present in a grid cell (or an area) with a fraction coverage of precipitation μ at a time step t. If we discretize the area within the fractional coverage μ into infinitesimal strips of area ydx (see Fig. 5.1), then the precipitation rate within each such strip is a constant. From the fourth assumption and Eqs. (2.25a) and (2.25b), the direct runoff $dQ_{\mu d}[N+1]$ (following the notation in Chapter 2, the land cover class N+1 is defined as bare soil) from strip ydx due to precipitation P(x) can be expressed as

$$dQ_{\mu d}[N+1] = (P(x) - \frac{W_1^c}{\Delta t} + \frac{W_{\mu 1}[N+1]}{\Delta t}) \, dx, \quad i_0 + P(x) \cdot \Delta t \geq i_m \quad (5.8a)$$

$$dQ_{\mu d}[N+1] = (P(x) - \frac{W_1^c}{\Delta t} + \frac{W_{\mu 1}[N+1]}{\Delta t} + \frac{W_1^c}{\Delta t}[1 - \frac{i_0 + P(x) \cdot \Delta t}{i_m}]^{1+b_i}) \, dx,$$

$$i_0 + P(x) \cdot \Delta t < i_m \quad (5.8b)$$

where, as defined in Chapter 2, W_1^c is the maximum soil moisture content of layer 1, i_0 and i_m are the infiltration capacity and maximum infiltration capacity respectively, b_i is the infiltration shape parameter, and Δt is the time step; and $W_{\mu 1}[N+1]$ is the soil moisture content in layer 1 within μ. Therefore,

the total direct runoff at time step t from μ is,

$$Q_{\mu d}[N+1] = \mu \cdot \int_0^a \{P(x) - \frac{W_1^c}{\Delta t} + \frac{W_{\mu 1}[N+1]}{\Delta t}\} \, dx +$$

$$\mu \cdot \int_a^1 \{P(x) - \frac{W_1^c}{\Delta t} + \frac{W_{\mu 1}[N+1]}{\Delta t} + \frac{W_1^c}{\Delta t} [\, ' - \frac{i_0 + P(x) \cdot \Delta t}{i_m}]^{1+b_i} \} dx,$$

$$(5.9)$$

where the first term represents the direct runoff generated when $i_0 + P(x) \cdot \Delta t \geq i_m$ is satisfied, and the second term represents the runoff when $i_0 + P(x) \cdot \Delta t < i_m$ is satisfied. The integral limit, a, represents the location, x, where $i_0 + P(x) \cdot \Delta t = i_m$ if $i_0 + P(1) \cdot \Delta t \leq i_m$. If $i_0 + P(1) \cdot \Delta t \geq i_m$, then $a = 1$ in Eq. (5.9).

In Eq. (5.9), W_1^c, b_i, i_m and Δt are constant. Based on assumption 2, the soil moisture $W_{\mu 1}[N+1]$ in Eq. (5.9) does not vary along the x axis. In addition, from Eq. (2.20) we can obtain the following relationship between i_0 and $W_{\mu 1}[N+1]$,

$$i_0 = i_m [1 - (1 - \frac{W_{\mu 1}[N+1]}{W_1^c})^{\frac{1}{1+b_i}}].$$

$$(5.10)$$

Thus, i_0 is independent of x. Therefore, only $P(x)$ varies with x in Eq. (5.9). If the expression of $P(x)$ is known, then the direct runoff $Q_{\mu d}[N+1]$ with the effects of spatial precipitation and infiltration can be calculated. For a constant precipitation rate within μ, Eq. (5.9) reduces to Eq. (2.25).

For evaporation, it is reasonable to ignore the effects of spatial variations in precipitation within the fractional coverage μ for big storms, which is equivalent to assuming that evaporation is small during storm periods compared

with dry periods. For small storms, the effects of spatial variations in precipitation are small, and so can be ignored also. Therefore, the evaporation from bare soil $(E_{\mu 1})$ can be determined by Eq. (2.22) multiplied by μ, as if the precipitation were uniformly distributed over μ. That is

$$E_{\mu 1} = \mu \cdot E_1. \tag{5.11}$$

The drainage term $Q_{\mu 12}[N+1]$ is determined by Eq. (2.27) multiplied by μ:

$$Q_{\mu 12}[N+1] = \mu \cdot K_s \cdot \left(\frac{W_{\mu 1}[N+1] - \theta_r}{W_1^c - \theta_r}\right)^{\frac{2}{B_p} + 3}. \tag{5.12}$$

The water balance in layer 1 over the fraction μ where precipitation occurs is then,

$$W_{\mu 1}^+[N+1] = W_{\mu 1}^-[N+1] + \left(\mu \int_0^1 P(x)dx - Q_{\mu d}[N+1] - Q_{\mu 12}[N+1] - E_{\mu 1}\right) \cdot \Delta t \tag{5.13}$$

where $W_{\mu 1}^+[N+1]$ and $W_{\mu 1}^-[N+1]$ are the soil moisture content at the end and the beginning of each time step in layer 1 within μ respectively. Similarly, the subsurface runoff $Q_{\mu b}[N+1]$ and the water balance for the lower layer within μ can be expressed as,

$$Q_{\mu b}[N+1] = \mu \cdot \frac{D_s D_m}{W_s W_2^c} W_{\mu 2}^-[N+1], \qquad 0 \le W_{\mu 2}^-[N+1] \le W_s W_2^c \tag{5.14a}$$

$$Q_{\mu b}[N+1] = \mu \cdot \left\{\frac{D_s D_m}{W_s W_2^c} W_{\mu 2}^-[N+1] + \left(D_m - \frac{D_s D_m}{W_s}\right)\left(\frac{W_{\mu 2}^-[N+1] - W_s W_2^c}{W_2^c - W_s W_2^c}\right)^2\right\},$$

$$W_{\mu 2}^-[N+1] \ge W_s W_2^c \tag{5.14b}$$

and

$$W_{\mu 2}^{+}[N+1]=W_{\mu 2}^{-}[N+1]+(Q_{\mu 12}[N+1]-Q_{\mu b}[N+1]-E_{\mu 2})\cdot\Delta t \qquad (5.15)$$

where $W_{\mu 2}^{+}[N+1]$ and $W_{\mu 2}^{-}[N+1]$ are the soil moisture content at the end and the beginning of each time step in layer 2 within μ, respectively. Other terms have the same definitions as used in Chapter 2.

For the area within the dry (no rain) fraction $1-\mu$, the evaporation from the bare soil $E_{(1-\mu)1}$, drainage from layer 1 to layer 2, $Q_{(1-\mu)12}[N+1]$, subsurface runoff $Q_{(1-\mu)b}[N+1]$, and soil moistures in layer 1 and layer 2, $W_{(1-\mu)1}[N+1]$, $W_{(1-\mu)2}[N+1]$, are calculated in the same way as described above, except using $W_{(1-\mu)1}[N+1]$, $W_{(1-\mu)2}[N+1]$, and $(1-\mu)$ instead of $W_{\mu 1}[N+1]$, $W_{\mu 2}[N+1]$, and μ in Eqs. (5.11)-(5.15). The direct runoff in this case, $Q_{(1-\mu)d}[N+1]$, is zero.

According to assumption 3, the soil moisture within area μ and $1-\mu$ is averaged immediately prior to the beginning of next storm that is larger than the specified threshold so that the entire area has the same soil moisture content when next storm arrives. Thus, the soil moisture in layer j (j=1, 2) immediately prior to the above threshold follow-up storm is,

$$W_{\mu j}^{-}[N+1] = \mu\cdot(W_{\mu j}^{+}[N+1]+W_{(1-\mu)j}^{+}[N+1]), \qquad (5.16a)$$

$$W_{(1-\mu)j}^{-}[N+1] = (1-\mu)\cdot(W_{\mu j}^{+}[N+1]+W_{(1-\mu)j}^{+}[N+1]). \qquad (5.16b)$$

5.2.2. One-dimensional representation for vegetation cover

For the area with different vegetation covers, the approach described above applies except that the rainfall rate $P(x)$ is replaced by the throughfall rate. It is assumed that the throughfall rate $P_t(x)$ is equal to $P(x)$ minus

interception where interception is calculated by Eq. (2.3). The approach for incorporating different vegetation covers and bare soil within μ is the same as described in Chapter 2.

Like the bare soil case, the soil moistures for different cover classes over the wet and dry fractions μ and $1 - \mu$ are averaged (or "smeared") prior to the beginning of the next storm that is larger than the specified threshold. That is, the soil moistures of bare soil ($W_{\mu j}[N+1]$, $j=1, 2$) and each vegetation type n ($W_{\mu j}[n]$, $n=1, 2, \cdots, N$) over the fractional coverage of precipitation μ, and the soil moistures of each such cover type over the dry fractional coverage $1 - \mu$ are averaged, so that the entire area (or grid cell) has the same soil moisture content at the onset of the next storm. For the fractional area μ covered by precipitation, the average soil moisture $W_{\mu j}$ ($j=1, 2$) can be expressed as,

$$W_{\mu j} = \sum_{n=1}^{N+1} C_v[n] \cdot W_{\mu j}^{+}[n]. \tag{5.17a}$$

Similarly, the average soil moisture $W_{(1-\mu)j}$ over the dry fractional area $1 - \mu$ can be expressed as,

$$W_{(1-\mu)j} = \sum_{n=1}^{N+1} C_v[n] \cdot W_{(1-\mu)j}^{+}[n]. \tag{5.17b}$$

The average soil moisture of layer j ($j=1, 2$) for the entire area, at the beginning of the next storm is,

$$W_{\mu j}^{-}[n] = \mu \cdot (W_{\mu j} + W_{(1-\mu)j}), \qquad n = 1, 2, \cdots, N+1 \tag{5.18a}$$

$$W_{(1-\mu)j}^{-}[n] = (1-\mu) \cdot (W_{\mu j} + W_{(1-\mu)j}), \qquad n = 1, 2, \cdots, N+1. \tag{5.18b}$$

There are two places in which the soil moisture is averaged. The first is over strips of area ydx within μ at each time step for each cover class using Eq. (5.13).

This avoids tracking the movement of a storm center during a storm. This averaging results in equal soil moisture within the same surface cover type within μ. It is different among the different surface cover classes, and it is different from the soil moisture for the dry fraction $1-\mu$ for the same surface cover class. The second averaging, described by Eq. (5.16) or Eqs. (5.17) and (5.18), is carried out only at the beginning of the next above-threshold storm.

The two advantages of this derived distribution approach are that it avoids the need to identify the specific area that receives a given precipitation rate within the fraction μ of an area (or a grid cell), and it considers the spatial variability of precipitation within the fractional area covered by the storm. This is because for $P(x)$ (or $P_t(x)$) within a strip ydx, $P(x)$ (or $P_t(x)$) is considered to be a constant, and the spatial variability of the infiltration function (Eq. (2.20)) is considered over a strip area ydx with the same initial soil moisture. The dry fraction $1-\mu$ of the area (or grid cell) is taken to have no precipitation throughout the storm. The fraction μ is assumed to be a constant within each storm, but it can vary from storm to storm.

5.2.3. Derivation of precipitation function along x axis

The one-dimensional statistical-dynamic model requires that the precipitation function $P(x)$ be known. In this section, an appropriate form of $P(x)$ is derived.

Eagleson (1984), Eagleson and Wang (1985), and Eagleson et al. (1987) have reported studies on the fraction μ of a grid area that is affected by precipitation reaching the surface. Warrilow et al. (1986) assumed that over a fraction of a grid cell (or an area), the point precipitation intensity is exponentially distributed (Eq. (5.1)). This exponential distribution assumption for precipitation seems appropriate in some cases as shown by an analysis of hourly observed precipitation data by Abdulla (1987). Abdulla (personal communication 1993) also found that precipitation over a large area in Oklahoma appears to follow the exponential distribution. Using the continental-scale radar data over northwestern Europe, Collier (1993) found that for frontal

precipitation, the exponential relationship (Eq. (5.1)) may not be appropriate. Instead, the log-normal relationship used by Foufoula-Georgiou and Wilson (1990) might be more appropriate. Gao and Sorooshian (1994) investigated ten years of hourly precipitation data over three GCM grid squares covering the southeast, southwest, and north central U.S. each having a size of 8 degrees of latitude by 10 degrees of longitude. They found that the exponential distribution assumption may be questionable and that the statistical patterns of precipitation depend on the locations and the interactions between atmospheric conditions and various land surface characteristics. On the basis of the previous work, two possible forms of the precipitation function P(x) (based on exponential and log-normal distribution) will be considered.

First, following Warrilow et al. (1986), the precipitation intensity is assumed to be described by Eq. (5.1) within μ. The percentage (x) that receives a precipitation rate larger than or equal to precipitation rate P over the fraction μ of a grid cell (or an area) can then be expressed as (see Fig. 5.1a),

$$x = \frac{\text{area that receives precipitation rate} > P}{\text{total area of } \mu} = 1 - F(P)$$

$$= 1 - \int_0^P f(P_i)dP_i = 1 - \int_0^P \frac{\mu}{P_m} \exp(-\frac{\mu P_i}{P_m})dP_i$$

$$= \exp(-\frac{\mu P}{P_m}) \ . \tag{5.19}$$

The inverse of Eq. (5.19) is then,

$$P(x) = -\frac{P_m}{\mu} \ln(x) \ , \qquad\qquad 0 < x \le 1. \tag{5.20}$$

In Eq. (5.20), P(1) = 0, that is, the probability of the area fraction μ that can receive precipitation greater than or equal to zero is one. This result is due to

the form of Eq. (5.1).

For the second case where the log-normal distribution is assumed (which is arguably more appropriate for frontal precipitation), the precipitation intensity function is expressed as (Collier 1993),

$$f(P_i) = \frac{\mu}{P_m} \exp\{ -\frac{\mu}{P_m} [\ln(1 + P_i)]^2 \}$$ (5.21)

where all the symbols have the same meaning as before. By approximating the integral of the probability distribution, Collier (1993) obtained,

$$F(P) = \int_0^P f(P_i)dP_i = 1 - \exp\{ -\frac{\mu}{P_m} [\ln(1 + P)]^2 \}.$$ (5.22)

Thus similarly to Eq. (5.19), the percentage (x) that receives a precipitation rate larger than or equal to precipitation rate P over the fraction μ can then be expressed as,

$$x = \frac{\text{area that receives precipitation rate} > P}{\text{total area of } \mu} = 1 - F(P)$$

$$= \exp\{ -\frac{\mu}{P_m} [\ln(1 + P)]^2 \} .$$ (5.23)

The inverse of Eq. (5.23) is then,

$$P(x) = \exp \{ -[-\frac{P_m}{\mu} \ln(x)]^{\frac{1}{2}} \} - 1, \quad 0 < x \leq 1.$$ (5.24)

Here again Eq. (5.24) yields P(1) = 0.

For the exponential distribution case, by substituting Eq. (5.20) into Eq.

(5.9), we obtain,

$$Q_{\mu d}[N+1] = \mu \cdot \int_0^a \{P(x) - \frac{W_1^c}{\Delta t} + \frac{W_{\mu 1}[N+1]}{\Delta t}\} \, dx +$$

$$\mu \cdot \int_a^1 \{P(x) - \frac{W_1^c}{\Delta t} + \frac{W_{\mu 1}[N+1]}{\Delta t} + \frac{W_1^c}{\Delta t}[1 - \frac{i_0 + P(x) \cdot \Delta t}{i_m}]^{1+b_i}\} dx$$

$$= \mu \cdot \int_0^a \{-\frac{P_m}{\mu} \ln(x) - \frac{W_1^c}{\Delta t} + \frac{W_{\mu 1}[N+1]}{\Delta t}\} \, dx +$$

$$\mu \cdot \int_a^1 \{-\frac{P_m}{\mu} \ln(x) - \frac{W_1^c}{\Delta t} + \frac{W_{\mu 1}[N+1]}{\Delta t} + \frac{W_1^c}{\Delta t}[1 - \frac{i_0 - \frac{P_m}{\mu} \ln(x) \cdot \Delta t}{i_m}]^{1+b_i}\} dx$$

$$= P_m - \mu \left(\frac{W_1^c}{\Delta t} + \frac{W_{\mu 1}[N+1]}{\Delta t}\right) + \mu \cdot \frac{W_1^c}{\Delta t} \int_a^1 [1 - \frac{i_0 - \frac{P_m}{\mu} \ln(x) \cdot \Delta t}{i_m}]^{1+b_i} dx,$$

$$(5.25)$$

The integral in Eq. (5.25), when $0 \le a < 1$, can be computed as,

$$\int_a^1 [1 - \frac{i_0 - \frac{P_m}{\mu} \ln(x) \cdot \Delta t}{i_m}]^{1+b_i} dx = \int_a^1 [\frac{i_m - i_0 + \frac{P_m}{\mu} \ln(x) \cdot \Delta t}{i_m}]^{1+b_i} dx$$

$$= (i_m)^{-(1+b_i)} \cdot \int_{t1}^{i_m - i_0} \frac{\mu}{P_m \cdot \Delta t} \cdot t^{1+b_i} \cdot e^{\frac{\mu}{P_m \cdot \Delta t}(t - i_m + i_0)} dt$$

$$= \frac{\mu}{P_m \cdot \Delta t} \cdot (i_m)^{-(1+b_i)} \cdot e^{-\frac{\mu \cdot (i_m - i_0)}{P_m \cdot \Delta t}} \cdot \int_0^{i_m - i_0} t^{1+b_i} \cdot e^{\frac{\mu \cdot t}{P_m \cdot \Delta t}} \cdot dt \qquad (5.26)$$

where $t = i_m - i_0 + \frac{P_m}{\mu} \ln(x) \cdot \Delta t$, and $t1 = i_m - i_0 + \frac{P_m \cdot \Delta t}{\mu} \ln(a)$. In fact, $t1 = i_m - i_0 + \frac{P_m \cdot \Delta t}{\mu} \ln(a)$ is equal to zero, since a is determined by $i_0 + P(x) \cdot \Delta t = i_m$ if $i_0 + P(1) \cdot \Delta t \le i_m$ (see Section 5.2.1).

An analytical expression can be obtained for the case where b_i is an integer in Eq. (5.26). Otherwise, numerical integration can be used to calculate the integral in Eq. (5.26), or to expand the term $\exp(\frac{\mu}{P_m \cdot \Delta t} t)$ into a power series which converges within $|t| < \infty$:

$$\exp(\frac{\mu \cdot t}{P_m \cdot \Delta t}) = 1 + \frac{\mu \cdot t}{P_m \cdot \Delta t} + \frac{1}{2!} [\frac{\mu \cdot t}{P_m \cdot \Delta t}]^2 + \cdots + \frac{1}{n!} [\frac{\mu \cdot t}{P_m \cdot \Delta t}]^n + \cdots,$$

$$|t| < \infty . \qquad (5.27)$$

For the log-normal distribution case, by substituting Eq. (5.24) into Eq. (5.9), $Q_{\mu d}[N+1]$ can be obtained through numerical integration.

5.2.4. Estimation of fractional coverage of precipitation

As for the fraction μ, Warrilow et al. (1986) noted that μ may be on the order of 0.95 and 0.60 for large-scale and convective rainfall, respectively. Currently the U.K. Meteorological Office (UKMO) sets μ to be 1.0 for large-scale rainfall and 0.3 for convective rainfall in their GCM. The observed spatial variability of total storm depth for air mass thunderstorm rainfall in Arizona (Eagleson et al. 1987) supports a wetted fraction of 0.5 to 0.66. While Warrilow et al. (1986), Entekhabi and Eagleson (1989), Pitman et al. (1990), and Famiglietti and Wood (1991) all used a prescribed fraction μ of a grid cell area, Eltahir and Bras (1993) found significant temporal variability in the fractional coverage of rainfall. They presented a procedure for estimating the fraction μ as,

$$\mu = \frac{P_m}{E(P_\mu)} \qquad (5.28)$$

where $E(P_\mu)$ is the areal mean precipitation over the rain-covered fraction μ of the grid cell. They suggested that P_m can be estimated by

$$P_m = \frac{V}{\Delta X \cdot \Delta X \cdot \Delta T}$$ (5.29)

where V is the volume of rainfall simulated by the climate model within a grid cell area, ΔX, and ΔT are the spatial and temporal resolutions of the model respectively. By invoking the ergodicity assumption, they estimated $E(P_\mu)$ by the mean of the rainfall rate at a point using rainfall records from a single location. Although the volume of rainfall, V, could be taken from a numerical weather prediction model, this can result in large biases; it is probably more realistic to use an average of observed station data instead of Eq. (5.29) to estimate P_m. Based on the observed hourly rainfall data in the southeast of France, Braud et al. (1993) found that the fractional area covered by rainfall exceeding a fixed threshold is highly correlated with the mean areal rainfall rate. Thus, this suggested that μ may also be estimated from the radar rainfall data.

5.3. Testing of the derived distribution approach

As described previously, there are four major assumptions involved in deriving the one-dimensional statistical-dynamical model. In this section, two computer experiments are designed to test these assumptions by applying Eq. (5.20) (i.e., the exponential distribution) to simulate spatially varying precipitation. The first is a "brute force" experiment (Figs. 5.2a and 5.2b) where a grid cell (or an area) is divided into $L \times M$ pixels. In the tests that were performed, there were $L \times M = 2500$ pixels (subgrid elements). At each specific time, the average precipitation depth of an area (or grid cell) defined the mean of the exponential precipitation distribution. Thus, the exponential precipitation distribution over the area at each time was determined. The precipitation rates for the 2500 pixels were taken randomly from the exponential distribution (Eq. (5.20)) and were then assigned to each pixel. In generating the rainfall field, the variable x in Eq. (5.20) was obtained from a uniform random generator. Within each pixel, the precipitation rate was assumed to be the same. The procedure of assigning the precipitation rate to each pixel was repeated at each time when there was rainfall. Using this random method, it is possible for a pixel to have

large value of precipitation in one time period and be followed by a random quantity drawn from the exponential distribution in the next time period. No attempt was made to incorporate the spatial correlation in precipitation amounts. It was assumed that one infiltration capacity distribution characterized the entire area. The infiltration capacity distribution for each pixel was obtained by randomly sampling from the infiltration capacity distribution for the entire area (Fig. 5.2b). These pixel hydrologic properties were kept unchanged during the simulations for a fixed spatial precipitation coverage μ. Since the precipitation rate was assumed to be the same within each pixel, the two-layer VIC model described in Chapter 2 can be applied. By applying the model described in Chapter 2 on a pixel by pixel basis, the direct runoff, evaporation, sensible heat flux, surface temperature and soil moisture were calculated for each pixel and then were aggregated to obtain results for the entire area.

In the second experiment (Fig. 5.2c), the derived distribution approach described in Section 5.2. was conducted to compute the direct runoff, evaporation, sensible heat flux, surface temperature, and soil moisture for the same area as in Experiment 1. In this experiment, the precipitation over the area μ followed an exponential distribution with the same distribution parameters used in Experiment 1.

Finally, the results of the direct runoff, soil moisture content, evaporation, sensible heat flux, and surface temperature from Experiments 1 and 2 were compared with the results obtained by assuming $P(x) = $ constant over the area.

The same forcing data and model parameters as were used in the Chapter 4 sensitivity analysis are used here, except for the vegetation cover parameter (C_V) which is taken as 1.0 for both the grassland and forest sites. Other parameter values are as listed in Table 4.1. Since the model does not represent variations in spatial snow properties, only summer month simulations for the grassland were conducted. At the forest site, snow does not occur, so the simulations were conducted for an entire year. For simplicity, the precipitation fractional coverage parameter μ was constant in each simulation, but three

different values of μ (0.3, 0.6, and 1.0) were investigated. In the following discussion of these experiments, we use "pixel-based", "derived distribution", and "average" to represent Experiment 1 (the "brute force" experiment), experiment 2, and the one with $P(x) = $ constant within the area, respectively. All simulations were conducted at an hourly time step.

At the forest site, the 12-month hourly results for the latent and sensible heat fluxes, surface temperature, soil moisture of the upper zone, and soil moisture for both zones of the three experiments are shown in Figs. 5.3 – 5.14 for $\mu = 0.3$. All experiments started with the same initial soil moisture which was taken as 50% of the maximum soil water content. On the same figure, the hourly area average precipitation time series is also plotted for comparison. Six-month (Feb., Mar., April, Oct., Nov., and Dec.) hourly runoff time series for months with maximum runoff peaks higher than 0.6 mm/hr are shown in Fig. 5.15 for μ=0.3.

In January (Fig. 5.3), many small storms with intensities less than 3.0 mm/hr were present. The evaporation simulated by the derived distribution approach is very close to that simulated by the pixel-based approach, while the average method predicts much larger evaporation. The reason is that the average approach assumes that precipitation is intercepted within the entire area while only 30% of the area has intercepted precipitation in the pixel-based and derived distribution approaches. Therefore, the average approach results in much more interception evaporation than the other two approaches, especially when the precipitation rate is small. Likewise, for the sensible heat flux and surface temperature, the derived distribution approach gives results that are much closer to the pixel-based approach than the average approach. The ratio of the monthly sum of the absolute difference between the average and pixel-based approaches to the monthly sum of the absolute difference between the derived distribution and pixel-based approaches is shown in Table 5.1a for the latent and sensible heat fluxes, and surface temperature. From this summary table, it can be seen that all the ratios are greater than 8, indicating that the difference between the derived distribution approach and the pixel-based approach is much

smaller than that between the average and pixel-based approaches.

From Fig. 5.3, it is also seen that the derived distribution approach better approximates the soil moisture content of the upper zone and also the moisture of the upper and lower zones combined than the average approach. The monthly maximum relative errors of the upper zone moisture content are 6.8% and 7.7% for the derived distribution and average approaches respectively, and 0.4% and 1.3% for the combined upper and lower zone moisture content for the derived distribution and average approaches respectively (Table 5.3a).

In January, the largest runoff peak is small (0.04 mm/hr) due to the small precipitation rate and the low soil moisture content. In Table 5.2a, a summary ratio for runoff is calculated in the same way as for the latent and sensible heat fluxes, and surface temperature shown in Table 5.1. For months with the maximum daily runoff rate less than 1.0 mm/day, the ratio is uninformative and is not calculated. In Table 5.2a, the monthly maximum hourly peak runoff is shown for the pixel-based, derived distribution, and average approaches as well.

In February (Fig. 5.4), there were not as many storms as in January, but their magnitudes were larger. Even though the evaporation from the average approach is still larger than the pixel-based and derived distribution approaches, the difference is not as large as in January due to smaller interception. The sensible heat flux and surface temperature also varied less among the three approaches than in January. However, the total runoff from the average approach was significantly undersimulated compared with the pixel-based one (Fig. 5.15). During the two big storms at the end of the month, the average soil moisture over the grid area is higher in the average approach, but the overall saturated area is smaller than in the pixel-based and derived distribution approaches, and thus the average approach generates much less direct runoff. The derived distribution approach produced simulations of runoff (Fig. 5.15), evaporation, sensible heat, surface temperature, and soil moisture (Fig. 5.4) that matched the pixel-based results quite closely. The ratios for runoff, latent and sensible heat fluxes, and surface temperature are 7.35 (Table 5.2a), 1.59,

1.88, and 1.56 respectively (Table 5.1a). The monthly maximum relative errors of the upper zone moisture content are 7.3% and 19.1% for the derived distribution and average approaches respectively, and 0.8% and 4.5% for the combined upper and lower zone moisture content for the derived distribution and average approaches respectively (Table 5.3a).

The simulated results for March (Fig. 5.5) are quite similar to the results for February. At the beginning of the month, both the pixel-based and derived distribution approaches predict much larger runoff (Fig. 5.15) than in January even though the storm magnitudes were similar to those for January. This is because of the wet soil from the large storms at the end of February. The average approach again gives much smaller runoff in this case. In comparison, the storm with peak rate more than 3 mm/hr occurring on the 19th of the month results in very small runoff in all the three approaches (only about one fifth of the runoff that occurred at the beginning of the month) due to the loss of soil moisture by evaporation during the period. The ratios for runoff, latent and sensible heat fluxes, and surface temperature are 2.41 (Table 5.2a), 1.72, 1.69, and 1.47 respectively (Table 5.1a). The monthly maximum relative errors of the upper zone moisture content are 8.0% and 14.0% for the derived distribution and average approaches respectively, and 0.7% and 4.9% for the combined upper and lower zone moisture content for the derived distribution and average approaches respectively (Table 5.3a).

In April, storms were smaller than in February, but larger than in January and March. Again, the derived distribution approach approximates the runoff (Fig. 5.15), surface fluxes, and soil moisture (Fig. 5.6) much better than the average approach. The ratios for the latent and sensible heat fluxes, and surface temperature are all greater than 2.0 (Table 5.1a), and greater than 4.0 for runoff (Table 5.2a). Although the evaporation simulated by the average approach is always larger than those from the pixel-based and derived distribution approaches, the much smaller runoff from the average approach results in higher soil moisture than for the other two approaches. The monthly maximum relative error of the upper zone moisture content is greater than 20%

for the average approach, but less than 10% for the derived distribution approach (Table 5.3a). For the combined moisture content, the monthly maximum relative errors are 0.7% and 6.2% for the derived distribution and average approaches respectively (Table 5.3a).

May, June, July, and August (Figs. 5.7–5.10) is the dry period. There is little runoff during these months, and the largest monthly runoff peak is less than 0.5 mm/day, except in June where it is 4.32 mm/day. During this period, the average approach continues to simulate larger evaporation due to more moisture, except for August. The soil moisture content for the average approach decreases and approaches the soil moisture from the pixel-based approach. During this time, the derived distribution approach still gives better approximations than the average approach with all the ratios for the latent and sensible heat fluxes, and surface temperature greater than 1.0 (Table 5.1a), except for August. For soil moisture, the comparison (Table 5.3a) shows that the derived distribution approach results in smaller monthly maximum relative errors than the average approach for both the upper layer and combined layers, except for the upper layer soil moisture in June and July, and the combined soil moisture in August, where the average approach gives slightly smaller relative errors.

In August (Fig. 5.10), there is almost no precipitation and the soil is quite dry. The soil moisture from the derived distribution approach is closer to the pixel-based approach than the average approach. The evaporation from the average approach is overestimated during the first half of the month, and also during the three very small precipitation events due to larger interception. The evaporation from the derived distribution approach is also overestimated in this month.

The reason that the derived distribution approach overpredicts the latent heat flux might be attributable to the way of calculating the soil moisture stress factor $g_{sm}[n]$ (Eq. 2.14). In the pixel-based approach, the subgrid spatial variability of soil moisture is included in the calculation of the soil moisture stress factor $g_{sm}[n]$, but it is not in the derived distribution and average

approaches. When the soil is dry, the pixel-based approach may result in a number of large $g_{sm}[n]$'s over a large portion of the area due to, for example, less soil moisture than the wilting point or critical point, while the derived distribution and average approaches give only one smaller lumped $g_{sm}[n]$ value. Therefore, both the derived distribution and average approaches predict larger evaporation than the pixel-based approach. This subgrid spatial effect would be more significant when the soil is drier since for example, the $g_{sm}[n]$ would be the same (i.e., 1.0) for the pixel-based, derived distribution, and average approaches if the entire area is saturated.

Although both the derived distribution and average approaches use the same lumped expression for $g_{sm}[n]$, the average approach simulates smaller evaporation than the derived distribution approach during this month (Fig. 5.10). This is because the upper zone soil moisture is drier in the average approach than in the derived distribution approach. Thus, the average approach can result in a larger soil moisture stress factor $g_{sm}[n]$ than the derived distribution approach and so simulates smaller evaporation. Therefore, the average approach simulates evaporation better than the derived distribution approach but for the wrong reasons.

From September to December (Figs. 5.11 – 5.14), the soil becomes wet again as a result of more storms, some of which are large. Therefore, the effect of subgrid spatial variability on $g_{sm}[n]$ is reduced among the three approaches. The evaporation from the average approach is oversimulated during most of these months and the runoff (Fig. 5.15) is significantly undersimulated for the large precipitation events compared with the pixel-based results. The derived distribution approach, however, gives much better approximations. All the ratios for the latent and sensible heat fluxes, and surface temperature are greater than 1.0 (Table 5.1a) during these months, and the ratio for runoff is as high as 5.68 in October (Table 5.2a). The monthly maximum relative error for the upper zone soil moisture is about 10% or less for the derived distribution approach, but about 20% in some months for the average approach (Table 5.3a). Similarly, the derived distribution approach results in monthly maximum

relative errors for combined soil moisture smaller than the average approach, except for September.

For the case $\mu=0.6$, similar results are obtained as for $\mu=0.3$, except that the underestimation of runoff and overestimation of evaporation by the average approach decreases for the larger μ value. The ratios for the latent and sensible heat fluxes, and surface temperature are greater than 1.0 for 9 out of 12 months, and are all above 0.9 for March (Table 5.1b). The ratios for runoff are greater than 1.0 except for March and November (Table 5.2b). The monthly maximum relative errors for the upper zone soil moisture are about 10% or less for the derived distribution approach, while they are as high as 21.3% for the average approach (Table 5.3b). The monthly maximum relative errors for the combined soil moisture are small for both approaches; the largest relative errors over the year are 2.5% and 3.2% for the derived distribution and average approaches respectively.

At the grassland site, which has a drier climate than the forest site, simulations for $\mu=0.3$, 0.6, and 1.0 were conducted for the summer months (May – September), with the initial soil moisture equal to the maximum soil moisture content for $\mu=0.6$, and half of the maximum soil moisture content in the other two cases.

For $\mu=0.3$, Figs. 5.16 and 5.17 show that May and June receive less precipitation than the remaining three months, and the maximum hourly runoff is 0.01 mm/hr and 0.03 mm/hr for May and June, respectively (Table 5.5a). The average approach oversimulates evaporation during the precipitation event due to large interception. The derived distribution approach produces much better approximations for evaporation, sensible heat flux and surface temperature. The ratios for the latent and sensible heat fluxes, and surface temperature are all greater than 3.0, and are as high as 10.53 (Table 5.4a). The derived distribution approach also results in smaller monthly maximum relative errors for the upper zone and combined soil moisture (Table 5.6a).

Evaporation is significantly overestimated by the average approach in July and August (Figs. 5.18 and 5.19) during the storm period, and thus the

sensible heat flux and surface temperature are underestimated; while the derived distribution approach yields the evaporation, sensible heat, and surface temperature similar to the pixel-based approach, with ratios greater than 5.0 (Table 5.4a). Although the simulated runoff is small during this period with a maximum rate of 0.09 mm/hr and 0.22 mm/hr for July and August respectively (Table 5.5a), both the derived distribution and average approaches give larger runoff than the estimates from the pixel-based approach. This is because both the derived distribution and average approaches always have some saturated area when the soil moisture in the upper zone is greater than zero according to the variable infiltration capacity formulation for the upper layer. Therefore, when there is some small rainfall, the precipitation that falls onto the saturated area will generate runoff in both cases. For the pixel-based approach, however, it is not necessary that such a saturated area always exists, and thus there is no runoff from light precipitation unless the antecedent soil moisture is saturated. When the precipitation rate is moderate or large, the effect of the perpetually saturated area in the derived distribution and average approaches becomes negligible. The derived distribution approach again results in smaller monthly maximum relative errors for the upper zone and combined soil moisture (Table 5.6a). Figure 5.20 shows the results for September in which the derived distribution approach again produces better simulations than the average approach (Tables 5.4a-5.6a).

For the case $\mu=1.0$, similar comparison results are obtained for the three approaches as for the $\mu=0.3$ case, except that underestimation of runoff and overestimation of evaporation by the average approach decreases as μ increases, as was the case for the forest site. The ratios for the latent and sensible heat fluxes, surface temperature, and runoff of the five m. nths (May – September) are all greater than 1.0, except for June where the ratio of latent heat flux is 0.97 (Tables 5.4b and 5.5b). Although for most months, the monthly maximum relative errors for the upper zone and combined soil moisture are slightly greater for the derived distribution approach than for the average approach, all the values of the relative errors are small, with the largest less than 3% (Table 5.6b).

To investigate the effect of initial soil moisture on the surface fluxes and runoff for the drier climate, a comparison of the three approaches with initial soil moisture set to the maximum for $\mu=0.6$ was made. Comparisons (Tables 5.4 – 5.6) show that the results are similar except that the runoff from the pixel-based approach is smoother than from the other two approaches in the $\mu=0.6$ case (plots not included). This is because more water goes into lower zone and comes out as subsurface runoff in the pixel-based approach. Tables 5.4c and 5.5c show that all the ratios for the latent and sensible heat fluxes, surface temperature, and runoff are greater than 1.0, except for the ratio of runoff in June which is 0.95. Also, the average approach shows larger relative errors for the soil moisture in general (Table 5.6c).

Tables 5.7 and 5.8 show the annual average latent and sensible heat fluxes at the forest site and the five-month average latent and sensible heat fluxes at the grassland site, respectively, for the three approaches. For all of the cases with $\mu=0.3$ and 0.6 at the forest site, and $\mu=0.3$, 0.6, and 1.0 at the grassland site, the derived distribution approach gives better approximations to the pixel-based approach than the average approach. At the forest site, the average approach gives about 20 Wm^{-2} bias for the latent and sensible heat fluxes, and the derived distribution approach gives about 5 Wm^{-2} bias. At the grassland site, the average approach gives about 20 Wm^{-2} bias for the latent heat flux and over 35 Wm^{-2} bias for the sensible heat flux for $\mu=0.3$. The derived distribution approach, however, gives less than 5 Wm^{-2} difference for both latent and sensible heat fluxes for $\mu=0.3$.

Although the experiments conducted here use hypothetical forcing data with specified initial soil moisture, the differences for the surface fluxes, surface temperature, runoff, and soil moisture between the average and pixel-based approaches indicate that the effect of spatial subgrid scale variability in precipitation can be significant. Comparison of the three approaches shows that the derived distribution approach approximates the pixel-based method reasonably well in terms of surface fluxes, surface temperature, runoff, and soil moisture.

5.4. Summary of the derived distribution approach

This chapter has described a one-dimensional statistical-dynamic model with a derived distribution approach that accounts for the effect of subgrid spatial variability of rainfall. The approach was tested against a pixel-based approach, and an approach which applied spatial average precipitation uniformly over the area. The comparison of the three approaches for the PILPS forest and grassland sites shows that:

(1). The derived distribution approach approximates the pixel-based approach much better than the average approach in the simulations of surface fluxes, surface temperature, runoff, and soil moisture;

(2). The effect of the spatial subgrid scale variability in precipitation is significant. The inclusion of the spatial variation of precipitation results in less evaporation, especially for small storms, due to less interception of rainfall, and more runoff, especially for moderate and large storms, due to a larger portion of saturated area. The soil moisture is lower in general when the spatial variation in precipitation is considered for moderate or large storms because more runoff occurs, while the soil moisture is higher for small storms due to less evaporation.

(3). The ratios of the monthly sum of the absolute difference between the average and pixel-based approaches to the monthly sum of the absolute difference between the derived distribution and pixel-based approaches for the latent and sensible heat fluxes, surface temperature, and runoff are greater than 1.0 for most cases. The monthly maximum relative errors for the upper zone soil moisture and for the combined soil moisture are smaller for the derived distribution approach than for the average approach for most cases.

(4). Comparisons with the pixel-based approach show that the annual average and five-month average latent and sensible heat fluxes at the forest and grassland

sites for the average approach have biases of about 20 Wm^{-2}, while the derived distribution approach has biases of about 5 Wm^{-2}. The average approach resulted in over 35 Wm^{-2} bias in the sensible heat flux for $\mu=0.3$ at the grassland site.

(5). The four assumptions described in Section 5.2 incorporated in the derived distribution approach seem justifiable based on the test results. Although the third assumption, which averages the soil moisture over the fractional coverage μ and the non-rainfall fractional coverage $1-\mu$, may seem questionable, the results suggest that it is defensible. Under a number of common situations, this assumption may not be critical. One is for the case of many small storms. In this case most of the rainfall is intercepted by the vegetation canopy. Thus, the soil moisture over the fractional coverage μ would remain close to that over the non-rainfall fractional coverage $1-\mu$. The second case is when several large storms occur, with most of the area covered by at least one storm. In this case, the soil moisture will be close to saturation everywhere. The third case is where the soils are relatively well drained, which will tend to minimize spatial differences in soil moisture.

Since the derived distribution approach is conceptually simple and has a closed form, it is computationally tractable. It appears to be a practical way of representing subgrid scale precipitation variation in a GCM land surface parameterization.

Table 5.1. Comparison of surface fluxes and temperature between the derived distribution and average approaches for the PILPS forest site

5.1a.

$(\mu=0.3,\ W_{initial}=0.5W^c)$

	Jan	Feb	Mar	Apr	May	Jun	Jul	Aug	Sep	Oct	Nov	Dec
R_E	9.26	1.89	1.72	2.67	2.91	1.60	1.61	0.85	3.86	2.84	1.32	1.88
R_H	9.17	1.88	1.69	2.72	2.97	1.60	1.64	0.83	3.95	2.91	1.31	1.97
R_{T_s}	8.93	1.56	1.47	2.31	2.82	1.50	1.79	0.82	3.86	2.72	1.17	1.79

5.1b.

$(\mu=0.6,\ W_{initial}=0.5W^c)$

	Jan	Feb	Mar	Apr	May	Jun	Jul	Aug	Sep	Oct	Nov	Dec
R_E	3.82	0.84	0.99	1.69	2.49	1.52	1.89	0.65	3.21	1.86	1.86	1.30
R_H	3.60	0.83	0.99	1.72	2.53	1.53	1.95	0.62	3.22	1.88	1.85	1.25
R_{T_s}	3.06	0.73	0.90	1.46	2.42	1.56	2.12	0.54	2.41	1.94	1.71	0.93

Note: $a = \sum |$ hourly quantity from average approach $-$ hourly quantity from pixel-based approach $|$,
$b = \sum |$ hourly quantity from derived dist. appro. $-$ hourly quantity from pixel-based appro. $|$,
where hourly quantity can be evaporation (E), sensible heat flux (H), or surface temperature
(T_s), and $R_E = \frac{a}{b}$, $R_H = \frac{a}{b}$, $R_{T_s} = \frac{a}{b}$.
$W_{initial}$ and W^c represent the initial and maximum soil moisture of combined upper and lower
layers respectively.

Table 5.2.   Comparison of runoff at the PILPS forest site

5.2a.

$(\mu=0.3, W_{initial}=0.5W^c)$

	Jan	Feb	Mar	Apr	May	Jun	Jul	Aug	Sep	Oct	Nov	Dec.
R_Q	–	7.35	2.41	4.44	–	0.75	–	–	0.81	5.68	1.38	2.50
$Q_m(P)$	0.04	9.81	0.99	5.45	0.02	0.18	0.02	0.004	0.59	10.85	1.08	2.55
$Q_m(D)$	0.09	9.83	1.02	5.45	0.09	0.16	0.10	0.02	0.16	11.41	1.23	3.08
$Q_m(A)$	0.07	6.50	0.19	0.51	0.08	0.13	0.07	0.02	0.12	6.35	0.17	0.34

5.2b.

$(\mu=0.6, W_{initial}=0.5W^c)$

	Jan	Feb	Mar	Apr	May	Jun	Jul	Aug	Sep	Oct	Nov	Dec
R_Q	–	4.59	0.77	1.70	–	–	–	–	–	3.41	0.78	1.10
$Q_m(P)$	0.01	8.06	0.13	2.94	0.01	0.02	0.01	0.004	0.03	8.85	0.07	1.41
$Q_m(D)$	0.08	8.43	0.25	2.11	0.09	0.15	0.09	0.02	0.14	9.81	0.22	1.33
$Q_m(A)$	0.07	6.50	0.19	0.51	0.08	0.13	0.07	0.02	0.12	6.35	0.17	0.34

Note: $a = \sum |$ hourly quantity from average approach – hourly quantity from pixel-based approach $|$,
$b = \sum |$ hourly quantity from derived dist. appro. – hourly quantity from pixel-based appro. $|$,
where hourly quantity is the total runoff Q, and $R_Q = \frac{a}{b}$.
$Q_m(P)$, $Q_m(D)$, and $Q_m(A)$ represent monthly maximum hourly runoff (mm/hr) from the pixel-based, derived distribution, and average approaches respectively.

Table 5.3. Comparison of soil moisture at the PILPS forest site

5.3a. $(\mu=0.3, W_{initial}=0.5W^c)$

	Jan	Feb	Mar	Apr	May	Jun	Jul	Aug	Sep	Oct	Nov	Dec
W_{1d}^{err}(%)	6.8	7.3	8.0	9.1	10.4	9.8	9.0	3.7	8.6	10.0	8.8	8.8
W_{1a}^{err}(%)	7.7	19.1	14.0	23.5	12.9	9.3	8.1	6.6	9.1	23.7	11.5	19.5
W_d^{err}(%)	0.4	0.8	0.7	0.7	0.8	1.3	2.3	3.2	3.3	3.8	3.9	3.9
W_a^{err}(%)	1.3	4.5	4.9	6.2	5.9	5.3	4.5	3.0	2.5	6.5	6.4	7.0

5.3b. $(\mu=0.6, W_{initial}=0.5W^c)$

	Jan	Feb	Mar	Apr	May	Jun	Jul	Aug	Sep	Oct	Nov	Dec
W_{1d}^{err}(%)	3.9	7.9	6.8	10.7	10.1	9.8	7.9	5.2	9.6	12.7	11.4	12.0
W_{1a}^{err}(%)	4.0	13.3	9.1	15.2	9.7	7.1	3.8	4.3	6.2	21.3	11.3	17.0
W_d^{err}(%)	0.2	0.4	0.5	0.5	0.4	0.7	1.1	1.8	2.0	2.3	2.5	2.5
W_a^{err}(%)	0.7	2.0	1.9	1.9	1.6	1.1	0.6	0.4	1.1	1.8	1.5	3.2

Note: W_{1d}^{err} = monthly maximum relative error obtained by $\dfrac{|W_1^d - W_1^{pixel}|}{W_1^{pixel}} \times 100\%$,

where W_1^d and W_1^{pixel} represent hourly soil moisture of layer 1 for the derived distribution

and pixel-based approaches respectively.

W_{1a}^{err} = monthly maximum relative error obtained by $\dfrac{|W_1^{avg} - W_1^{pixel}|}{W_1^{pixel}} \times 100\%$,

where W_1^{avg} represents hourly soil moisture of layer 1 from the average approach.

W_d^{err} and W_a^{err} represent the monthly maximum relative error of soil moisture of combined

upper and lower layers for the derived distribution and average approaches respectively.

Table 5.4. Comparison of surface fluxes and temperature between the derived distribution and average approaches for the PILPS grassland site

5.4a. ($\mu = 0.3$, $W_{initial}$=0.5W^c)

	May	Jun	Jul	Aug	Sep
R_E	3.48	8.55	5.62	6.80	5.21
R_H	7.35	8.40	8.55	12.35	13.70
R_{T_s}	9.01	10.53	10.31	15.15	13.33

5.4b. ($\mu = 1.0$, $W_{initial}$=0.5W^c)

	May	Jun	Jul	Aug	Sep
R_E	1.24	0.97	1.00	1.62	1.39
R_H	5.35	4.02	2.26	4.31	4.35
R_{T_s}	5.75	5.00	2.78	5.08	5.68

5.4c. (μ=0.6, $W_{initial}$=W^c)

	May	Jun	Jul	Aug	Sep
R_E	2.25	3.72	3.41	2.82	1.97
R_H	7.19	8.00	6.80	6.67	7.52
R_{T_s}	8.13	8.93	7.69	6.76	8.62

Note: $a = \sum |$ hourly quantity from average approach – hourly quantity from pixel-based approach $|$,
$b = \sum |$ hourly quantity from derived dist. appro. – hourly quantity from pixel-based appro. $|$,
where hourly quantity can be evaporation (E), sensible heat flux (H), or surface temperature (T_s), and $R_E = \frac{a}{b}$, $R_H = \frac{a}{b}$, $R_{T_s} = \frac{a}{b}$.
$W_{initial}$ and W^c represent the initial and maximum soil moisture of combined upper and lower layers respectively.

Table 5.5.   Comparison of runoff at the PILPS grassland site

5.5a. $(\mu = 0.3,\ W_{initial}=0.5W^c)$

	May	Jun	Jul	Aug	Sep
R_Q	–	–	0.47	0.72	0.79
$Q_m(P)$	0.01	0.03	0.09	0.22	1.02
$Q_m(D)$	0.08	0.14	0.33	0.60	0.88
$Q_m(A)$	0.08	0.12	0.23	0.38	0.64

5.5b. $(\mu = 1.0,\ W_{initial}=0.5W^c)$

	May	Jun	Jul	Aug	Sep
R_Q	–	–	–	–	1.00
$Q_m(P)$	0.01	0.01	0.02	0.02	0.07
$Q_m(D)$	0.08	0.12	0.24	0.39	0.65
$Q_m(A)$	0.08	0.12	0.23	0.38	0.64

5.5c. $(\mu=0.6,\ W_{initial}=W^c)$

	May	Jun	Jul	Aug	Sep
R_Q	1.08	0.95	1.01	1.20	1.19
$Q_m(P)$	16.2	0.07	0.13	0.69	0.65
$Q_m(D)$	16.2	0.18	0.31	0.85	1.00
$Q_m(A)$	16.2	0.17	0.28	0.76	0.95

Note: $a = \sum$ | hourly quantity from average approach – hourly quantity from pixel-based approach |,
$b = \sum$ | hourly quantity from derived dist. appro. – hourly quantity from pixel-based appro. |,
where hourly quantity is the total runoff Q, and $R_Q = \dfrac{a}{b}$.
$Q_m(P)$, $Q_m(D)$, and $Q_m(A)$ represent monthly maximum hourly runoff (mm/hr) from the
pixel-based, derived distribution, and average approaches respectively.

Table 5.6. Comparison of soil moisture at the PILPS grassland site

5.6a. ($\mu = 0.3$, $W_{initial}=0.5W^c$)

	May	Jun	Jul	Aug	Sep
W^{err}_{1d}(%)	0.6	1.3	6.5	19.5	7.6
W^{err}_{1a}(%)	2.0	5.1	7.2	23.0	13.1
W^{err}_{d}(%)	0.1	0.2	1.3	3.3	3.7
W^{err}_{a}(%)	0.2	0.6	2.8	5.0	5.5

5.6b. ($\mu = 1.0$, $W_{initial}=0.5W^c$)

	May	Jun	Jul	Aug	Sep
W^{err}_{1d}(%)	0.7	1.5	2.2	2.1	1.5
W^{err}_{1a}(%)	0.3	0.9	1.8	1.8	1.3
W^{err}_{d}(%)	0.1	0.2	0.6	2.3	2.8
W^{err}_{a}(%)	0.1	0.1	0.6	2.0	2.4

5.6c. ($\mu=0.6$, $W_{initial}=W^c$)

	May	Jun	Jul	Aug	Sep
W^{err}_{1d}(%)	0.6	1.6	5.8	13.1	10.5
W^{err}_{1a}(%)	0.5	1.9	6.2	13.5	12.1
W^{err}_{d}(%)	0.1	0.1	0.3	1.2	1.2
W^{err}_{a}(%)	0.1	0.2	0.4	1.2	1.3

Note: W^{err}_{1d} = monthly maximum relative error obtained by $\dfrac{|W^{d}_{1} - W^{pixel}_{1}|}{W^{pixel}_{1}} \times 100\%$,

where W^{d}_{1} and W^{pixel}_{1} represent hourly soil moisture of layer 1 for the derived distribution and pixel-based approaches respectively.

W^{err}_{1a} = monthly maximum relative error obtained by $\dfrac{|W^{avg}_{1} - W^{pixel}_{1}|}{W^{pixel}_{1}} \times 100\%$,

where W^{avg}_{1} represents hourly soil moisture of layer 1 from the average approach.

W^{err}_{d} and W^{err}_{a} represent the monthly maximum relative error of soil moisture of combined upper and lower layers for the derived distribution and average approaches respectively.

Table 5.7. Comparison of annual average latent and sensible
heat fluxes at the PILPS forest site

	$\mu=0.3$		$\mu=0.6$	
	latent (Wm^{-2})	sensible (Wm^{-2})	latent (Wm^{-2})	sensible (Wm^{-2})
pixel-based	66.5	64.5	73.7	57.8
derived dist.	72.0	59.3	76.9	54.7
average	87.7	44.5	87.7	44.5

Table 5.8. Comparison of five-month average latent and sensible
heat fluxes at the PILPS grassland site

	$\mu=0.3$		$\mu=0.6$		$\mu=1.0$	
	latent (Wm^{-2})	sensible (Wm^{-2})	latent (Wm^{-2})	sensible (Wm^{-2})	latent (Wm^{-2})	sensible (Wm^{-2})
pixel-based	50.8	40.2	73.3	20.5	72.6	21.2
derived dist.	53.4	39.7	77.7	18.5	73.9	21.8
average	71.5	2.0	83.9	-8.6	71.5	2.0
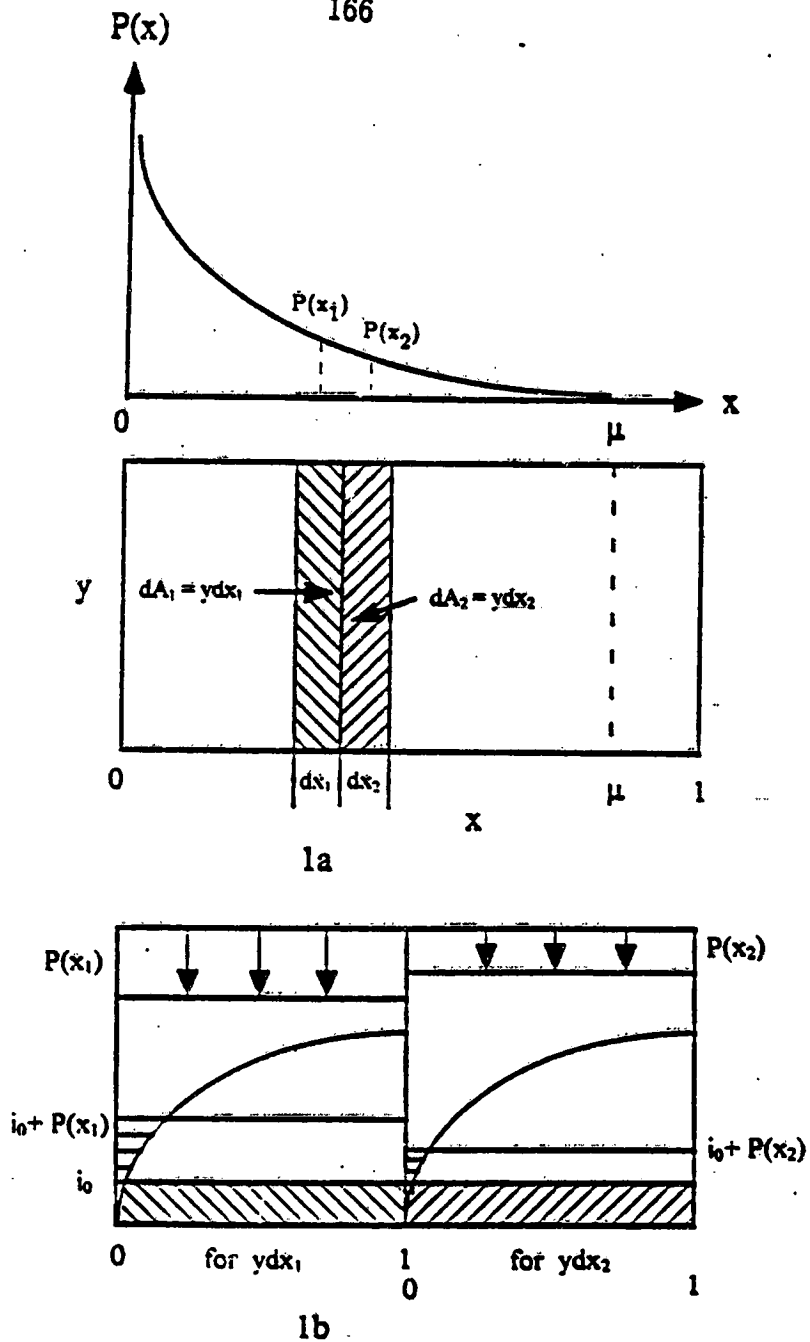
Fig. 5.1   Schematic representation of the derived distribution approach to represent spatial variability of rainfall for two-layer VIC model: (a) exponential precipitation distribution in x direction, and plan view of a grid cell (or area) with strips of ydx_1 and ydx_2, (b) two-layer VIC representation for the strips ydx_1 and ydx_2.
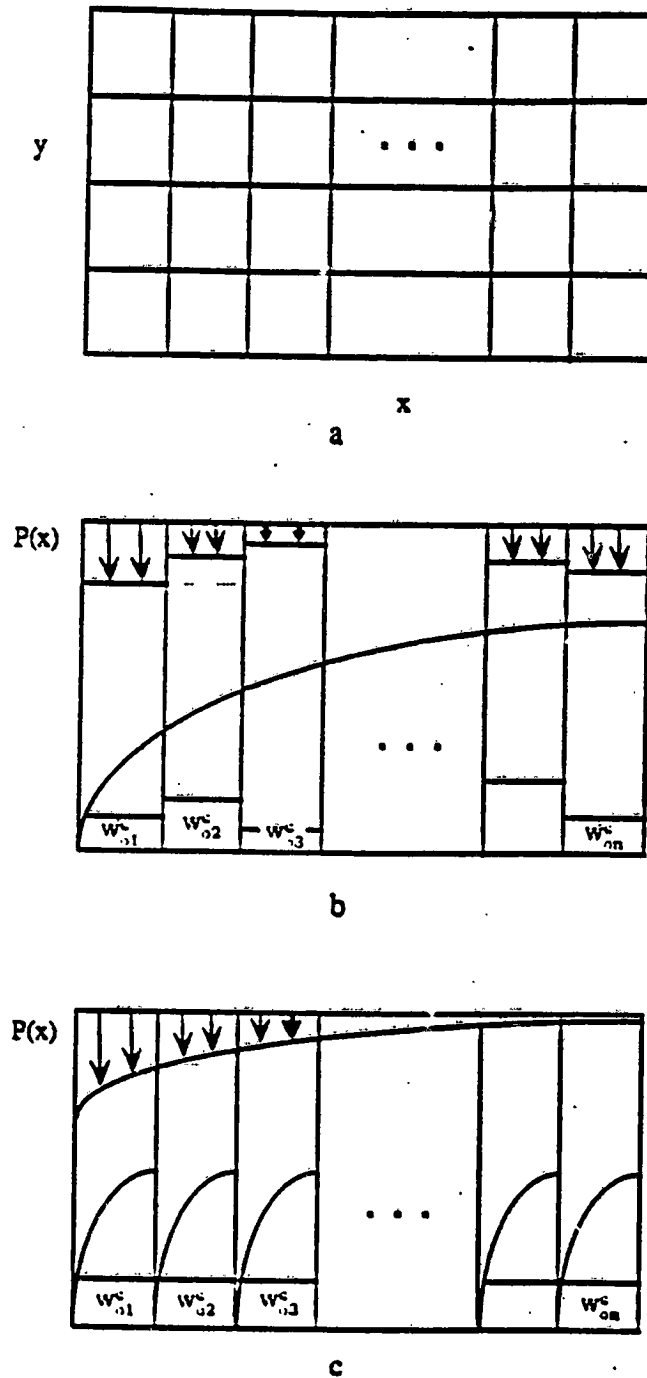
Fig. 5.2 Schematic representation of experiments 1 (5.2a and 5.2b) and 2
(5.2c): (a) 2500 pixels for a grid cell, (b) VIC-2L representation for
each pixel, and (c) the derived distribution approach of the VIC-2L
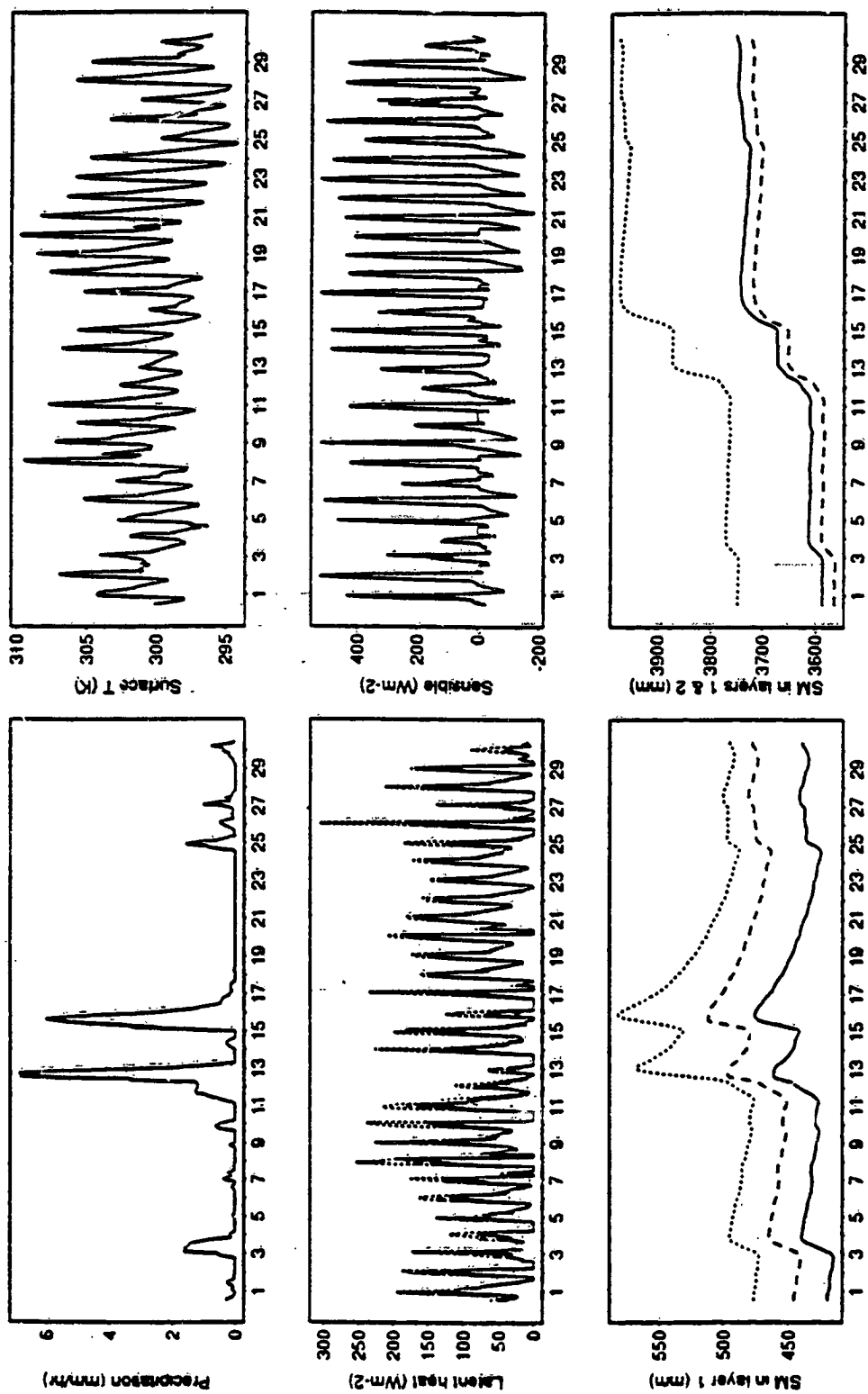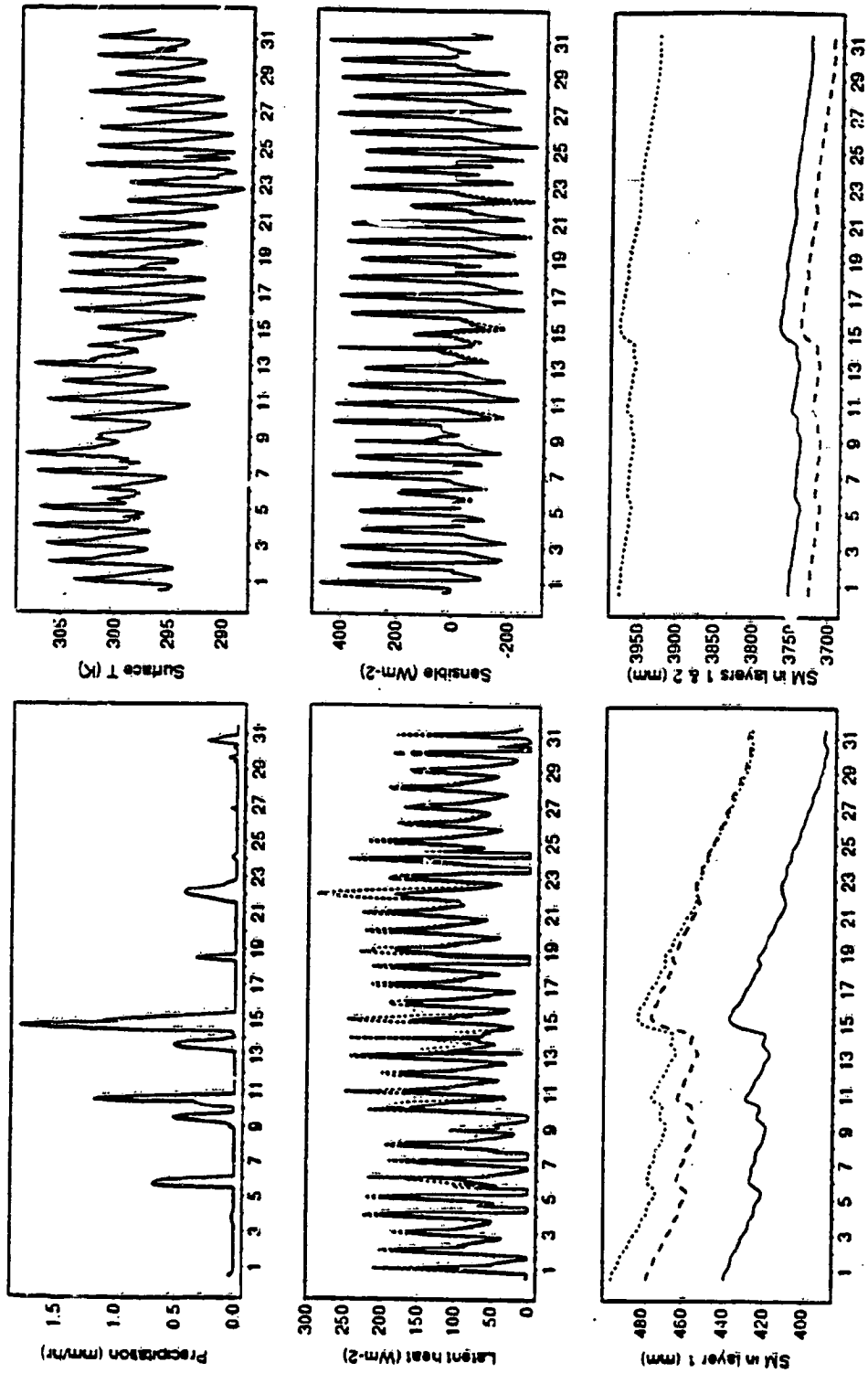representation for the area that receives the rainfall.
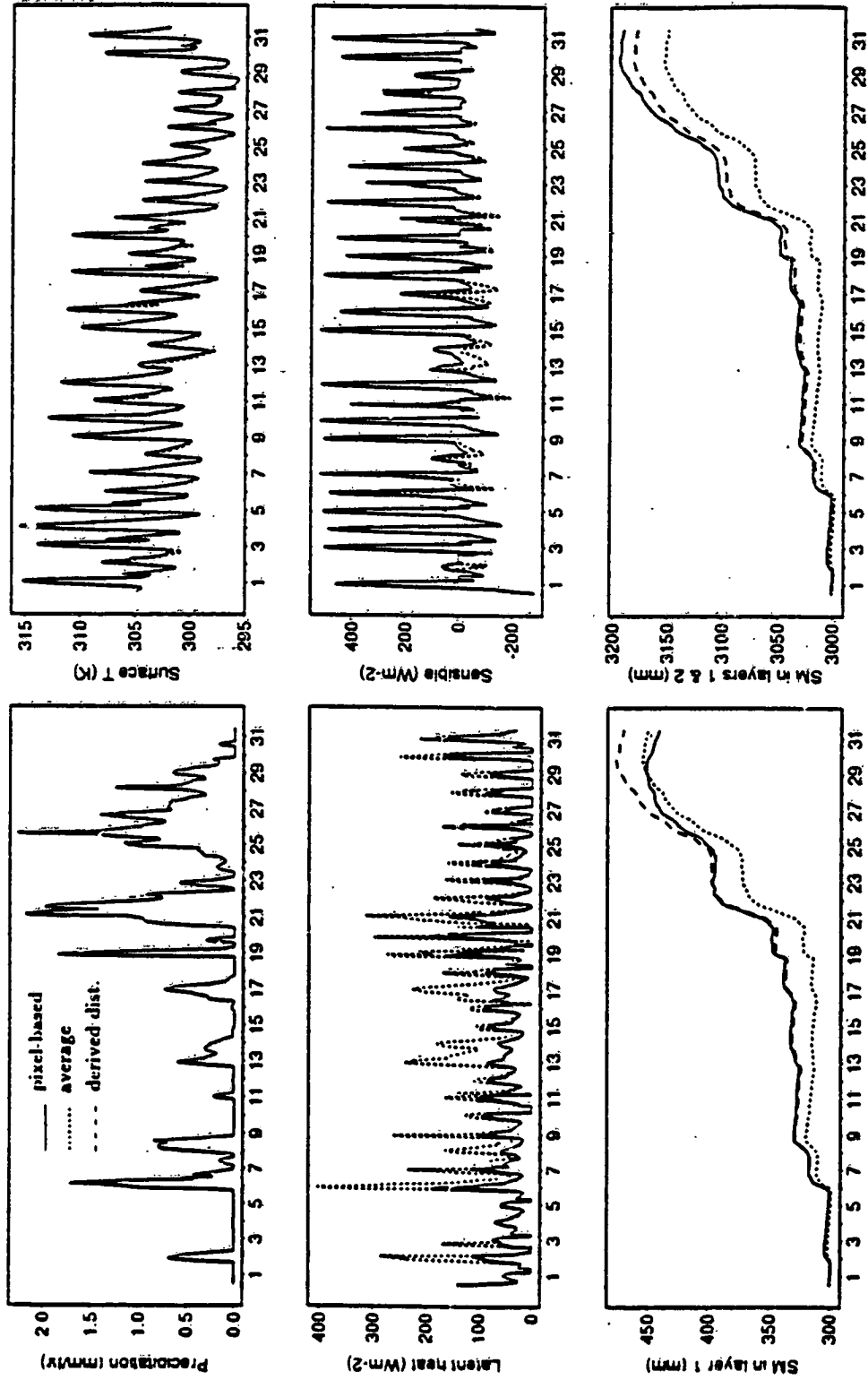
Fig. 5.3 Comparison of effective surface fluxes, temperature, and soil moisture among pixel-based (solid), derived distribution (dashed) and average (dotted) approaches for January with μ=0.3 for PILPS forest site.
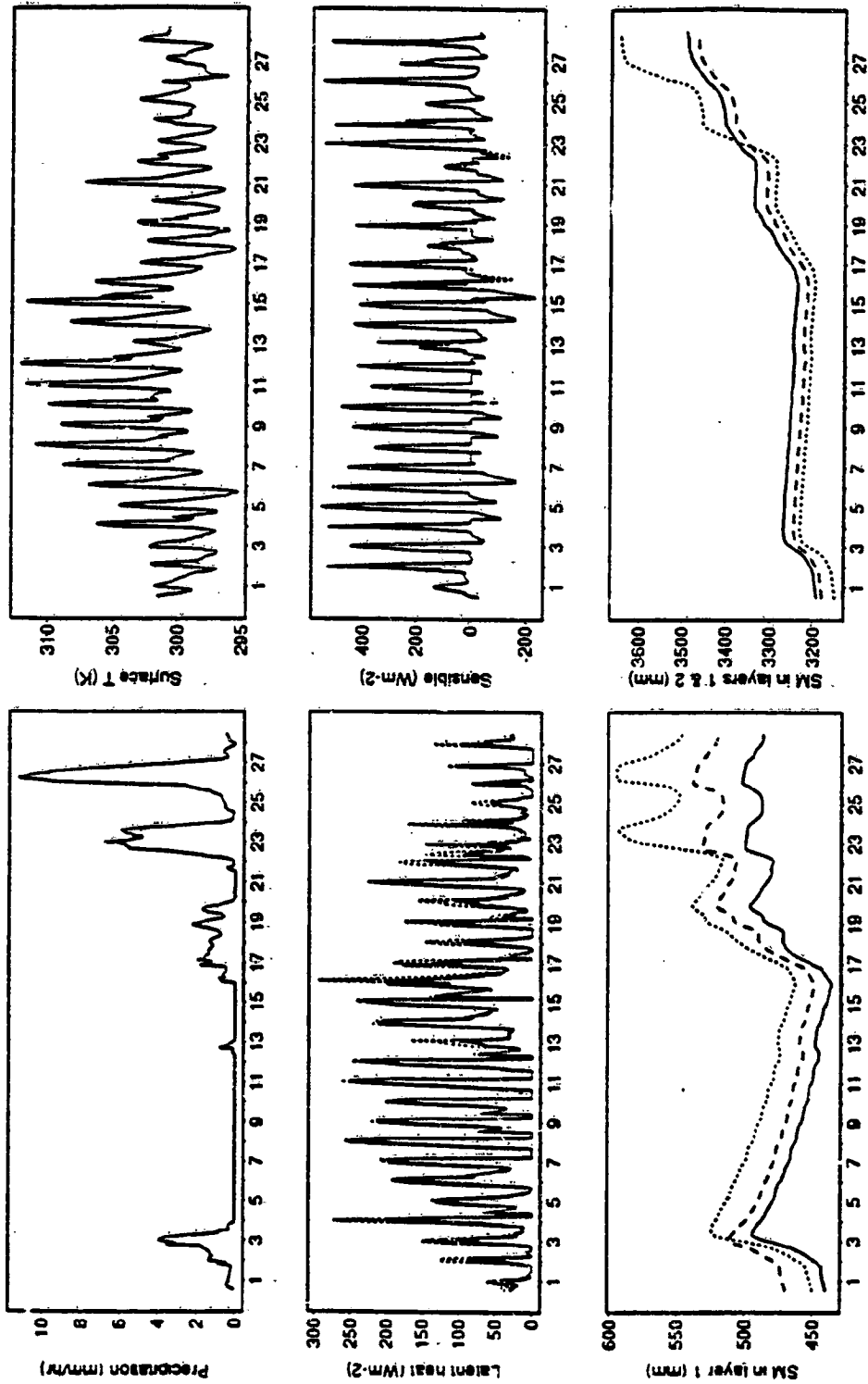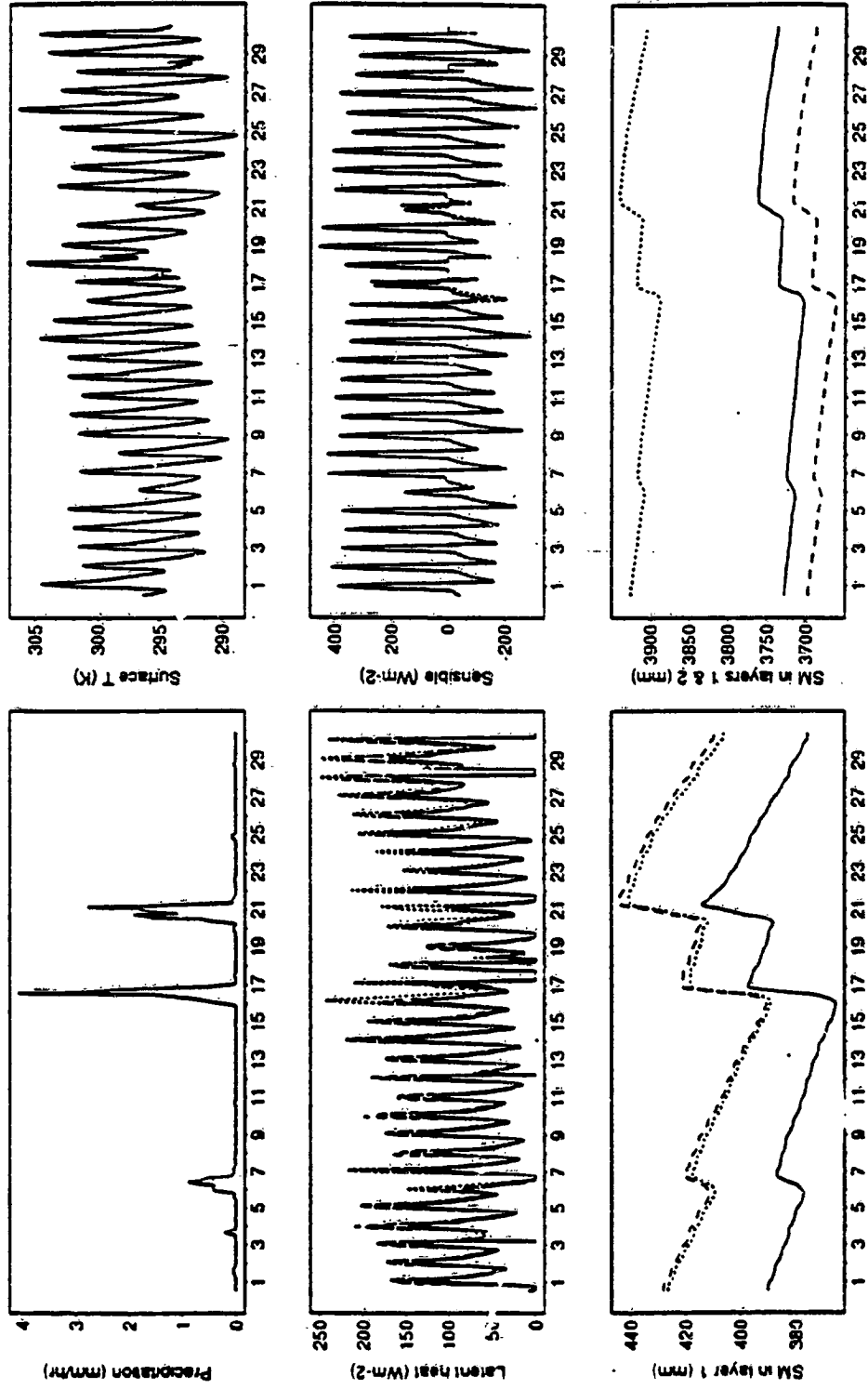
Fig. 5.4 Comparison of effective surface fluxes, temperature, and soil moisture among pixel-based (solid), derived distribution (dashed) and average (dotted) approaches for February with $\mu=0.3$ for PILPS forest site.
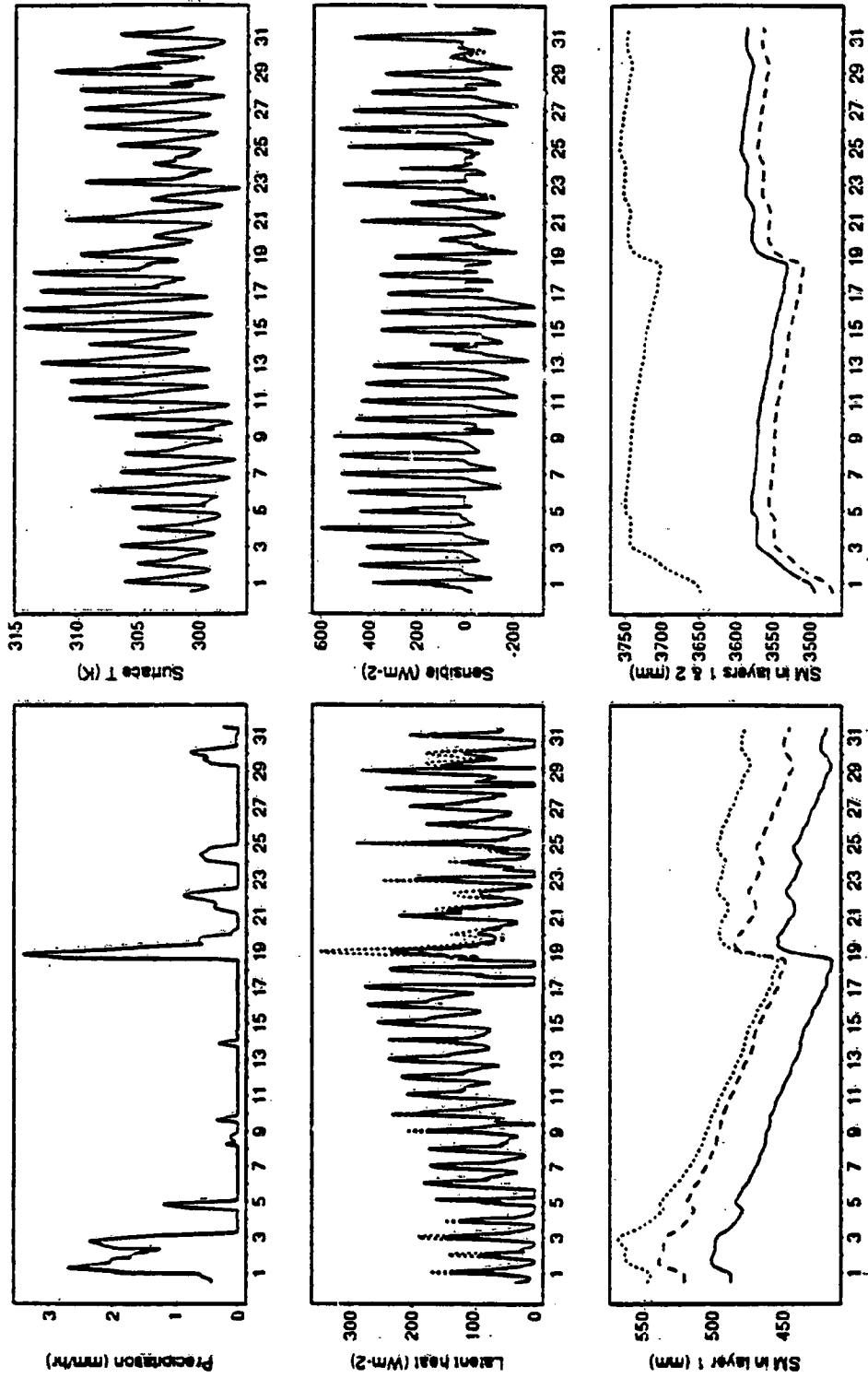
Fig. 5.5 Comparison of effective surface fluxes, temperature, and soil moisture among pixel-based (solid), derived distribution (dashed) and average (dotted) approaches for March with $\mu=0.3$ for PILPS forest site.
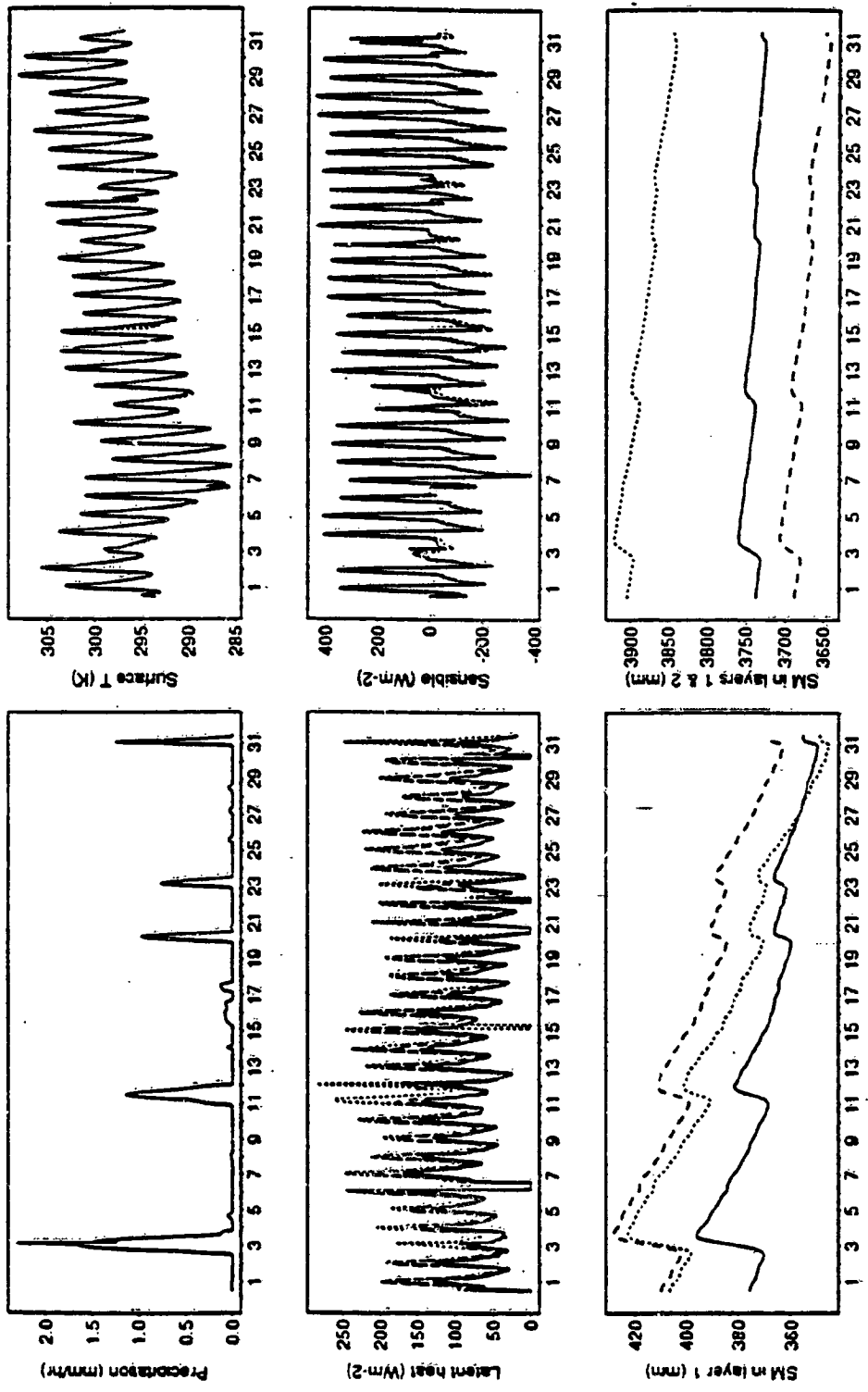
Fig. 5.6 Comparison of effective surface fluxes, temperature, and soil moisture among pixel-based (solid), derived distribution (dashed) and average (dotted) approaches for April with $\mu=0.3$ for PILPS forest site.

Fig. 5.7 Comparison of effective surface fluxes, temperature, and soil moisture among pixel-based (solid), derived distribution (dashed) and average (dotted) approaches for May with $\mu=0.3$ for PILPS forest site.

Fig. 5.8. Comparison of effective surface fluxes, temperature, and soil moisture among pixel-based (solid), derived distribution (dashed) and average (dotted) approaches for June with $\mu=0.3$ for PILPS forest site.
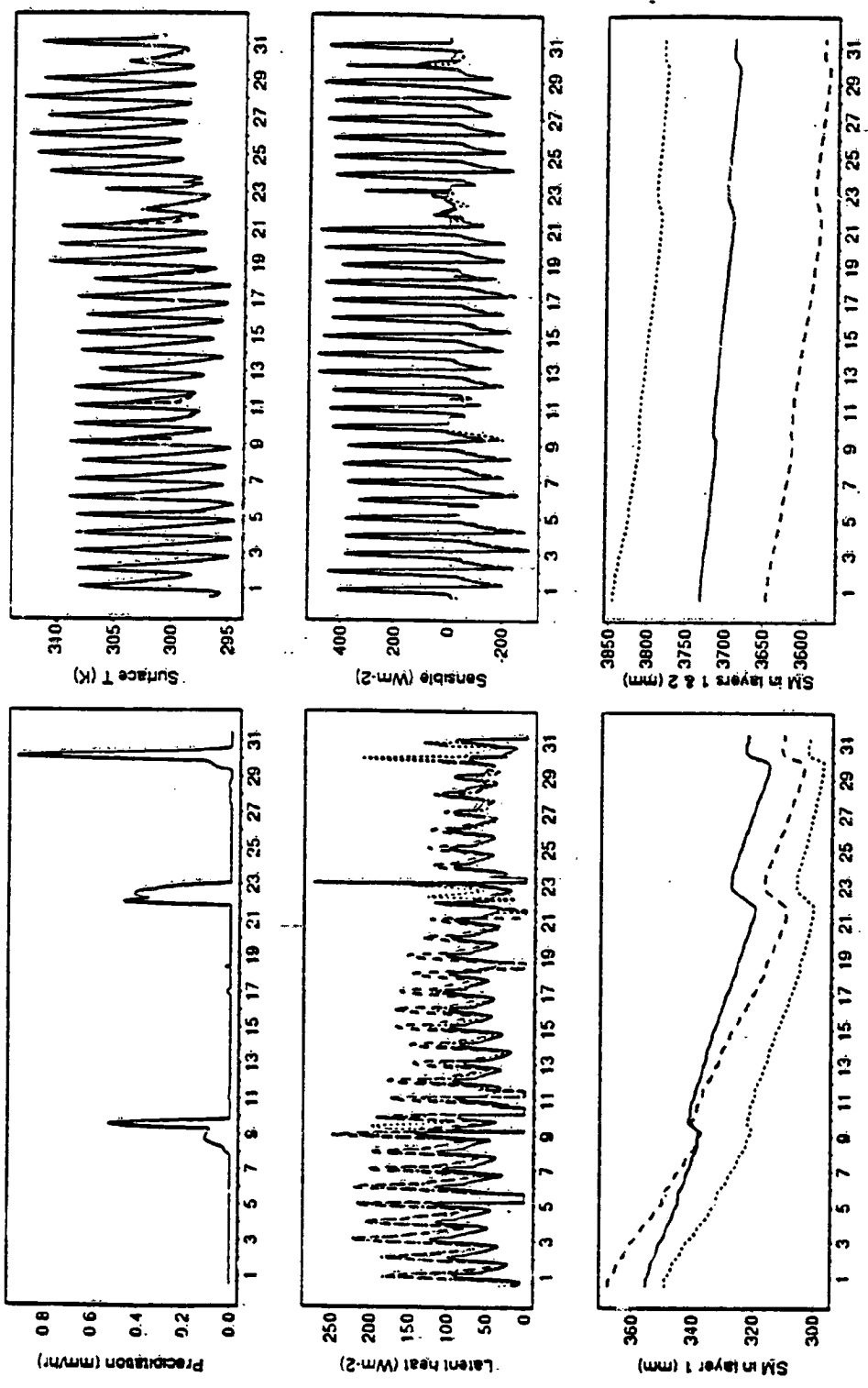
Fig. 5.9 Comparison of effective surface fluxes, temperature, and soil moisture among pixel-based(solid), derived distribution (dashed) and average (dotted) approaches for July with $\mu=0.3$ for PILPS forest site.

Fig. 5.10 Comparison of effective surface fluxes, temperature, and soil moisture among pixel-based (solid), derived distribution (dashed) and average (dotted) approaches for August with $\mu=0.3$ for PILPS forest site.
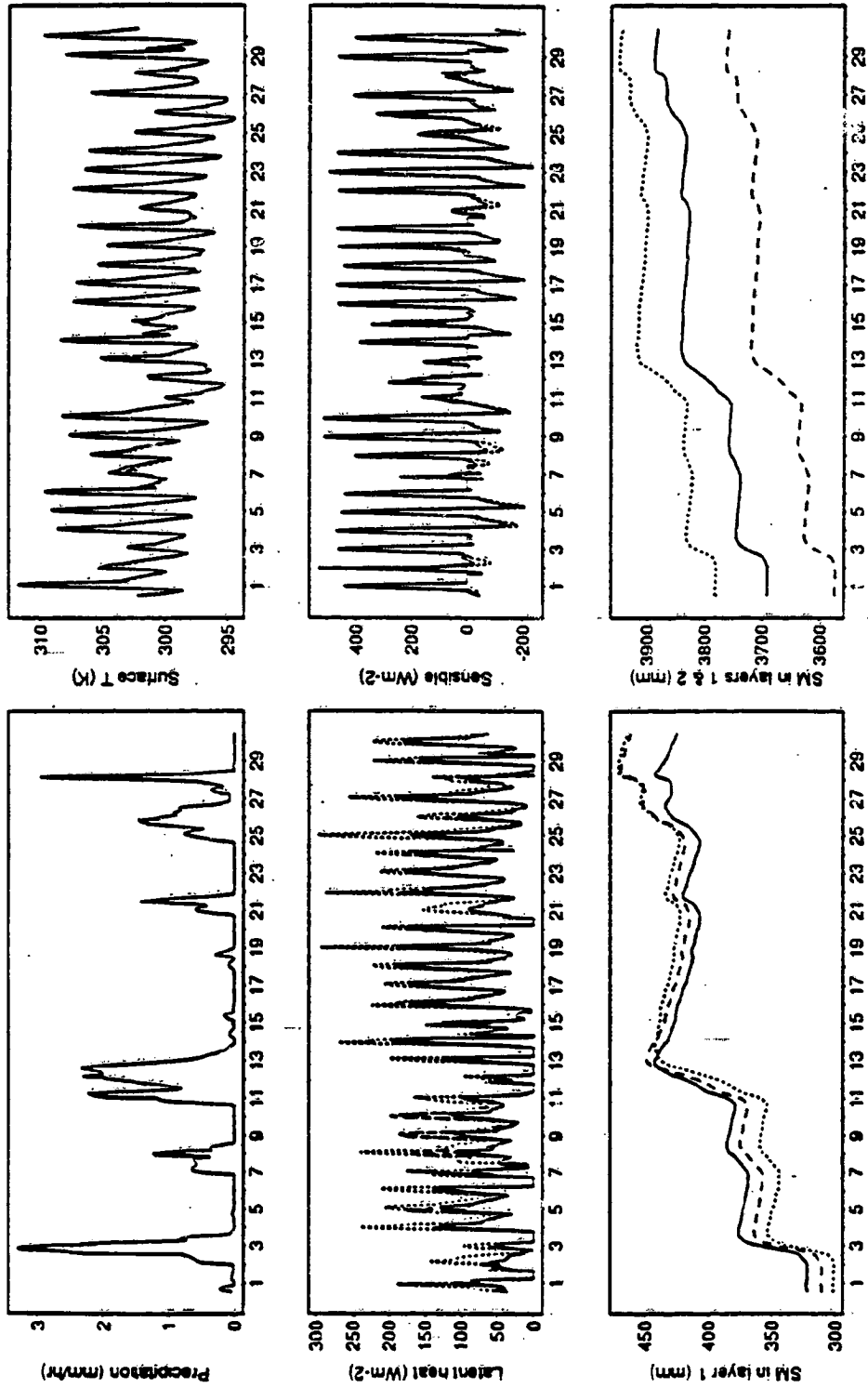
Fig. 5.11 Comparison of effective surface fluxes, temperature, and soil moisture among pixel-based (solid), derived distribution (dashed) and average (dotted) approaches for September with $\mu=0.3$ for PILP forest site.
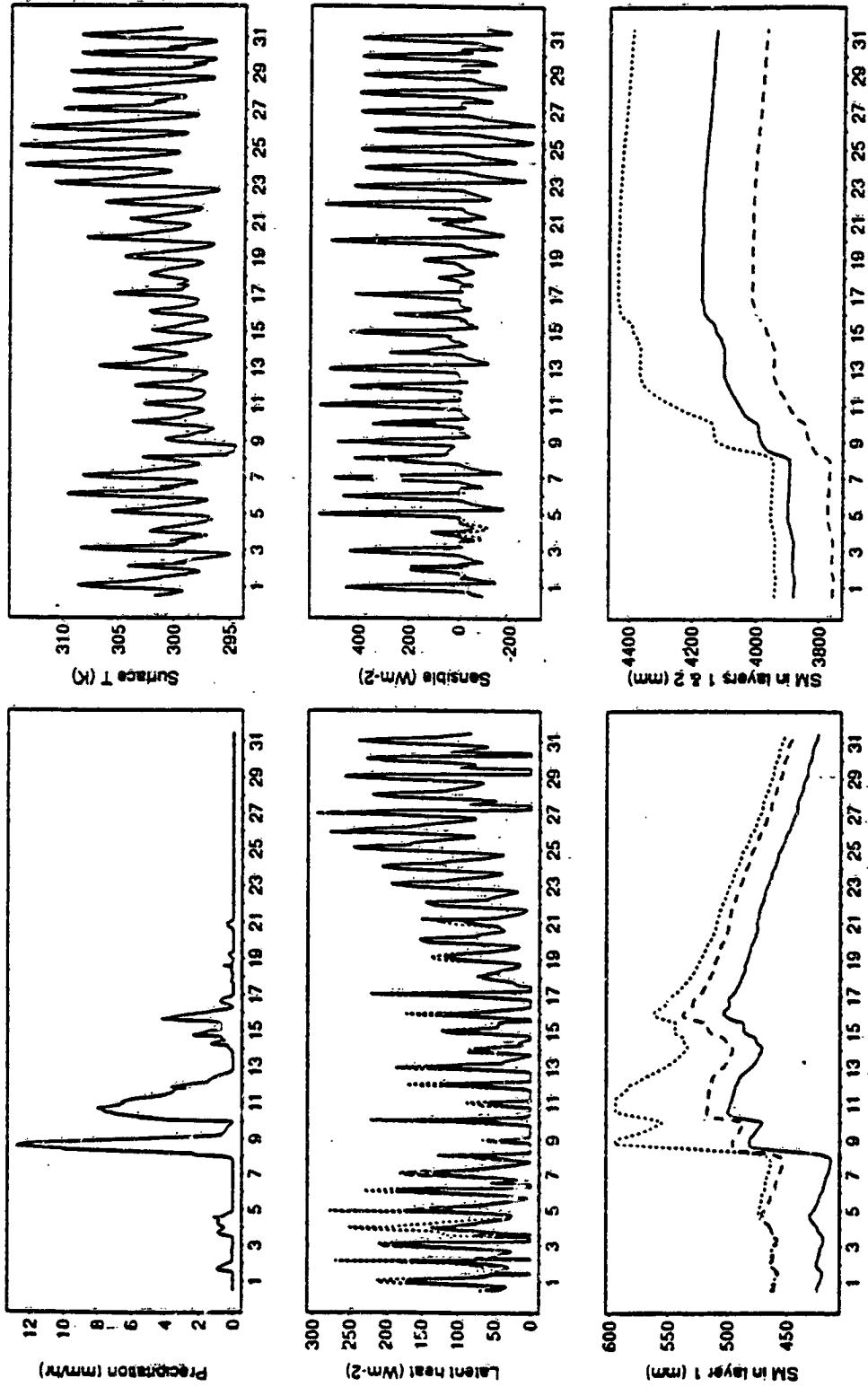
Fig. 5.12 Comparison of effective surface fluxes, temperature, and soil moisture among pixel-based (solid), derived distribution (dashed) and average (dotted) approaches for October with $\mu=0.3$ for PILPS forest site.
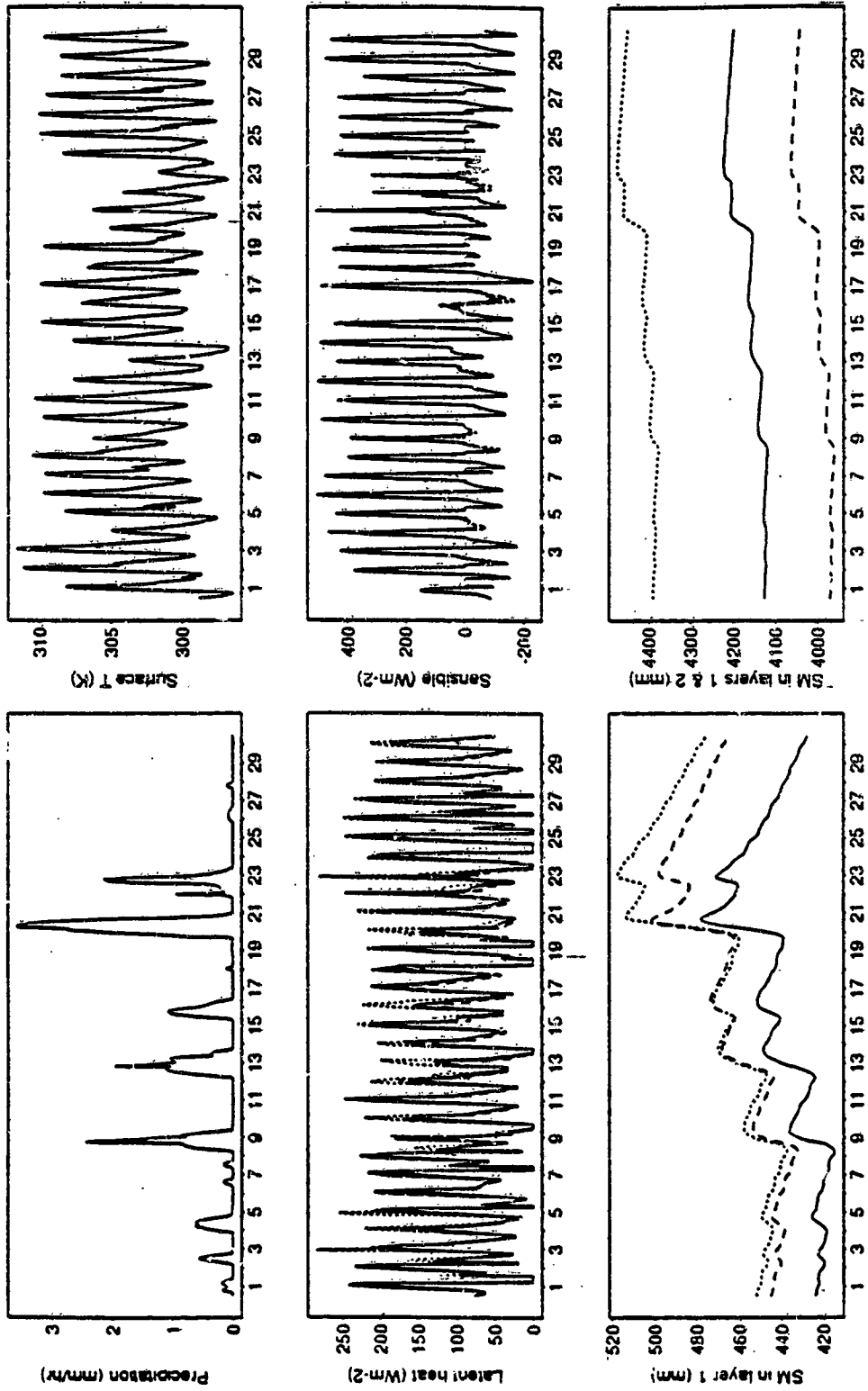
Fig. 5.13 Comparison of effective surface fluxes, temperature, and soil moisture among pixel-based (solid), derived distribution (dashed) and average (dotted) approaches for November with μ=0.3 for PILPS forest site.
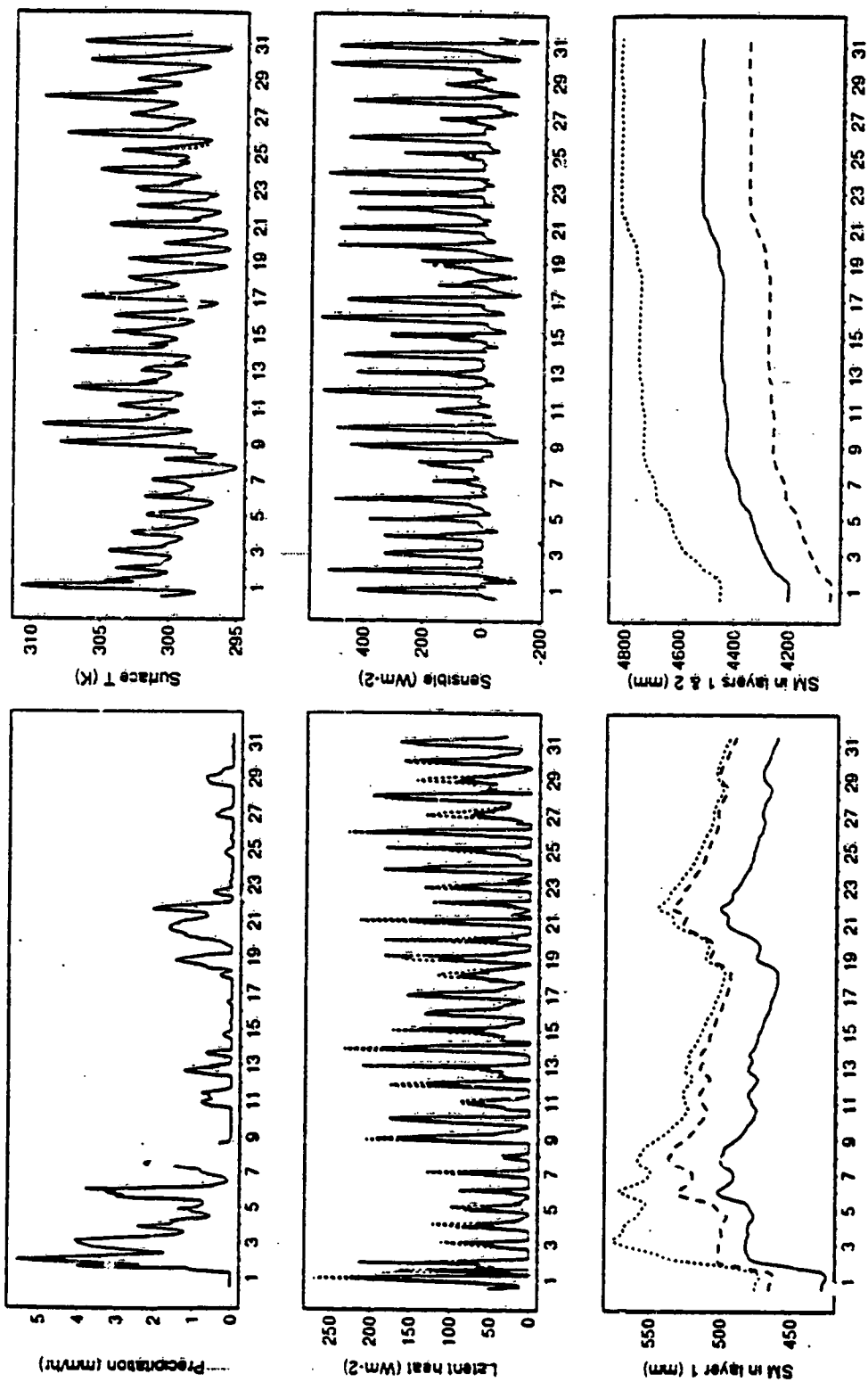
Fig. 5.14 Comparison of effective surface fluxes, temperature, and soil moisture among pixel-based (solid), derived distribution (dashed) and average (dotted) approaches for December with $\mu=0.3$ for PILPS forest site.
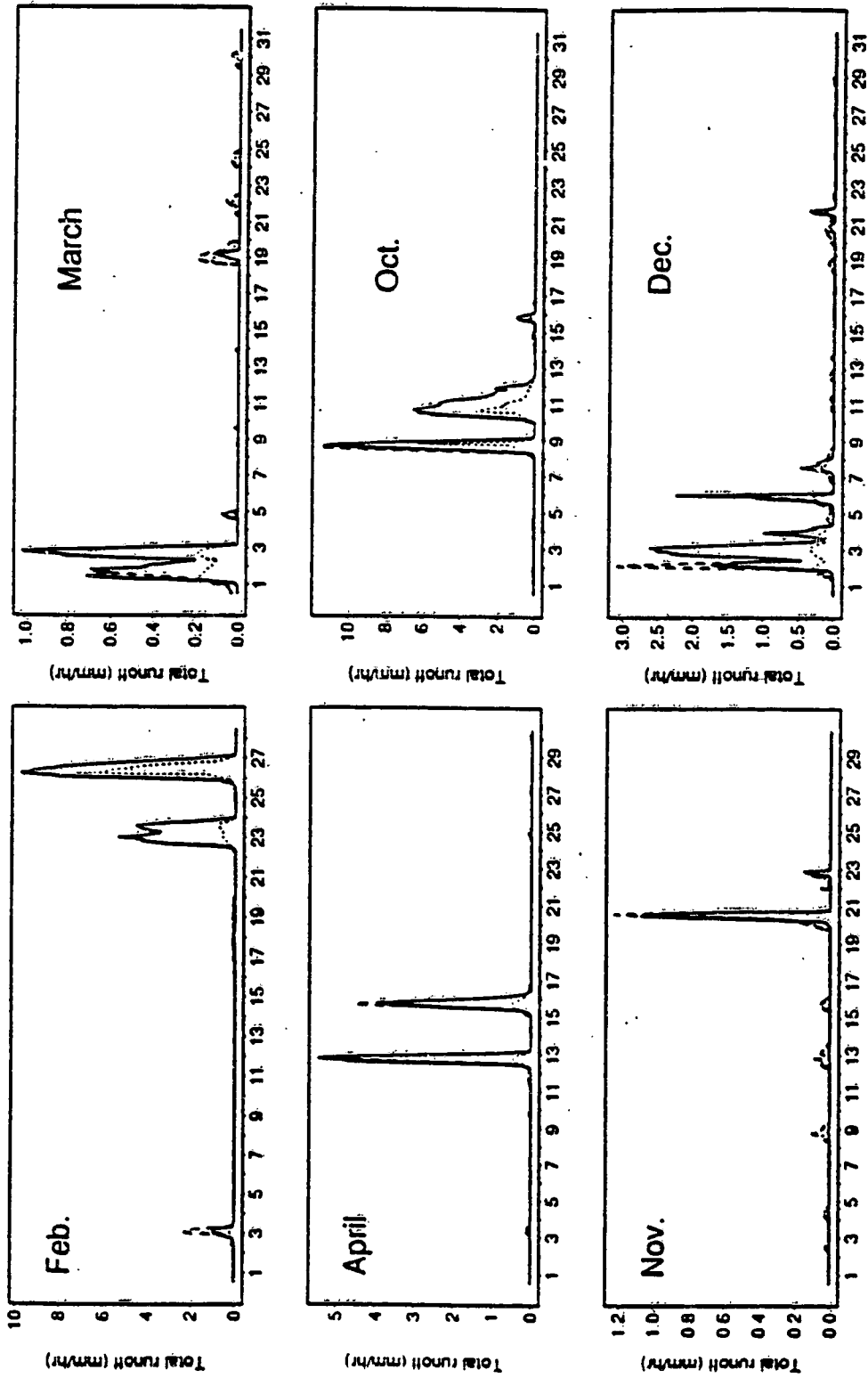
Fig. 5.15 Comparison of runoff among pixel-based (solid), derived distribution (dashed) and average (dotted) approaches for $\mu=0.3$ for the PILPS forest site.

Fig. 5.16 Comparison of effective surface fluxes, temperature, and soil moisture among pixel-based (solid), derived distribution (dashed) and average (dotted) approaches for May with $\mu=0.3$ for PILPS grassland site.

Fig. 5.17 Comparison of effective surface fluxes, temperature, and soil moisture among pixel-based (solid), derived distribution (dashed) and average (dotted) approaches for June with $\mu=0.3$ for PILPS grassland site.
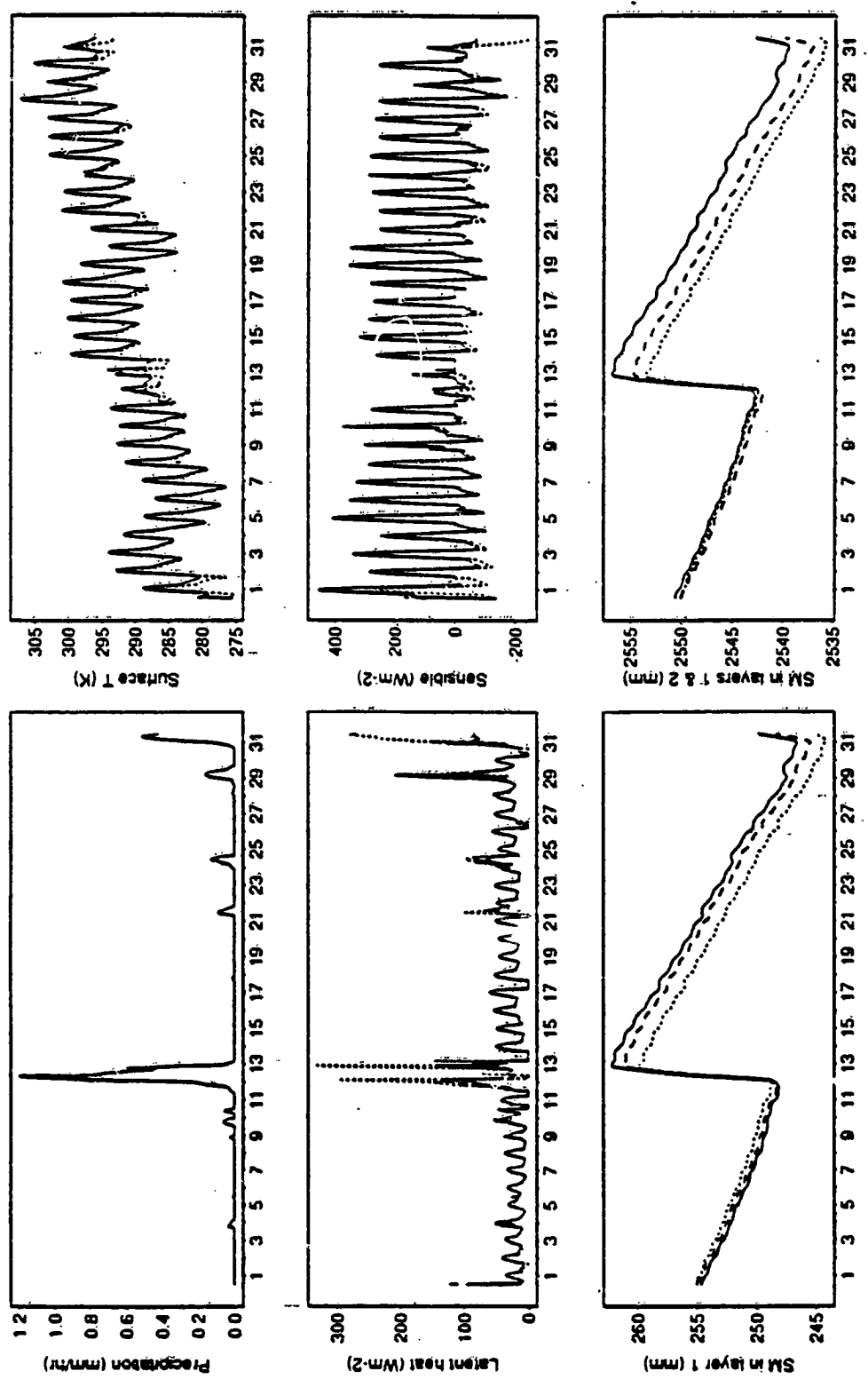
Fig. 5.18 Comparison of effective surface fluxes, temperature, and soil moisture among pixel-based (solid), derived distribution (dashed) and average (dotted) approaches for July with $\mu=0.3$ for PILPS grassland site.

Fig. 5.19 Comparison of effective surface fluxes, temperature, and soil moisture among pixel-based (solid), derived distribution (dashed) and average (dotted) approaches for August with $\mu=0.3$ for PILPS grassland site.
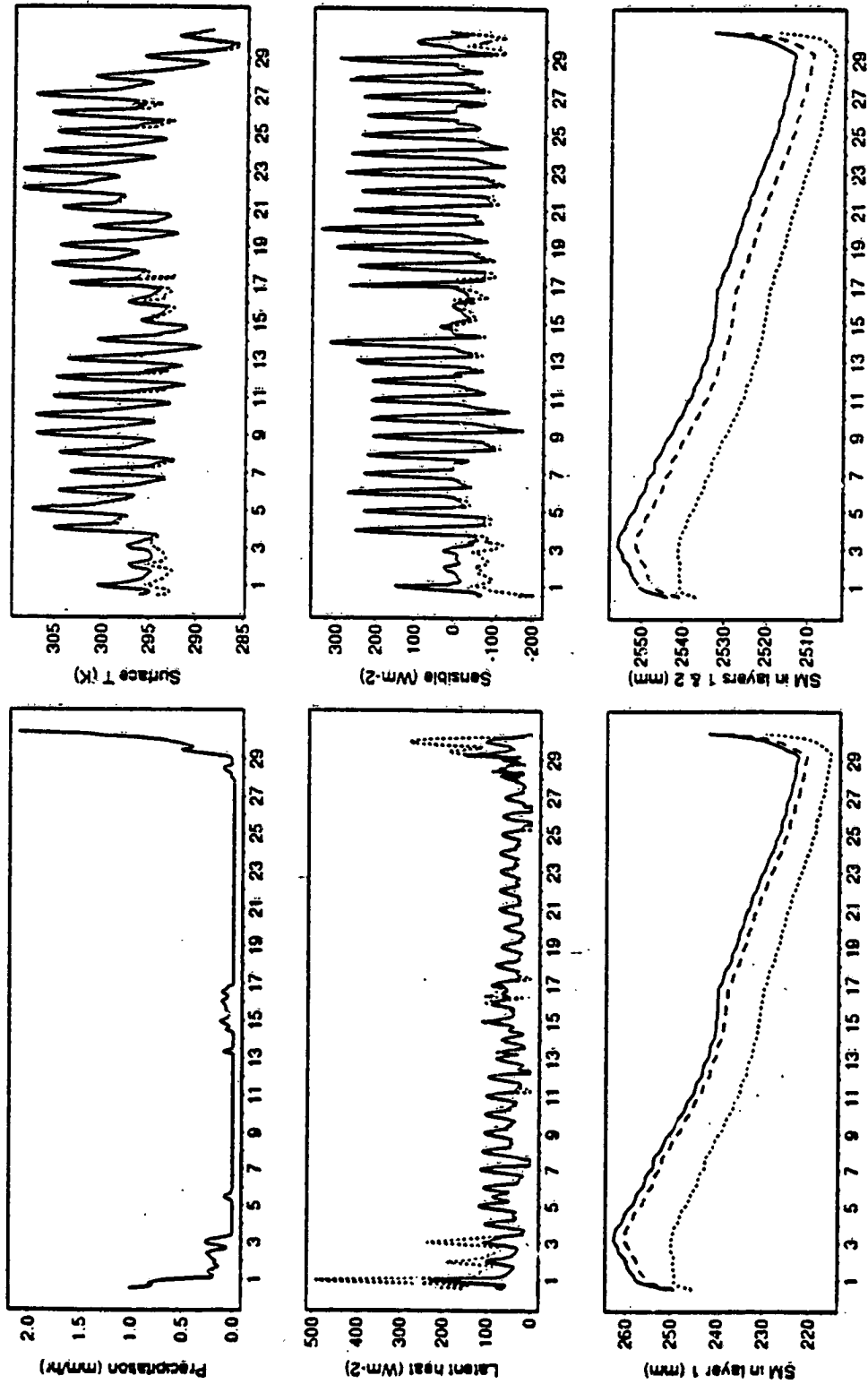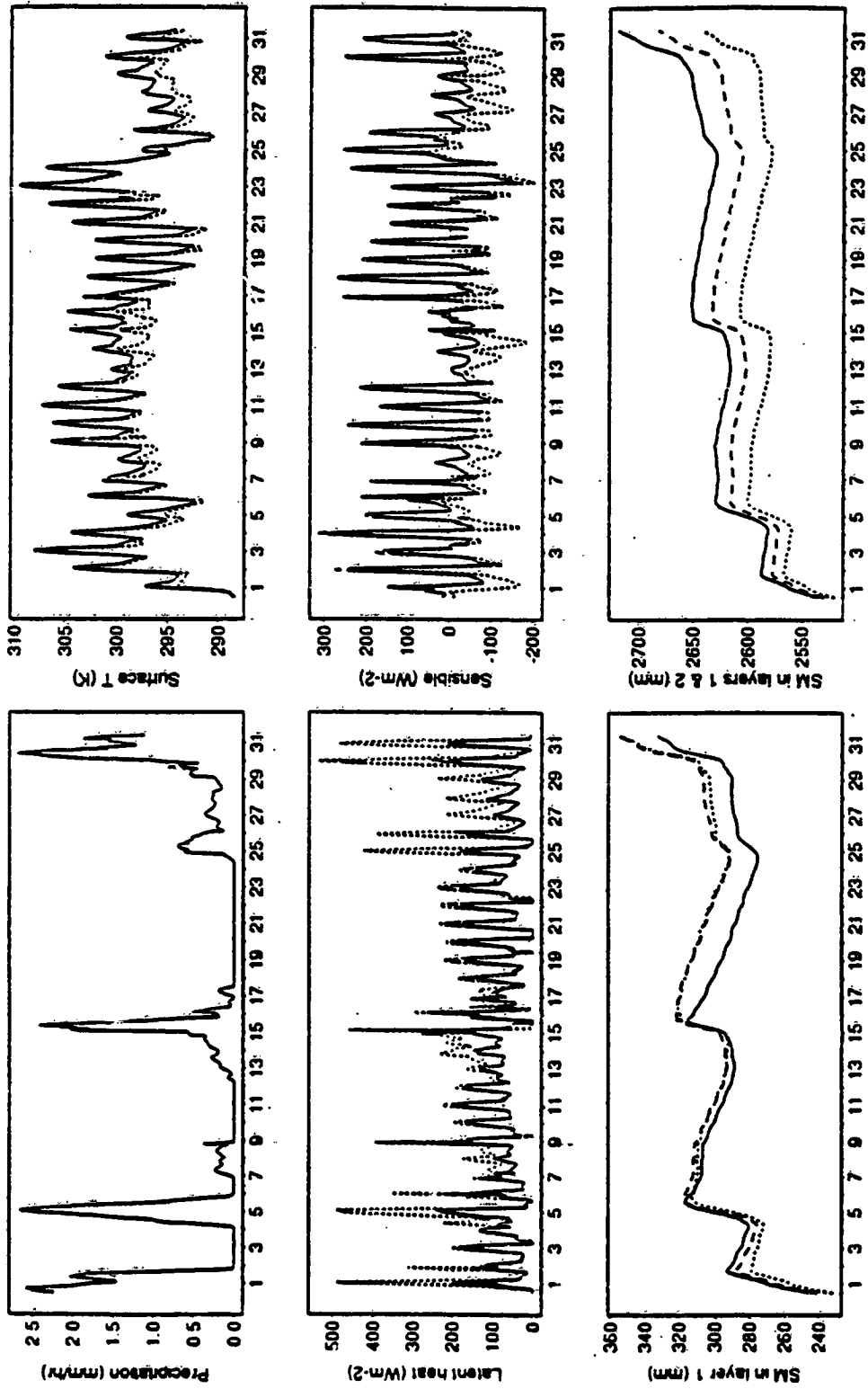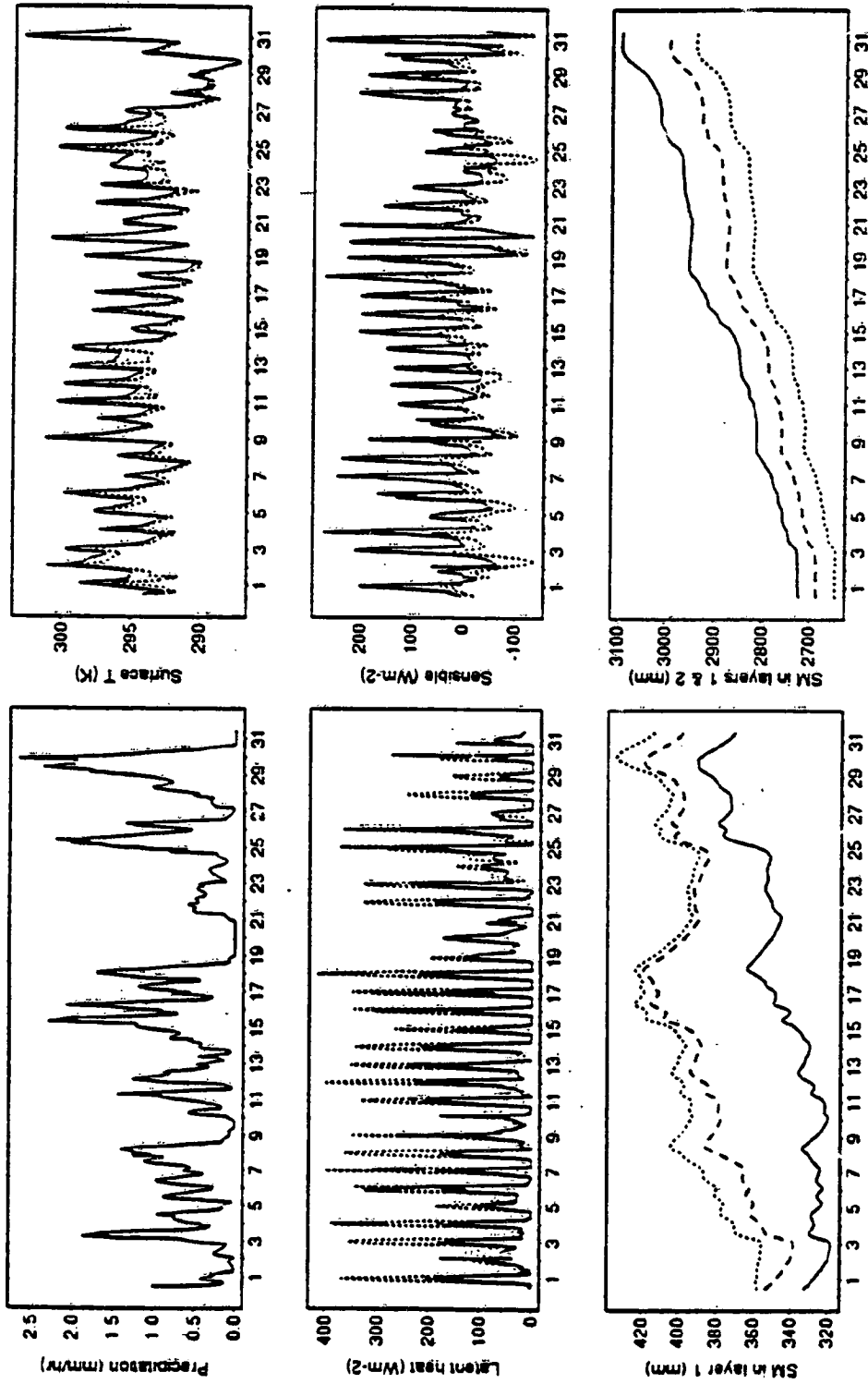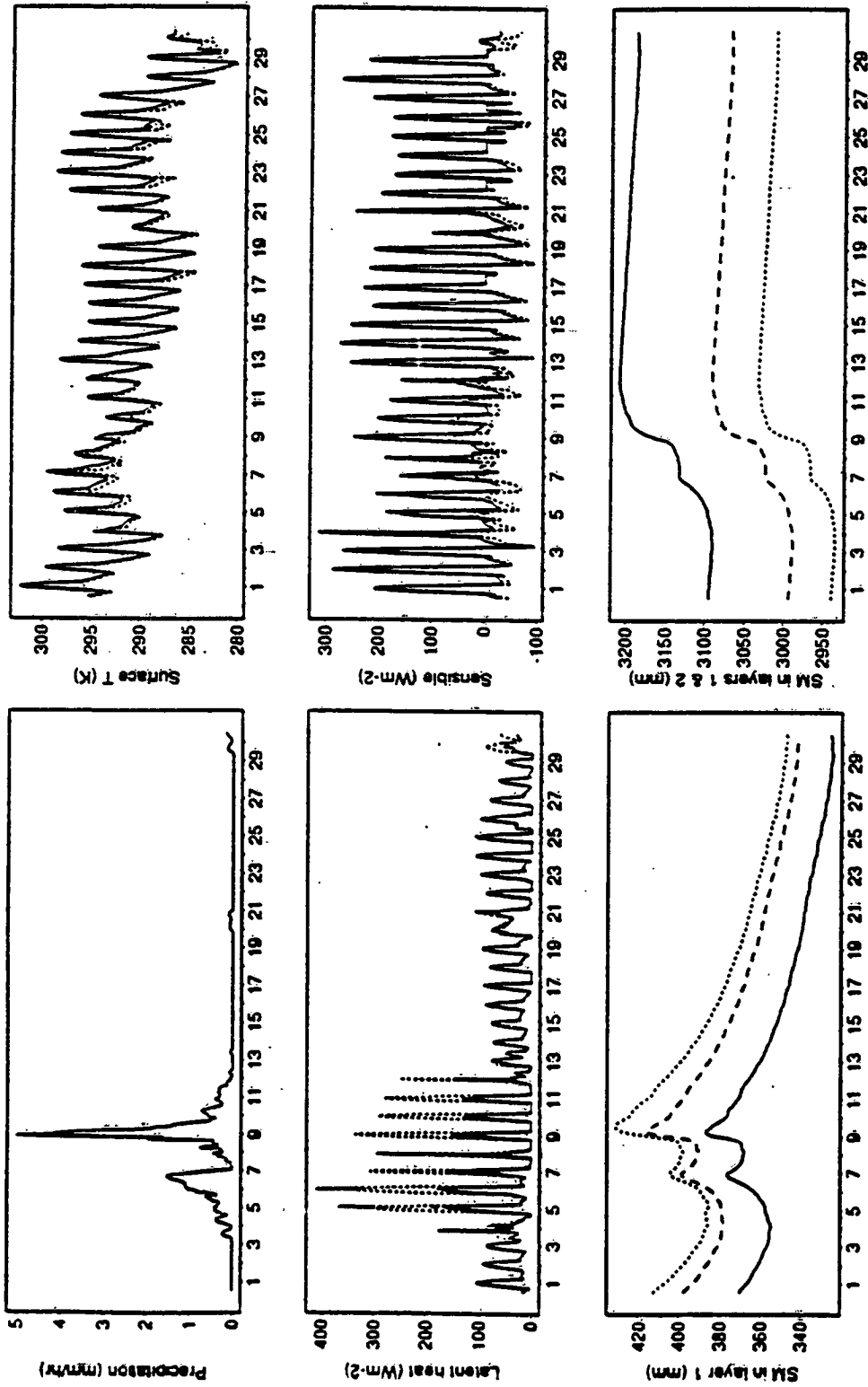
Fig. 5.20 Comparison of effective surface fluxes, temperature, and soil moisture among pixel-based (solid), derived distribution (dashed) and average (dotted) approaches for September with $\mu=0.3$ for PILP grassland site.

CHAPTER 6 CONCLUSIONS AND RECOMMENDATIONS FOR FUTURE WORK

A simple two-layer variable infiltration capacity (VIC-2L) model has been developed to model land-atmosphere interactions at the scale of general circulation models used for numerical weather prediction and climate change studies. The model includes a canopy layer, which partitions the area of interest into N land surface cover types. For each land cover type, the fraction of roots in the upper and lower layer is specified. Evaporation occurs via canopy evaporation, evaporation from bare soil (land cover class N+1), and transpiration, which is represented via a canopy and architectural resistance formulation. In the soil, the effects of spatial subgrid variability of soil moisture with hydrologically plausible runoff mechanism are represented through the upper layer and lower layer. The upper layer, which is designed to represent the dynamic behavior of the soil as it responds to rainfall, is characterized by spatial distributions of infiltration and soil moisture capacities. The lower layer, which is used to characterize the seasonal soil moisture behavior, is spatially lumped and uses the Arno drainage representation. Drainage from the upper layer to the lower layer is assumed to be driven by gravity. The effect of the subgrid spatial distribution of rainfall is accounted using a derived distribution approach. This approach results in a one-dimensional statistical-dynamic closure form based on four assumptions. The four assumptions are: (1) precipitation varies along x axis within a fractional coverage μ; (2) the soil moisture content of each strip within the fractional coverage μ of the same vegetation cover is averaged at the end of each time step; (3) the soil moisture is averaged over the fractional coverage μ and the non-rainfall fractional coverage $1-\mu$ prior to the beginning of next storm; and (4) each strip has an identical infiltration capacity distribution function. The VIC-2L model includes both atmospheric and hydrologic model parameters.

6.1. Conclusions

The VIC-2L model performed well for two applications where the climate regimes are quite different. The first application was to the FIFE site in central Kansas, where the climate was relatively dry, and the land cover was tall grass. The second site was in north central Brazil, which has a moist, tropical rainforest climate, and where the land cover is a ranch clearing surrounded by forest.

At both the FIFE (35 days of data) and ABRACOS (59 days of data) sites, the VIC-2L model reproduced the latent heat flux well, with 80% and 90%, respectively, of the daytime hourly peaks having relative errors less than 15%. Although more than 80% of the days (FIFE and ABRACOS) had sensible heat flux daytime hourly peaks less than $200Wm^{-2}$, there were still about 60% and 55%, respectively, of the daytime hourly peaks with relative errors less than 15%. For the ground heat flux, the majority of days had daytime hourly peaks on the order of $50Wm^{-2}$, and there were about 40% and 55% of the daytime peaks, respectively, with relative errors less than 15%. For the upper layer soil moisture, the comparison at the ABRACOS site (no observed soil moisture data were available at the FIFE site) showed that the largest relative difference between the model simulated and the observed soil moisture was less than 8%. There were 70% of the days with surface temperature difference less than 2 °C at the FIFE site. For the streamflow at the FIFE site (not available at the ABRACOS site), the reproduction of dry period flows and the timing of the major peaks of the observed streamflow was satisfactory, although the magnitudes of the large peaks were subject to substantial errors.

Since most rain over land is convective, the inclusion of spatial subgrid scale variability in precipitation should provide a better representation of land surface dynamics than the average precipitation representation for those areas. The effects of subgrid spatial variability of precipitation on surface fluxes, soil moisture, and runoff were incorporated into the VIC-2L model. The model performance was evaluated by comparing hourly simulations of latent and sensible heat fluxes, surface temperature, runoff, and soil moistures with the

pixel-based approach simulations for two different (hypothetical) climate regimes. In addition, the simulated latent and sensible heat fluxes, surface temperature, runoff, and soil moisture were compared with the results obtained by assuming constant precipitation over the area. The comparison showed that the derived distribution approach approximated the pixel-based approach quite well, and it was superior to constant precipitation approach in terms of predicted surface fluxes, surface temperature, runoff, and soil moistures almost all the time. The simulations with constant precipitation over the area overestimated latent heat flux and underestimated sensible heat flux compared with the pixel-based simulations due to much more interception evaporation, especially when the precipitation rate is small. Also, the constant precipitation experiment simulated much smaller runoff, particularly for median and large precipitation, as compared with the pixel-based results. In addition, the bias of the annual average and five-month average latent and sensible heat fluxes at the forest and grassland sites was about 20 Wm^{-2} from the average precipitation approach, while it was only about 5 Wm^{-2} from the derived distribution approach.

Finally, the VIC-2L model parameters were explored for two different climate regimes through both fractional factorial and one-at-a-time sensitivity analyses. Three metrics were chosen: annual total evaporation, annual total runoff, and annually averaged sensible heat flux. For these metrics, the leaf area index, porosity, and the minimum stomatal resistance were found to be important, while the soil thermal conductivity and soil heat capacity were found to be most sensitive for the minimum hourly surface temperature metric. These results are similar to those obtained by Henderson-Sellers (1992, 1993) using the BATS model. When the sum of the absolute difference of monthly evaporation and sensible heat flux between the control experiment and the 32 experiments were used as metrics, the model was found to be most sensitive to a similar set of parameters as those indicated by using the annual total evaporation and annually averaged sensible heat flux as metrics. However, for the absolute difference metrics, it was the interactions of these parameters rather than the single parameter effects that were found to be most important.

The infiltration shape parameter, the fraction of maximum subsurface flow, and the fraction of the lower layer maximum soil moisture were found to have minimal influence on the annual total runoff metric. Although the two fraction parameters redistribute the monthly runoff within a year, they did not change the total amount of the annual runoff. However, these three parameters and their interactions among themselves and with the parameters of porosity and wilting point were found to be sensitive when the sum of the absolute difference of monthly runoff from the control experiment was used as the metric.

6.2. Recommendations for future work

There are a number of research topics related to the current work that are suggested by this work, and are worthy of future exploration. Three suggestions for immediate follow up work related to representation of subgrid scale variability of the soil moisture stress factor associated with transpiration, subgrid scale variability in snow properties, and model validation and implementation into GCMs are described briefly.

6.2.1. Subgrid scale spatial variability in g_{sm}

From Chapter 2, it is seen that the representation of evaporation from bare soil (Eq. 2.22) accounts for subgrid spatial variability in soil moisture, but the effect of subgrid spatial variability of soil moisture on transpiration from vegetation (Eqs. 2.12-2.14) is only partially accounted for. The weakness of Eq. 2.14 is shown in Chapter 5 when comparing with the exhaustive experiment results for the forest site in August. Therefore, it is necessary to account for the subgrid spatial variability of soil moisture on transpiration in a manner similar to that used for bare soil evaporation. This can be done through the soil moisture stress factor $g_{sm}[n]$ (Eqs. 2.13 and 2.14) which depends on the water available in the root zone. Due to the definition of the upper layer and lower layer, the soil moisture in the upper layer is more spatially variable than that in the lower layer. Thus, the soil moisture stress factor $g_{sm}[n]$ of layer 1 should have larger variations within a grid cell (or an area) than that of layer 2. We can, therefore,

only consider the influence of subgrid variability of soil moisture in layer 1 on $g_{sm}[n]$. A lumped soil moisture content expression of $g_{sm}[n]$ can be used for layer 2 as before. From the definition of $g_{sm}[n]$ (Eqs. 2.14a-2.14c), we obtain,

$$g_{sm}^{-1}[n] = A_{cr}[n] \cdot 1 + \int_{A_{cr}[n]}^{A_w[n]} \frac{dW_1[n] - dW_1^w}{dW_1^{cr} - dW_1^w} \, dA + \int_{A_w[n]}^{1} 0 \cdot dA \qquad (6.1)$$

where $W_1[n]$, W_1^w, and W_1^{cr} have the same meanings as in Chapter 2, and $A_{cr}[n]$ and $A_w[n]$ represent the fraction of the soil whose soil moisture is greater than or equal to the critical value above which the transpiration is not affected by the moisture stress in the soil, and the value associated with the permanent wilting point respectively, and (see Fig. 2.2),

$$dW_1[n] = i_0 \cdot dA$$

$$dW_1^w = \theta_w \cdot i \cdot dA$$

$$dW_1^{cr} = \theta_{cr} \cdot i \cdot dA$$

where θ_w is the permanent wilting point (dimensionless), θ_{cr} is the critical value (dimensionless), i_0 represents the point infiltration capacity corresponding to the soil moisture $W_1[n]$, and A is the fraction of the area for which the infiltration capacity is less than i (see Eq. 2.20). Let

$$i_w = \theta_w \cdot i \,,$$
$$i_{cr} = \theta_{cr} \cdot i,$$

then combining with Eq. 2.20, we have

$$i_w = \theta_w \cdot i_m \, [1 - (1 - A)^{1/b_i}] \qquad (6.2)$$

$$i_{cr} = \theta_{cr} \cdot i_m \left[1 - (1 - A)^{1/b_i}\right] \tag{6.3}$$

Thus, in Eq. (6.1), the second term can be expressed as,

$$\int_{A_{cr}[n]}^{A_w[n]} \frac{dW_1[n] - dW_1^w}{dW_1^{cr} - dW_1^w} dA = \int_{A_{cr}[n]}^{A_w[n]} \frac{i_0 \cdot dA - i_w \cdot dA}{i_{cr} \cdot dA - i_w \cdot dA} dA = \int_{A_{cr}[n]}^{A_w[n]} \frac{i_0 - i_w}{i_{cr} - i_w} dA$$

$$= \frac{i_0}{(\theta_{cr} - \theta_w) \cdot i_m} \int_{A_{cr}[n]}^{A_w[n]} \frac{1}{1 - (1 - A)^{1/b_i}} dA - \frac{\theta_w(A_w[n] - A_{cr}[n])}{\theta_{cr} - \theta_w}. \tag{6.4}$$

The integrand of Eq. (6.4) can be either numerically integrated or expanded into a power series. The terms $A_w[n]$ and $A_{cr}[n]$ are determined as follows. From Eq. 2.20, we can obtain the relationship between i_0 and $W_1[n]$,

$$i_0 = i_m\left[1 - \left(1 - \frac{W_1[n]}{W_1^c}\right)^{\frac{1}{1+b_i}}\right] \tag{6.5}$$

Equating Eq. (6.2) with Eq. (6.5), and Eq. (6.3) with Eq. (6.5) respectively, then,

$$i_0 = \theta_w \cdot i_m \left[1 - (1 - A_w[n])^{1/b_i}\right] = i_m\left[1 - \left(1 - \frac{W_1[n]}{W_1^c}\right)^{\frac{1}{1+b_i}}\right] \tag{6.6}$$

$$i_0 = \theta_{cr} \cdot i_m \left[1 - (1 - A_{cr}[n])^{1/b_i}\right] = i_m\left[1 - \left(1 - \frac{W_1[n]}{W_1^c}\right)^{\frac{1}{1+b_i}}\right]. \tag{6.7}$$

Therefore, if $i_m \cdot \theta_w > i_0$, we have for $A_w[n]$,

$$A_W[n] = 1 - [1 - \frac{1 - (1 - \frac{W_1[n]}{W_1^C})^{\frac{1}{1+b_i}}}{\theta_W}]^{b_i} \qquad (6.8)$$

and if $i_m \cdot \theta_{cr} > i_0$, we have for $A_{cr}[n]$,

$$A_{cr}[n] = 1 - [1 - \frac{1 - (1 - \frac{W_i[n]}{W_1^C})^{\frac{1}{1+b_i}}}{\theta_{cr}}]^{b_i}. \qquad (6.9)$$

If $i_m \cdot \theta_W \leq i_0$, then $A_W[n]=1$; while if $i_m \cdot \theta_{cr} \leq i_0$, $A_{cr}[n]=1$.

6.2.2. Subgrid scale spatial variability in a snowpack

In the midcontinents of North American and Eurasia, winter snow and spring melt are important components of the hydrologic cycle. Snowmelt in spring generally produces spring peaks in streamflow. Numerous snowmelt models are described in the literature. These models can be grouped into three classes (Morris 1985): regression models, lumped conceptual models, and distributed models. Each class of these models has its strengths and weaknesses. The subgrid spatial variability in snowpack properties has not been included into the present form of the VIC-2L model. However, in a context consistent with the approach described in Chapter 5 for the subgrid spatial variability of precipitation, the subgrid spatial variability related to snowpack properties could be accounted for with a similar degree of complexity.

One way to include the subgrid spatial variability of snow is to incorporate Donald's (1992) findings of a log-normal spatial distribution for snow depth and linear relationship of snow depletion curve into the snowmelt module (Wigmosta et al. 1994) of the VIC-2L model by using the derived distribution

approach described in Chapter 5. Based on snow surveys conducted in southern Ontario, Canada, Donald found that snow depth can be described by a lognormal distribution within a shallow and often discontinuous snow covered area. In addition, he showed when snowmelt is assumed to occur uniformly over the snowcovered area, the redistribution and accumulation of snow within an area classified by vegetation cover types can be summarized by linear snow depletion curves (SDC) for different cover types. The snow depletion curve, which can be characterized by two classes, forest and non-forest, describes the relationship between average snowcover depth and snowcovered area for a given vegetation cover type (Donald 1992).

Two assumptions are needed to incorporate Donald's findings. The first is that the area (or a grid cell) is relatively flat so that topographic effects such as slopes, aspects, and shading are insignificant over the snowcovered area (i.e., the net radiation received over the snowcovered area is relatively uniform). The second is that the rain falling on the snowcovered area will be redistributed in such a way that the heat advected to the snowpack by the rainfall will be the same within the snowcovered area. With these two assumptions, it can be assumed that the snowmelt will occur uniformly over the snowcovered area, and Donald's linear relationship of SDC can then be applied.

6.2.3. Validation and implementation into GCMs

As seen in Chapters 3 and 5, the VIC-2L model was only applied to two specific sites, both of which were small. Therefore, the model should be applied to more sites with different soil type properties and climate conditions. In addition, observed data when available over a large area should be used to test the one-dimensional statistical-dynamic model described in Chapter 5, since the approach of including the subgrid spatial variability of precipitation (see Chapter 5) was not tested using observed data. One possibility is to use the data from HAPEX-MOBILHY (Hydrological Atmospheric Pilot Experiment) which were collected over an area on the order of 100×100 km. The observations were conducted in 1986 with one Intensive Field Campaign (IFC) of duration several

months in southwestern France (Shuttleworth 1991b). The study area with multisite measurements consists of forest, agricultural land, and some wood cover area. The observed data include surface pressure, air temperature, dewpoint temperature, wind, vegetation information, radiation information, and streamflow (Goutorbe and Tarrieu 1991).

To test the global performance of the VIC-2L model, the effects of feedbacks from GCMs should be investigated. Therefore, implementation of the VIC-2L model into a GCM is a logical next step in evaluation of the model.

REFERENCES

Abdulla, F.A.M., Development of a stochastic single-site seasonal rainfall simulator (for application in Irbid region), M.S. thesis, Jordan Univ. of Science and Technology, Jordan, July 1987.

Abramopoulos, F., C. Rosenzweig, and B. Choudhury, Improved ground hydrology calculations for global climate models (GCMs): Soil water movement and evapotranspiration, *J. Clim.*, *1*, 921-941, 1988.

Arola, A., Effects of subgrid scale spatial variability on mesoscale snow modeling, M.S. thesis, Dept. of Civil Eng., Univ. of Washington, Seattle, June, 1993.

Arya, S.P., *Introduction to Micrometeorology*, 307 pp., Academic, San Diego, Calif., 1988.

Avissar, R., and R.A. Pielke, A parameterization of heterogeneous land surface for atmospheric numerical models and its impact on regional meteorology, *Mon. Weather Rev.*, *117*, 2113-2136, 1989.

Avissar, R., A statistical-dynamical approach to parameterize subgrid-scale land-surface heterogeneity in climate models, *Land Surface-Atmospheric Interactions for Climate Modeling: Observations, Models and Analysis*, E.F. Wood, Ed., Kluwer Academic Publishers, 155-178, 1991.

Avissar, R., Conceptual aspects of a statistical-dynamical approach to represent landscape subgrid-scale heterogeneities in atmospheric models, *J. Geophys. Res.*, *97*(D3), 2729-2742, 1992.

Avissar, R., Observations of leaf stomatal conductance at the canopy scale: An atmospheric modeling perspective, *Bound.-layer Meteor.*, *64*, 127-148, 1993.

Betts, A.K., J.H. Ball, and A.C.M. Beljaars, Comparison between the land

surface response of the ECMWF model and the FIFE-1987 data, *Q.J.R. Meterorol. Soc., 119*, 975-1001, 1993.

Beven, K.J., and M.J. Kirkby, A physically based variable contributing area model of basin hydrology, *Hydrol. Sci. Bull., 24*(1), 43-69, 1979.

Blondin, C., Parameterization of land-surface processes in numerical weather prediction, in *Land Surface Evaporation: Measurements and Parameterization*, T.J. Schmugge and J.C. Andre, Ed., pp. 31-54, Springer-Verlag, New York, 1991.

Blyth, E.M., A.J. Dolman, and J. Noilhan, Aggregation of surface fluxes from partially wet mesoscale areas, in *Proceedings of the Yokohama Symposium, IAHS Pub. 212*, pp. 325-330, July 1993.

Bonan, G.B., D. Pollard, and S.L. Thompson, Effects of boreal forest vegetation on global climate, *Nature, 359*, 716-718, 1992.

Bonan, G.B., D. Pollard, and S.L. Thompson, Influence of subgrid-scale heterogeneity in leaf area index, stomatal resistance, and soil moisture on grid-scale land-atmosphere interactions, *J. Clim., 6*, 1882-1897, 1993.

Bougeault, P., Parameterization schemes of land-surface processes for mesoscale atmospheric models, *Land Surface Evaporation: Measurements and Parameterization*, T.J. Schmugge and J.C. Andre, Ed., pp. 55-92, Springer-Verlag, New York, 1991.

Box, G.E.P., W.G. Hunter, and J.S. Hunter, *Statistics for experiments: An introduction to design, data analysis, and modeling building*, 653 pp., John Wiley and Sons, Inc., New York, 1978.

Braud, I., J.D. Creutin, and C. Barancourt, The relation between the mean areal rainfall and the fractional area where it rains above a given threshold, *J. Appl.*

Meteor., 32, 193-202, 1993.

Brooks, R.H., and A.T. Corey, Hydraulic properties of porous media, *Hydrol. Pap. 3,* Colo. State Univ., Ft. Collins, 1964.

Brutsaert, W.H., *Evaporation into the atmosphere, theory, history and applications,* 299 pp., D. Reidel Publ. Comp., Dordrecht, Boston, 1982.

Campbell, G.S., *An introduction to environmental biophysics,* 159 pp., Springer-Verlag, New York, 1977.

Collier, C.G., The application of a continental-scale radar database to hydrological process parameterization within atmospheric general circulation models, *J. Hydrol., 142,* 301-318, 1993.

Deardorff, J.W., Efficient prediction of ground surface temperature and moisture, with inclusion of a layer of vegetation, *J. Geophy. Res., 83,* 1889-1903, 1978.

Dickinson, R.E., Modelling evapotranspiration for three-dimensional global climate models, in *Climate Processes and Climate Sensitivity, Geophys. Monogr. Ser., 29,* J.E. Hansen and T. Takahashi, ed., pp. 58-72, AGU, Washington, D.C., 1984.

Dickinson, R.E., A. Henderson-Sellers, P.J. Kennedy, and M.F. Wilson, Biosphere-atmosphere transfer scheme (BATS) for the NCAR community climate model, *NCAR Tech. Note, TN-275+STR,* 1986.

Dickinson, R.E., and A. Henderson-Sellers, Modelling tropical deforestation: A study of GCM land-surface parameterizations, *Q.J.R. Meteorol. Soc., 114*(B), 439-462, 1988.

Dickinson, R.E., Global change and terrestrial hydrology – a review, *Tellus, 43AB,*

176-181, 1991.

Dickinson, R.E., and P.J. Kennedy, Land surface hydrology in a general circulation model – global and regional fields needed for validation, in *Land Surface-Atmospheric Interactions for Climate Modeling: Observations, Models and Analysis*, E.F. Wood, Ed., pp. 115-126, Kluwer Academic Publishers, 1991.

Dickinson, R.E., A. Henderson-Sellers, and P.J. Kennedy, Biosphere-atmosphere transfer scheme (BATS) version 1e as coupled to the NCAR community climate model, *NCAR Tech. Note, TN-387+STR*, 1993.

Dolman, A.J., and D. Gregory, The parameterization of rainfall interception in GCMs, *Q.J.R. Meteorol. Soc., 118*, 455-467, 1992.

Donald, J.R., Snowcover depletion curves and satellite snowcover estimates for snowmelt runoff modeling, Ph.D. dissertation, Univ. of Waterloo, Canada, 1992.

Ducoudre, N.I., K. Laval, and A. Perrier, SECHIBA, a new set of parameterizations of the hydrologic exchanges at the land-atmosphere interface within the LMD atmospheric general circulation model, *J. Clim., 6*, 248-273, 1993.

Dumenil, L., and E. Todini, A rainfall-runoff scheme for use in the Hamburg climate model, in *Advances in Theoretical Hydrology, A Tribute to James Dooge*, J.P. O'Kane, Ed., pp. 129-157, European Geophys. Soc. Series on Hydrological Sciences, 1, Elsevier, Amsterdam, 1992.

Duynkerke, P.G., The roughness length for heat and other vegetation parameters for a surface of short grass, *J. App. Meteorol., 31*, 579-586, 1992.

Eagleson, P.S., *Dynamic hydrology*, 462 pp., McGraw-Hill Book Comp., New York,

1970.

Eagleson, P.S., The distribution of catchment coverage by stationary rainstorms, *Water Resour. Res.*, *20*(5), 581-590, 1984.

Eagleson, P.S., and Q. Wang, Moments of catchment storm area, *Water Resour. Res.*, *21*(8), 1185-1194, 1985.

Eagleson, P.S., N.M. Fennessey, Q. Wang, and I. Rodriguez-Iturbe, Application of spatial Poisson models to air mass thunderstorm rainfall, *J. Geophys. Res.*, *92*(D8), 9661-9678, 1987.

Eltahir, E.A.B., and R.L. Bras, Estimation of the fractional coverage of rainfall in climate models, *J. Clim.*, *6*, 639-644, 1993.

Entekhabi, D., and P.S. Eagleson, Land surface hydrology parameterization for atmospheric general circulation models including subgrid scale spatial variability, *J. Clim.*, *2*, 816-831, 1989.

Environmental Protection Agency (EPA), Global ecosystems database documentation, in *EPA Global Climate Research Program NOAA/NGDC Global Change Database Program*, EPA Res. Lab., Corvallis, Ore., 1991.

Famiglietti, J.S., and E.F. Wood, Evapotranspiration and runoff from large land areas; Land surface hydrology for atmospheric general circulation models, in *Land Surface-Atmospheric Interactions for Climate Modeling: Observations, Models and Analysis*, E.F. Wood, Ed., pp. 179-204, Kluwer Academic Publishers, 1991.

Famiglietti, J.S., E.F. Wood, M. Sivapalan, and D.J. Thongs, A catchment scale water balance model for FIFE, *J. Geophys. Res.*, *97*(D17), 18,997-19,007, 1992.

Famiglietti, J.S., and E.F. Wood, Multi-scale modeling of spatially-variable water and energy balance processes, *Water Resour. Res.,* in press, 1994a.

Famiglietti, J.S., and E.F. Wood, Application of multi-scale water and energy balance model on a tall grass prairie, *Water Resour. Res.,* in press, 1994b.

Foufoula-Georgiou, E., and L.L. Wilson, In search of regularities in extreme rainstorms, *J. Geophys. Res., 95*(D3), 2061-2072, 1990.

Francini, M., and M. Pacciani, Comparative analysis of several conceptual rainfall-runoff models, *J. Hydrol., 122,* 161-219, 1991.

Gao, X., and S. Sorooshian, A stochastic precipitation disaggregation scheme for GCM applications, *J. Clim., 7,* 238-247, 1994.

Garratt, J.R., and B.B. Hicks, Momentum, heat and water vapour transfer to and from natural and artificial surfaces, *Q.J.R. Meteorol. Soc., 99,* 680-687, 1973.

Garratt, J.R., Transfer characteristics for a heterogeneous surface of large aerodynamic roughness, *Q.J.R. Meteorol. Soc., 104,* 491-502, 1978.

Garratt, J.R., Sensitivity of climate simulations to land-surface and atmospheric boundary-layer treatments – a review, *J. Clim., 6,* 419-449, 1993.

Goutorbe, J.P., and C. Tarrieu, HAPEX-MOBILHY data base, in *Land Surface Evaporation: Measurements and Parameterization,* T.J. Schmugge and J.C. Andre, Ed., pp. 403-410, Springer-Verlag, 1991.

Hamon, R.W., L.L. Weiss, and W.T. Wilson, Insolation as an empirical function of daily sunshine duration, *Mon. Weather Rev., 82,* 141-146, 1954.

Hamon, R.W., Estimating potential evapotranspiration, *J. Hydraulics Div., Am. Soc.*

Civ. Eng., *87*, 107-120, 1961.

Henderson-Sellers, A., Assessing the sensitivity of a land-surface scheme to parameters used in tropical-deforestation experiments, *Q.J.R. Meteorol. Soc.*, *118*, 1101-1116, 1992.

Henderson-Sellers, A., and A. Pitman, Land-surface schemes for future climate models: specification, aggregation, and heterogeneity, *J. Geophys. Res.*, *97*(D3), 2687-2696, 1992.

Henderson-Sellers, A., A factorial assessment of the sensitivity of the BATS land-surface parameterization scheme, *J. Clim.*, *6*, 227-247, 1993.

Henderson-Sellers, A., R.E. Dickinson, T.B. Durbidge, P.J. Kennedy, K. McGuffie, and A.J. Pitman, Tropical deforestation: modeling local- to regional-scale climate change, *J. Geophys. Re.*, *98*(D4), 7289-7315, 1993.

Hodnett, M.G., L.P. da Silva, H.R. Rocha, and R. Cruz Senna, Seasonal soil water storage changes beneath central Amazonian pasture land and rainforest, *manuscript*, 1993.

Johnson, K.D., D. Entekhabi, and P.S. Eagleson, The implementation and validation of improved land-surface hydrology in an atmospheric general circulation model, *J. Clim.*, *6*, 1009-1026, 1993.

Kondo, J., and T. Watanabe, Studies on the bulk transfer coefficients over a vegetated surface with a multilayer energy budget model, *J. Atmos. Sci.*, *49*(23), 2183-2199, 1992.

Koster, R.D., and M.J. Suarez, Modeling the land surface boundary in climate models as a composite of independent vegetation stands, *J. Geophys. Res.*, *97*(D3), 2697-2715, 1992a.

Koster, R.D., and M.J. Suarez, A comparative analysis of two land surface heterogeneity representations, *J. Clim., 5*, 1379-1390, 1992b.

Lean, J., and D.A. Warrilow, Simulation of the regional climatic impact of Amazon deforestation, *Nature, 342*, 411-413, 1989.

Lean, J., and P.R. Rowntree, A GCM simulation of the impact of Amazonian deforestation on climate using an improved canopy representation, *Q.J.R. Meteorol. Soc., 119*, 509-530, 1993.

Liang, X., D.P. Lettenmaier, and E.F. Wood, A two-layer variable infiltration c· city land surface parameterization for GCMs, Paper presented at '93 Joint International Meeting, IAMAP·IAHS, Yokohama, Japan, July 1993.

Liang, X., D.P. Lettenmaier, E.F. Wood, and S.J. Burges, A simple hydrologically based model of land surface water and energy fluxes for general circulation models, *J. Geophys. Res.*, accepted, 1994.

Louis, J., A parametric model of vertical eddy fluxes in the atmosphere, *Boundary Layer Met. 17*, 187-202, 1979.

Mahrt, L., and M. Ek, The influence of atmospheric stability on potential evaporation, *J. Clim. Appl. Meteor., 23*, 222-234, 1984.

Mahrt, L., and H. Pan, A two-layer model of soil hydrology, *Bound.-Layer Meteor., 29*, 1-20, 1984.

Manabe, S., Climate and the ocean circulation I. The atmospheric circulation and the hydrology of the Earth surface, *Mon. Weather Rev., 97*, 739-774, 1969.

McWilliam, A.L.C., J.M. Roberts, O.M.R. Cabral, M.V.B.R. Leitao, A.C.L. de

Costa, G.T. Maitelli, and C.A.G.P. Zamparoni, Leaf area index and above-ground biomass of terra firm rain forest and adjacent clearings in Amazonia, *Functional Ecology*, *7*, 1-8, 1993.

Milly, P.C.D., Potential evaporation and soil moisture in general circulation models, *J. Clim.*, *5*, 209-226, 1992.

Mintz, Y., The sensitivity of numerically simulated climates to land-surface boundary conditions, in *Global Climate*, J.T. Houghton, Ed., pp. 79-105, Cambridge Univ. Press, 1984.

Monteith, J.L., and M.H. Unsworth, *Principles of Environmental Physics*, 291 pp., 2nd ed., Routledge, Chapman and Hall, New York, 1990.

Morris, E.M., Snow and ice, in *Hydrological Forecasting*, M.G. Anderson and T.P. Burt Ed., pp. 153-182, Wiley, Chichester, 1985.

Myers, N., Tropical forests: present status and future outlook, *Clim. Change, 19,* 3-32, 1991.

Noilhan, J., and S. Planton, A simple parameterization of land surface processes for meteorological models, *Mon. Weather Rev., 117,* 536-549, 1989.

Pan, H., A simple parameterization scheme of evapotranspiration over land for the NMC medium-range forecast model, *Mon. Weather Rev., 118,* 2500-2512, 1990.

Pielke, R.A., G.A. Dalu, J.S. Snook, T.J. Lee, and T.G.F. Kittel, Nonlinear influence of mesoscale land use on weather and climate, *J. Clim., 4,* 1053-1069, 1991.

Pitman, A.J., A. Henderson-Sellers, and Z.L. Yang, Sensitivity of regional

climates to localized precipitation in global models, *Nature, 346*, 734-737, 1990.

Pitman, A.J., Z.L. Yang, J.G. Cogley, and A. Henderson-Sellers, Description of bare essentials of surface transfer for the bureau of meteorology research center AGCM, *BMRC Research report*, Bureau of meteorology research center, Melbourne, Victoria, Australia, 32, 1991.

Pitman, A.J., T.B. Durbidge, A. Henderson-Sellers, and K. McGuffie, Assessing climate model sensitivity to prescribed deforested landscapes, *Int. J. Climatol.*, *13*, 879-898, 1993.

Pitman, A.J., A. Henderson-Sellers, D.P. Lettenmaier, X. Liang, E.F. Wood, et al., Project for intercomparison of land-surface parameterization schemes (PILPS): Results from off-line control simulation (phase 1a), *GEWEX IGPO Pub. Series 7*, Dec., 1993.

Raupach, M.R., The averaging of surface flux densities in heterogeneous landscapes, in *Proceedings of the Yokohama Symposium, IAHS Pub. 212*, pp. 343-355, July 1993.

Rowntree, P.R., Review of GCMs as a basis for predicting the effects of vegetation change on climate, in *Forests, Climate, and Hydrology – RegionalImpacts*, E.R.C. Reynolds and F.B. Thompson, Eds., pp. 162-196, The United Nations Univ., 1988.

Saugier, B., and N. Katerji, Some plant factors controlling evapotranspiration, *Agricultural and Forest Met., 54*, 263-277, 1991.

Sellers, P.J., Y. Mintz, Y.C. Sud, and A. Dalcher, A simple biosphere model (SiB) for use within general circulation models, *J. Atmos. Sci., 43(6)*, 505-531, 1986.

Sellers, P.J., and J.L. Dorman, Testing the simple biosphere model (SiB) using point micrometeorological and biophysical data, *J. Appl. Meteor.*, *26*, 622-651, 1987.

Sellers, P.J., F.G. Hall, G. Asrar, D.E. Strebel, and R.E. Murphy, The first ISLSCP field experiment (FIFE), *Bull. Am. Met. Soc.*, *69*, 22-27, 1988.

Shukla, J., and Y. Mintz, Influence of land-surface evapotranspiration on the earth's climate, *Science*, *215*, 1498-1501, 1982.

Shuttleworth, W.J., Macrohydrology – the new challenge for process hydrology, *J. Hydrol.*, *100*, 31-56, 1988.

Shuttleworth, W.J., Insight from large-scale observational studies of land/atmosphere interactions, in *Land Surface-Atmospheric Interactions for Climate Modeling: Observations, Models and Analysis*, E.F. Wood, Ed., pp. 3-30, Kluwer Academic Publishers, 1991a.

Shuttleworth, W.J., The modellion concept, *Rev. Geophys.*, *29*(4), 585-606, 1991b.

Shuttleworth, W.J., J.H.C. Gash, J.M. Roberts, C.A. Norbe, L.C.B. Molion, and M. de Nazare Goes Ribeiro, Post-deforestation Amazonian climate: Anglo-Brazilian research to improve prediction, *J. Hydrol.*, *129*, 71-85, 1991.

Shuttleworth, W.J., Evaporation, in *Handbook of Hydrology*, D.R. Maidment, Ed., pp.4.1-4.53, McGraw-Hill, Inc., New York, 1993.

Siebert, J., U. Sievers, and W. Zdunkowski, A one-dimensional simulation of the interaction between land surface processes and the atmosphere, *Bound.-Layer Meteor.*, *59*, 1-34, 1992.

Sievers, U., R. Forkel, and W.G. Zdunkowski, Transport equations for heat and

moisture in the soil and their application to boundary layer problems, *Beitr. Phys. Atmoph., 56,* 58-83, 1983.

Sivapalan, M.K., K.Beven, and E.F. Wood, On hydrologic similarity, 2, A scaled model of storm runoff production, *Water Resour. Res., 23*(12), 2266-2278, 1987.

Smith, E.A., W.L. Crosson, and B.D. Tanner, Estimation of surface heat and moisture fluxes over a prairie grassland 1. In situ energy budget measurements incorporating a cooled mirror dew point hygrometer, *J. Geophys. Res., 97*(D17), 18,557-18,582, 1992a.

Smith, E.A., A.Y. Hsu, W.L. Crosson, et al., Area-averaged surface fluxes and their time-space variability over the FIFE experimental domain, *J. Geophys. Res., 97*(D17), 18,599-18,622, 1992b.

Smith, E.A., H.J. Cooper, W.L. Crosson, and H. Weng, Estimation of surface heat and moisture fluxes over a prairie grassland 3. Design of a hybrid physical/remote sensing biosphere model, *J. Geophys. Res., 98*(D3), 4951-4978, 1993.

Stamm, J.F., E.F. Wood, and D.P. Lettenmaier, Sensitivity of a GCM simulation of global climate to the representation of land surface hydrology, *J. Clim.,* in press, 1994.

Sud., Y.C., P.J. Sellers, Y. Mintz, M.D. Chou, G.K. Walker, and W.E. Smith, Influence of the biosphere on the global circulation and hydrologic cycle – A GCM simulation experiment, *Agric. Forest Meteor., 52,* 133-180, 1990.

Sugita, M., and W. Brutsaert, Wind velocity measurements in the neutral boundary layer above hilly prairie, *J. Geophys. Res., 95*(D), 7617-7624, 1990.

Thomas, G. and A. Henderson-Sellers, An evaluation of proposed representation

of subgrid hydrologic processes in climate models, *J. Clim.*, *2*, 898-910, 1991.

Verseghy, D.L., CLASS – A Canadian land surface scheme for GCMs, I. Soil model, *Int. J. Climatol.*, *11*, 111-133, 1991.

Verseghy, D.L., N.A. McFarlane, and M. Lazare, CLASS – A Canadian land surface scheme for GCMs, II. Vegetation model and coupled runs, *Int. J. Climatol.*, *13*, 347-370, 1993.

Wetzel, P., and J. Chang, Evapotranspiration from nonuniform surfaces: A first approach for short-term numerical weather prediction, *Mon. Weather Rev.*, *116*, 600-621, 1988.

Wigmosta, M., L. Vail, and D.P. Lettenmaier, A distributed hydrology-vegetation model for complex terrain, *Water Resour. Res.*, in press, 1994.

Wilson, M.F., R.E. Dickinson, and P.J. Kennedy, Sensitivity of the Biosphere-Atmosphere Transfer Scheme (BATS) to the inclusion of the variable soil characteristics, *J. Clim. Appl. Meteor.*, *26*, 341-362, 1987.

Wolock, D.M., G.M. Hornberger, K.J. Beven, and W.G. Campbell, The relationship of catchment topography and soil hydraulic characteristics to Lake Alkalinity in the Northeastern United States, *Water Resour. Res.*, *25*(5), 829-837, 1989.

Wood, E.F., Global scale hydrology: Advances in land surface modeling, *U.S. Natl. Rep. Int. Union Geod. Geophys. 1987-1990, Rev. Geophys.*, *29*, Supplement, 193-201, 1991.

Wood, E.F, D.P. Lettenmaier, and V.G. Zartarian, A land-surface hydrology parameterization with subgrid variability for general circulation models, *J. Geophys. Res.*, *97*(D3), 2717-2728, 1992.

Wright, I.R., J.H.C. Gash, H.R. Da Rocha, W.J. Shuttleworth, C.A. Nobre, G.T. Maitelli, C.A.G.P. Zamparoni, and P.R.A. Carvalho, Dry season micrometeorology of central Amazonian ranchland, *Q.J.R. Meteorol. Soc., 118,* 1083-1099, 1992.

Xue, Y., P.J. Sellers, J.L. Kinter and J. Shukla, A simplified biosphere model for global climate studies, *J. Clim., 4,* 345-364, 1991.

Yang, Z.L., and A.J. Pitman, Land-surface parameterizations for climate models: a new method for composite fluxes, in *Proceedings of the Yokohama Symposium, IAHS Pub. 212,* pp. 551-559, July 1993.

Zhao, R.J., Y.L. Zhang, L.R. Fang, X.R. Liu, and Q.S. Zhang, The Xinanjiang model, in *Hydrological Forecasting Proceedings Oxford Symposium, IASH 129,* pp. 351-356, 1980.

VITA

. Xu Liang was born on ████████ ████████████ ███. She received her Bachelor of Engineering from the Department of Hydraulic Engineering at Chengdu University of Science and Technology in 1984. She received her Master of Science in Hydraulic Engineering from Chengdu University of Science and Technology in 1987. After graduation, she was a lecturer in the Department of Hydraulic Engineering at the university. In 1988, she was given a teaching assistantship to study at the Department of Civil Engineering at the University of Washington and received her Master of Science in Environmental Engineering and Science in 1990. She began her Ph.D. study, supported by research assistantships, in the Department of Civil Engineering at the University of Washington in 1991. from which she received her Ph.D. in 1994.